Université de Liège
Faculté des Sciences

An observational study
of line-profile variable B stars

par

Maryline Briquet

Promoteurs:

Conny Aerts
Richard Scuflaire

MEMBERS OF THE SCIENTIFIC COMMITTEE:

Contents

Summary

S.1 Introduction

In this thesis we interpret the variability of line profiles for several main-sequence B-type stars. This study is carried out in the framework of a long-term monitoring of candidate slowly pulsating B stars led by members of the Institute of Astronomy of the University of Leuven.

In Sect. S.2 we present the kinds of B-type stars that we study in the scope of this thesis. Sect. S.3 describes shortly the methodology that we use to analyse data of these stars. In Sect. S.4, S.5 and S.6 we summarize the three contributions of our work. First we propose a significant improvement of the moment method for mode identification of multiperiodic rotating stars. Secondly we study northern slowly pulsating B stars discovered from the HIPPARCOS mission and more thoroughly the brightest northern SPB of our sample, HD 147394. Finally we outline and analyse four B-type stars that we modelled by rotational modulation. Sect. S.7 gives our outlook for future work.

S.2 Line-profile B variables

We study several main-sequence variable B stars belonging to two classes: the slowly pulsating B stars and the Bp variables. The characteristics of both groups are summarized in the following.

Slowly pulsating B stars

The slowly pulsating B stars (SPBs) were introduced as a new class of pulsating B-type stars by Waelkens (1991). They are situated along the main sequence with spectral types ranging between B 2 to B 9 and masses ranging between 3 $M_\odot$ to 7 $M_\odot$. They show light and line-profile variations, which are multiperiodic with periods of the order of days. This variability is understood in terms of non-radial stellar pulsations and their oscillation modes are high-order g-modes. Theoretical models attribute the pulsational nature of SPBs to the κ-mechanism, acting in the iron opacity bump at $2\,10^5$ K. The HIPPARCOS mission greatly increased the number of known SPB stars. About 100 candidate SPBs have been discovered up to now.

Bp/Ap variables

Bp/Ap variables are main-sequence chemically peculiar (CP) stars for which certain chemical elements show abnormal abundances compared to the Sun. Their temperatures range between 7 000 K and 18 000 K. The hotter members of Bp/Ap stars are characterized by strong silicon enhancements (Si stars) but appear to be helium weak (He-weak stars) in general. They show monoperiodic photometric and spectroscopic variations which are explained by the rotation of the star in presence of non-homogeneous distributions of elements on the stellar surface. Theoretical models have been developed for Ap stars. These ones explain the peculiarities of Ap stars by complex interactions between radiatively driven diffusion processes and a stellar magnetic field. The origin of magnetic fields observed for many Ap stars is not yet clearly understood.

S.3   Methodology

Non-radial pulsation theory

For slowly pulsating B stars we consider the non-radial stellar pulsation theory by Lee & Saio (1987, 1990), which takes into account the Coriolis force under some approximations that are reasonably good for low-frequency non-radial modes. We describe the theory that is useful for a comparison with our spectroscopic observations, i.e. an expression for the pulsational velocity at the stellar surface, which is then used for the modelling of line-profile variations.

In this work we also compare observed frequencies to theoretical ones. These latter are computed with the Code Liégeois d'Evolution Stellaire, that computes equilibrium models, and with the standard adiabatic code OSC that computes the oscillation frequencies. Both codes were implemented by Dr. R. Scuflaire. We have adapted OSC to include the Coriolis force in the framework of this thesis.

Line-profile modelling

Line-profile variations of a pulsating star are mainly caused by the velocity field at the stellar surface due to oscillatory displacements and by the brightness variations due to temperature variations. The modelling of the line-profile variations is done as follows. The stellar surface is divided in many surface elements. Each visible local line profile is computed to be summed up over the visible stellar surface. Local line profiles are intrinsic profiles rotationally broadened and Doppler shifted by the velocity field caused by pulsation. The intrinsic profile is time dependent because of varying effective temperature and gravity. We underline that this latter effect can be neglected for the modelling of the Si II 4128-4130 Å doublet in the case of slowly-rotating non-radially pulsating B stars as was shown by De Ridder et al. (2002a) and Dupret et al. (2002). In this work we generate

theoretical line-profile variations with the publicly available code BRUCE implemented by Townsend (1997).

Line-profile variations of chemically peculiar stars are caused by the stellar rotation and a non-homogeneous distribution of elements on the stellar surface. A simple model is the following. The flux of a circular spot (or several spots) differs from the flux of the rest of the stellar surface. Local intrinsic line profiles, taken gaussian and rotationally broadened, are computed taking into account this different abundance of the considered element in the spot. They are finally summed up over the visible stellar surface. In this work we use a code kindly put at our disposal by Dr. L. Balona.

Existing analysis methods

We derive frequencies in the datasets of our studied B variables by means of techniques commonly used by astronomers, which are Fourier methods (Scargle 1981, Roberts et al. 1987) and the Phase Dispersion Minimization (PDM) method (Jurkevich 1971, Stellingwerf 1978). The first type of methods is based on the fact that the Fourier transform of a harmonic signal underlines the frequencies present in this signal. The idea of the PDM method is that the dispersion of the observations in a phase diagram with respect to a mean curve is minimal for the frequency which is present in the data. In this work we use frequency analysis codes kindly put at our disposal by Dr. J. Cuypers and Dr. J. Telting.

The modes of pulsating stars are identified by comparing theoretically computed line-profile variations for many wavenumbers (ℓ,m) and values of continuous parameters (the amplitude of the pulsation velocity A_p, the projected rotational velocity v_Ω, the angle of inclination i between the rotation axis and the line of sight, the intrinsic line-profile width σ) to observed line-profile variations and by choosing the mode and the parameters that lead to the best fit. Even with current computers, this technique is feasible only for a monoperiodic star because of computation time. For this reason, among others, the moment method is particularly useful. The principle of this latter technique is the same as for the line-profile fitting technique but it considers the first three moments of a line profile instead of the entire profile. We use the moment method developed by Aerts et al. (1992) and Aerts (1996) together with our new version improved for multiperiodic rotating stars (see the following).

The surface abundance distribution of CP variables is obtained from line-profile variations by an inversion method called Doppler mapping. This technique is an iterative process that assumes a start abundance distribution, computes a new "improved" abundance map by minimizing an appropriate error function and iterates until the difference between computed and observed profiles is of the order of the signal-to-noise ratio of the spectra. We obtain abundance distributions of silicon and helium on the stellar surface for several B stars by means of the code INVERS11 implemented by Prof. N. Piskunov.

S.4 A new version of the moment method

A first contribution of this thesis is a significant improvement of the moment method which is a technique to identify pulsation modes from high-resolution spectroscopic data. It was first introduced by Balona (1986ab, 1987) and further developed by Aerts et al. (1992) and Aerts (1996).

The idea of the method is to consider the first three moments of a line profile and to compare their temporal variations to the ones of theoretically computed moments for many wavenumbers (ℓ, m) and for a large grid of other continuous parameters A_p, v_Ω, i, σ in order to identify the modes that best fit the observations.

The formulation by Aerts (1996) is valid for slowly-rotating pulsating stars ($P_{rot} > 10$ P_{puls}) and is very powerful for monoperiodic stars. In the case of multiple modes, all the information contained in the first three moment is not used and multiple modes are determined independently, often leading to inconsistent values of the continuous parameters. For an application of the method to slowly pulsating B stars, the version of Aerts (1996) is unsatisfactory since these stars are multiperiodic and may have a rotation period of the same order as pulsation periods.

In this thesis we propose a new version of the moment method. The improvements compared to the previous version are the following. We rewrite the theoretical moment expressions in order to generalize the technique to rotating pulsating stars by using the pulsational velocity field derived by Lee & Saio (1987, 1990) for low-frequency non-radial g-modes. The implementation of our numerical moment method is efficient in computation time so that we can now consider all the coupling terms appearing in the moment expressions, in particular the constant term of the second moment. Consequently, all modes of a multiperiodic star are identified simultaneously, leading to only one consistent value for v_Ω, i, σ. We use a new discriminant which compares theoretical to observed first three moments at each time of observation instead of their amplitudes which can have large uncertainties. Tests on synthetic data show that the method performs very well. We also point out two additional interests of computing moments. For chosen $(\ell,\ m,\ i, K)$ the range of the amplitude A_p can be restricted to be compatible with the observed first moment amplitude, which avoids to test useless values. A large number of combinations of wavenumbers and other parameters can be excluded directly from the observed values of the first moment amplitude together with the constant term of the second moment.

We applied the new moment method to two β Cephei stars and to one SPB star. For β Crucis we confirm the $\ell = 1$ nature for the main mode and the higher-degree nature of two lower-amplitude modes, in agreement with recent space photometry obtained with the WIRE satellite (Cuypers et al. 2002). Our mode identification for three observed modes of 16 Lacertae is in full agreement with the one by Dupret et al. (2003) derived from photometry. For the SPB star HD 74195 the identifications of four modes need to be confirmed by additional data.

We point out that, in current practical applications, several combinations of modes may lead to very close values of the discriminant. A statistically justified way to discriminate between these solutions has not been found up to now. De Ridder et al. (2002b) have taken the first steps to solve this difficult problem for a monoperiodic pulsation. The power of our new method, however, lies in the fact that it allows to exclude all but some tens of solutions for the modes and such elimination is crucial for future seismic modelling.

S.5 The slowly pulsating B star HD 147394

The second contribution of this thesis constitutes the analyses of slowly pulsating B stars and more precisely the detailed study of HD 147394. This work is performed in the framework of a long-term spectroscopic monitoring led by Mathias et al. (2001) at the Observatoire de Haute-Provence in France for ten northern candidate SPBs discovered thanks to the HIPPARCOS mission. The conclusions of this campaign are the following. A period analysis on the Si II 4128-4130 Å doublet and on HIPPARCOS measurements shows evidence of multiperiodicity of all except one studied stars, which confirms the pulsation nature of these B stars. A list of the observed frequencies for our target SPBs is given. In general the main frequency in photometry is also the main one in spectroscopy, as was also the case for the sample studied by De Cat (2001). We note that none of the stars has been reported as chemically peculiar in the literature. Despite the observational effort done for our sample stars, multiperiodicity in the spectroscopic data is found in only one star: HD 147394 for which we can perform a mode identification.

HD 147394 is a B 5 IV star falling in the centre of the SPB instability strip. From the analysis of variations of the Si II 4128-4130 Å doublet, we report three frequencies which are $f_1 = 0.8008$ c d^{-1}, $f_2 = 0.7813$ c d^{-1} and $f_3 = 0.7175$ c d^{-1} or one of the aliases of f_3 due to bad time sampling. The first frequency is also found in HIPPARCOS photometry. An objective mode identification is done by means of our new version of the moment method. Our mode identification for the first two frequencies is not influenced by the value chosen for the third frequency and we conclude that the three modes are non-axisymmetric modes with $\ell \leq 3$. We find that 15-20 combinations of (ℓ, m) fit the moments in a similar way. These best solutions are found to be the same whatever is the expression for the pulsational velocity field (usual non-rotating one or Lee & Saio's one including the Coriolis force). The rotation period of the star is found to be between 5 and 19 days. We have too limited information to perform seismic modelling at this stage, but we do show that the different possibilities for the mode identifications are compatible with current pulsational models for SPBs. Such detailed confrontation between the outcome of a line-profile study and theoretical models is the first of its kind.

S.6 Four B-type variable stars modelled by rotational modulation

The third contribution of our work is to underline a distinct group of several stars in the sample of southern and northern candidate SPBs selected by Aerts et al. (1999) and Mathias et al. (2001). A priori the HIPPARCOS photometry and the spectroscopic variations of these stars are similar to those of other stars of the sample. However our detailed analyses of the moments of the Si II 4128-4130 Å doublet and of the He I 4121 Å line exclude pulsation as being the cause of their observed monoperiodic variability. We show that a rotational modulation model allows us to succeed in explaining the behaviour of the line-profile variations. More precisely it reproduces the non-sinusoidal first moment variations, the different temporal behaviour and phasing between the moments of the Si and He lines as well as the large equivalent width variations. We conclude that the best explanation for the variability of these four stars is the presence of non-homogeneous distributions of elements on the stellar surface. The observed periods, that are the stellar rotation periods, are the following: 1.569 days for HD 131120, 1.295 days for HD 105382, 2.089 days for HD 138769 and 2.769 days for HD 55522. By means of the Doppler Imaging technique we derive abundance maps of the stellar surface of both considered elements. We show that HD 131120, HD 105382 and HD 138769 are stars for which helium is globally underabundant compared to the Sun. HD 55522 has on average a helium solar abundance but show very high contrasts over the stellar surface leading to a variation of 0.8 dex for the observed mean abundance over the cycle of rotation. For the two stars HD 131120 and HD 105382 we find that regions on the stellar surface where helium is more enhanced correspond to regions where silicon is more depleted and inversely. We also find that the equatorial rotation velocities of the four stars are around 100 km s^{-1}. Note that HD 131120 and HD 138769 were already reported as Bp stars but this is not the case for HD 105382 and HD 55522.

S.7 Outlook

De Cat et al. (2003) are presently identifying the pulsation modes of several slowly pulsating B stars which show a larger number of detected modes than HD 147394 (De Cat & Aerts 2002). The mode identifications are performed by means of our new version of the moment method for spectroscopy and by means of the improved method of photometric amplitudes by Dupret et al. (2003) for photometry. This observational study constitutes the starting point for our future asteroseismic modelling of SPBs.

In order to better understand the chemical inhomogeneities of the four studied rotationally modulated B-type stars, we plan to make a comparison with theoretical models of diffusion for such stars with a T_{eff} of about 17 500 K. Attempts to detect magnetic fields, which may be present in these stars, would also be very relevant.

Résumé

R.1 Introduction

Dans cette thèse, nous interprétons la variabilité des profils de raie de plusieurs étoiles de type B de la séquence principale. Cette étude est réalisée dans le cadre d'un suivi à long terme consacré aux étoiles de type Slowly Pulsating B (SPB), mené par des membres de l'Institut d'Astronomie de l'Université de Leuven.

Dans la section R.2 de ce résumé, sont présentés les différents types d'étoiles B étudiées dans cette thèse. La section R.3 décrit brièvement la méthodologie utilisée pour analyser les données de ces étoiles. Les sections R.4, R.5 et R.6 résument les trois contributions de ce travail. Premièrement, nous proposons une amélioration significative de la méthode des moments pour l'identification des modes d'étoiles multi-périodiques en rotation. Ensuite, sont étudiées des étoiles de type SPB découvertes par la mission HIPPARCOS et, plus particulièrement, l'étoile SPB la plus brillante de notre échantillon du Nord, HD 147394. Finalement, nous mettons en évidence quatre étoiles de type B pour lesquelles la variabilité est interprétée en termes de modulation rotationnelle. La section R.7 donne les perspectives pour notre travail futur.

R.2 Etoiles B à profils de raie variables

Nous étudions plusieurs étoiles variables de type B de la séquence principale appartenant à deux classes : les étoiles de type Slowly Pulsating B et les étoiles variables Bp. Les caractéristiques des deux groupes sont résumées comme suit.

Etoiles de type Slowly Pulsating B

Waelkens (1991) a introduit une nouvelle classe d'étoiles pulsantes de type B : les étoiles de type Slowly Pulsating B. Celles-ci sont situées le long de la séquence principale et possèdent des types spectraux de B 2 à B 9. Leur masse se situe entre 3 et 7 masses solaires. Elles présentent des variations de luminosité et des variations de profils de raie. Celles-ci sont multi-périodiques avec des périodes comprises entre 1 et 4 jours. Leur variabilité est interprétée en termes de pulsations stellaires non-radiales. Les modes d'oscillation sont des modes g d'ordre élevé. Les modèles théoriques montrent que le mécanisme d'excitation

des étoiles SPB est le mécanisme κ associé à la barrière d'opacité de la zone d'ionisation partielle du fer à 2 10^5 K. Un grand nombre de nouvelles étoiles SPB a été découvert grâce au satellite HIPPARCOS. Jusqu'à présent, une centaine de candidates SPB ont été découvertes.

Etoiles variables Bp/Ap

Les étoiles variables Bp/Ap sont des étoiles de la séquence principale chimiquement particulières (CP) pour lesquelles certains éléments présentent des abondances anormales par rapport à celles du Soleil. Leur température est comprise entre 7 000 K et 18 000 K. En général, les étoiles les plus chaudes du groupe Bp/Ap sont caractérisées par une surabondance en silicium (étoiles Si) mais sont sous-abondantes en hélium (étoiles déficientes en He). Elles présentent des variations photométriques et spectroscopiques mono-périodiques. Celles-ci sont expliquées par la rotation stellaire en présence de distributions non-homogènes de certains éléments à la surface de l'étoile. Des modèles théoriques ont été développés pour les étoiles Ap. Ceux-ci expliquent les particularités de ces étoiles par des interactions complexes entre les processus de diffusion et un champ magnétique stellaire. L'origine des champs magnétiques observés pour un grand nombre d'étoiles Ap n'est pas encore clairement comprise.

R.3   Méthodologie

Théorie des pulsations non-radiales

Pour les étoiles de type SPB, nous considérons la théorie des pulsations stellaires non-radiales de Lee & Saio (1987, 1990). Celle-ci tient compte de la force de Coriolis, en considérant certaines approximations valables pour des modes non-radiaux de longue période. Nous décrivons la théorie nécessaire pour une comparaison avec les observations spectroscopiques. Une expression du champ de vitesse de pulsation à la surface stellaire est déduite. Celle-ci est utilisée lors de la modélisation des variations des profils de raie.

Dans ce travail, nous comparons également les fréquences observées aux fréquences théoriques. Celles-ci sont calculées à l'aide de deux programmes développés par Dr. R. Scuflaire : le Code Liégeois d'Evolution Stellaire et le programme adiabatique OSC. Le premier calcule les modèles d'équilibre et le second les fréquences d'oscillation. Dans le cadre de cette thèse, nous avons adapté OSC pour y inclure la force de Coriolis.

Modélisation des profils de raie

Les variations de profils de raie d'une étoile pulsante sont principalement dues au champ de vitesse de pulsation à la surface stellaire et aux variations de luminosité causées par des variations de température. Les variations de profils de raie sont modélisées comme

suit. La surface de l'étoile est divisée en éléments de surface. Chaque profil de raie local est calculé pour être intégré sur la surface stellaire visible. Les profils de raie locaux sont des profils intrinsèques élargis et déplacés par effet Doppler à cause de la rotation stellaire et du champ de vitesse de pulsation. Le profil intrinsèque dépend du temps en raison des variations de la température effective et de la gravité. Nous insistons sur le fait que ce dernier effet peut être négligé pour la modélisation du doublet Si II 4128-4130 Å dans le cas d'étoiles B pulsant non radialement et en rotation lente. Ceci a été prouvé par De Ridder et al. (2002a) et Dupret et al. (2002). Dans cette thèse, nous générons des variations de profils de raie théoriques au moyen du programme BRUCE développé par Townsend (1997). Ce programme est disponible publiquement.

Les variations des profils de raies d'étoiles chimiquement particulières sont dues à la rotation stellaire et à la distribution non-homogène de certains éléments chimiques à la surface de l'étoile. Le flux d'une (ou plusieurs) tache(s) circulaire(s) diffère du flux du reste de la surface stellaire. Des profils de raie intrinsèques locaux, gaussiens et élargis par la rotation, sont calculés en tenant compte de la différence d'abondance de l'élément considéré dans la tache. Ils sont finalement intégrés sur la surface stellaire visible. Dans ce travail, nous utilisons un programme mis à notre disposition par Dr. L. Balona.

Méthodes d'analyse disponibles

Au moyen de techniques couramment utilisées par les astronomes, nous avons déterminé, à partir de plusieurs ensembles d'observations, les fréquences des étoiles variables étudiées. Ces techniques sont les méthodes de Fourier (Scargle 1981, Roberts et al. 1987) et la méthode PDM (Phase Dispersion Minimization) (Jurkevich 1971, Stellingwerf 1978). Les premières sont basées sur le fait que la transformée de Fourier d'un signal harmonique met en évidence les fréquences présentes dans ce signal. L'idée de la méthode PDM est que la dispersion des observations dans un diagramme de phase par rapport à une courbe moyenne est minimale pour la fréquence présente dans les données. Dans ce travail, nous utilisons des programmes de détermination des fréquences mis à notre disposition par Dr. J. Cuypers et Dr. J. Telting.

Les modes des étoiles pulsantes sont identifiés en calculant un grand nombre de variations de profils de raie théoriques pour différents nombres d'onde (ℓ, m) et différentes valeurs des paramètres continus (l'amplitude de la vitesse de pulsation A_p, la vitesse de rotation projetée v_Ω, l'inclinaison i entre l'axe de rotation et la ligne de visée, la largeur du profil intrinsèque σ). On choisit alors les modes et les paramètres qui reproduisent au mieux les variations de profils de raie observées (line-profile fitting technique). Même avec les ordinateurs actuels, à cause du temps de calcul trop long, cette technique n'est applicable qu'à des étoiles mono-périodiques. Pour cette raison, entre autres, la méthode des moments est particulièrement utile. Le principe de cette technique est le même que celui de la technique "line-profile fitting" mais considère les trois premiers moments d'un profil de raie à la place du profil entier. Nous utilisons la méthode des moments développée

par Aerts et al. (1992) and Aerts (1996) ainsi que notre nouvelle version optimisée pour des étoiles multi-périodiques en rotation (voir ci-dessous).

La distribution des abondances de surface des variables CP est obtenue à partir des variations de profils de raie au moyen d'une méthode d'inversion appelée "Doppler Mapping". Celle-ci est basée sur le processus itératif suivant. On considère une distribution d'abondance initiale. Une nouvelle distribution en surface est calculée de manière à mieux reproduire les observations en minimisant une fonction d'erreur appropriée. L'itération se poursuit jusqu'à ce que la différence entre les profils calculés et observés soit de l'ordre du rapport signal sur bruit des spectres. Dans cette thèse, nous obtenons les distributions d'abondance du silicium et de l'hélium à la surface de plusieurs étoiles B au moyen du programme INVERS11 développé par Prof. N. Piskunov.

R.4 Une nouvelle version de la méthode des moments

Une première contribution de cette thèse est une amélioration significative de la méthode des moments. Celle-ci est une technique qui permet d'identifier les modes de pulsation à partir de données spectroscopiques à haute résolution. Elle a d'abord été introduite par Balona (1986ab, 1987) et ensuite développée par Aerts et al. (1992) et Aerts (1996).

L'idée de la méthode des moments est de considérer les trois premiers moments d'un profil de raie et de comparer leurs variations temporelles à celles des moments théoriquement calculés pour beaucoup de nombres d'onde (ℓ, m) et pour une large grille des paramètres continus A_p, v_Ω, i, σ. Le but est d'identifier les modes qui correspondent au mieux aux observations.

La version développée par Aerts (1996) est valable pour des étoiles pulsantes à rotation lente ($P_{\rm rot} > 10\, P_{\rm puls}$) et est très efficace pour des étoiles mono-périodiques. En cas de multi-périodicité, toutes les informations contenues dans les trois premiers moments ne sont pas utilisées et les modes multiples sont déterminés indépendamment. Ceci conduit souvent à des valeurs incohérentes des paramètres continus. Cette version de la méthode n'est donc pas appropriée aux étoiles de type Slowly Pulsating B puisqu'elles sont multi-périodiques et peuvent présenter une période de rotation du même ordre que les périodes de pulsation.

Dans cette thèse, nous proposons une nouvelle version de la méthode des moments. Les améliorations par rapport à la version précédente sont les suivantes. Dans le but de généraliser la technique aux étoiles pulsantes en rotation, nous réécrivons les expressions des moments théoriques en employant le champ de vitesse de pulsation obtenu par Lee & Saio (1987, 1990) pour des modes g non-radiaux de longue période. La programmation de notre méthode numérique est efficiente en temps de calcul, de sorte que tous les termes couplés qui apparaissent dans les expressions des moments peuvent dorénavant être considérés (en particulier, le terme constant du deuxième moment). Par conséquent,

tous les modes d'une étoile multi-périodique sont identifiés simultanément, impliquant une seule valeur cohérente pour v_Ω, i, σ. La comparaison entre moments observés et moments théoriques n'est plus réalisée sur les amplitudes en raison des trop grandes incertitudes que celles-ci peuvent présenter. Nous utilisons un nouveau discriminant qui compare les trois premiers moments théoriques aux moments observés à chaque moment d'observation. Des tests sur des données synthétiques montrent que la méthode fonctionne très bien. Nous attirons également l'attention sur deux intérêts supplémentaires de calculer ces moments. Pour des ℓ, m, i et K choisis, le domaine de variation de l'amplitude A_p peut être limité afin d'être compatible avec l'amplitude du premier moment observé, ce qui permet d'éviter de tester des valeurs inutiles. Des valeurs observées de l'amplitude du premier moment et du terme constant du deuxième, un grand nombre de combinaisons de couples (ℓ, m) et d'autres paramètres peut être directement exclu.

Nous avons appliqué la nouvelle méthode des moments à deux étoiles β Cephei et à une étoile de type Slowly Pulsating B. Pour β Crucis, nous confirmons la valeur $\ell = 1$ du mode principal et les degrés élevés des deux modes de plus faible amplitude. Ceci est en accord avec la photométrie obtenue pour l'étoile par le satellite WIRE (Cuypers et al. 2002). Notre identification de modes pour les trois modes observés de 16 Lacertae est en accord avec celle obtenue à partir de la photométrie par Dupret et al. (2003). Pour l'étoile SPB HD 74195, l'identification des quatre modes doit être confirmée par des données supplémentaires.

Nous soulignons que, pour les applications pratiques, plusieurs combinaisons de modes peuvent conduire à des valeurs très proches du discriminant. On n'a pas encore trouvé de méthode statistiquement justifiée permettant de discriminer ces solutions. De Ridder et al. (2002b) ont commencé à tenter de résoudre ce problème difficile pour une pulsation mono-périodique. Cependant, la puissance de notre nouvelle méthode réside dans le fait qu'elle permet d'exclure toutes les combinaisons de modes, excepté quelques dizaines. Une telle élimination de solutions est cruciale pour une modélisation sismique future.

R.5 L'étoile de type Slowly Pulsating B HD 147394

Les analyses d'étoiles de type Slowly Pulsating B et plus précisément l'étude détaillée de l'étoile HD 147394 constituent la deuxième contribution de cette thèse. Ce travail est réalisé dans le cadre du projet à long terme mené par Mathias et al. (2001) à l'Observatoire de Haute-Provence (France) de dix étoiles candidates SPB, découvertes lors de la mission HIPPARCOS. Les conclusions de cette campagne sont les suivantes. Une analyse de période sur le doublet Si II 4128-4130 Å et sur les mesures HIPPARCOS montrent de manière évidente la multi-périodicité de toutes les étoiles, sauf une. Ceci confirme la nature pulsationnelle de ces étoiles de type B. Nous donnons une liste des fréquences observées pour les étoiles SPB considérées. En général, la fréquence principale obtenue par l'analyse des données photométriques est aussi celle provenant des

données spectroscopiques, comme ce fut aussi le cas dans l'échantillon étudié par De Cat (2001). Nous notons qu'aucune de ces étoiles n'est mentionnée comme étoile chimiquement particulière dans la littérature. Malgré les efforts d'observations consacrés à ces étoiles, une seule d'entre elles présente clairement plusieurs modes dans les données spectroscopiques : HD 147394, pour laquelle nous pouvons donc effectuer une identification des modes.

HD 147394 est une étoile de type B 5 IV et se situe au centre de la bande d'instabilité des étoiles de type Slowly Pulsating B. De l'analyse des variations du doublet Si II 4128-4130 Å, nous déterminons trois fréquences, qui sont $f_1 = 0.8008$ c j^{-1}, $f_2 = 0.7813$ c j^{-1} et $f_3 = 0.7175$ c j^{-1} ou un des alias de f_3, en raison d'un mauvais échantillonnage temporel. La première fréquence est également déduite de la photométrie HIPPARCOS. Une identification objective des modes est effectuée au moyen de notre nouvelle version de la méthode des moments. Notre identification pour les deux premières fréquences n'est pas influencée par la valeur choisie pour la troisième fréquence et nous concluons que les trois modes sont des modes non-axisymétriques, avec $\ell \leq 3$. De 15 à 20 combinaisons de nombres d'onde (ℓ, m) reproduisent les moments de manière similaire. Ces meilleures solutions ne dépendent pas de l'expression du champ de vitesse de la pulsation (expression usuelle ou expression de Lee & Saio incluant la force de Coriolis). La période de rotation de l'étoile est comprise entre 5 et 19 jours. Actuellement, nous possédons trop peu d'informations pour réaliser une modélisation sismique de l'étoile, mais nous montrons que les différentes possibilités pour l'identification des modes sont compatibles avec les modèles actuels de pulsation pour les étoiles de type Slowly Pulsating B. Une telle confrontation entre les résultats de l'étude des profils de raie et les modèles théoriques est la première du genre.

R.6   Quatre étoiles de type B modélisées par modulation rotationnelle

La troisième contribution de ce travail est la mise en évidence d'un groupe distinct de plusieurs étoiles dans l'ensemble des candidates SPB du Sud et du Nord sélectionnées par Aerts et al. (1999) et Mathias et al. (2001). A priori, les variations de la photométrie HIPPARCOS et de la spectroscopie de ces étoiles sont semblables à celles des autres étoiles de l'échantillon. Cependant, nos analyses détaillées des moments du doublet Si II 4128-4130 Å et de la raie He I 4121 Å excluent la pulsation comme cause de leur variabilité mono-périodique observée. Ensuite, nous montrons qu'un modèle de modulation rotationnelle parvient à expliquer le comportement des variations de profils de raie. Plus précisément, il reproduit les variations non-sinusoidales du premier moment, le comportement temporel différent et le déphasage entre les moments des raies Si et He, de même que les grandes variations de largeur équivalente. Nous concluons que la meilleure explication pour la variabilité de ces quatre étoiles est la présence de distributions non-homogènes d'éléments à la surface de l'étoile. Les périodes observées, qui sont donc les périodes

de rotation des étoiles, sont les suivantes : 1.569 jours pour HD 131120, 1.295 jours pour HD 105382, 2.089 jours pour HD 138769 et 2.769 jours pour HD 55522. Au moyen de la technique de "Doppler Imaging", nous déterminons des cartes d'abondance des deux éléments considérés à la surface de l'étoile. Nous montrons que HD 131120, HD 105382 et HD 138769 sont des étoiles pour lesquelles l'hélium est globalement sous-abondant par rapport au Soleil. Par contre, HD 55522 a en moyenne une abondance en hélium identique au Soleil mais présente des contrastes très importants à la surface conduisant à une variation de 0.8 dex de l'abondance moyenne observée sur un cycle de rotation. Pour les deux étoiles HD 131120 et HD 105382, des régions de la surface stellaire où l'hélium est plus présent correspondent à celles où le silicium est plus rare, et inversement. Nous trouvons aussi que les vitesses équatoriales des quatre étoiles sont d'environ 100 km s^{-1}. Nous notons que HD 131120 et HD 138769 sont déjà classées comme étoiles Bp dans la littérature, contrairement aux deux autres étoiles.

R.7 Perspectives

Actuellement, De Cat et al. (2003) identifient les modes de pulsation de plusieurs étoiles de type Slowly Pulsating B qui présentent un plus grand nombre de modes détectés que HD 147394 (De Cat & Aerts 2002). Les identifications des modes sont réalisées au moyen de notre nouvelle méthode des moments pour la spectroscopie et à l'aide de la méthode des amplitudes photométriques améliorée par Dupret et al. (2003) pour la photométrie. Cette étude observationnelle-ci constitue le point de départ de notre future modélisation astérosismique des étoiles de type Slowly Pulsating B.

Dans le but de mieux comprendre les inhomogénéités chimiques des quatre étoiles B modélisées par la modulation rotationnelle, il est nécessaire d'entreprendre une comparaison avec les modèles théoriques de diffusion pour de telles étoiles possédant une T_{eff} d'environ 17 500 K, mais également de tenter de détecter des champs magnétiques qui pourraient être présents dans ces étoiles.

Introduction

Variability of brightness and spectra in main-sequence B stars is common. When the observed variations are periodic, they are attributed to two main causes: stellar pulsation or the presence of non-homogeneous distribution of elements on the stellar surface.

The study of pulsating stars is of particular interest since it provides a way to probe internal structure of stars by using their observed pulsational characteristics (pulsation periods and modes). The study of spotted stars contributes to a better understanding of diffusion mechanisms in stellar atmospheres, which are responsible of chemical peculiarities.

High-resolution spectroscopy is very suited to derive pulsation frequencies and modes of pulsators as well as to map surface abundance distributions of elements of chemically peculiar stars. Such analyses of observed line-profile variations of B stars were performed in the scope of this thesis.

The manuscript is subdivided in three parts. Part I is devoted to the methodology. We first describe the two classes of B variables for which we studied several of their members: the slowly pulsating B stars and the Bp variables (Chapter 1). Then, Chapter 2 describes theoretical aspects of stellar pulsation needed for a comparison with observations. Chapter 3 gives the ingredients for the modelling of line-profile variations of both kinds of stars. Chapter 4 explains different techniques for frequency analysis, mode identification and Doppler mapping. We end this part by proposing a new version of the moment method for mode identification, improved for multiperiodic rotating pulsating stars (Chapter 5).

In Part II, we present the analyses of pulsating B stars. Chapter 6 shows the results of the frequency analysis on spectroscopic data of a sample of eight new northern slowly pulsating B stars discovered from the HIPPARCOS mission. Chapter 7 is devoted to a detailed study of one of these stars, HD 147394, for which we also performed a mode identification and a comparison with theoretical models.

In Part III, we describe the analyses of chemically peculiar B stars. Chapters 8, 9, 10 and 11 are devoted respectively to the following four stars: HD 131120, HD 105382, HD 138769 and HD 55522. We explain why we attributed the variations of these stars to rotational modulation instead of stellar pulsation. Then we show the abundance mapping of two elements (silicon and helium) on the stellar surface. We end the thesis with conclusions and outlook for follow-up studies of line-profile variable B stars.

Part I

Methodology

Chapter 1

Line-profile B variables

In this chapter, we describe one class of pulsating B stars as well as one group of chemically peculiar B stars for which we studied the line-profile variations of several of their members. They are respectively the slowly pulsating B stars (Sect. 1.1) and the Bp variables (Sect. 1.2).

1.1 Slowly pulsating B stars

In this section, we remind the main observational and theoretical steps achieved in the understanding of slowly pulsating B stars (SPBs) from their discovery in the 1980s to current studies. In particular, we present the long-term project led by members of the Institute of Astronomy of the University of Leuven which is devoted to this kind of pulsating B-type stars and in which we are involved.

1.1.1 Their discovery

In the 1980s, C. Waelkens carried out a systematic survey of early-type star photometric variability, using the Geneva photometry. This study allowed the discovery of a new group of B-type main-sequence photometric variables (Waelkens & Rufener 1985). The group was composed of seven stars which have the following photometric characteristics. Multiperiodic photometric variability with periods of the order of days (0.5 to 4 days) is observed. The amplitudes are of a few millimagnitudes and decrease for increasing wavelength. No phase lag is found between the variations in different colours. At that time, a class of B-type line-profile variables was known: the 53 Persei stars (Smith 1977) whose variability is multiperiodic with periods of the order of days. It was then natural to think that the two groups of stars form a unique group.

In 1991, C. Waelkens interpreted the photometric variability in terms of non-radial pulsation in high-order g-modes and introduced a new class of pulsating B-type stars: the slowly pulsating B stars (SPBs, Waelkens 1991).

In 1993, the interpretation of the variability was confirmed by theoretical models. The latter ones predict that many high-order g-modes are unstable simultaneously for stars close to the main sequence and with masses below 7 $M_\odot$. Gautschy & Saio (1993) and Dziembowski et al. (1993) attribute the pulsation mechanism of SPBs to the κ-mechanism, acting in the metal opacity bump at 2 10^5 K.

In 1998, it was confirmed that SPBs and 53 Persei stars have several members in common. In particular, Chapellier et al. (1998) showed that the prototype of 53 Persei stars satisfies all the observational characteristics of an SPB and De Ridder et al. (1999) showed that this star is situated within the theoretical SPB instability strip.

1.1.2   The HIPPARCOS mission

The principal objective of the HIPPARCOS mission was the production of a star catalogue of unprecedented precision for the astrometric position parameters (i.e. ecliptic longitude and latitude), the parallaxes and the proper motions of about 120 000 stars. Besides this, the satellite gathered photometric measurements, which allowed the discovery of an enormous number of new variable stars, including 267 B-type variables with periods ranging from a few hours up to 0.5 years (Eyer 1998). Among these B-type variables, 72 were classified as new candidate slowly pulsating B stars (Waelkens et al. 1998). Fig. 1.1 illustrates the position of these SPB candidates in the HR diagram. They are situated along the main sequence with spectral types ranging between B 2 to B 9, which corresponds to effective temperatures of 12 000 K up to 18 000 K. Their masses range between 3 $M_\odot$ to 7 $M_\odot$. We point out that the new SPBs almost fully cover the theoretical instability strip calculated by Pamyatnykh (1999).

We note that, before the HIPPARCOS mission, about 100 β Cephei stars were already known while only 12 SPBs were discovered. The space mission underlined only 8 new β Cephei stars but 72 new SPBs. This imbalance can be explained as a selection effect. Indeed, ground-based surveys are more likely to detect stars with periods of hours than periods of the order of one day while the opposite is true for the HIPPARCOS data.

To discriminate between the different classes of B-type variables a multivariate discriminant analysis was performed by Waelkens et al. (1998). The parameters were the main frequency f found in the HIPPARCOS data and the Geneva parameters X, Y, Z which are closely related to the effective temperature, the surface gravity and the surface magnetic field respectively (Golay 1980). The classes to discriminate were SPBs, β Cephei stars and CP (chemically peculiar) variables of spectral type B[1], which were represented by 11, 39 and 21 prototypes respectively. We point out that the prototypes of the CP variables were chosen so that they are distinguished as clearly as possible from both other

---

[1]Stars which could not be classified in one of the three classes were then assigned to one of the other groups (B-type supergiants, Be stars and eclipsing binaries) by means of bivariate plots of Y versus X and f versus Z.
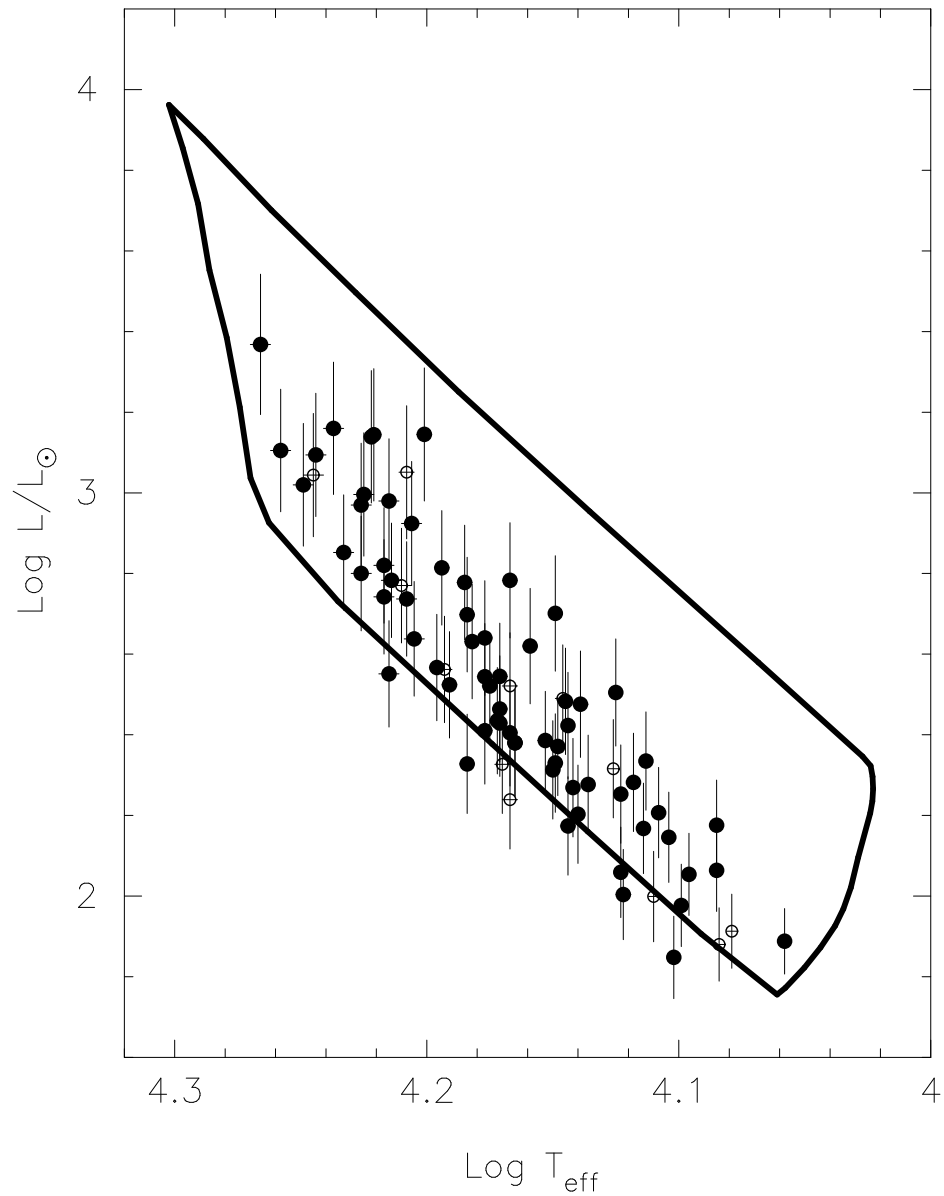
Figure 1.1: Position of known SPBs in the HR diagram (open symbols: SPBs known before HIPPARCOS, full symbols: candidate SPBs discovered thanks to HIPPARCOS). The theoretical SPB instability strip is calculated by Pamyatnykh (1999) and is based on OPAL G93/21 opacities for a chemical composition (X,Z) = (0.70,0.02), without overshooting.

classes. Consequently, this way of selection does not discriminate CP variables falling in the SPB domain from real SPBs. In Part III, we show that two stars were misclassified as SPBs and are in fact CP variables for which the monoperiodic variability is explained by rotational modulation.

1.1.3 Long-term ground-based photometric and spectroscopic monitoring of a sample of bright SPBs

In the course of 1996, asteroseismologists of the *Katholieke Universiteit Leuven* started a long-term ground-based photometric and spectroscopic monitoring of seventeen selected candidate SPBs in the southern hemisphere (Aerts et al. 1999, De Cat et al. 2000, De Cat & Aerts 2002). The goal of such a study was to provide an inventory of the observational characteristics of the pulsations of SPBs for a sample of stars that covers the whole instability strip in the HR diagram. This observational study of bright southern slowly pulsating B stars constitutes the PhD thesis of P. De Cat (2001). In order to increase the sample selected in the southern hemisphere, ten bright northern candidate SPBs were chosen for long-term spectroscopic monitoring in the course of 1998 (Mathias et al. 2001). The basic analysis of this sample is described in Chapter 6. A detailed study of one of the northern targets, the SPB HD 147394, is performed in Chapter 7.

Both sets of SPBs were selected among the many SPBs discovered from the HIPPARCOS mission (Waelkens et al. 1998) as well as among the confirmed SPBs that were studied by Waelkens (1991). We had then at our disposal HIPPARCOS photometry for the selected HIPPARCOS SPBs but also for the selected confirmed SPBs. Besides HIPPARCOS photometry, two other datasets were gathered during several years[2]: multicolour Geneva photometry and high-resolution spectroscopy (high S/N profiles of the Si II-doublet centered at 4128-4130 Å). In the southern hemisphere, the observations were obtained with the Swiss Telescope of the Geneva Observatory situated at La Silla in Chile and with the Coudé Auxiliary Telescope / Coudé Echelle Spectrometer (CAT/CES) combination of the European Southern Observatory, also situated at La Silla. In the northern hemisphere, the spectroscopic observations were obtained with the AURELIE spectrograph at the Coudé focus at the 1.52 m telescope situated at the Observatoire de Haute-Provence in France. Geneva photometric observations are presently being gathered with the Mercator telescope of the University of Leuven, which is situated at La Palma in Spain.

Observational properties of the southern SPBs

Among the seventeen southern SPBs studied by De Cat (2001), at least nine are found to be close spectroscopic binaries for which the orbital parameters are derived. Single-lined as well as double-lined spectroscopic binaries were observed. Orbits with a large eccentricity

---

[2]Such a long-term monitoring and an even much longer one is needed because of the long (beat) periods of SPBs.

were found as well as circular orbits. Two stars turn out to be chemically peculiar variables instead of SPBs. Their modelling in terms of rotational modulation is performed in this thesis (Part III). Another star turns out to be misclassified as an SPB because no temporal shifts due to binarity and no changes in shape are observed in its line profiles. Nine of the targets are confirmed to be multiperiodic stars and are therefore pulsators. A mode identification was performed from the photometric and from the spectroscopic data. In some cases, no consistency was found between the results derived from both datasets, which underlines the necessity to improve current mode identification methods.

The properties resulting from the datasets can be summarized as follows. All the confirmed SPBs exhibit line-profile variations. For most of the targets, the derived equivalent widths of the profiles of the Si II-doublet are in full agreement with the expected values for their effective temperature. For all the pulsating targets, the observed equivalent width (EW) variations during the pulsation cycle are well below 10% of the average equivalent width value. There is no evidence for a correlation between the EW variations and the amplitudes of the variations in the radial velocity, nor between the EW variations and the photometric variations. For most of the observed pulsation frequencies, the amplitudes of the photometric variations show a strict correlation with the amplitudes in the radial velocity. The phase difference between the radial velocity and light variations is close to 0.25 for all the observed pulsation modes. The variations in the different photometric filters of the Geneva systems are in phase.

Based on a set of 22 confirmed and 50 suspected SPBs, the following other characteristics were derived by De Cat (2002). The observed frequencies are centered around 0.8 c d^{-1}; the observed K-values[3] are centered around 10-25, which means that the horizontal component of the velocity is larger than the vertical one. A marginal increase in the observed frequencies towards lower temperatures is observed. The observed ratios of the rotational frequency to the main pulsational frequency are generally larger than 0.1. The correlation between stellar rotation and pulsation has been investigated by De Cat (2002). No firm evidence is found for amplitude damping due to rotation, nor for the excitation of higher degree modes in rapid rotators. However, more observations of fast-rotating SPBs are needed for more definitive conclusions.

1.2   Bp/Ap variables

In our sample of candidate SPBs, we discovered that several stars were misclassified and are in fact chemically peculiar B variables. In this section we remind observational properties of Bp/Ap variables as well as proposed theories to explain their peculiarities.

---

[3]The K-value is defined as the amplitude of the ratio of the horizontal component of the velocity to the amplitude of the vertical component of the velocity. To a good approximation, it is given by $K \approx \frac{GM}{\sigma^2 R^3}$ were M is the stellar mass, R is the stellar radius and σ is the angular pulsation frequency.

1.2.1   Observational peculiarities

Chemically peculiar (CP) stars are stars for which certain chemical elements show abnormal abundances compared to solar values. Chemically peculiar A and B-type stars are situated on or close to the main sequence in the temperature range of 7 000 to 18 000 K.

Several groups of CP stars have been defined (Preston 1974); some of them appear at the same positions in the HR diagram. In this work, we studied four members of the class of Bp/Ap stars. We note that these stars are situated in a part of the HR diagram which corresponds partly to the instability domain of SPBs. The hotter members of Bp/Ap stars are characterized by strong silicon enhancements (Si stars) but appear to be helium weak (He-weak stars) in general.

The Bp/Ap stars show monoperiodic photometric and spectroscopic variations as well as for many of them magnetic field variations, with the same period in each dataset. These light and line-profile variations are explained by the rotation of the star in presence of non-homogeneous distributions of elements on the stellar surface. Magnetic variations are attributed to the stellar rotation together with a magnetic axis oblique to the rotation axis. This latter model is referred to as the oblique rotator model.

The presently known values of the rotation periods of peculiar stars are in agreement with the conclusion that these stars rotate on average much slower than normal stars of the same spectral type (Catalano & Renson 1997).

1.2.2   Proposed theories

Many mechanisms and models have been introduced to attempt to explain the abundance anomalies and the non-homogeneous distribution of certain elements at the stellar surface of Bp/Ap stars. At present, the most convincing theoretical models are based on complex interactions between radiatively driven diffusion processes and the stellar magnetic field. A diffusion model that explains abundance anomalies was first introduced by Michaud (1970). It assumes that in a stellar atmosphere only two main forces affect a particle: the gravitation and the radiative pressure. Depending on which force is dominant on a certain element in a certain atmospheric layer, a particle may diffuse upwards driven by radiation or settle down below the line forming region via gravitation, which corresponds respectively to an observed overabundance or underabundance of the element. Moreover, diffusing elements are guided by the magnetic field, leading to patches. We point out that a slow rotation rate is assumed a necessary condition for a diffusive segregation of elements to occur in atmospheres of these stars. Abt & Morrell (1995) suggest that a slow rotation is even a sufficient condition for a star to become chemically peculiar.

Note that the origin of the observed magnetic fields is not clearly understood. Two different theories exist. The first one proposes that a severe field strength has been developed already in the proto-stellar medium and was involved in the star formation process

until the present. The second model assumes that the star functions as a dynamo due to differential rotation which is responsible for the surface magnetic field. Moreover, in the Sun and in other late-type stars, such a dynamo is believed to be driven by outer layer convection zones, which are certainly not present in early A- and in B-type stars.

Chapter 2

Non-radial pulsation theory

In this chapter, we outline the basic equations describing stellar pulsations of a rotating star as derived by Lee & Saio (1987, 1990). In particular, we give the theoretical background that is directly relevant for a comparison between theory and observations. More precisely, we show how to derive theoretical pulsation frequencies (Sect. 2.1) as well as a theoretical expression of the pulsational velocity field at the stellar surface (Sect. 2.2), which manifests itself through spectral line variations.

2.1   Pulsation frequencies

Basic equations

We introduce a right-handed inertial frame of orthogonal cartesian coordinates. The linearized perturbed equations of hydrodynamics in the **adiabatic** assumption, written in the Eulerian formalism, are

- the equation of motion:

$$\frac{\partial^2 \vec{\xi}}{\partial t^2} = - \text{ grad } \Phi' \ + \ \frac{\rho'}{\rho^2} \text{ grad } P \ - \ \frac{1}{\rho} \text{ grad } P', \tag{2.1}$$

- the continuity equation:

$$\rho' \ + \ \text{div}(\rho \, \vec{\xi}) = 0, \tag{2.2}$$

- the Poisson equation:

$$\Delta \Phi' = 4\pi G \rho', \tag{2.3}$$

- the adiabatic equation:

$$\frac{P'}{P} + \frac{\vec{\xi}}{P} \ . \ \text{grad } P = \Gamma_1 \left[\frac{\rho'}{\rho} + \frac{\vec{\xi}}{\rho} \ . \ \text{grad } \rho \right], \tag{2.4}$$

where primes indicate Eulerian perturbations, $\vec{\xi}$ is the displacement vector and $\Gamma_1 \equiv \left(\frac{\partial \ln P}{\partial \ln \rho} \right)_S$ is one of the generalized adiabatic coefficients. The symbols Φ, P, and ρ are

respectively the gravitational potential, the pressure and the mass density of the non-perturbed configuration.

We consider a star which rotates **uniformly** and we denote its constant angular velocity vector by $\vec{\Omega}$. The absolute acceleration is the acceleration in the co-rotating frame plus a Coriolis term and a centrifugal term.

We note that, if convection is not considered, the equilibrium configuration of the star is solely affected by the centrifugal force, because of which the star deviates from its spherical symmetry. In this thesis, we drop the centrifugal force and consider a **spherically symmetric** star in hydrostatic equilibrium. This implies that the formalism is valid for small Ω. Note that the centrifugal term that we neglect is of second order in Ω.

The equation of motion is then written in the co-rotating frame:

$$\frac{\partial \vec{v_c}}{\partial t} + 2\, \vec{\Omega} \wedge \vec{v_c} = -\,\operatorname{grad}\,\Phi' \,+\, \frac{\rho'}{\rho^2}\,\operatorname{grad}\,P \,-\, \frac{1}{\rho}\,\operatorname{grad}\,P', \qquad (2.5)$$

where $\vec{v_c}$ is the velocity in the co-rotating frame.

We search for solutions for which the temporal dependence is expressed by $\exp(i\,\sigma_c\mathrm{t})$. Equation (2.5) is then written as

$$-\sigma_c^2\vec{\xi} + 2i\sigma_c\vec{\Omega} \wedge \vec{\xi} = -\,\operatorname{grad}\,\Phi' \,+\, \frac{\rho'}{\rho^2}\,\operatorname{grad}\,P \,-\, \frac{1}{\rho}\,\operatorname{grad}\,P'. \qquad (2.6)$$

Naturally we pass on to a system of spherical coordinates (r, θ, ϕ) whose polar axis coincides with the axis of rotation. By using the expressions of the differential operators in spherical coordinates, and since $\vec{\Omega} = (\Omega\cos\theta, -\Omega\sin\theta, 0)$ in spherical coordinates, the equations (2.6), (2.2), (2.3) and (2.4) become

• the r-component of the equation of motion:

$$-\sigma_c^2\xi_r \,-\, 2i\sigma_c\Omega\sin\theta\,\,\xi_\phi = \,-\frac{\partial\Phi'}{\partial r} \,+\, \frac{\rho'}{\rho^2}\frac{dP}{dr} \,-\, \frac{1}{\rho}\frac{\partial P'}{\partial r}, \qquad (2.7)$$

• the θ-component of the equation of motion:

$$-\sigma_c^2\xi_\theta \,-\, 2i\sigma_c\Omega\cos\theta\,\,\xi_\phi = -\frac{1}{r}\,\frac{\partial\Phi'}{\partial\theta} \,-\, \frac{1}{\rho r}\frac{\partial P'}{\partial\theta}, \qquad (2.8)$$

• the ϕ-component of the equation of motion:

$$-\sigma_c^2\xi_\phi \,+\, 2i\sigma_c\Omega\,(\cos\theta\,\,\xi_\theta + \sin\theta\,\,\xi_r) = -\frac{1}{r\sin\theta}\,\frac{\partial\Phi'}{\partial\phi} \,-\, \frac{1}{\rho r\sin\theta}\frac{\partial P'}{\partial\phi}, \qquad (2.9)$$

• the continuity equation:

$$\rho' \,+\, \xi_r\frac{d\rho}{dr} \,+\, \rho\left\{\frac{1}{r^2}\frac{\partial}{\partial r}(r^2\xi_r) \,+\, \frac{1}{r\sin\theta}\frac{\partial}{\partial\theta}(\sin\theta\,\,\xi_\theta) \,+\, \frac{1}{r\sin\theta}\frac{\partial\xi_\phi}{\partial\phi}\right\} = 0, \qquad (2.10)$$

• the Poisson equation:

$$\frac{1}{r^2} \frac{\partial}{\partial r} \left(r^2 \frac{\partial \Phi'}{\partial r} \right) \; - \; \frac{1}{r^2} L^2 \Phi' = 4\pi G \rho', \tag{2.11}$$

• the adiabatic equation:

$$\frac{P'}{P} + \frac{\xi_r}{P} \frac{dP}{dr} = \Gamma_1 \left[\frac{\rho'}{\rho} + \frac{\xi_r}{\rho} \frac{d\rho}{dr} \right], \tag{2.12}$$

where

$$L^2 \;\; = \;\; -\frac{1}{\sin\theta} \frac{\partial}{\partial\theta} \left(\sin\theta \frac{\partial}{\partial\theta} \right) - \frac{1}{\sin^2\theta} \frac{\partial^2}{\partial\phi^2}.$$

These equations form a system of 6 partial differential equations for the 6 unknown functions ρ', P', Φ', ξ_r, ξ_θ, ξ_ϕ.

In treating the horizontal components of the equation of motion, it is more appropriate to use the equation obtained by taking the divergence in the θ- and ϕ-directions of equation (2.6) and the equation for the radial component of vorticity i.e., the r-component of the curl of equation (2.6) instead of equations (2.7)-(2.9). These three new equations are

• the r-component of the equation of motion:

$$-\sigma_c^2 \xi_r \; - \; 2i\sigma_c \Omega \sin\theta \; \xi_\phi \;\; = \;\; -\frac{\partial \Phi'}{\partial r} \; + \; \frac{\rho'}{\rho^2} \frac{dP}{dr} \; - \; \frac{1}{\rho} \frac{\partial P'}{\partial r}, \tag{2.13}$$

• the divergence in the θ- and ϕ-directions of the equation of motion:

$$-\sigma_c^2 \left[\frac{1}{r\sin\theta} \frac{\partial}{\partial\theta} (\sin\theta \; \xi_\theta) \; + \; \frac{1}{r\sin\theta} \frac{\partial \xi_\phi}{\partial\phi} \right]$$

$$+ \, 2i\sigma_c\Omega \left[-\frac{1}{r\sin\theta} \frac{\partial}{\partial\theta} (\cos\theta \; \sin\theta \; \xi_\phi) \; + \; \frac{1}{r\sin\theta} \frac{\partial}{\partial\phi} (\cos\theta \; \xi_\theta \; + \; \sin\theta \; \xi_r) \right]$$

$$-\frac{1}{r^2} \, L^2 \left(\frac{P'}{\rho} + \Phi' \right) = 0, \tag{2.14}$$

• the r-component of the curl of the equation of motion:

$$-\sigma_c^2 \left[\frac{1}{r\sin\theta} \frac{\partial}{\partial\theta} (\sin\theta \; \xi_\phi) - \frac{1}{r\sin\theta} \frac{\partial \xi_\theta}{\partial\phi} \right]$$

$$+2i\sigma_c\Omega \left[\frac{1}{r\sin\theta} \frac{\partial}{\partial\theta} (\cos\theta \; \sin\theta \; \xi_\theta + \sin^2\theta \; \xi_r) + \frac{1}{r\sin\theta} \frac{\partial}{\partial\phi} (\cos\theta \; \xi_\phi) \right] = 0. \tag{2.15}$$

One subsequently makes use of the fact (see Appendix A.1) that the displacement vector $\vec{\xi}(r, \theta, \phi)$ can be decomposed in terms of three functions $S(r, \theta, \phi)$, $H(r, \theta, \phi)$ and $T(r, \theta, \phi)$ in the following way:

$$\frac{\vec{\xi}}{r} = S \, \vec{e_r} \, + \, \left(\frac{\partial H}{\partial \theta} \, + \, \frac{1}{\sin \theta} \, \frac{\partial T}{\partial \phi} \right) \, \vec{e_\theta} \, + \, \left(\frac{1}{\sin \theta} \, \frac{\partial H}{\partial \phi} \, - \, \frac{\partial T}{\partial \theta} \right) \, \vec{e_\phi}, \tag{2.16}$$

where $\vec{e_r}$, $\vec{e_\theta}$ and $\vec{e_\phi}$ are the unit vectors in r-, θ-, ϕ-directions. The terms proportional to H and T are respectively called the *spheroidal* and the *toroidal* components of the horizontal motion.

The functions ρ', P', Φ', S, H, T are then developed in terms of the spherical harmonics, which form a complete orthogonal basis:

$$f(r, \theta, \phi) = \sum_{\ell=0}^{\infty} \sum_{m=-\ell}^{\ell} f_{\ell m}(r) \, Y_\ell^m(\theta, \phi),$$

with

$$Y_\ell^m(\theta, \phi) = (-1)^{(m+|m|)/2} \left[\frac{2\ell + 1}{4\pi} \frac{(\ell - |m|)!}{(\ell + |m|)!} \right]^{1/2} P_\ell^{|m|}(\cos \theta) \, e^{im\phi},$$

where $P_\ell^{|m|}(\cos \theta)$ denotes the associated Legendre polynomials (see Appendix A.2).

The displacement vector $\vec{\xi}(r, \theta, \phi, t)$ is then given by

$$\frac{\vec{\xi}}{r} = \sum_{\ell=0}^{\infty} \sum_{m=-\ell}^{\ell} \left\{ S_{\ell m}(r) \, \vec{e_r} \, + \, \vec{e_\theta} \left(H_{\ell m}(r) \, \frac{\partial}{\partial \theta} \, + \, T_{\ell m}(r) \, \frac{1}{\sin \theta} \, \frac{\partial}{\partial \phi} \right) \right.$$

$$\left. + \, \vec{e_\phi} \left(H_{\ell m}(r) \, \frac{1}{\sin \theta} \, \frac{\partial}{\partial \phi} \, - \, T_{\ell m}(r) \, \frac{\partial}{\partial \theta} \right) \right\} Y_\ell^m(\theta, \phi) \, \exp(i\sigma_c t) \tag{2.17}$$

and the Eulerian perturbation of any scalar quantity $f'(r, \theta, \phi, t)$ is expressed as

$$f'(r, \theta, \phi, t) = \sum_{\ell=0}^{\infty} \sum_{m=-\ell}^{\ell} f'_{\ell m}(r) \, Y_\ell^m(\theta, \phi) \, \exp(i\sigma_c t). \tag{2.18}$$

By introducing (2.17) and (2.18) into the equations (2.13)-(2.15) and (2.10)-(2.12) one obtains:

$$\sum_{\ell=0}^{\infty} \sum_{m=-\ell}^{\ell} \left\{ -\sigma_c^2 r S_{\ell m} \, - \, 2i\sigma_c \Omega r \left[H_{\ell m} \frac{\partial}{\partial \phi} - T_{\ell m} \, \sin \theta \, \frac{\partial}{\partial \theta} \right] \right.$$

$$\left. + \frac{d\Phi'_{\ell m}}{dr} \, - \, \frac{\rho'_{\ell m}}{\rho^2} \frac{dP}{dr} \, + \, \frac{1}{\rho} \frac{dP'_{\ell m}}{dr} \right\} Y_\ell^m(\theta, \phi) \, \exp(i\sigma_c t) = 0, \tag{2.19}$$

$$\sum_{\ell=0}^{\infty} \sum_{m=-\ell}^{\ell} \left\{ \sigma_c^2 \; H_{\ell m} \; L^2 \; + \; 2i\sigma_c\Omega \; H_{\ell m} \; \frac{\partial}{\partial \phi} \; - \; 2i\sigma_c\Omega \; T_{\ell m} \left[\sin\theta \; \frac{\partial}{\partial \theta} \; + \; \cos\theta \; L^2 \right] \right.$$

$$\left. + \; 2i\sigma_c\Omega \; S_{\ell m} \; \frac{\partial}{\partial \phi} \; - \; \frac{1}{r^2} \left(\frac{P'_{\ell m}}{\rho} \; + \; \Phi'_{\ell m} \right) \; L^2 \right\} Y_\ell^m(\theta,\phi) \; \exp(i\sigma_c t) = 0, \qquad (2.20)$$

$$\sum_{\ell=0}^{\infty} \sum_{m=-\ell}^{\ell} \left\{ -\sigma_c^2 \; T_{\ell m} \; L^2 \; - \; 2i\sigma_c\Omega \; H_{\ell m} \left[\cos\theta \; L^2 \; + \; \sin\theta \; \frac{\partial}{\partial \theta} \right] \right.$$

$$\left. - \; 2i\sigma_c\Omega \; T_{\ell m} \; \frac{\partial}{\partial \phi} \; + \; 2i\sigma_c\Omega \; S_{\ell m} \left[2\cos\theta \; + \; \sin\theta \; \frac{\partial}{\partial \theta} \right] \right\} Y_\ell^m(\theta,\phi) \; \exp(i\sigma_c t) = 0, \quad (2.21)$$

$$\sum_{\ell=0}^{\infty} \sum_{m=-\ell}^{\ell} \left\{ \rho'_{\ell m} \; + \; rS_{\ell m}\frac{d\rho}{dr} \; + \; \rho\frac{1}{r^2}\frac{d}{dr}(r^3 S_{\ell m}) \; - \; \rho \; H_{\ell m} \; L^2 \right\} Y_\ell^m(\theta,\phi) \; \exp(i\sigma_c t) = 0,$$

$$(2.22)$$

$$\sum_{\ell=0}^{\infty} \sum_{m=-\ell}^{\ell} \left\{ \frac{1}{r^2}\frac{d}{dr}\left(r^2\frac{d\Phi'_{\ell m}}{dr} \right) \; - \; \frac{1}{r^2}\Phi'_{\ell m}L^2 - 4\pi G\rho'_{\ell m} \right\} Y_\ell^m(\theta,\phi) \; \exp(i\sigma_c t) = 0, \quad (2.23)$$

$$\sum_{\ell=0}^{\infty} \sum_{m=-\ell}^{\ell} \left\{ \frac{P'_{\ell m}}{P} + \frac{rS_{\ell m}}{P}\frac{dP}{dr} - \Gamma_1 \left[\frac{\rho'_{\ell m}}{\rho} + \frac{rS_{\ell m}}{\rho}\frac{d\rho}{dr} \right] \right\} Y_\ell^m(\theta,\phi) \; \exp(i\sigma_c t) = 0. \quad (2.24)$$

These equations contain $L^2 \; Y_\ell^m(\theta,\phi)$, $\cos\theta \; Y_\ell^m(\theta,\phi)$ and $\sin\theta\dfrac{\partial Y_\ell^m(\theta,\phi)}{\partial \theta}$. By using the following relations of spherical harmonics:

$$L^2 \; Y_\ell^m(\theta,\phi) \; = \; \ell(\ell+1) \; Y_\ell^m(\theta,\phi), \qquad (2.25)$$

$$\cos\theta \; Y_\ell^m(\theta,\phi) \; = \; J_{\ell+1}^m \; Y_{\ell+1}^m(\theta,\phi) \; + \; J_\ell^m \; Y_{\ell-1}^m(\theta,\phi), \qquad (2.26)$$

and

$$\sin\theta\frac{\partial Y_\ell^m(\theta,\phi)}{\partial \theta} \; = \; \ell \; J_{\ell+1}^m \; Y_{\ell+1}^m(\theta,\phi) \; - \; (\ell+1) \; J_\ell^m \; Y_{\ell-1}^m(\theta,\phi), \qquad (2.27)$$

where

$$J_\ell^m \; = \; \begin{cases} \left(\dfrac{\ell^2 - m^2}{4\ell^2 - 1} \right)^{1/2} & \text{if } \ell > |m|, \\ 0 & \text{if } \ell \leq |m|, \end{cases}$$

one succeeds in writing the equations in the following form:

$$\sum_{\ell=0}^{\infty} \sum_{m=-\ell}^{\ell} F_{\ell m}(r) \; Y_\ell^m(\theta,\phi) \; \exp(i\sigma_c t) = 0.$$

In that way the coefficients $F_{\ell m}(r)$ of the sum of spherical harmonics vanish, as these latter functions form a basis. We note that equation (2.25) is a well-known property of spherical harmonics and equations (2.26) and (2.27) are directly deduced from the recurrence relations of the associated Legendre polynomials (see Appendix A.2).

For each m, we obtain an infinite set of equations coupled in ℓ:

$$rS_{\ell m} \; - \; m\eta r H_{\ell m} \; - i\eta r \; \left[(\ell - 1)J_\ell^m T_{\ell-1,m} \; - \; (\ell + 2)J_{\ell+1}^m T_{\ell+1,m} \right]$$
$$= \frac{1}{\sigma_c^2} \left(\frac{d\Phi'_{\ell m}}{dr} \; - \; \frac{\rho'_{\ell m}}{\rho^2} \frac{dP}{dr} \; + \; \frac{1}{\rho} \frac{dP'_{\ell m}}{dr} \right), \tag{2.28}$$

$$\left[\ell(\ell+1) - m\eta \right] H_{\ell m} \; - \; i\eta \left[(\ell^2 - 1)J_\ell^m T_{\ell-1,m} \; + \; \ell(\ell+2)J_{\ell+1}^m T_{\ell+1,m} \right]$$
$$-m\eta \; S_{\ell m} \; - \; \frac{\ell(\ell+1)}{r^2\sigma_c^2} \left(\frac{P'_{\ell m}}{\rho} \; + \; \Phi'_{\ell m} \right) = 0, \tag{2.29}$$

$$\left[\ell(\ell+1) - m\eta \right] T_{\ell m} \; + \; i\eta \left[(\ell^2 - 1)J_\ell^m H_{\ell-1,m} \; + \; \ell(\ell+2)J_{\ell+1}^m H_{\ell+1,m} \right]$$
$$-i\eta \left[(\ell+1)J_\ell^m S_{\ell-1,m} \; - \; \ell \; J_{\ell+1}^m S_{\ell+1,m} \right] = 0, \tag{2.30}$$

$$\rho'_{\ell m} \; + \; r\frac{d\rho}{dr} S_{\ell m} \; + \; \rho\frac{1}{r^2}\frac{d}{dr}(r^3 S_{\ell m}) \; - \; \rho \; \ell(\ell+1) \; H_{\ell m} = 0, \tag{2.31}$$

$$\frac{1}{r^2}\frac{d}{dr}\left(r^2\frac{d\Phi'_{\ell m}}{dr} \right) \; - \; \frac{1}{r^2} \; \ell(\ell+1) \; \Phi'_{\ell m} = 4\pi G\rho'_{\ell m}, \tag{2.32}$$

$$\frac{P'_{\ell m}}{P} + \frac{rS_{\ell m}}{P} \; \frac{dP}{dr} = \Gamma_1 \left[\frac{\rho'_{\ell m}}{\rho} + \frac{rS_{\ell m}}{\rho} \; \frac{d\rho}{dr} \right], \tag{2.33}$$

where $\eta = \dfrac{2\Omega}{\sigma_c}$.

Equations (2.28) and (2.29) show that the spheroidal components associated with ℓ couple with toroidal components associated with $\ell-1$ and $\ell+1$. Moreover equation (2.30) shows that the toroidal components associated with ℓ couple with spheroidal components associated with $\ell - 1$ and $\ell + 1$. For each m, we are then dealing with two independent sets of infinitely coupled differential equations. The first infinite set of equations corresponds to spheroidal components with $\ell = |m|, \; |m| + 2, \ldots$ and toroidal components with $\ell' = |m| + 1, |m| + 3, \ldots$. The second corresponds to spheroidal components with $\ell = |m| + 1, \; |m| + 3, \ldots$ and toroidal components with $\ell' = |m|, \; |m| + 2, \ldots$. Lee & Saio (1987) speak of *even-modes* and *odd-modes* respectively.

Let us write the system of equations in a vectorial form. We introduce the column vectors with infinite dimensions Y_1, Y_2, Y_3, Y_4, H and T whose j-th ($j = 1, \; 2, \; \ldots, \; \infty$) elements are given by $S_{\ell_j m}$, $\rho'_{\ell_j m}$, $P'_{\ell_j m}$, $\Phi'_{\ell_j m}$, $H_{\ell_j m}$ and $T_{\ell'_j m}$, where

$$_1\begin{cases} \ell_j = |m| + 2(j-1), \ \ell'_j = |m| + 2(j-1) + 1 & \text{for even-modes,} \\ \ell_j = |m| + 2(j-1) + 1, \ \ell'_j = |m| + 2(j-1) & \text{for odd-modes.} \end{cases}$$

Equations (2.28)-(2.33) are then written as:

$$rY_1 - m\eta r H - i\eta r C T = \frac{1}{\sigma_c^2} \left(\frac{dY_4}{dr} - \frac{Y_2}{\rho^2} \frac{dP}{dr} + \frac{1}{\rho} \frac{dY_3}{dr} \right), \qquad (2.34)$$

$$LH - i\eta \bar{M} T - m\eta \Lambda^{-1} Y_1 = \frac{1}{r^2 \sigma_c^2} \left(\frac{Y_3}{\rho} + Y_4 \right), \qquad (2.35)$$

$$\bar{L}T + i\eta M H - i\eta K Y_1 = 0, \qquad (2.36)$$

$$Y_2 + r\frac{d\rho}{dr}Y_1 + \rho\frac{1}{r^2}\frac{d}{dr}\left(r^3 Y_1\right) - \rho\Lambda H = 0, \qquad (2.37)$$

$$\frac{1}{r^2}\frac{d}{dr}\left(r^2\frac{dY_4}{dr}\right) - \frac{1}{r^2}\Lambda Y_4 = 4\pi G Y_2, \qquad (2.38)$$

$$\frac{Y_3}{P} + \frac{rY_1}{P}\frac{dP}{dr} = \Gamma_1\left[\frac{Y_2}{\rho} + \frac{rY_1}{\rho}\frac{d\rho}{dr}\right], \qquad (2.39)$$

where Λ, L and $\bar{L}$ are infinite diagonal matrices whose j-th element is given by

$$\Lambda_{jj} = \ell_j(\ell_j + 1),$$

$$L_{jj} = 1 - \frac{m\eta}{\ell_j(\ell_j + 1)},$$

$$\bar{L}_{jj} = \begin{cases} 1 - \dfrac{m\eta}{(\ell_j + 1)(\ell_j + 2)} & \text{for even-modes,} \\ 1 - \dfrac{m\eta}{\ell_j(\ell_j - 1)} & \text{for odd-modes,} \end{cases}$$

and where C, K, M, and $\bar{M}$ are infinite bi-diagonal matrices whose non-zero elements are given by

$$\begin{cases} C_{jj} = -(\ell_j + 2)J^m_{\ell_j+1}, & C_{j+1,j} = (\ell_j + 1)J^m_{\ell_j+2}, \\[2mm] K_{jj} = \dfrac{J^m_{\ell_j+1}}{\ell_j + 1}, & K_{j,j+1} = -\dfrac{J^m_{\ell_j+2}}{\ell_j + 2}, \\[2mm] M_{jj} = \dfrac{\ell_j}{\ell_j + 1}J^m_{\ell_j+1}, & M_{j,j+1} = \dfrac{\ell_j + 3}{\ell_j + 2}J^m_{\ell_j+2}, \\[2mm] \bar{M}_{jj} = \dfrac{\ell_j + 2}{\ell_j + 1}J^m_{\ell_j+1}, & \bar{M}_{j+1,j} = \dfrac{\ell_j + 1}{\ell_j + 2}J^m_{\ell_j+2}, \end{cases}$$

for even-modes, and,

---
[1]One speaks of even-modes and odd-modes because these have respectively even and odd $\ell - |m|$, corresponding to a symmetry and an antisymmetry around the equator.

$$
\left\{
\begin{array}{ll}
C_{jj} = (\ell_j + 1) J^m_{\ell_j}, & C_{j,j+1} = -(\ell_j + 2) J^m_{\ell_j+1}, \\[2ex]
K_{jj} = -\dfrac{J^m_{\ell_j}}{\ell_j}, & K_{j+1,j} = \dfrac{J^m_{\ell_j+1}}{\ell_j + 1}, \\[2ex]
M_{jj} = \dfrac{\ell_j + 1}{\ell_j} J^m_{\ell_j}, & M_{j+1,j} = \dfrac{\ell_j}{\ell_j + 1} J^m_{\ell_j+1}, \\[2ex]
\bar{M}_{jj} = \dfrac{\ell_j - 1}{\ell_j} J^m_{\ell_j}, & \bar{M}_{j,j+1} = \dfrac{\ell_j + 2}{\ell_j + 1} J^m_{\ell_j+1},
\end{array}
\right.
$$

for odd-modes (Lee & Saio 1987).

Approximations

We show in what follows that, under some approximations, we may decompose the infinite system of equations into an infinite number of independent systems of equations.

First we neglect the horizontal component of the angular velocity of rotation $-\Omega \sin\theta$, which corresponds to neglecting the Coriolis force associated with the radial motion $-\Omega \sigma_c \sin\theta \, \xi_r$ and the radial component of the Coriolis force associated with horizontal motion $\Omega \sigma_c \sin\theta \, \xi_\phi$. This approximation, which is called the **traditional approximation** in the literature, is reasonably good for low-frequency non-radial modes (g-modes), in which the horizontal motion dominates the oscillation[2]. The traditional approximation is in general fine for the treatment of the g-modes in SPBs. We do point out that it is not valid in the core regions where the radial motion is comparable with the horizontal motion, even for low-frequency modes.

In the traditional approximation, the terms with $\sin\theta \, \xi_r$ disappear in equations (2.14) and (2.15) so that the terms proportional to Y_1 in the algebraic equations (2.35) and (2.36) disappear. One can then express H in terms of Y_3 and Y_4 as well as T in terms of H:

$$
\left\{
\begin{array}{l}
H = \dfrac{1}{r^2 \sigma_c^2} \left(L - \eta^2 \bar{M} \bar{L}^{-1} M \right)^{-1} \left(\dfrac{Y_3}{\rho} + Y_4 \right), \\[2ex]
iT = \eta \bar{L}^{-1} M H.
\end{array}
\right.
$$

Moreover, the term with $\sin\theta \, \xi_\phi$ disappears in equation (2.13) so that the terms proportional to the toroidal components T and to the spheroidal components H in equation (2.34) disappear. In that way, equations (2.34), (2.37), (2.38) and (2.39) form a system for Y_1, Y_2, Y_3 and Y_4:

---

[2]For high-frequency modes (p-modes), the perturbation-expansion formalism (e.g. Aerts & Waelkens 1993) is still more appropriate.

$$\sigma_c^2 r \, Y_1 = \frac{dY_4}{dr} \; - \; \frac{Y_2}{\rho^2} \frac{dP}{dr} \; + \; \frac{1}{\rho} \frac{dY_3}{dr}, \tag{2.40}$$

$$Y_2 + r\frac{d\rho}{dr} Y_1 + \rho \frac{1}{r^2} \frac{d}{dr}\left(r^3 Y_1\right) - \frac{\rho}{r^2 \sigma_c^2} W \left(\frac{Y_3}{\rho} + Y_4\right) = 0, \tag{2.41}$$

$$\frac{1}{r^2} \frac{d}{dr}\left(r^2 \frac{dY_4}{dr}\right) \; - \; \frac{1}{r^2} \Lambda Y_4 = 4\pi G Y_2, \tag{2.42}$$

$$\frac{Y_3}{P} + \frac{rY_1}{P} \frac{dP}{dr} = \Gamma_1 \left[\frac{Y_2}{\rho} + \frac{rY_1}{\rho} \frac{d\rho}{dr}\right], \tag{2.43}$$

where W is an infinite symmetric tri-diagonal matrix defined by

$$W = \Lambda \left(L - \eta^2 \bar{M} \bar{L}^{-1} M\right)^{-1},$$

with the elements of the matrix W^{-1} given by

$$(W^{-1})_{jj} =$$

$$\frac{1}{\ell_j(\ell_j+1)} \left\{ 1 - \frac{m\eta}{\ell_j(\ell_j+1)} - \frac{\eta^2(\ell_j^2-1)(J_{\ell_j}^m)^2}{\ell_j^2\left[1 - \frac{m\eta}{\ell_j(\ell_j-1)}\right]} - \frac{\eta^2\ell_j(\ell_j+2)(J_{\ell_j+1}^m)^2}{(\ell_j+1)^2\left[1 - \frac{m\eta}{(\ell_j+1)(\ell_j+2)}\right]} \right\},$$

and

$$(W^{-1})_{j,j+1} = (W^{-1})_{j+1,j} = -\eta^2 \frac{J_{\ell_j+1}^m J_{\ell_j+2}^m}{(\ell_j+1)(\ell_j+2) - m\eta}.$$

We point out that the coupling between equations is now expressed by the single matrix W. Moreover, this matrix can be brought into the form

$$W = BD\tilde{B},$$

where D is a diagonal matrix whose non-zero elements are given by the eigenvalues of W, and B is an orthogonal matrix (the matrix inverse is the matrix transpose: $B^{-1} \equiv \tilde{B}$).

Multiplying equations (2.40)-(2.43) by B^{-1} from the left, we obtain

$$\sigma_c^2 r \, Z_1 = \left(\frac{dZ_4}{dr} \; - \; \frac{Z_2}{\rho^2} \frac{dP}{dr} \; + \; \frac{1}{\rho} \frac{dZ_3}{dr}\right), \tag{2.44}$$

$$Z_2 + r\frac{d\rho}{dr} Z_1 + \rho \frac{1}{r^2} \frac{d}{dr}\left(r^3 Z_1\right) - \frac{\rho}{r^2 \sigma_c^2} D \left(\frac{Z_3}{\rho} + Z_4\right) = 0, \tag{2.45}$$

$$\frac{1}{r^2} \frac{d}{dr}\left(r^2 \frac{dZ_4}{dr}\right) \; - \; \frac{1}{r^2} B^{-1}\Lambda Y_4 = 4\pi G Z_2, \tag{2.46}$$

$$\frac{Z_3}{P} + \frac{rZ_1}{P} \frac{dP}{dr} = \Gamma_1 \left[\frac{Z_2}{\rho} + \frac{rZ_1}{\rho} \frac{d\rho}{dr}\right], \tag{2.47}$$

where

$$Z_1 = B^{-1}Y_1, \ Z_2 = B^{-1}Y_2, \ Z_3 = B^{-1}Y_3, \ Z_4 = B^{-1}Y_4,$$

and where $D = B^{-1}WB$ is a diagonal matrix.

Diagonalizing W into D corresponds to changing the basis of spherical harmonics into a new basis and allows to decouple the system of equations. In equation (2.46), the matrix B^{-1} does not commute with the diagonal matrix Λ, which shows that the change of basis is not appropriate for the Poisson equation. This can be understood in another way: the operator L^2 disappears in the Poisson equation because the spherical harmonics are eigenfunctions of L^2, which is not the case of another basis. To decouple the equations, we are then obliged to make the **Cowling approximation**, which assumes that $\Phi' = 0$. This approximation is quite good for modes with a large number of nodes, as is the case for the modes in SPBs.

For each ℓ_j $(j = 1, \ldots, \infty)$, we then have

$$\sigma_c^2 r(Z_1)_j = -\ \frac{(Z_2)_j}{\rho^2}\ \frac{dP}{dr}\ +\ \frac{1}{\rho}\ \frac{d(Z_3)_j}{dr}, \tag{2.48}$$

$$(Z_2)_j + r\frac{d\rho}{dr}(Z_1)_j + \rho\frac{1}{r^2}\frac{d}{dr}\left(r^3(Z_1)_j\right) - \frac{\rho}{r^2\sigma_c^2}\lambda_{\ell_j m}\left(\frac{(Z_3)_j}{\rho}\right) = 0, \tag{2.49}$$

$$\frac{(Z_3)_j}{P} + \frac{r(Z_1)_j}{P}\ \frac{dP}{dr} = \Gamma_1\left[\frac{(Z_2)_j}{\rho} + \frac{r(Z_1)_j}{\rho}\ \frac{d\rho}{dr}\right], \tag{2.50}$$

where we recall that $\lambda_{\ell_j m}$ is an eigenvalue of the matrix W. We note that, in order to compute the eigenvalues, the infinite matrix W must be truncated (Lee & Saio 1987).

We observe that, under both the traditional approximation and the Cowling approximation, the adiabatic equations governing the pulsations of a spherically symmetric star rotating uniformly are identical to the non-rotating pulsation equations with the replacement of $\ell(\ell+1)$ by $\lambda_{\ell m}$ in the continuity equation. These equations may be solved as an eigenvalue problem $Ax = \lambda x$ $(\lambda \equiv \sigma_c^2)$ with appropriate boundary conditions.

The theoretical frequencies reported in this thesis were computed by using two codes implemented by Dr. R. Scuflaire. They are OSC, which solves the equations (2.48) - (2.50) for a non-rotating star and CLES (Code Liégeois d'Evolution Stellaire), which computes the equilibrium models. We point out that we have adapted OSC to the formalism described above by computing $\lambda_{\ell m}$ instead of $\ell(\ell+1)$ in equations (2.48) - (2.50) in the framework of this thesis. To achieve this, we have made use of subroutines written by Dr. R. Townsend (BRUCE, Townsend 1997).

We note that, in the non-rotating case, pulsational frequencies are the same for modes with the same ℓ regardless of the value of m. One speaks of a $(2\ell + 1)$-fold *degeneracy*, which is lifted for a rotating star.

2.2   Pulsational velocity field at the stellar surface

In order to model line-profile variations, one needs an expression for the pulsational velocity field at the stellar surface. As the perturbed velocity vector in the co-rotating frame is given by $\vec{v_c} = \partial \vec{\xi}/\partial t = i\,\sigma\,\vec{\xi}$, we derive an expression for the displacement vector at the stellar surface in what follows.

In the previous section, we have shown that introducing the Coriolis force leads to eigenfunctions which contain only spherical harmonics of the same azimutal order m. Moreover, only harmonics of the same parity (even-modes or odd-modes) are coupled.

In vectorial form, the displacement vector $\vec{\xi}(r, \theta, \phi)$ is written as

$$\frac{\vec{\xi}}{r} = Y_1 \,.\, \Phi \,\vec{e}_r + \nabla_h(H \,.\, \Phi) + \nabla_h \wedge (T \,.\, \Phi'\vec{e}_r), \qquad (2.51)$$

where ∇_h is the horizontal component of the gradient operator in spherical coordinates,

$$\nabla_h = \left(0, \frac{1}{r}\frac{\partial}{\partial \theta}, \frac{1}{r\sin\theta}\frac{\partial}{\partial \phi}\right).$$

$Y_1(r), T(r)$ and $H(r)$ are vectors of infinite dimension, containing information concerning the radial dependence; $\Phi(\theta, \phi)$ and $\Phi'(\theta, \phi)$ are again vectors of infinite dimension, describing the angular dependence and whose j-th $(j = 1,\ 2,\ \ldots,\ \infty)$ elements are given by

$$\Phi_j = Y_{\ell_j}^m(\theta, \phi) \text{ and } \Phi'_j = Y_{\ell'_j}^m(\theta, \phi),$$

where

$$\begin{cases} \ell_j = |m| + 2(j-1),\ \ell'_j = |m| + 2(j-1) + 1 & \text{for even-modes,} \\ \ell_j = |m| + 2(j-1) + 1,\ \ell'_j = |m| + 2(j-1) & \text{for odd-modes.} \end{cases}$$

By analogy to the transformation of the radial displacement vector function $Z_1 = B^{-1}Y_1$, the horizontal and toroidal displacement vector functions are given by $Z_5 = B^{-1}H$ and $Z_6 = B'^{-1}T$ where B' is the eigenvector matrix of the coupling matrix W' associated with the same value of m but the opposite parity to that of W. Equation (2.51) is then given by

$$\frac{\vec{\xi}}{r} = Z_1 \,.\, \Psi \,\vec{e}_r + \nabla_h(Z_5 \,.\, \Psi) + \nabla_h \wedge (Z_6 \,.\, \Psi'\vec{e}_r),$$

where the identity $BZ_1 \,.\, \Phi \equiv Z_1 \,.\, B^{-1}\Phi$, and similar expressions, have been used to define a new angular basis Ψ, given by

$$\Psi = B^{-1}\Phi \text{ and } \Psi' = B'^{-1}\Phi',$$

and, more explicitely, by

$$\Psi_j = \sum_{k=0}^{\infty} (B^{-1})_{jk} \, Y_{\ell_k}^m(\theta, \phi)$$

and

$$\Psi'_j = \sum_{k=0}^{\infty} (B'^{-1})_{jk} \, Y_{\ell'_k}^m(\theta, \phi).$$

For chosen ℓ_j, one may impose $(Z_1)_k = 0$, $(Z_2)_k = 0$ and $(Z_3)_k = 0$ for $k \neq j$ so that

$$Z_5 = h_j \frac{(Z_3)_j}{r^2 \sigma_c^2 \rho}$$

and

$$Z_6 = -it_j \frac{(Z_3)_j}{r^2 \sigma_c^2 \rho},$$

where the two vectors h_j and t_j are given by

$$(h_j)_i = (B^{-1} \Lambda^{-1} W B)_{ij}$$

and

$$(t_j)_i = (\eta B'^{-1} \bar{L} M \Lambda^{-1} W B)_{ij}.$$

Following Lee & Saio (1990), at the surface of the star, the Z-boundary[3] may be used to find an expression for $(Z_3)_j$ in terms of $(Z_1)_j$, which is $(Z_1)_j = \dfrac{1}{g\rho}(Z_3)_j$ in the Cowling approximation.

At the stellar surface, the displacement vector for a pulsation mode associated with m and ℓ_j is then given by

$$\frac{\vec{\xi}(R, \theta, \phi, t)}{R} =$$

$$A_p \Re \left\{ \left[\Psi_j \vec{e}_r + \frac{GM}{R^3 \sigma_c^2} \left(\nabla_h \sum_{k=1}^{\infty} (h_j)_k \Psi_k + \nabla_h \wedge \sum_{k=1}^{\infty} -i(t_j)_k \Psi'_k \vec{e}_r \right) \right] \exp(i\sigma_c t) \right\},$$

where A_p is the value of $(Z_1)_j$ at this boundary, M the stellar mass and R the stellar radius. (Lee & Saio 1990)

We point out that the functions Ψ_j represent the normal mode set of angular functions for a rotating star (within the traditional and Cowling approximations) in analogy to the spherical harmonics in the non-rotating case.

We also point out that the dimensionless quantity $\dfrac{GM}{R^3 \sigma_c^2} = \dfrac{\xi_h(R)}{\xi_r(R)}$ is generally denoted by K. This so-called K-value indicates which of the horizontal or vertical displacement is dominant for a given pulsation mode. In general, the horizontal one is much larger than the vertical one for low frequencies (g-modes) while the opposite is true for high frequencies (p-modes). Note that the co-rotating angular frequency is related to the observed angular frequency with $\sigma_{\mathrm{obs}} = \sigma_c - m\Omega$.

---

[3]The Z-boundary refers to the so-called zero boundary condition which imposes a vanishing pressure at the stellar surface.

Chapter 3

Line-profile modelling

For the B-type stars that we studied, two models were considered in order to interpret observed line-profile variations: the non-radial stellar pulsation model (Sect. 3.1) and the rotational modulation model (Sect. 3.2). In this chapter, we explain the ingredients of both models.

3.1 Non-radial pulsation model

A short description of line-profile modelling is the following. First, the intrinsic broadening of the spectral line is due to different mechanisms: atomic broadening, pressure broadening and thermal broadening. This so-called *intrinsic profile* is often taken gaussian[1] and constant:

$$I(\lambda) = I_0 \frac{1}{\sqrt{2\pi}\sigma} \exp\left(-\frac{(\lambda - \lambda_0)^2}{2\sigma^2}\right), \tag{3.1}$$

where σ is called the intrinsic line-profile width. One can also use flux spectra calculated for a given temperature T and surface gravity g by using a stellar atmosphere code. For both cases, we take into account angular dependence using a limb-darkening law which has often a linear form:

$$I_\lambda(\mu) = I_\lambda(0)(1 - u_\lambda + u_\lambda \cos\mu) = I_\lambda(0)h_\lambda(\cos\mu), \tag{3.2}$$

where $u_\lambda \in [0; 1]$ is called the limb-darkening coefficient and depends on the considered wavelength range, $\cos\mu$ is the cosine of the angle between the normal of a surface element and the line of sight, $I_\lambda(0)$ is the intensity of a surface element in the line of sight represented by the gaussian or the flux spectra. A third possibility (the better one but time-consuming) is to use angle-dependent intensity spectra calculated for a given temperature T, surface gravity g and angle parameter $\cos\mu$.

---

[1] The thermal broadening is the dominant broadening mechanism in hot stars and is described by a gaussian. Note also that the Si II-doublet centered at 4128-4130 Å, that we used for the analysis of B-type stars, is well approximated by a gaussian.

Another cause of line broadening is the rotation of the star. Particles moving towards the observer cause a blue shift and particles moving from the observer cause a red shift. This rotational broadening is symmetric and independent of time if we assume a uniform rotation.

The two main causes leading to temporal variations of the line profiles of a pulsating star are the velocity field generated by oscillatory displacements and the brightness variations due to temperature variations.

At a given time, the synthetic spectra of a star which undergoes pulsations is calculated as follows. We consider an inertial frame and we use the spherical coordinates (r, θ, ϕ) whose polar axis coincides with the axis of rotation. We divide the stellar surface into many surface elements (θ, ϕ) by taking steps of $\Delta\theta$ in θ and $\Delta\phi$ in ϕ. An expression for $\cos\mu$ is then given by $\cos\mu = \cos\theta\cos i - \sin\theta\cos\phi\sin i$ where i is the angle of inclination, i.e. the angle between the line-of-sight and the rotation axis. For each surface element, the intensity at the observed wavelength λ is given by

$$I_{\lambda_r}(\mu)A_{\mathrm{proj}}, \tag{3.3}$$

where A_{proj} is the projection on the line of sight of the surface element and is given by $R^2\sin\theta\cos\mu\Delta\theta\Delta\phi$ with R the stellar radius. λ_r is the rest wavelength related to the observed wavelength λ through the Doppler formula:

$$\lambda_r = \frac{\lambda}{1 - v_{\mathrm{proj}}/c} \tag{3.4}$$

where v_{proj} is the sum of the pulsation and rotation velocity in the line of sight, c is the speed of light. An expression for the pulsational velocity field at the surface of a rotating star in the co-rotating frame was already derived in Chapter 2. The rotational velocity in the line of sight is given by $v_{\mathrm{rot}} = \Omega\,R\,\sin i\,\sin\theta\,\sin\phi \equiv v_\Omega\,\sin\theta\,\sin\phi$ with Ω the angular frequency of rotation. Finally, the line profile $p(\lambda, t)$ is obtained by summing up all the contributions for all the visible surface elements:

$$p(\lambda, t) = \sum_{j,k} I_{\lambda_r}(\mu_{jk})R^2\sin\theta_j\cos\mu_{jk}\Delta\theta_j\Delta\phi_k,$$

where the sum is taken over the visible surface (i.e. $\cos\mu_{jk} > 0$).

We generated theoretical line-profile variations by using a code called BRUCE implemented by Dr. R. Townsend (1997) and made publicly available, which uses the pulsational velocity field derived by Lee & Saio (1987, 1990) for rotating stars, taking into account the Coriolis force within the traditional and Cowling approximations (Chapter 2). This code uses temperature variations at the stellar surface given by:

$$\frac{\delta T(\phi, \theta)}{T} = \Delta_T \nabla_{\mathrm{ad}} \left[\frac{\lambda_{\ell_j,m}}{\sigma_c^2} - 4 - \sigma_c^2 \right] \frac{\xi_r(\theta, \phi)}{r} \exp(i\psi_T),$$

where Δ_T and ψ_T are introduced to take into account the deviations of the temperature perturbation amplitude and phase from adiabaticity; in the purely adiabatic case, Δ_T and ψ_T take the values 1 and 0 respectively. The term with $\lambda_{\ell_j,m}$ is a generalisation of the one occurring for a non-rotating formulation in the traditional approximation. We note that BRUCE also takes into account geometric perturbations, which are essentially a variation in the area associated with the surface element and a variation in the surface normal of the element.

Recently, De Ridder (2001) implemented a code called PULSTAR, which generates line-profile variations using the usual velocity field of a non-rotating star but which takes into account temperature variations at the stellar surface by using non-adiabatic eigen-functions in the outer layers of the star. The latter were computed with a new non-adiabatic pulsation code called EXSTAR developed by Dupret (2001). We point out that Dupret et al. (2002) and De Ridder et al. (2002a) show that, for slowly-rotating non-radially pulsating B stars such as SPBs, the line-profile variations of silicon lines are very little affected by temperature variations at the stellar surface and can be well approximated with a pulsational velocity field only.

3.2   Rotational modulation model

In order to compare observed line-profile variations with a rotational modulation model we used a code implemented by Dr. L. Balona who kindly put it at our disposal. Such a model assumes that the line-profile variations are due to the rotation of the star in the presence of one (or more) spot(s), whose intensity of radiation differs from the intensity of the rest of the star. The observed period of the variations in the data is considered as the rotation period and consequently the observed period must be equal to the calculated rotation period $P_{\rm rot} = \dfrac{2\pi R}{v_{\rm eq}}$, where R is the radius of the star and $v_{\rm eq}$ its equatorial velocity.

We introduce a right-handed inertial frame of orthogonal cartesian coordinates (x'', y'', z'') with its origin at the centre of the star and the z''-axis pointing towards the observer. In this frame of reference we pass on to a system of spherical coordinates (r'', θ'', ϕ'') whose polar axis coincides with the z''-axis. We divide the visible stellar surface ($\theta'' \in [0°; 90°], \phi'' \in [0°; 360°[$) into surface elements by taking steps of $\Delta\theta''$ in θ'' and $\Delta\phi''$ in ϕ''.

The contribution of a surface element to the line profile is given by

$$\frac{I}{\sqrt{2\pi}\,\sigma}\,\exp\left(-\frac{(\lambda_r - \lambda_0)^2}{2\sigma^2}\right) h_\lambda(\theta'')\,R^2\,\sin\theta''\,\cos\theta''\,\Delta\theta''\,\Delta\phi'',$$

as derived in Sect. 3.1 (see equations (3.1), (3.2), (3.3)) where $v_{\rm proj}$ of equation (3.4) is now the projected rotation velocity in the line of sight. The line profile $p(\lambda, t)$ is obtained by summing up all the contributions from all the visible surface elements.

A difference between the flux of a spot $I = I_{\mathrm{spot}}$ and the flux of the rest of the star $I = I_{\mathrm{star}}$ causes variations in the line profile. $I_{\mathrm{spot}} < I_{\mathrm{star}}$ corresponds to an underabundance of the considered element in the spot compared to the rest of the star while $I_{\mathrm{spot}} > I_{\mathrm{star}}$ corresponds to an overabundance of the element.

We must determine if the point (R'', θ'', ϕ'') on the stellar surface belongs to the spot or not. This is done by considering a co-rotating frame of right-handed orthogonal cartesian coordinates (x', y', z') with its origin at the centre of the star and z'-axis coinciding with rotation axis. The angle between the z'-axis and the z''-axis is then the inclination angle of the star. We use spherical coordinates (r', θ', ϕ') with polar axis z'.

Let α be the longitude, β the latitude and γ the radius of a circular spot in the system (x', y', z'). All these quantities are expressed in degrees. A point of the surface (R, θ', ϕ') belongs to the spot if $\alpha - \gamma < \phi' < \alpha + \gamma$ and if the angle between the centre of the spot and the considered point is smaller than the spot radius. By using spherical trigonometric relations one can show that this latter condition comes down to $\cos \gamma > \cos(90° - \beta) \; \cos \theta' + \sin(90° - \beta) \; \sin \theta' \; \cos(\alpha - \phi')$.

We still have to determine the spherical coordinates of (R, θ'', ϕ'') in the system (x', y', z'): (R, θ', ϕ'). By considering a right-handed inertial frame of orthogonal cartesian coordinates (x, y, z) with its origin at the centre of the star, the z-axis coinciding with the z'-axis, the x-axis and the y-axis coinciding respectively to the x''-axis and the y''-axis at $t_0 = 0$, we have

$$\begin{cases} \cos \theta = \cos i \; \cos \theta'' + \sin i \; \sin \theta'' \; \cos \phi'' \\ \cos \phi = \dfrac{\cos i \; \sin \theta'' \; \cos \phi'' - \sin i \; \cos \theta''}{\sqrt{1 - \cos^2 \theta}}. \end{cases}$$

From these latter expressions we deduce (θ, ϕ). Finally, $\theta' = \theta$ and $\phi' = \phi + \Omega t$, where Ω is the angular frequency of rotation.

Summarising, Balona's code prompts for the following parameters: the radius R, the projected rotational velocity v_Ω, the angle of inclination i, the linear limb-darkening coefficient u_λ, the intrinsic line-profile width σ, the longitude α, the latitude β, the spot radius γ in degrees, the flux of the spot relative to the photosphere F. One then obtains emission profiles without continuum. To match them to the observed profiles one needs to invert them and scale them so that the equivalent width matches the observed equivalent width.

We note that the inclination angle can be restricted to the range $[0°, 90°]$. Indeed a line profile with the parameters v_Ω, i, α, β at the time t is equivalent to a line profile with the parameters v_Ω, $180° - i$, α, $-\beta$, at the time t or $-v_\Omega$, $180° + i$, α, $-\beta$, at the time $t + P_{\mathrm{rot}}/2$ or $-v_\Omega$, $360° - i$, α, β, at the time $t + P_{\mathrm{rot}}/2$. Moreover, to take $-v_\Omega$ instead of v_Ω is equivalent to making a symmetric image of the line profile. We also note that modifying the longitude is equivalent to making a temporal translation. Consequently the longitude can be restricted to the range $[0°; 90°]$ if the observed profiles are shifted by 0.25, 0.5, 0.75 period.

Chapter 4

Existing analysis methods

In this chapter, we give a description of the methods that we used for the analysis of data of several pulsating B stars (Part II) and chemically peculiar B stars (Part III). First, we remind the basic ideas to find frequencies in astronomical time series (Sect. 4.1). Then, we describe how line-profile variations (LPVs) are used to identify modes of pulsating stars (Sect. 4.2) and to derive surface abundance structures of chemically peculiar stars (Sect. 4.3).

4.1 Frequency analysis

A variable star is a star for which observable variations in time are detected in certain of its physical properties such as its brightness, colour index, spectrum and magnetic field. In order to search for periodicity in astronomical time series, different techniques have been developed. The Fourier techniques (Scargle 1981, Roberts et al. 1987) and the Phase Dispersion Minimization method (Jurkevich 1971, Stellingwerf 1978) are described hereafter. To perform frequency analysis, we used codes implemented by Dr. J. Cuypers and Dr. J. Telting, who kindly made them available to us.

4.1.1 The Fourier methods

4.1.1.1 Basic idea, classical and Lomb-Scargle periodograms

The Fourier transform of $x(t)$ is defined as

$$F(f) = \int_{-\infty}^{+\infty} x(t) \exp(i2\pi ft) \ dt.$$

In particular, for $x(t) = \cos(2\pi f_0 t)$, we have

$$F(f) = \frac{\delta(f - f_0) + \delta(f + f_0)}{2},$$

where $\delta(f)$ indicates the δ-Dirac function. Consequently, $F(f) = 0$ except at $\pm f_0$. The Fourier transform hence underlines the frequency which is present in the signal. Generally

speaking, the Fourier transform of an harmonic signal for which the frequencies are f_1, ..., f_M takes zero values except at $\pm f_1$, ..., $\pm f_M$.

In practice, we know $x(t)$ at t_j $(j = 1, \ldots, N)$ and we define:

$$x_s(t) = x(t) \, \frac{\sum_{j=1}^{N} \delta(t - t_j)}{N} = x(t) \, s(t).$$

So, instead of $F(f)$, we are able to calculate the Fourier transform of $x_s(t)$:

$$F_s(f) = \sum_{j=1}^{N} x(t_j) \, \exp(i2\pi f t_j),$$

as well as the Fourier transform of $s(t)$, which is called the *spectral window*:

$$W(f) = \frac{1}{N} \sum_{j=1}^{N} \exp(i2\pi f t_j).$$

By the convolution theorem, we have

$$F_s(f) = F(f) * W(f),$$

where $*$ denotes the convolution product.

For $x(t_j) = \cos(2\pi f_0 t_j)(j = 1, \ldots, N)$, we have

$$F_s(f) = \frac{W(f - f_0) + W(f + f_0)}{2},$$

and, in the case of equidistant observations, i.e. $x(t)$ is observed at $t_j = t_1 + (j-1)\Delta t$ $(j = 1, \ldots, N)$, it is easy to show that,

$$W(f) = \frac{1}{N} \frac{\sin(\pi f N \Delta t)}{\sin(\pi f \Delta t)}.$$

Knowing the signal on a limited total span time $T = N\Delta t$ leads to *spectral leakage*, i.e. there is a spreading of the "energy" of the frequency f_0 towards close frequencies and knowing the signal at discrete values leads to the presence of *alias* frequencies, i.e. $|F_s(f)|$ has maxima at $\pm f_0$, but also, at $\pm f_0 \pm \frac{k}{\Delta t}$ (k integer). The more common aliases are one-day-aliases ($\pm f \pm k$ c d^{-1}) since ground-based observations are taken only during the local nights. We also point out that errors on the measurements may introduce false peaks in the periodogram.

Due to the fact that real observations are non-equidistant, the spectral window is a complex function. One then determines $|W(f)|$, which exhibits a forest of peaks. One also calculates the so-called *classical periodogram*

$$P_{cl}(f) = \frac{|F_s(f)|^2}{N} = \frac{1}{N} \left\{ \left(\sum_{j=1}^{N} x(t_j) \sin(2\pi f t_j) \right)^2 + \left(\sum_{j=1}^{N} x(t_j) \cos(2\pi f t_j) \right)^2 \right\}.$$

We note that $P_{cl}(f)$ depends on the reference epoch chosen to treat the data.

If the signal has several periodic components, each frequency produces its sidelobes. Consequently, the value of the periodogram at certain frequencies is influenced by the values at other frequencies. We speak of "*dependent frequencies*". Moreover, if the signal has a constant component, the peak which is situated at $f = 0$ contaminates the whole periodogram. The adopted solution is to subtract the average of the data before calculating the periodogram.

We notice that, if the signal is multiperiodic, it may happen that the highest peak does not correspond to a real frequency. We also note that there is no rigorous mathematical expression allowing to calculate the accuracy of the frequency found. This latter remark is valid for each of the methods described here. Generally, one searches for the frequency with the step $\frac{1}{T}$, where T is of the order of the total time base of the data.

Another periodogram has been proposed and is now commonly used by astronomers. It was introduced by Lomb (1976) and was further developed by Scargle (1981). It is defined as

$$P_{LS}(f) = \frac{1}{2} \left\{ \frac{\left(\sum_{j=1}^{N} x(t_j) \sin\left(2\pi f(t_j - \tau)\right)\right)^2}{\sum_{j=1}^{N} \sin^2\left(2\pi f(t_j - \tau)\right)} + \frac{\left(\sum_{j=1}^{N} x(t_j) \cos\left(2\pi f(t_j - \tau)\right)\right)^2}{\sum_{j=1}^{N} \cos^2\left(2\pi f(t_j - \tau)\right)} \right\},$$

where

$$\tau = \frac{1}{4\pi f} \arctan\left(\frac{\sum_{j=1}^{N} \sin(4\pi f t_j)}{\sum_{j=1}^{N} \cos(4\pi f t_j)}\right).$$

This periodogram comes from a least-squares method for which the model is a cosine. It is independent of the reference epoch, i.e. it is independent of the phase of the signal. To remove the influence of $f = 0$, we subtract the average of the data before calculating the periodogram.

J. D. Scargle proposed a statistical test allowing to know if one peak in the periodogram is due to a periodic component or to noise. Unfortunately, we cannot use it because of the problem of "*frequencies dependence*" which still remains for multiperiodic stars.

4.1.1.2   The CLEAN method

As explained above

$$F_s(f) = F(f) * W(f),$$

where $*$ denotes the convolution product and where $F_s(f)$ and $W(f)$ are known. The aim of the CLEAN method is to remove the sidelobes due to the structure of $W(f)$, i.e. to construct an estimation of $F(f)$ from $F_s(f)$ and $W(f)$.

Let us describe the method proposed by Roberts et al. (1987) for a single cosinusoid $x(t) = A \cos(2\pi f_0 t + \psi)$.

We have

$$F(f) = a\delta(f - f_0) + a^*\delta(f + f_0),$$

where $a = \dfrac{A}{2}\exp(i\psi)$ and

$$F_s(f) = aW(f - f_0) + a^*W(f + f_0).$$

A few calculations lead to

$$a = \frac{F_s(f_0) - F_s^*(f_0)W(2f_0)}{1 - |W(2f_0)|^2}.$$

In the case of a single cosinusoid without noise, the sidelobes are removed completely by subtracting the spectral window shifted to the frequency of the signal. However, for real observations, there is an error on the frequency derived from $|F_s(f)|$. One then needs an iterative process for which one peak and its sidelobes are reduced to a fraction g at each iteration in order to ensure the stability of the procedure.

The CLEAN algorithm performs as follows:
(1) We search the frequency $f_{\max}$ for which $|F_s(f)|$ is maximum.
(2) We remove partly the contribution of this so-called *clean component* with its sidelobes by subtracting from $F_s(f)$

$$cW(f - f_{\max}) + c^*W(f + f_{\max}),$$

where

$$c = g\frac{F_s(f_{\max}) - F_s^*(f_{\max})W(2f_{\max})}{1 - |W(2f_{\max})|^2},$$

with $0.1 \leq g \leq 1$.
One obtains a residual spectrum, which is then a new $F_s(f)$.
We repeat (1) and (2) N_{iter} times.
Generally one takes $g = 0.2$ and $N_{iter} = 100$, but an in-depth statistical study of the influence of chosen values for g and N_{iter} does not exist.
(3) We convolve the clean components with an appropriate gaussian to make the frequency resolution $\sim 1/T$ and we add the final residual spectrum to preserve the noise level.
The clean spectrum is formed.

We note that, if the higher peak does not correspond to a real frequency, which may happen for multiperiodic stars, CLEAN will subtract a component that does not exist and will fail. Moreover, we do not know the efficiency of the method in the presence of noise.

4.1.2   The PDM method

Let $x(t)$ be a function of the time t. The phase corresponding to the frequency f is given by

$$\psi(t) = [f(t - t_0)],$$

where t_0 is a chosen reference epoch and brackets indicate the decimal part. The graph which represents x in function of ψ is called a *phase diagram.*

In practice, we have N observations x_i at different times t_i, which are spread over the time T. For a set of tested frequencies, we can construct phase diagrams. If the tested frequency is close to the frequency which is in the data, the dispersion of the observations in the phase diagram with respect to the mean curve will be small. On the other hand, the dispersion will be large if the tested frequency is not present in the data. The Phase Dispersion Minimization (PDM) method searches for the frequency for which the dispersion of the observations with respect to the mean curve is minimal.

Let us describe the method more precisely. We divide the phase interval $[0;1]$ into M equal intervals called *bins.* We assume that the j-th bin contains N_j observations $(j = 1, \ldots, M)$. The mean and the variance of the observations of the j-th bin are

$$\begin{cases} \bar{x}_j = \displaystyle\sum_{i=1}^{N_j} \frac{x_{ij}}{N_j}, \\ s_j^2 = \dfrac{\displaystyle\sum_{i=1}^{N_j} (x_{ij} - \bar{x}_j)^2}{N_j - 1}, \end{cases}$$

where x_{ij} is the observation x_i which is in the j-th bin. We denote $s^2 = \displaystyle\sum_{j=1}^{M} s_j^2$.

The mean and the variance of all observations are

$$\begin{cases} \bar{x} = \displaystyle\sum_{i=1}^{N} \frac{x_i}{N}, \\ \mathrm{S}^2 = \dfrac{\displaystyle\sum_{i=1}^{N} (x_i - \bar{x})^2}{N - 1}. \end{cases}$$

For a set of tested frequencies, the PDM method chooses the one for which the so-called Θ-*statistic* $\dfrac{s^2}{\mathrm{S}^2}$ is minimal. We have explicitly

$$\Theta = \frac{\dfrac{\sum\limits_{j=1}^{M}\sum\limits_{i=1}^{N_j}(x_{ij}-\bar{x}_j)^2}{\sum\limits_{j=1}^{M}N_j - M}}{\dfrac{\sum\limits_{i=1}^{N}(x_i-\bar{x})^2}{N-1}}.$$

We note that Θ-statistics are contaminated by aliases due to the temporal distribution and the errors on data. Moreover, sidelobes are found at the harmonics kf and the sub-harmonics f/k (k integer) of the real frequency.

This technique was proposed by Jurkevich (1971) and was then generalized by Stellingwerf (1978). The latter author proposed the same statistic Θ with another bin structure. We divide the phase interval [0;1] into N_b bins of length $\frac{1}{N_b}$. The phase interval is then covered by N_c *covers* of N_b bins, each cover shifted in phase by $\frac{1}{N_b N_c}$ from the previous cover. Such a bin structure is denoted by (N_b, N_c). N_b is generally taken from 5 to 20 and N_c from 1 to 10.

It would be interesting to find a stastistical test in which the null hypothesis H_0 is $s^2 \approx \mathrm{S}^2$. In this way, if the test rejects H_0, we can affirm that the frequency is significantly present in the data. Unfortunately, no precise test has been found up to now.

4.1.3   Search for multiperiodicity

We search for several frequencies in the measurements in the following way. By applying the methods of period determination, we find a significant frequency f. Then, we subtract from the measurements the sine

$$A\sin(2\pi f t + \psi) + C,$$

which best fits the measurements (we *prewhiten* the data with the significant frequency). A, C and ψ are obtained by the least-squares method. Afterwards, we search for another frequency in the *residuals*. We repeat the prewhitening until we obtain only peaks at the noise level, i.e. until the standard deviation of the residuals is smaller than the errors on the measurements.

We point out that there is no statistically justified criterion allowing to decide if the frequency corresponding to one peak in the periodogram is really present in the data or is due to noise. At present, some astronomers use the *4S/N criterion*, which was introduced by Breger et al. (1993). They defined the noise level as the average amplitude in an oversampled periodogram in the surroundings of the suspected frequency, computed after prewhitening of the suspected frequencies. Frequencies for which the peak amplitude is higher than 4 times the noise level are retained.

4.2 Mode identification

The pulsation of a star manifests itself through an observed periodic variability in its brightness and/or in its spectra. The natural way to identify the pulsation modes is then the following: by comparing the theoretically calculated variations with observed photometric and/or spectroscopic ones for different values of the wavenumbers (ℓ, m), one chooses the modes which best fit the observations. In this thesis, we describe only two methods which are based on spectroscopy: line-profile fitting and the moment method. These are the only two methods available thus far which allow the complete determination of all the unknown parameters of the velocity field.

4.2.1 The line-profile fitting technique

The identification of modes is performed by comparing the observed line-profile variations with theoretically calculated ones. We refer to Chapter 3 for the description of theoretical line-profile variations due to non-radial stellar pulsation.

The determination of pulsation modes is done as follows. For a given mode (ℓ, m), the free parameters needed to construct line-profile variations caused by non-radial pulsation are: the projected rotational velocity v_Ω, the angle of inclination i between the rotation axis and the line of sight, the amplitude of the radial part of the pulsation velocity A_p, the intrinsic line-profile width σ (if the intrinsic profile is assumed to be gaussian) and the initial phase of the mode ψ. We search for the parameters for which the calculated profiles best fit the observed profiles by considering a large grid of possible wavenumbers and parameters. We define the *"best fit model"* as the one which has the smallest standard deviation in the intensity over all profiles $\Sigma \equiv \frac{1}{N} \sum_{j=1}^{N} \sqrt{\frac{1}{n_j} \sum_{i=1}^{n_j} \left(I_{i,\text{obs}}^{j} - I_{i,\text{th}}^{j}\right)^2}$, with N the number of spectra and n_j the number of wavelength pixels in the spectra j.

4.2.2 The moment method

The method of line-profile fitting suffers of a major drawback: the unrealistic computation time for a simultaneous identification of multiple modes. The idea of the moment method is to replace each line profile by its first three moments, which are connected to respectively the centroid velocity of the line, the line width and the line skewness. The wavenumbers (ℓ, m) and the other continuous velocity parameters are then determined in such a way that the theoretically computed moment variations best fit the observed ones. The moment method was first introduced by Balona (Balona 1986ab, 1987) and was further developed by Aerts et al. (1992) and Aerts (1996). They derived analytical expressions of the first three moment variations, which are valid for stars with a long rotational period compared to the pulsational periods.

In this thesis, we propose a new numerical version of the technique which is more efficient than the previous one for rotating multiperiodic stars (see Chapter 5).

4.3 Doppler Imaging

The surface abundance distributions of elements can be obtained by a technique called Doppler Imaging, which inverts rotationally modulated line-profile variations into a two dimensional abundance distribution. To do this, we used a code called INVERS11 implemented and made available to us by Prof. N. Piskunov. We refer to Piskunov & Rice (1993) and Rice (1996) who describe Doppler Imaging methods in general.

4.3.1 Procedure

The input parameters for performing surface mapping are the effective temperature T_{eff}, the gravity $\log g$, the projected rotational velocity v_Ω, the inclination angle of the star i. The observed period in the line-profile variations is considered to be the rotation period of the star P_{rot}.

A short description of the Doppler Imaging procedure is the following. An initial guess for abundances of the considered elements is made. The stellar surface is divided into many surface elements and local line profiles and continuum intensity are obtained from model atmospheres that are calculated from Kurucz's ATLAS programs (Kurucz 1993). They are then used for the integration over the visible stellar surface, resulting in rotationally broadened line profiles, computed at observed phases ψ:

$$p(\lambda, \psi) = \frac{\int \int I(\lambda + \Delta\lambda_D, M, \mu) \, \cos\mu \, dM}{\int \int I_c(M, \mu) \, \cos\mu \, dM},$$

where M is the position on the stellar surface, μ is the angle between the normal to the surface at M and the line of sight, $I(\lambda)$ is the intensity of the line at the wavelength λ, $\Delta\lambda_D$ is the Doppler shift at M caused by the rotation of the star, I_c is the continuous intensity (i.e. the intensity that would be observed if the line was absent). Followed by the line-profile calculation for a start abundance distribution $A_0(M)$, the error

$$E = \sum_\psi \sum_\lambda \left[p_{\mathrm{calc}}(\lambda, \psi) - p_{\mathrm{obs}}(\lambda, \psi) \right]^2$$

is computed. An improved abundance map $A(M)$ is then determined by minimizing the error function

$$E + r[A(M)]$$

where

$$r[A(M)] = -\int \int_M |\mathrm{grad} A(M)|^2 \, dM$$

is a regularization component of Tikhonov's (1963) form[1], which involves the abundance gradient between adjacent surface elements and hence favors distributions with smooth

---

[1]The use of a selection algorithm is needed to find a distinctive map among the huge number of possible solutions of that ill-posed inverse problem.

contrasts. The minimization itself is performed using the conjugate gradient method. From this new map, new line-profile variations are computed and the error function is minimized in order to find a better map. This process is iterated until the difference between the calculated and observed line profiles is of the order of the signal-to-noise ratio of the input spectra. Procedures that have to be performed for the inversion of observed spectra into a surface abundance pattern of a star are illustrated in Fig. 4.1.

4.3.2   Observational requirements

Observational requirements, such as good phase coverage (30 spectra well distributed over the rotation period), high signal-to-noise ratio (S/N of at least 200) and an appropriate spectral resolution, have to be fulfilled when applying the Doppler Imaging technique.

Kuschnig (1998) tested the influence of the uncertainties of the input parameters on the results of the inversion process. Deviations of v_Ω of one or two percent of the real value do not severely affect the results. A precision of 0.01% for the rotation period is sufficient. The influence of incorrect determinations of model atmosphere parameters T_{eff} and $\log g$ generally do not affect the overall elemental distribution on the surface of the star but mainly the abundance values of the determined structure.

Lüftinger (2000) tested the influence of the wavelength and continuum shifts respectively caused by, e.g., errors in the wavelength calibration and introduced during the normalization of the spectra. Wavelength shifts, as long as they are much smaller than the width of the line, do not cause significant changes in the surface abundance distributions. However, continuum shifts can cause severe changes in the abundance structures. As they are introduced during the reduction procedure of data and affect different spectral lines in a different way, it is in principle needed to map several lines of the same element in different spectral regions in order to check the reliability of the mapping.

Note also that the best mappings are obtained for intermediate values of the angle of inclination i (around 40°). Indeed, for i near 90°, features at the northern hemisphere also appear at the same southern latitudes even if they do not exist. For angles below 20°, the star is almost seen pole on and, due to geometrical projection, the rotational modulation of the line profile appears to be very weak.
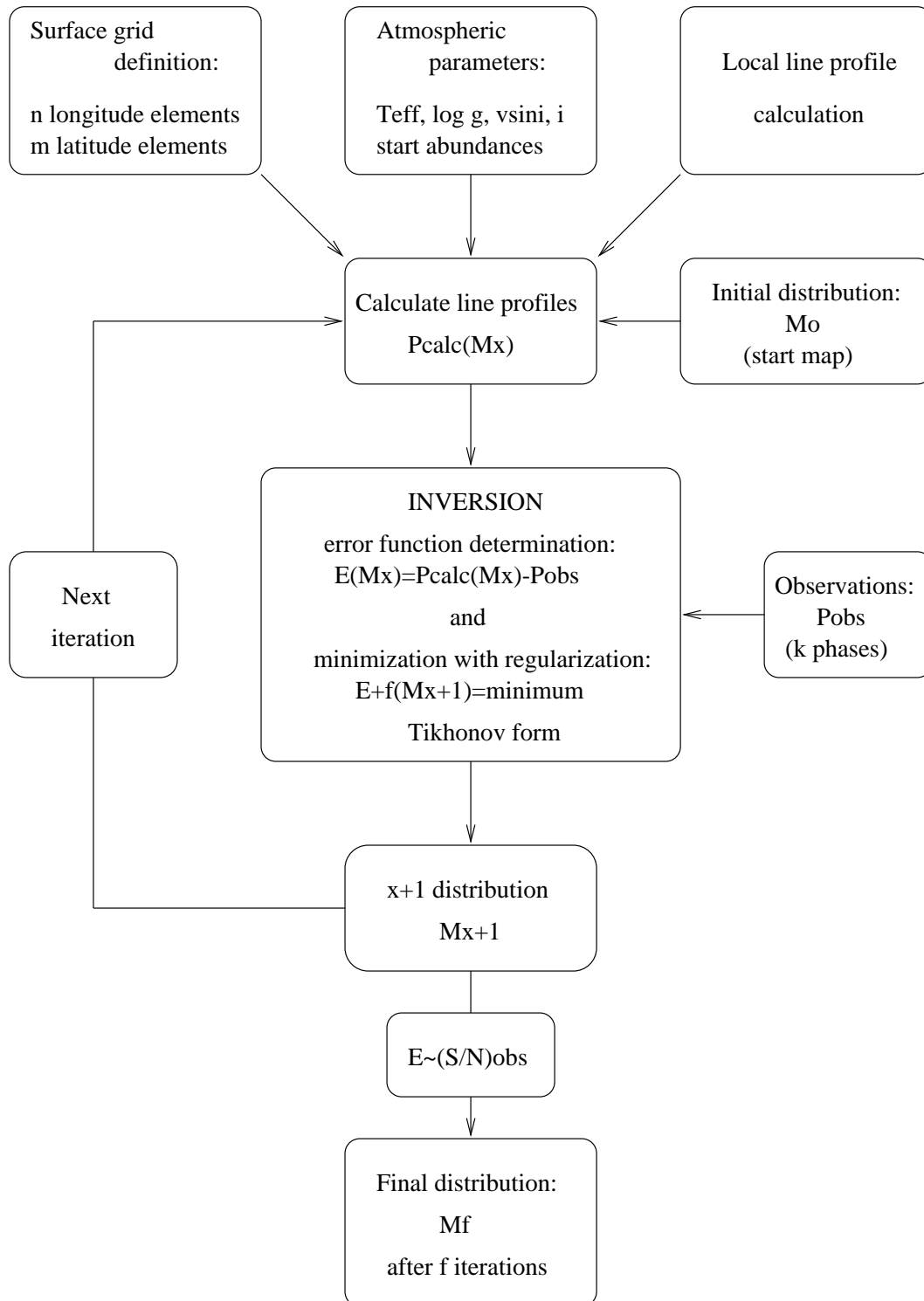
Figure 4.1: Principle steps and procedures needed to perform an inversion of observed spectral line-profile variations into a two-dimensional abundance map (from Kuschnig 1998).

Chapter 5

A new version of the moment method

(this chapter was originally published as **Briquet M.**, **Aerts C.**, 2003, A&A 398, 687, *A new version of the moment method, optimized for mode identification in multiperiodic stars*)

5.1   Introduction

Recent studies of multiple datasets of non-radial oscillators have shown the need to improve current mode identification methods. In particular, the outcomes of mode identification based on photometric and spectroscopic data of the same star and for the same mode are often discrepant (e.g. De Cat 2001). This is very unsatisfactory if one wants to use the non-radial oscillations for detailed modelling of the internal structure of the stars. This thesis contributes to the improvement of one of the identification methods which is developed for the interpretation of time-series of high-resolution spectroscopic data.

The idea of the moment method is the following. By comparing theoretical moment variations of a line profile to observed ones, one derives the wavenumbers (ℓ,m) and other continuous velocity parameters that lead to the best fit. Balona (1986ab, 1987), Aerts et al. (1992) and Aerts (1996) derived analytical expressions of the first three moment variations that are valid for stars with a long rotational period compared to the pulsational periods ($P_{rot} > 10\ P_{puls}$). The major drawback of the moment method in the formulation by Aerts (1996) is the fact that all the modes are identified separately in the case of multiple modes. With such an approach, one cannot force there to be only one unique solution for the inclination angle of the star and the stellar rotational velocity. This is rather unsatisfactory, as conflicting values of these parameters are quite often encountered in practical applications of the method. The reason of Aerts (1996) for not performing one unified mode identification for all occurring modes simultaneously was of numerical origin, as it resulted in unrealistic computation times. This is no longer the case with the efficiency of current computers and with some clever re-arrangements of the theoretical moment

expressions. In this thesis, we present a numerical version of the moment method, which improves considerably the efficiency of the technique by performing the simultaneous identification of all the modes that are present in the data. Our identification code is available upon request.

The chapter is organized as follows. In Sect. 5.2, we describe the new version of the method. Tests on synthetic data are performed in Sect. 5.3. Sect. 5.4 provides a summary of the best optimal mode identification strategy. In Sect. 5.5, we apply our new method to three multiperiodic B-type stars: β Crucis, 16 Lacertae and HD 74195. Finally, we give conclusions in Sect. 5.6.

5.2   A numerical version

In order to be able to outline our new application of the moment method, we repeat here its basic ingredients, adapted to our numerical approach. The reader is referred to Aerts et al. (1992) and Aerts (1996) for a more in-depth description of the moment method.

5.2.1   The moments of a line profile

Let v be the observed velocity (in $\mathrm{km\,s^{-1}}$) of a point on the stellar surface. The n-th normalized moment of a line profile $I(v,t)$ is defined as

$$< v^n >_I (t) = \frac{\displaystyle\int_{-\infty}^{+\infty} v^n \ I(v,t) \ dv}{\displaystyle\int_{-\infty}^{+\infty} I(v,t) \ dv}.$$

We note that the denominator in this formula is the equivalent width of the line.

A line profile is the convolution of an intrinsic profile g and the component of the velocity field f. We assume that g is time-independent and symmetric, which is a good approximation. The first three moments can then be written as

$$< v >_I = < v >_f,$$
$$< v^2 >_I = < v^2 >_f + \sigma^2,$$
$$< v^3 >_I = < v^3 >_f + 3\sigma^2 < v >_f,$$

where the constant $< v^2 >_g$ is denoted by σ^2.

Let v_{rot} and v_{puls} be respectively the velocity in the line of sight due to rotation and pulsation. We use a system of spherical coordinates (r, θ, ϕ) whose polar axis coincides with the axis of rotation and we consider a star which rotates uniformly. We assume also a constant intensity over the stellar surface and we use a limb-darkening law of the form $h_\lambda(\mu) = 1 - u_\lambda + u_\lambda \cos \mu$ where μ is the angle between the local radial vector and the line of sight. We divide the stellar surface into surface elements by taking steps of $d\theta$ in θ and $d\phi$ in ϕ. One then has the following approximation

$$< v^n >_f = \frac{1}{m_0} \sum_{k=0}^{n} \frac{n!}{k!(n-k)!} \int \int v_{\text{rot}}^{n-k}(\theta, \phi) \; v_{\text{puls}}^k(\theta, \phi, t) \; (1 + \beta \cos \mu) \cos \mu \; \sin \theta \; d\theta \; d\phi,$$

(5.1)

where the integral is taken over the visible stellar surface ($\cos \mu > 0$). In this expression, $\beta \equiv u_\lambda/(1 - u_\lambda)$ and $m_0 \equiv \int \int (1 + \beta \cos \mu) \cos \mu \; \sin \theta \; d\theta \; d\phi$. The rotational velocity in the line of sight is given by $v_{\text{rot}} = \Omega \; R \; \sin i \; \sin \theta \; \sin \phi \equiv v_\Omega \; \sin \theta \; \sin \phi$ with Ω the angular frequency of rotation, R the radius of the star and i the angle of inclination of the star.

We note that we neglect temperature effects on moment variations. For slowly-rotating pulsating B stars this is justified, as the moment variations are very well approximated with a pulsational velocity field only (Dupret et al. 2002 and De Ridder et al. 2002a).

5.2.2 The pulsation velocity field

For linear theory, the general form for the temporal dependence of the projected pulsation velocity field due to N modes is given by

$$v_{\text{puls}} = \sum_{j=1}^{N} A_{\ell_j}^{m_j} \cos(2\pi f_j t + \psi_j) + B_{\ell_j}^{m_j} \sin(2\pi f_j t + \psi_j),$$

(5.2)

with

$$A_{\ell_j}^{m_j} = A_p^j [C_{\ell_j}^{m_j}(i) + K_j D_{\ell_j}^{m_j}(i)],$$

(5.3)

and

$$B_{\ell_j}^{m_j} = A_p^j [E_{\ell_j}^{m_j}(i) + K_j F_{\ell_j}^{m_j}(i)],$$

(5.4)

where the parameters A_p and K denote respectively the velocity amplitude and the ratio of the amplitude of the horizontal and of the vertical motion.

In Eqs. (5.3) and (5.4), the quantities $C_{\ell_j}^{m_j}$, $D_{\ell_j}^{m_j}$, $E_{\ell_j}^{m_j}$ and $F_{\ell_j}^{m_j}$ are given by

$$C_{\ell_j}^{m_j} = (\cos i \; \cos \theta + \sin i \; \sin \theta \cos \phi) \; V_r^j(\theta) \; \cos(m_j \phi),$$

$$D_{\ell_j}^{m_j} = (-\cos i \; \sin \theta + \sin i \; \cos \theta \; \cos \phi) \; V_\theta^j(\theta) \; \cos(m_j \phi) - \sin i \; \sin \phi \; V_\phi^j(\theta) \; \sin(m_j \phi),$$

$$E_{\ell_j}^{m_j} = -(\cos i \; \cos \theta + \sin i \; \sin \theta \; \cos \phi) \; V_r^j(\theta) \; \sin(m_j \phi),$$

$$F_{\ell_j}^{m_j} = (\cos i \; \sin \theta - \sin i \; \cos \theta \; \cos \phi) \; V_\theta^j(\theta) \; \sin(m_j \phi) - \sin i \; \sin \phi \; V_\phi^j(\theta) \; \cos(m_j \phi),$$

where

$$V_r(\theta) = N_{\ell_j}^{m_j} \; P_{\ell_j}^{m_j}(\cos \theta),$$

$$V_\theta(\theta) = N_{\ell_j}^{m_j} \; \frac{\partial P_{\ell_j}^{m_j}(\cos \theta)}{\partial \theta},$$

$$V_\phi(\theta) = \frac{m_j}{\sin \theta} N_{\ell_j}^{m_j} \; P_{\ell_j}^{m_j}(\cos \theta),$$

for a pulsating star in the non-rotating formalism. In these latter expressions, P_ℓ^m is the associated Legendre polynomial and N_ℓ^m is a normalisation factor.

5.2.3 The first three moments

For the identification of the modes, we only use the first three moments $< v >$, $< v^2 >$ and $< v^3 >$ because the higher order observed moments are often too noisy. Moreover, the first three moments suffice to determine correctly the pulsation modes (Aerts et al. 1992).

From Eqs. (5.1) and (5.2) and after deleting the terms that equal zero due to symmetry properties, we have

$$< v >= \sum_{j=1}^{N} A_1^j \cos(2\pi f_j t + \psi_j),$$

$$< v^2 >= \sum_{j=1}^{N} C_1^j \cos(2(2\pi f_j)t + 2\psi_j) + \sum_{j=1}^{N} D_2^j \sin(2\pi f_j t + \psi_j)$$
$$+ \sum_{j=1}^{N} \sum_{k \neq j}^{N} C_{b1}^{jk} \cos(2\pi(f_j - f_k)t + \psi_j - \psi_k) + \sum_{j=1}^{N} \sum_{k \neq j}^{N} C_{s1}^{jk} \cos(2\pi(f_j + f_k)t + \psi_j + \psi_k)$$
$$+ \sum_{j=1}^{N} E_{12}^j + E_{\mathrm{rot}} + \sigma^2,$$

$$< v^3 >= \sum_{j=1}^{N} F_1^j \cos(3(2\pi f_j)t + 3\psi_j) + \sum_{j=1}^{N} G_2^j \sin(2(2\pi f_j)t + 2\psi_j) + \sum_{j=1}^{N} RST_1^j \cos(2\pi f_j t + \psi_j)$$
$$+ \sum_{j=1}^{N} \sum_{k \neq j}^{N} G_{b2}^{jk} \sin(2\pi(f_j - f_k)t + \psi_j - \psi_k) + \sum_{j=1}^{N} \sum_{k \neq j}^{N} G_{s2}^{jk} \sin(2\pi(f_j + f_k)t + \psi_j + \psi_k)$$
$$+ \sum_{j=1}^{N} \sum_{k \neq j \ or \ n \neq j}^{N} F_{11}^{jkn} \cos(2\pi(f_j + f_k + f_n)t + \psi_j + \psi_k + \psi_n)$$
$$+ \sum_{j=1}^{N} \sum_{k \neq j \ or \ n \neq j}^{N} F_{21}^{jkn} \cos(2\pi(-f_j + f_k + f_n)t - \psi_j + \psi_k + \psi_n)$$
$$+ \sum_{j=1}^{N} \sum_{k \neq j \ or \ n \neq j}^{N} F_{31}^{jkn} \cos(2\pi(f_j - f_k + f_n)t + \psi_j - \psi_k + \psi_n)$$
$$+ \sum_{j=1}^{N} \sum_{k \neq j \ or \ n \neq j}^{N} F_{41}^{jkn} \cos(2\pi(f_j + f_k - f_n)t + \psi_j + \psi_k - \psi_n),$$

where

$$X^{j(kn)} = \frac{1}{m_0} \int \int x^{j(kn)} \left(1 + \beta \cos \mu\right) \cos \mu \ \sin \theta \ d\theta \ d\phi$$

with

$X^{j(kn)}$	$x^{j(kn)}$
A_1^j	$A_{\ell_j}^{m_j}$
C_1^j	$\frac{1}{2}[(A_{\ell_j}^{m_j})^2 - (B_{\ell_j}^{m_j})^2]$
D_2^j	$2\,v_{\text{rot}}\,B_{\ell_j}^{m_j}$
C_{b1}^{jk}	$\frac{1}{2}(A_{\ell_j}^{m_j}\,A_{\ell_k}^{m_k} + B_{\ell_j}^{m_j}\,B_{\ell_k}^{m_k})$
C_{s1}^{jk}	$\frac{1}{2}(A_{\ell_j}^{m_j}\,A_{\ell_k}^{m_k} - B_{\ell_j}^{m_j}\,B_{\ell_k}^{m_k})$
E_{12}^j	$\frac{1}{2}((A_{\ell_j}^{m_j})^2 + (B_{\ell_j}^{m_j})^2)$
E_{rot}	v_{rot}^2
F_1^j	$\frac{1}{4}[(A_{\ell_j}^{m_j})^3 - 3A_{\ell_j}^{m_j}\,(B_{\ell_j}^{m_j})^2]$
G_2^j	$3\,v_{\text{rot}}\,A_{\ell_j}^{m_j}\,B_{\ell_j}^{m_j}$
RST_1^j	$3(v_{\text{rot}}^2 + \sigma^2)\,A_{\ell_j}^{m_j} + \frac{3}{4}[(A_{\ell_j}^{m_j})^3 + A_{\ell_j}^{m_j}\,(B_{\ell_j}^{m_j})^2]$
G_{b2}^{jk}	$-3\,v_{\text{rot}}\,A_{\ell_j}^{m_j}\,B_{\ell_k}^{m_k}$
G_{s2}^{jk}	$3\,v_{\text{rot}}\,A_{\ell_j}^{m_j}\,B_{\ell_k}^{m_k}$
F_{11}^{jkn}	$-\frac{3}{4}\,B_{\ell_j}^{m_j}\,A_{\ell_k}^{m_k}\,B_{\ell_n}^{m_n} + \frac{1}{4}\,A_{\ell_j}^{m_j}\,A_{\ell_k}^{m_k}\,A_{\ell_n}^{m_n}$
F_{21}^{jkn}	$\frac{3}{4}\,B_{\ell_j}^{m_j}\,A_{\ell_k}^{m_k}\,B_{\ell_n}^{m_n} + \frac{1}{4}\,A_{\ell_j}^{m_j}\,A_{\ell_k}^{m_k}\,A_{\ell_n}^{m_n}$
F_{31}^{jkn}	$-\frac{3}{4}\,B_{\ell_j}^{m_j}\,A_{\ell_k}^{m_k}\,B_{\ell_n}^{m_n} + \frac{1}{4}\,A_{\ell_j}^{m_j}\,A_{\ell_k}^{m_k}\,A_{\ell_n}^{m_n}$
F_{41}^{jkn}	$\frac{3}{4}\,B_{\ell_j}^{m_j}\,A_{\ell_k}^{m_k}\,B_{\ell_n}^{m_n} + \frac{1}{4}\,A_{\ell_j}^{m_j}\,A_{\ell_k}^{m_k}\,A_{\ell_n}^{m_n}$

We point out that $< v >$ varies with frequency f_j; $< v^2 >$ varies with frequency f_j and $2f_j$ and also with the coupling frequencies $f_j + f_k$ and $f_j - f_k$; $< v^3 >$ varies with f_j, $2f_j$, $3f_j$ and also with coupling frequencies $f_j + f_k$, $f_j - f_k$, $f_j + f_k + f_n$, $-f_j + f_k + f_n$, $f_j - f_k + f_n$, $f_j + f_k - f_n$ for $j, k, n = 1, \ldots, N$. All these coupling characteristics were also already given in Mathias et al. (1994), but were never implemented so far.

From Eqs. (5.3) and (5.4) and by denoting

$$I[x] \equiv \frac{1}{m_0} \int \int x\,(1 + \beta \cos \mu)\cos \mu\,\sin \theta\,d\theta\,d\phi,$$

we have

$$A_1^j = A_p^j \left\{ I[C_{\ell_j}^{m_j}] + K_j I[D_{\ell_j}^{m_j}] \right\}.$$

The expressions for the amplitudes of the second and third moments are given in Appendix A.3 in order to keep this section readable.

The great advantage of such a writing is that the integrals $I[x]$ can be computed and memorized in files once and for all for chosen wavenumbers (ℓ, m) and inclinations i. This leads to an important gain of computation time in the computation of the moments for different values of the other parameters A_p, K, σ and v_Ω.

We point out that, for chosen $(\ell,\ m,\ K,\ i)$, the amplitude A_p is no longer a free parameter. We limit its range by imposing that the theoretical first moment amplitude $A_{\mathrm{th}} = A_p\, A(\ell,\ m,\ K,\ i)$ must be equal to the observed one A_{obs}. This condition, which was not considered by Aerts (1996), allows us to reduce greatly the grid of tested parameters. Such an approach is fully justified, as the relative standard error of A_{obs} is always much smaller than the ones of any of the other amplitudes of the higher-order moments.

5.2.4   A new discriminant

In the version of Aerts (1996), the mode identification is achieved by comparing the theoretically calculated amplitudes of $< v >$, $< v^2 >$ and $< v^3 >$ with the observed ones through a discriminant. In general, the observed amplitudes of the first moment as well as the constant term of the second moment are determined accurately. However, the other observed moment amplitudes can have large uncertainties. For this reason, we prefer using the moment values calculated at each time of observation t_k ($k = 1,\ \ldots,\ N_{\mathrm{obs}}$) instead of the amplitudes of their fit.

We propose to choose the modes and the parameters for which the following new discriminant attains the lowest value

$$
\Sigma = \Big\{ \frac{1}{N_{\mathrm{obs}}} \sum_{k=1}^{N_{\mathrm{obs}}} \Big[\big(< v > (t_k) - < v >_{\mathrm{obs}} (t_k) \big)^2
$$
$$
+ \Big| < v^2 > (t_k) - < v^2 >_{\mathrm{obs}} (t_k) \Big|
$$
$$
+ \big(< v^3 > (t_k) - < v^3 >_{\mathrm{obs}} (t_k) \big)^{2/3} \Big] \Big\}^{1/2},
$$

where $< v^n >_{\mathrm{obs}}$ denotes the n-th observed moment.

5.2.5   An upper limit for the degree ℓ

The moment method is particularly suited to identify modes whose frequency is clearly present in the observed moments. Consequently, the degrees of the modes corresponding to these frequencies are expected to be relatively low ($\ell \leq 6$).

In what follows, we give a simple criterion allowing to derive an upper limit for ℓ using the observed first moment amplitude A_{obs} and the constant term of the observed second moment C_{obs}, which can both be very accurately determined from the observed line-profile variations. By imposing the theoretical positive constant E_{12} to be smaller than C_{obs}, we have the following condition:

$$
\Big(a\, (A_{\mathrm{obs}})^2 + b\, C_{\mathrm{obs}} \Big) K^2 + \Big(c\, (A_{\mathrm{obs}})^2 + d\, C_{\mathrm{obs}} \Big) K + \Big(e\, (A_{\mathrm{obs}})^2 + f\, C_{\mathrm{obs}} \Big) < 0 \quad (5.5)
$$

with

$$a = I\big[(D_\ell^m)^2\big] + I\big[(F_\ell^m)^2\big],$$
$$b = -2\big(I\big[D_\ell^m\big]\big)^2,$$
$$c = 2I\big[C_\ell^m\ D_\ell^m\big] + 2I\big[E_\ell^m\ F_\ell^m\big],$$
$$d = -4I\big[C_\ell^m\big]\ I\big[D_\ell^m\big],$$
$$e = I\big[(C_\ell^m)^2\big] + I\big[(E_\ell^m)^2\big],$$
$$f = -2\big(I\big[C_\ell^m\big]\big)^2.$$

The quantities a, b, c, d, e and f are precomputed for several values of the inclination i. Considering (5.5) as an inequation in $K > 0$, one can exclude the modes with degree ℓ for which no solution is found. One then avoids to test useless modes, which again saves a considerable amount of computation time.

5.2.6   Generalization to rotating pulsating stars

The technique described above is no more restricted to slow rotators as was the case for the method by Aerts (1996). Here we extend the application to rotating pulsating stars by using the theory derived by Lee & Saio (1987, 1990, Chapter 2). We remind that the velocity field depends on the ratio $\eta = 2\Omega/\sigma_c$ between the angular frequency of rotation and the angular co-rotating frequency of pulsation. Note that taking $\Omega = 0$ leads to the same description as the one of a non-rotating pulsating star.

We implemented this version of the moment method by using Townsend's code (1997) BRUCE, which computes the pulsation velocity field for this theory. A nice feature of our current version of the method is that this numerical version can be easily generalized to an improved formalism for the pulsational velocity, e.g. one that would take into account the effects of the centrifugal forces, should this become available.

5.3   Tests on synthetic data

We applied the moment method in our present new version to a large number of synthetic datasets in order to test its efficiency and our implemented version. Sets of artificial data were generated in such a way that they resemble real data as much as possible. For each set, we computed 254 line profiles at times of real observations. We added gaussian noise corresponding to a signal-to-noise of about 200 and finally we computed the first three moment variations.

We first tested the method for a monoperiodic star for all the sectoral, tesseral, and axisymmetric modes with $0 \le \ell \le 3$ ($m = -\ell$, ..., ℓ). It performs the identification without any problem, as it was already the case with the previous version (Aerts 1996). We note that, as expected, axisymmetric modes may be confused with axisymmetric

Table 5.1: Examples of mode identification through the discriminant Σ with the new version of the moment method for two modes. The input parameters are shown, followed by the five best solutions of the mode identification. A_p is the amplitude of the radial part of the pulsation velocity, expressed in $\mathrm{km\,s^{-1}}$; i is the inclination angle; v_Ω is the projected rotational velocity, expressed in $\mathrm{km\,s^{-1}}$ and σ is the intrinsic line-profile width, also expressed in $\mathrm{km\,s^{-1}}$.

(ℓ_1,m_1)	(ℓ_2,m_2)	A_p^1	A_p^2	K_1	K_2	i	v_Ω	σ	Σ
$(1,-1)$	$(1,0)$	2.25	0.53	65.54	12.03	6	26	5.5	
$(1,-1)$	$(1,0)$	2.86	0.58	56.64	10.39	5	22	4	1.68
$(1,-1)$	$(2,0)$	2.86	0.32	56.64	10.39	5	22	4	1.77
$(1,-1)$	$(3,0)$	2.86	0.58	56.64	10.39	5	22	4	2.85
$(1,1)$	$(1,0)$	2.86	0.58	56.64	10.39	5	22	4	4.99
$(1,1)$	$(2,0)$	2.86	0.32	56.64	10.39	5	22	4	5.07

(ℓ_1,m_1)	(ℓ_2,m_2)	A_p^1	A_p^2	K_1	K_2	i	v_Ω	σ	Σ
$(2,0)$	$(1,1)$	10.38	21.92	0.082	0.086	16	23	5.5	
$(2,0)$	$(1,1)$	9.99	23.27	0.094	0.099	15	21	7	1.53
$(1,0)$	$(3,3)$	9.06	93.26	0.094	0.099	35	10	7	1.68
$(1,0)$	$(2,1)$	7.92	12.82	0.094	0.099	20	25	3	1.87
$(2,0)$	$(2,1)$	10.82	12.82	0.094	0.099	20	24	4	1.95
$(2,0)$	$(3,1)$	9.99	24.59	0.094	0.099	15	13	10	1.95

(ℓ_1,m_1)	(ℓ_2,m_2)	A_p^1	A_p^2	K_1	K_2	i	v_Ω	σ	Σ
$(3,2)$	$(1,-1)$	1.69	0.77	6.48	17.40	52	19	5.5	
$(3,2)$	$(1,-1)$	1.45	0.52	8.20	22.02	60	19	5	2.56
$(1,-1)$	$(2,2)$	4.90	2.19	8.20	22.02	20	14	1	2.87
$(3,2)$	$(2,2)$	2.64	0.61	4.41	11.86	60	19	5	2.99
$(1,-1)$	$(1,-1)$	3.37	0.90	8.20	22.02	30	17	6	3.17
$(2,2)$	$(1,-1)$	10.00	1.90	4.41	11.86	25	16	3	3.29

(ℓ_1,m_1)	(ℓ_2,m_2)	A_p^1	A_p^2	K_1	K_2	i	v_Ω	σ	Σ
$(3,-3)$	$(2,0)$	32.97	9.60	0.085	0.095	87	10	5.5	
$(3,-3)$	$(2,0)$	38.49	10.44	0.051	0.057	80	9	5	2.39
$(2,-2)$	$(2,0)$	17.16	11.88	0.051	0.057	75	18	2	2.40
$(3,-3)$	$(1,1)$	38.49	5.42	0.051	0.057	80	9	5	2.53
$(3,-3)$	$(2,1)$	49.42	10.12	0.051	0.057	65	8	3	2.57
$(3,-2)$	$(1,1)$	40.01	6.17	0.051	0.057	60	11	5	2.64

(ℓ_1,m_1)	(ℓ_2,m_2)	A_p^1	A_p^2	K_1	K_2	i	v_Ω	σ	Σ
$(2,2)$	$(1,-1)$	4.02	0.91	5.61	19.74	37	19	5.5	
$(1,-1)$	$(1,-1)$	2.88	0.66	7.05	24.79	45	23	2	2.19
$(2,2)$	$(1,-1)$	4.30	1.18	3.79	13.35	45	23	1	2.20
$(1,-1)$	$(2,2)$	6.09	1.67	4.34	15.25	30	21	3	2.23
$(3,1)$	$(1,-1)$	2.10	0.46	7.05	24.79	90	22	1	3.04
$(2,2)$	$(3,1)$	2.16	0.85	3.79	13.35	85	22	2	3.19

Table 5.2: Examples of mode identification through the discriminant Σ with the new version of the moment method for two modes. The input parameters are shown, followed by the five best solutions of the mode identification. The meanings of the symbols are the same as in Table 5.1.

(ℓ_1,m_1)	(ℓ_2,m_2)	A_p^1	A_p^2	K_1	K_2	i	v_Ω	σ	Σ
$(2,-1)$	$(1,-1)$	30.45	21.69	0.085	0.099	17	11	5.5	
$(3,-1)$	$(2,-1)$	40.09	11.17	0.054	0.062	30	16	2	2.30
$(3,-1)$	$(1,-1)$	42.16	15.91	0.054	0.062	25	14	3	2.52
$(2,-1)$	$(2,-1)$	29.18	15.16	0.054	0.062	20	14	6	2.53
$(3,-2)$	$(2,-2)$	46.16	12.86	0.054	0.062	60	14	4	2.54
$(2,-1)$	$(1,-1)$	29.18	19.72	0.054	0.062	20	15	6	2.56
(ℓ_1,m_1)	(ℓ_2,m_2)	A_p^1	A_p^2	K_1	K_2	i	v_Ω	σ	Σ
$(2,0)$	$(1,1)$	0.45	6.98	11.45	4.91	16	23	5.5	
$(2,0)$	$(1,1)$	0.30	1.84	16.99	5.21	15	19	8	1.88
$(1,0)$	$(1,1)$	0.58	1.84	16.99	5.21	15	19	8	1.91
$(3,0)$	$(1,1)$	0.69	1.84	9.14	12.82	10	16	9	2.44
$(2,-1)$	$(1,1)$	0.70	1.84	16.99	3.97	20	18	8	3.72
$(1,0)$	$(3,2)$	2.93	1.84	9.14	2.67	70	25	1	3.74
(ℓ_1,m_1)	(ℓ_2,m_2)	A_p^1	A_p^2	K_1	K_2	i	v_Ω	σ	Σ
$(3,-2)$	$(2,2)$	35.19	13.21	0.086	0.091	52	16	5.5	
$(3,-2)$	$(2,2)$	36.24	12.33	0.071	0.075	55	16	4	2.39
$(3,-3)$	$(3,2)$	37.90	30.83	0.071	0.075	75	13	2	2.57
$(2,-2)$	$(2,2)$	30.80	16.56	0.071	0.075	45	19	2	2.79
$(3,-3)$	$(2,2)$	37.90	8.85	0.071	0.075	75	13	5	2.87
$(3,-3)$	$(3,1)$	34.14	23.50	0.071	0.075	90	14	4	3.43
(ℓ_1,m_1)	(ℓ_2,m_2)	A_p^1	A_p^2	K_1	K_2	i	v_Ω	σ	Σ
$(3,3)$	$(2,1)$	2.04	1.88	5.14	8.81	81	24	5.5	
$(3,3)$	$(2,1)$	1.35	1.10	7.84	13.45	80	26	4	2.25
$(3,3)$	$(3,0)$	2.22	0.98	5.43	9.31	70	23	7	2.82
$(3,3)$	$(2,0)$	2.46	0.92	4.22	7.24	80	25	6	2.85
$(3,3)$	$(2,-1)$	1.35	1.10	7.84	13.45	80	26	4	3.53
$(3,3)$	$(3,1)$	4.32	0.72	6.64	11.38	45	17	8	3.68
(ℓ_1,m_1)	(ℓ_2,m_2)	A_p^1	A_p^2	K_1	K_2	i	v_Ω	σ	Σ
$(3,2)$	$(1,-1)$	36.20	7.24	0.078	0.097	52	19	5.5	
$(3,2)$	$(1,-1)$	36.61	6.96	0.076	0.095	55	20	5	1.79
$(2,2)$	$(1,-1)$	37.95	8.88	0.076	0.095	40	21	5	2.07
$(3,2)$	$(2,-1)$	36.61	8.36	0.076	0.095	55	20	5	2.16
$(2,2)$	$(2,-1)$	37.95	7.99	0.076	0.095	40	21	5	2.45
$(3,2)$	$(1,0)$	39.91	5.69	0.076	0.095	45	16	7	2.93

Table 5.3: Examples of mode identification through the discriminant Σ with the new version of the moment method for two modes. The input parameters are shown, followed by the five best solutions of the mode identification. The meanings of the symbols are the same as in Table 5.1.

(ℓ_1,m_1)	(ℓ_2,m_2)	A_p^1	A_p^2	K_1	K_2	i	v_Ω	σ	Σ
(2,1)	(1,0)	16.10	4.80	0.080	0.095	37	12	5.5	
(2,1)	(1,0)	22.63	4.48	0.054	0.064	25	10	6	1.95
(1,1)	(1,0)	34.83	4.33	0.054	0.064	20	10	6	2.01
(2,1)	(2,0)	27.09	6.17	0.054	0.064	20	8	6	2.07
(3,1)	(1,0)	44.34	4.33	0.054	0.064	20	6	2	2.08
(3,1)	(2,0)	44.34	6.17	0.054	0.064	20	6	1	2.13

(ℓ_1,m_1)	(ℓ_2,m_2)	A_p^1	A_p^2	K_1	K_2	i	v_Ω	σ	Σ
(3,−1)	(2,−2)	0.84	0.21	16.40	27.36	86	25	5.5	
(3,−1)	(2,−2)	0.88	0.23	15.54	25.93	90	27	3	1.83
(1,1)	(2,−2)	1.04	0.37	19.43	32.42	45	19	10	1.94
(1,1)	(3,−1)	0.89	0.19	25.26	42.14	40	16	11	2.28
(1,1)	(2,−1)	1.13	0.34	13.60	22.69	65	28	2	2.64
(1,1)	(3,−2)	0.59	0.31	25.26	42.14	75	14	11	3.16

(ℓ_1,m_1)	(ℓ_2,m_2)	A_p^1	A_p^2	K_1	K_2	i	v_Ω	σ	Σ
(1,1)	(1,0)	25.54	4.34	0.080	0.095	27	12	5.5	
(1,1)	(1,0)	74.02	4.41	0.053	0.063	10	4	4	2.07
(1,1)	(2,0)	29.54	7.27	0.053	0.063	25	10	6	2.12
(2,1)	(2,0)	23.82	7.27	0.053	0.063	25	9	6	2.12
(2,1)	(1,0)	18.44	5.56	0.053	0.063	40	14	4	2.16
(3,1)	(1,0)	41.23	4.71	0.053	0.063	25	7	3	2.31

(ℓ_1,m_1)	(ℓ_2,m_2)	A_p^1	A_p^2	K_1	K_2	i	v_Ω	σ	Σ
(3,−2)	(2,−1)	0.54	0.35	21.86	16.32	47	15	5.5	
(3,−2)	(2,−1)	0.94	0.62	12.30	9.18	50	15	6	1.88
(3,−3)	(2,−1)	0.86	0.35	22.84	17.06	55	11	6	2.10
(3,−3)	(2,−2)	0.47	0.33	22.84	17.06	90	13	7	2.22
(3,−1)	(2,−1)	0.44	0.38	22.84	17.06	30	19	2	2.59
(3,−2)	(2,−2)	0.55	0.41	22.84	17.06	65	18	3	2.60

(ℓ_1,m_1)	(ℓ_2,m_2)	A_p^1	A_p^2	K_1	K_2	i	v_Ω	σ	Σ
(3,−1)	(2,1)	34.05	7.83	0.084	0.093	42	12	5.5	
(3,−1)	(1,1)	33.13	9.81	0.058	0.065	35	12	6	2.27
(3,−1)	(2,1)	33.13	8.60	0.058	0.065	35	12	6	2.29
(3,−2)	(1,1)	58.29	5.81	0.058	0.065	75	11	2	2.55
(2,−1)	(2,1)	17.56	9.31	0.058	0.065	60	20	1	2.65
(2,−1)	(1,1)	15.47	8.75	0.058	0.065	40	17	5	2.67

Table 5.4: Examples of mode identification through the discriminant Σ with the new version of the moment method for two modes. The input parameters are shown, followed by the five best solutions of the mode identification. The meanings of the symbols are the same as in Table 5.1.

(ℓ_1,m_1)	(ℓ_2,m_2)	A_p^1	A_p^2	K_1	K_2	i	v_Ω	σ	Σ
(3,−3)	(2,1)	0.57	0.64	40.24	8.95	52	18	5.5	
(3,−3)	(2,1)	0.51	1.89	26.24	5.83	75	19	5	2.77
(3,−2)	(2,1)	0.26	0.53	48.73	10.84	50	22	2	2.99
(3,−3)	(2,0)	0.26	0.71	48.73	10.84	80	18	6	3.50
(3,−3)	(3,0)	0.55	1.75	26.24	5.83	70	18	5	3.56
(3,−3)	(3,1)	1.31	1.57	26.24	5.83	45	14	1	3.60

(ℓ_1,m_1)	(ℓ_2,m_2)	A_p^1	A_p^2	K_1	K_2	i	v_Ω	σ	Σ
(2,0)	(2,2)	12.62	44.62	0.082	0.082	26	30	5.5	
(2,0)	(2,2)	10.02	68.16	0.11	0.11	20	25	9	2.01
(2,0)	(3,2)	16.22	25.03	0.11	0.11	35	30	5	2.02
(1,0)	(2,2)	7.53	68.16	0.11	0.11	20	25	9	2.22
(1,0)	(3,2)	7.36	108.36	0.11	0.11	15	13	2	2.31
(3,0)	(2,2)	20.27	120.87	0.11	0.11	15	17	10	3.18

(ℓ_1,m_1)	(ℓ_2,m_2)	A_p^1	A_p^2	K_1	K_2	i	v_Ω	σ	Σ
(3,0)	(3,2)	1.52	1.93	11.45	7.49	32	10	5.5	
(3,1)	(3,2)	3.42	2.44	7.03	4.60	70	16	1	3.78
(3,0)	(3,2)	3.29	2.09	7.03	4.60	45	14	2	4.04
(3,0)	(2,2)	1.74	5.31	7.03	4.60	30	19	1	4.31
(2,0)	(3,2)	3.81	1.95	7.03	4.60	50	14	6	4.50
(2,0)	(2,2)	3.81	2.25	7.03	4.60	50	20	1	4.78

(ℓ_1,m_1)	(ℓ_2,m_2)	A_p^1	A_p^2	K_1	K_2	i	v_Ω	σ	Σ
(3,1)	(2,−1)	44.57	43.88	0.080	0.097	86	24	5.5	
(3,1)	(2,−1)	42.84	33.76	0.095	0.11	85	25	6	2.59
(3,1)	(1,0)	42.84	35.41	0.095	0.11	85	22	9	3.29
(3,1)	(2,1)	42.84	33.76	0.095	0.11	85	27	3	3.30
(2,2)	(3,−1)	25.31	19.44	0.095	0.11	50	13	13	3.43
(2,2)	(2,−1)	14.94	33.76	0.095	0.11	85	16	12	3.57

(ℓ_1,m_1)	(ℓ_2,m_2)	A_p^1	A_p^2	K_1	K_2	i	v_Ω	σ	Σ
(2,1)	(1,0)	1.11	0.68	7.81	12.03	32	17	5.5	
(2,1)	(2,0)	1.43	0.31	8.78	13.52	20	11	8	2.47
(2,1)	(1,0)	2.15	1.02	4.73	7.28	25	12	8	2.48
(3,1)	(1,0)	2.22	1.02	4.73	7.28	25	5	9	2.49
(3,1)	(2,0)	1.22	0.35	8.78	13.52	25	4	9	2.49
(3,3)	(1,0)	5.03	1.44	4.73	7.28	50	3	7	2.64

Table 5.5: Examples of mode identification through the discriminant Σ with the new version of the moment method for three modes. The input parameters are shown, followed by the five best solutions of the mode identification. The meanings of the symbols are the same as in Table 5.1.

(ℓ_1,m_1)	(ℓ_2,m_2)	(ℓ_3,m_3)	A_p^1	A_p^2	A_p^3	K_1	K_2	K_3	i	v_Ω	σ	Σ
(3,0)	(1,−1)	(3,1)	1.45	0.67	0.57	11.45	14.11	13.75	73	11	5.5	
(3,0)	(1,−1)	(3,1)	1.17	0.53	0.38	14.88	18.34	17.87	75	10	6	2.07
(3,0)	(2,2)	(3,1)	1.17	0.30	0.38	14.88	18.34	17.87	75	12	5	2.11
(2,1)	(1,−1)	(3,1)	4.03	0.65	0.33	11.45	14.11	13.75	85	7	2	2.28
(3,0)	(2,2)	(1,−1)	2.16	0.55	0.46	8.01	9.87	9.62	75	11	6	2.29
(3,0)	(1,−1)	(1,−1)	2.16	0.93	0.46	8.01	9.87	9.62	75	11	6	2.30

(ℓ_1,m_1)	(ℓ_2,m_2)	(ℓ_3,m_3)	A_p^1	A_p^2	A_p^3	K_1	K_2	K_3	i	v_Ω	σ	Σ
(2,−1)	(1,−1)	(2,1)	25.13	14.05	10.05	0.084	0.086	0.092	64	20	5.5	
(2,−1)	(1,−1)	(2,1)	28.31	15.86	11.51	0.084	0.085	0.092	60	16	7	2.22
(1,−1)	(1,−1)	(1,1)	17.00	15.15	6.91	0.084	0.085	0.092	65	19	6	2.44
(1,−1)	(1,−1)	(2,1)	18.81	16.77	10.61	0.084	0.085	0.092	55	17	7	2.46
(2,−1)	(1,−1)	(1,1)	28.31	15.86	7.23	0.084	0.085	0.092	60	18	6	2.47
(1,−1)	(1,−1)	(2,1)	17.00	15.15	13.01	0.084	0.085	0.092	65	20	5	2.53

(ℓ_1,m_1)	(ℓ_2,m_2)	(ℓ_3,m_3)	A_p^1	A_p^2	A_p^3	K_1	K_2	K_3	i	v_Ω	σ	Σ
(3,2)	(2,−2)	(1,0)	1.55	0.50	0.31	7.6	20.46	16.31	44	12	5.5	
(3,2)	(2,−2)	(2,−1)	1.34	0.51	0.15	9.12	24.55	19.57	40	14	5	2.06
(3,2)	(2,−2)	(1,0)	1.46	0.56	0.27	8.36	22.51	17.94	40	14	5	2.07
(3,2)	(2,−2)	(2,0)	2.26	0.87	0.41	5.32	14.32	11.41	40	14	5	2.21
(3,2)	(3,−1)	(2,0)	1.82	0.24	0.13	9.88	26.60	21.20	30	11	5	2.26
(3,2)	(3,−1)	(1,0)	1.82	0.24	0.20	9.88	26.60	21.20	30	11	5	2.30

(ℓ_1,m_1)	(ℓ_2,m_2)	(ℓ_3,m_3)	A_p^1	A_p^2	A_p^3	K_1	K_2	K_3	i	v_Ω	σ	Σ
(1,1)	(3,−2)	(2,0)	3.01	0.21	0.21	7.35	49.73	16.31	37	23	5.5	
(1,1)	(3,−2)	(1,0)	2.85	0.19	0.26	7.35	49.73	16.31	40	25	2	1.87
(1,1)	(3,−2)	(2,0)	3.12	0.21	0.28	6.61	44.76	14.68	40	25	1	1.92
(1,1)	(3,−2)	(2,−1)	3.45	0.24	0.20	5.88	39.78	13.05	40	25	2	2.28
(1,1)	(3,−3)	(2,−1)	1.77	0.21	0.13	9.56	64.65	21.20	55	22	5	2.48
(1,1)	(3,−3)	(1,0)	2.05	0.33	0.22	9.56	64.65	21.20	45	19	6	2.61

(ℓ_1,m_1)	(ℓ_2,m_2)	(ℓ_3,m_3)	A_p^1	A_p^2	A_p^3	K_1	K_2	K_3	i	v_Ω	σ	Σ
(2,−1)	(1,0)	(2,2)	0.85	1.54	0.29	13.93	12.03	10.90	68	13	5.5	
(2,−2)	(1,0)	(1,−1)	0.56	2.06	0.42	15.33	13.23	11.99	75	9	7	2.20
(2,−2)	(1,0)	(2,2)	0.62	2.25	0.27	13.93	12.03	10.90	75	9	7	2.20
(2,−1)	(1,0)	(1,−1)	0.82	1.56	0.44	15.33	13.23	11.99	70	12	6	2.22
(2,−1)	(1,0)	(2,2)	0.90	1.70	0.29	13.93	12.03	10.90	70	15	4	2.23
(2,−1)	(2,0)	(1,−1)	0.58	1.14	0.63	13.93	12.03	10.90	45	9	7	2.28

Table 5.6: Examples of mode identification through the discriminant Σ with the new version of the moment method for three modes. The input parameters are shown, followed by the five best solutions of the mode identification. The meanings of the symbols are the same as in Table 5.1.

(ℓ_1,m_1)	(ℓ_2,m_2)	(ℓ_3,m_3)	A_p^1	A_p^2	A_p^3	K_1	K_2	K_3	i	v_Ω	σ	Σ
(1,0)	(1,−1)	(1,1)	0.91	0.77	1.39	11.45	28.75	8.19	27	24	5.5	
(1,0)	(1,−1)	(1,1)	1.13	0.87	1.48	9.16	23.00	6.55	30	26	3	2.15
(2,0)	(1,−1)	(1,1)	0.54	0.83	1.44	11.45	28.75	8.19	25	22	7	2.24
(1,0)	(2,2)	(1,1)	1.17	2.40	2.42	8.01	20.12	5.73	20	21	2	2.68
(2,0)	(2,2)	(1,1)	0.67	2.40	2.42	8.01	20.12	5.73	20	21	2	2.77
(2,0)	(1,−1)	(2,2)	0.43	1.34	5.55	11.45	28.75	8.19	15	14	8	2.93

(ℓ_1,m_1)	(ℓ_2,m_2)	(ℓ_3,m_3)	A_p^1	A_p^2	A_p^3	K_1	K_2	K_3	i	v_Ω	σ	Σ
(3,−2)	(1,1)	(3,2)	0.60	1.72	0.70	26.05	8.74	8.29	34	14	5.5	
(3,−2)	(1,1)	(3,2)	0.72	2.09	0.88	20.84	6.99	6.63	35	16	5	2.34
(3,−2)	(1,−1)	(3,2)	0.72	2.09	0.88	20.84	6.99	6.63	35	16	5	3.13
(3,−3)	(1,1)	(3,2)	0.72	1.38	0.63	20.84	6.99	6.63	60	18	3	3.43
(3,−2)	(1,1)	(2,2)	1.38	3.17	2.74	18.24	6.12	5.80	25	13	1	3.69
(3,−3)	(1,−1)	(3,2)	1.07	1.39	0.54	26.05	8.74	8.29	45	14	2	3.71

(ℓ_1,m_1)	(ℓ_2,m_2)	(ℓ_3,m_3)	A_p^1	A_p^2	A_p^3	K_1	K_2	K_3	i	v_Ω	σ	Σ
(2,0)	(1,0)	(2,2)	0.49	0.55	6.00	11.45	12.03	3.91	22	25	5.5	
(2,0)	(1,0)	(2,2)	0.49	0.61	15.52	10.30	10.82	3.52	15	17	8	2.06
(2,0)	(1,0)	(3,2)	0.63	0.76	11.75	8.01	8.42	2.74	15	7	10	2.12
(2,0)	(2,0)	(2,2)	0.49	0.32	15.52	10.30	10.82	3.52	15	17	8	2.15
(1,0)	(1,0)	(2,2)	0.93	0.61	15.52	10.30	10.82	3.52	15	17	8	2.24
(1,0)	(2,0)	(1,−1)	0.68	0.24	3.41	14.88	15.64	5.08	20	28	2	2.24

(ℓ_1,m_1)	(ℓ_2,m_2)	(ℓ_3,m_3)	A_p^1	A_p^2	A_p^3	K_1	K_2	K_3	i	v_Ω	σ	Σ
(1,0)	(3,3)	(1,1)	1.44	1.94	0.49	11.45	6.33	12.40	56	15	5.5	
(1,0)	(3,3)	(1,1)	0.93	1.96	0.41	14.88	8.23	16.12	50	13	6	2.15
(2,−1)	(3,3)	(1,1)	2.00	1.32	0.45	10.30	5.70	11.16	80	16	4	2.54
(2,−1)	(3,3)	(2,0)	1.06	1.52	0.48	10.30	5.70	11.16	70	16	5	2.78
(1,0)	(3,3)	(3,0)	2.49	2.15	0.54	8.01	4.43	8.68	65	16	5	2.81
(2,−1)	(3,3)	(3,−1)	2.54	1.68	0.67	8.01	4.43	8.68	80	16	4	2.81

(ℓ_1,m_1)	(ℓ_2,m_2)	(ℓ_3,m_3)	A_p^1	A_p^2	A_p^3	K_1	K_2	K_3	i	v_Ω	σ	Σ
(3,3)	(2,0)	(1,0)	1.47	0.65	0.86	7.67	12.03	16.31	75	11	5.5	
(3,3)	(2,0)	(1,0)	2.05	0.88	1.11	5.37	8.42	11.41	75	11	6	2.26
(3,3)	(3,0)	(1,0)	2.49	0.97	0.68	5.37	8.42	11.41	65	10	6	2.28
(3,3)	(2,0)	(2,−2)	2.23	1.08	0.26	5.37	8.42	11.41	70	11	6	2.33
(3,3)	(3,0)	(2,−1)	2.49	0.97	0.30	5.37	8.42	11.41	65	10	6	2.34
(3,3)	(2,0)	(2,−1)	1.12	0.48	0.25	9.97	15.64	21.20	75	11	6	2.36

Table 5.7: Examples of mode identification through the discriminant Σ with the new version of the moment method for three modes. The input parameters are shown, followed by the five best solutions of the mode identification. The meanings of the symbols are the same as in Table 5.1.

(ℓ_1,m_1)	(ℓ_2,m_2)	(ℓ_3,m_3)	A_p^1	A_p^2	A_p^3	K_1	K_2	K_3	i	v_Ω	σ	Σ
(1,1)	(2,1)	(2,−2)	1.88	0.61	0.09	8.38	8.74	45.84	57	21	5.5	
(1,1)	(2,1)	(2,−2)	1.35	0.68	0.05	10.89	11.36	59.60	70	23	3	2.04
(1,1)	(2,1)	(3,−1)	1.80	0.44	0.08	10.89	11.36	59.60	45	17	8	2.21
(1,1)	(2,1)	(2,−1)	1.93	0.47	0.05	10.05	10.48	55.01	45	19	7	2.27
(3,−1)	(2,0)	(2,−2)	2.41	0.99	0.09	5.86	6.11	32.09	85	22	3	2.60
(1,1)	(2,1)	(2,0)	3.69	0.69	0.03	10.89	11.36	59.60	20	10	10	2.60
(ℓ_1,m_1)	(ℓ_2,m_2)	(ℓ_3,m_3)	A_p^1	A_p^2	A_p^3	K_1	K_2	K_3	i	v_Ω	σ	Σ
(2,2)	(3,2)	(1,0)	110.38	100.95	4.34	0.078	0.080	0.095	26	10	5.5	
(3,2)	(3,2)	(2,0)	82.39	75.46	14.96	0.048	0.049	0.058	40	12	7	3.62
(3,2)	(3,2)	(1,0)	82.39	75.46	5.38	0.048	0.049	0.058	40	12	7	3.67
(3,2)	(3,2)	(1,−1)	86.03	78.79	6.21	0.048	0.049	0.058	40	11	8	4.39
(3,2)	(3,2)	(2,−1)	82.39	75.46	9.45	0.048	0.049	0.058	40	11	8	4.87
(3,2)	(3,2)	(1,1)	86.03	78.79	6.21	0.048	0.049	0.058	70	17	4	4.88
(ℓ_1,m_1)	(ℓ_2,m_2)	(ℓ_3,m_3)	A_p^1	A_p^2	A_p^3	K_1	K_2	K_3	i	v_Ω	σ	Σ
(2,0)	(3,1)	(1,1)	0.42	4.90	7.28	11.45	2.74	3.15	8	23	5.5	
(2,0)	(2,1)	(1,1)	0.58	13.17	14.55	8.01	1.92	2.21	5	22	5	2.26
(1,0)	(2,1)	(1,1)	1.03	13.17	14.55	8.01	1.92	2.21	5	22	5	2.32
(3,0)	(2,1)	(1,1)	0.93	11.76	13.20	9.16	2.19	2.52	5	22	3	3.11
(2,0)	(2,−1)	(1,−1)	0.58	13.17	14.55	8.01	1.92	2.21	5	22	5	3.29
(2,0)	(3,1)	(1,1)	0.43	3.97	5.83	11.45	5.83	2.64	10	27	1	3.32
(ℓ_1,m_1)	(ℓ_2,m_2)	(ℓ_3,m_3)	A_p^1	A_p^2	A_p^3	K_1	K_2	K_3	i	v_Ω	σ	Σ
(3,−3)	(3,−1)	(2,1)	1.14	0.43	0.24	34.30	16.43	11.95	38	13	5.5	
(3,−3)	(3,−1)	(2,1)	1.41	0.64	0.31	24.01	11.50	8.37	40	15	7	2.76
(3,−3)	(2,−2)	(2,1)	0.49	0.56	0.40	24.01	11.50	8.37	65	22	7	2.77
(3,−3)	(2,−2)	(3,0)	0.57	0.62	0.54	24.01	11.50	8.37	60	20	8	2.81
(3,−3)	(2,−2)	(2,0)	0.44	0.52	0.59	24.01	11.50	8.37	70	21	8	2.82
(3,−2)	(2,−1)	(2,1)	0.70	0.53	0.36	24.01	11.50	8.37	30	19	8	2.94
(ℓ_1,m_1)	(ℓ_2,m_2)	(ℓ_3,m_3)	A_p^1	A_p^2	A_p^3	K_1	K_2	K_3	i	v_Ω	σ	Σ
(2,−1)	(3,1)	(3,−2)	0.38	0.88	0.04	21.71	7.33	135.78	33	22	5.5	
(2,−1)	(3,1)	(3,−2)	0.53	1.27	0.05	15.20	5.13	95.05	35	23	5	1.78
(2,−1)	(3,1)	(3,−3)	0.50	1.38	0.14	15.20	5.13	95.05	40	21	6	2.88
(2,−2)	(3,1)	(3,−2)	0.54	0.88	0.02	28.22	9.53	176.52	45	24	1	3.00
(2,−2)	(3,1)	(3,−3)	1.21	1.38	0.14	15.20	2.30	95.05	40	20	6	3.16
(1,0)	(3,1)	(3,−2)	0.72	1.25	0.07	15.20	5.13	95.05	30	20	8	3.38

Table 5.8: Examples of mode identification through the discriminant Σ with the new version of the moment method for three modes. The input parameters are shown, followed by the five best solutions of the mode identification. The meanings of the symbols are the same as in Table 5.1.

(ℓ_1,m_1)	(ℓ_2,m_2)	(ℓ_3,m_3)	A_p^1	A_p^2	A_p^3	K_1	K_2	K_3	i	v_Ω	σ	Σ
(2,2)	(1,1)	(2,1)	26.12	14.77	8.92	0.077	0.081	0.091	58	28	5.5	
(2,2)	(1,1)	(1,1)	25.32	14.33	6.66	0.102	0.107	0.121	70	28	6	1.86
(2,2)	(1,1)	(2,1)	23.96	13.94	19.93	0.102	0.107	0.121	75	29	4	1.99
(2,2)	(2,1)	(1,1)	27.23	27.97	6.91	0.102	0.107	0.121	65	26	7	2.57
(2,2)	(2,1)	(2,1)	38.16	21.77	10.13	0.102	0.107	0.121	50	23	9	3.05
(3,2)	(1,1)	(1,1)	67.14	14.86	6.91	0.102	0.107	0.121	70	22	1	3.20

(ℓ_1,m_1)	(ℓ_2,m_2)	(ℓ_3,m_3)	A_p^1	A_p^2	A_p^3	K_1	K_2	K_3	i	v_Ω	σ	Σ
(1,−1)	(2,2)	(3,2)	1.95	8.23	2.29	20.64	5.18	6.30	18	12	5.5	
(1,−1)	(2,2)	(3,2)	1.50	5.82	1.55	24.77	6.22	7.56	20	14	7	2.34
(1,−1)	(2,2)	(2,2)	2.03	6.24	2.82	14.45	3.63	4.41	25	20	6	3.58
(1,−1)	(3,2)	(3,2)	1.72	4.44	2.00	14.45	3.63	4.41	30	23	4	3.68
(1,−1)	(1,1)	(3,2)	2.21	4.53	2.30	16.51	4.14	5.04	20	14	9	3.74
(1,−1)	(1,−1)	(3,2)	0.83	1.81	0.57	26.84	6.74	8.19	35	24	2	3.75

(ℓ_1,m_1)	(ℓ_2,m_2)	(ℓ_3,m_3)	A_p^1	A_p^2	A_p^3	K_1	K_2	K_3	i	v_Ω	σ	Σ
(1,0)	(1,1)	(3,1)	13.79	18.09	20.30	0.08	0.081	0.092	43	19	5.5	
(1,0)	(1,1)	(3,1)	14.30	20.86	27.55	0.078	0.077	0.087	40	17	6	2.08
(1,0)	(1,1)	(2,1)	19.09	16.34	11.00	0.078	0.077	0.087	55	21	4	2.51
(1,0)	(1,1)	(1,1)	15.49	18.95	9.19	0.078	0.077	0.087	45	19	6	2.89
(1,0)	(2,1)	(2,1)	15.49	21.32	10.34	0.078	0.077	0.087	45	17	7	3.01
(1,0)	(2,1)	(1,1)	12.66	24.70	13.03	0.078	0.077	0.087	30	11	9	3.15

(ℓ_1,m_1)	(ℓ_2,m_2)	(ℓ_3,m_3)	A_p^1	A_p^2	A_p^3	K_1	K_2	K_3	i	v_Ω	σ	Σ
(2,1)	(2,2)	(3,1)	2.21	13.34	0.64	5.22	3.05	6.58	17	21	5.5	
(2,1)	(2,2)	(3,1)	1.48	8.42	0.45	6.79	3.96	8.56	20	25	1	2.42
(3,1)	(3,2)	(3,3)	2.40	3.08	2.83	3.65	2.13	4.61	40	18	9	2.92
(2,1)	(1,−1)	(3,1)	1.91	5.87	0.57	6.79	3.96	8.56	15	22	7	3.10
(3,1)	(3,2)	(3,−3)	1.48	4.47	0.45	6.79	3.96	8.56	20	27	1	3.19
(2,1)	(2,2)	(3,−1)	1.59	9.06	0.49	6.27	3.66	7.90	20	25	1	3.36

(ℓ_1,m_1)	(ℓ_2,m_2)	(ℓ_3,m_3)	A_p^1	A_p^2	A_p^3	K_1	K_2	K_3	i	v_Ω	σ	Σ
(3,3)	(2,2)	(1,1)	164.32	43.79	8.68	0.075	0.079	0.092	42	19	5.5	
(3,3)	(2,2)	(1,1)	123.82	34.74	7.49	0.071	0.075	0.087	55	20	8	4.02
(3,3)	(3,2)	(1,1)	123.82	63.13	10.40	0.071	0.075	0.087	55	19	3	4.30
(3,3)	(3,2)	(2,1)	123.82	63.13	10.40	0.071	0.075	0.087	55	19	3	4.30
(3,3)	(2,2)	(2,1)	151.52	39.75	9.92	0.071	0.075	0.087	50	17	1	4.50
(3,3)	(2,2)	(1,0)	151.52	39.75	6.74	0.071	0.075	0.087	50	18	1	4.89

modes of another degree for low values of the inclination, because of their very similar visible configuration.

We then tested 144 combinations of two modes including all kinds of modes until $\ell = 3$. The value for v_Ω was randomly chosen between 10 and 30 $\mathrm{km\,s^{-1}}$ and σ was taken equal to 5.5 $\mathrm{km\,s^{-1}}$. A_p was chosen so that the value of the radial velocity amplitude is compatible with observed values for β Cephei stars and SPB stars. Each time, the velocity amplitude of the second mode was chosen so that its first moment amplitude is smaller than the one of the first dominant mode. The K-values were also taken according to typical values of these two kinds of B-type oscillators. In Tables 5.1, 5.2, 5.3 and 5.4, we show the values of the input parameters for several sets, together with the five best solutions of the mode identification. We can conclude that the method performs the identification very well. However, sometimes, the real combination of the two modes does not correspond to *the* lowest value of the discriminant but appears in the list of the few best solutions. In general, the estimates for the continuous parameters (A_p, K, i, v_Ω, σ) are good, although large deviations do sometimes occur. Such failing of estimating these parameters well was already put forward by De Ridder et al. (2002b).

For evident computational reasons, we made less tests for three modes than for two. Some examples are given in Tables 5.5, 5.6, 5.7 and 5.8. Also for these testcases the identifications are very conclusive, while the same remark as above for the continuous parameters applies here.

We strongly encourage users of our mode identifcation method to study Tables 5.1 to 5.8 in order to obtain a feeling of the accuracy and the power, but also of the limitations, of the identification method.

A large number of tests indicates that the first three moments suffice to identify the modes correctly. In Appendix A.4, we show in a rigorous way that it is indeed not necessary to add higher order moments. Finally, we note that the computation time required to calculate the discriminant depends very much on the number of modes. It ranges from about half an hour for a monoperiodic star to several days for stars with three modes (with a Pentium 4, 2.4 GHz / 512 Mb RAM). We note that, with the previous version of the moment method, the identification of one mode required several days of computation, and the identification of three modes simultaneously would have required several months or more.

5.4   Mode identification strategy

It is evident from Tables 5.1 to 5.8 that, in many cases, one clear combination of different wavenumbers does not occur from the discriminant, as several solutions are almost equivalent in fitting the moment variations. This situation is inherent to the problem of mode identification, with whatever method, as several combinations of the velocity parameters

result in almost the same line-profile variations. The strength of the moment method is precisely that it allows one to severely restrict the number of possible solutions.

One would hope that a statistically justified test would inform the user how many of the candidate modes can be rejected with safety from comparison of the different values of Σ. At present, such a significance test is still lacking. The main difficulty lies in defining a suitable test for the combination of discrete and continuous parameters. De Ridder et al. (2002b) have taken the first steps in this direction for a monoperiodic pulsation.

In view of the lack of a significance test, one needs to evaluate the "few" best solutions resulting from the moment method, by constructing theoretical line-profile variations and by comparing these with the observed ones. One can do this for the profiles themselves, or else for their variation of amplitude and phase across the profile (for a definition of the latter diagnostic values, we refer to Schrijvers et al. 1997). The value of a "few" depends on the complexity of the pulsation. We advise the user to look at at least the 5 best (ℓ, m) for a monoperiodic star, the 10 best combinations of the wavenumbers for a biperiodic oscillator and so on. A recent example of such a procedure is provided in Aerts et al. (2003a) for the β Cep star EN Lac — see also below. We strongly urge users of our method not to omit this last step. We also stress, however, that, even after such an additional test, ambiguity among the solutions that survive the test will still remain, i.e. one single outcome will seldomly be reached. However, the number of possibilities will have decreased significantly, to such an extent that seismic modelling can be tried on the basis of the remaining accepted combinations of the wavenumbers.

5.5 Application to β Ceps and SPBs

5.5.1 β Crucis

Aerts et al. (1998) presented numerous high signal-to-noise spectroscopic data of the β Cephei star β Crucis with a total time span of 13 years. They found three frequencies in the moments of the Si III 4553 Å line: $f_1 = 5.2305468$ c d^{-1}, $f_2 = 5.958666$ c d^{-1} and $f_3 = 5.472165$ c d^{-1}. The corresponding observed first moment amplitudes are $A_{\text{obs}}^1 = 1.41$ km s^{-1}, $A_{\text{obs}}^2 = 0.62$ km s^{-1} and $A_{\text{obs}}^3 = 0.34$ km s^{-1}. Note that only the first frequency was known and detected in photometric observations before their study. A mode identification with the 1996-version of the moment method was performed. It pointed towards non-axisymmetric and non-radial modes. The mode corresponding to f_1 was found to be a low-degree sectoral mode with $\ell = 1$ while f_2 and f_3 clearly correspond to higher degrees ($\ell = 3$ or $\ell = 4$), explaining why the two newly found frequencies were not detected photometrically. Meanwhile, these two additional modes have also been detected clearly in space photometry gathered by the WIRE satellite (Cuypers et al. 2002), as well as two additional candidates. It is then clear that this star exhibits multiple non-radial modes and is hence an interesting asteroseismic target.

Table 5.9: The ten best solutions of the mode identification through the discriminant Σ for the β Cephei star β Crucis, using the Si III 4553 Å line for which the amplitudes of the first moment are $A_{\text{obs}}^1 = 1.41$ km s^{-1}, $A_{\text{obs}}^2 = 0.62$ km s^{-1} and $A_{\text{obs}}^3 = 0.34$ km s^{-1}. A_p is the amplitude of the radial part of the pulsation velocity, expressed in km s^{-1}; i is the inclination angle; v_Ω is the projected rotational velocity, expressed in km s^{-1} and σ is the intrinsic line-profile width, also expressed in km s^{-1}.

(ℓ_1,m_1)	(1,0)	(1,−1)	(0,0)	(1,−1)	(0,0)	(1,0)	(0,0)	(1,0)	(0,0)	(2,0)
(ℓ_2,m_2)	(4,2)	(4,3)	(4,2)	(4,2)	(3,3)	(3,3)	(3,2)	(3,2)	(4,3)	(4,2)
(ℓ_3,m_3)	(3,3)	(3,3)	(3,3)	(3,2)	(2,2)	(2,2)	(3,1)	(3,1)	(3,3)	(2,2)
A_p^1	6.51	8.32	7.24	10.66	7.24	5.88	7.24	5.41	7.24	11.21
A_p^2	104.70	108.18	104.70	102.16	165.87	165.87	172.12	172.12	108.18	120.19
A_p^3	36.35	9.21	36.35	7.93	15.92	15.92	13.25	13.25	9.21	11.39
i	35	65	35	45	25	25	10	10	65	30
v_Ω	15	16	15	19	23	23	13	13	17	14
σ	19	19	19	19	19	19	11	11	19	17
Σ	5.43	5.43	5.44	5.44	5.45	5.45	5.45	5.46	5.46	5.47

In order to validate and/or improve the mode identification done by Aerts et al. (1998), we performed a mode identification by our new optimized version of the moment method, using the same K-values as adopted by Aerts et al. (1998): $K_1 = 0.028$, $K_2 = 0.021$ and $K_3 = 0.025$. In doing so, we force the amplitudes of the first moment to be equal to the observed values mentioned above. The outcome, which is given in Table 5.9, is compatible with the previous one. In particular, we recover the $\ell = 1$ nature of the main mode and the higher-degree nature of the two lower-amplitude modes. While Aerts et al. (1998) found $\ell = 3$ and 4 for respectively f_2 and f_3, we find the reverse here. This is not too surprising as these two modes resemble each other for a view at moderate inclination. The continuous parameter estimates (i, v_Ω, σ) we find here are intermittent to the three different values for the three modes in Aerts et al. (1998).

Data with a better time spread are needed to check the validity of the best solutions as outlined in Sect. 5.4, as the beating between the three modes is very badly covered. We therefore cannot yet perform seismic modelling of the star, but the studies by Aerts et al. (1998) and by Cuypers et al. (2002) have pushed this star upward in the list of potential asteroseismic targets for future space missions.

5.5.2   EN (16) Lacertae

EN (16) Lacertae is one of the most studied β Cep stars ever. Lehmann et al. (2001) made for the first time a detailed spectroscopic study of EN (16) Lacertae, which is an eclipsing and spectroscopic binary. Besides providing accurate orbital parameters, they recovered and refined the three intrinsic frequencies known for this star from photometry in their

Table 5.10: The ten best solutions of the mode identification through the discriminant Σ for the β Cephei star 16 Lacertae, using the He I 6678 Å line for which the amplitudes of the first moment are $A_{\mathrm{obs}}^1 = 2.57$ km s^{-1}, $A_{\mathrm{obs}}^2 = 2.71$ km s^{-1} and $A_{\mathrm{obs}}^3 = 1.10$ km s^{-1}. The meanings of the symbols are the same as in Table 5.9.

(ℓ_1,m_1)	(0,0)	(0,0)	(0,0)	(1,0)	(0,0)	(1,0)	(0,0)	(0,0)	(0,0)	(0,0)
(ℓ_2,m_2)	(2,0)	(1,0)	(2,0)	(2,0)	(2,0)	(2,0)	(2,0)	(2,0)	(1,0)	(1,0)
(ℓ_3,m_3)	(1,0)	(2,0)	(2,−2)	(2,−2)	(2,2)	(2,2)	(2,−1)	(2,1)	(1,−1)	(1,1)
A_p^1	13.45	13.45	12.10	8.38	12.10	8.38	12.10	12.10	13.45	13.45
A_p^2	27.71	29.21	16.80	16.80	16.80	16.80	27.71	27.71	26.29	26.29
A_p^3	12.38	11.98	39.99	39.99	39.99	39.99	12.69	12.69	4.82	4.82
i	75	70	25	25	25	25	75	75	70	70
v_Ω	38	39	1	1	1	1	6	6	7	7
σ	5	2	19	19	19	19	19	19	19	19
Σ	3.86	3.86	3.87	3.87	3.87	3.87	3.88	3.89	3.90	3.90

radial-velocity data: $f_1 = 5.91128$ c d^{-1}, $f_2 = 5.85290$ c d^{-1} and $f_3 = 5.50279$ c d^{-1}. The corresponding observed first moment amplitudes are $A_{\mathrm{obs}}^1 = 2.57$ km s^{-1}, $A_{\mathrm{obs}}^2 = 2.71$ km s^{-1} and $A_{\mathrm{obs}}^3 = 1.10$ km s^{-1} (Aerts et al. 2003a). Chapellier et al. (1995) summarized all photometric mode identification efforts so far and concluded that $\ell_1 = 0$, $\ell_2 = 2$ and $\ell_3 = 1$.

The first spectroscopic mode identification for this star was recently done by Aerts et al. (2003a) who considered a subset of 940 high-resolution high S/N spectra gathered by Lehmann et al. (2001). Our mode identification presented here, which was done using $K_1 = 0.0824$, $K_2 = 0.0841$ and $K_3 = 0.0951$, is one of the identification results adapted by Aerts et al. (2003a), who considered also other spectroscopic diagnostics for identification. Our result is given in Table 5.10. It is compatible with the one resulting from the other method adapted by Aerts et al. (2003a). We refer to Aerts et al. (2003a) for an in-depth interpretation of the spectroscopic variability of this star and for a comparison of the moment method outcome with the observed line-profile variations as described in Sect. 5.4. We also note that a more recent and improved photometric mode identification by Dupret et al. (2003) leads to the same outcome.

5.5.3 HD 74195

De Cat (2001) studied the slowly pulsating B star HD 74195, among 12 other such stars. Based on multicolour Geneva photometry and high-resolution spectroscopy, he found four frequencies: $f_1 = 0.35475$ c d^{-1}, $f_2 = 0.35033$ c d^{-1}, $f_3 = 0.34630$ c d^{-1} and $f_4 = 0.39864$ c d^{-1}. The corresponding observed first moment amplitudes are $A_{\mathrm{obs}}^1 = 2.36$ km s^{-1}, $A_{\mathrm{obs}}^2 = 2.36$ km s^{-1}, $A_{\mathrm{obs}}^3 = 1.18$ km s^{-1} and $A_{\mathrm{obs}}^4 = 1.43$ km s^{-1}. The mode identification from the moments of the Si II 4128 Å line based on the moment method in the version

Table 5.11: The ten best solutions of the mode identification through the discriminant Σ for the slowly pulsating B star HD 74195, using the Si II 4128 Å line for which the amplitudes of the first moment are $A^1_{\mathrm{obs}} = 2.36$ km s^{-1}, $A^2_{\mathrm{obs}} = 2.36$ km s^{-1}, $A^3_{\mathrm{obs}} = 1.18$ km s^{-1} and $A^4_{\mathrm{obs}} = 1.43$ km s^{-1}. The meanings of the symbols are the same as in Table 5.9. The table corresponds to an identification using the non-rotating formalism and fixing K-values.

(ℓ_1,m_1)	(1,0)	(1,0)	(2,0)	(2,0)	(2,−1)	(2,0)	(2,−1)	(1,0)	(1,0)	(2,0)
(ℓ_2,m_2)	(2,−2)	(2,−2)	(2,−2)	(3,−1)	(3,−1)	(2,−2)	(3,−1)	(3,−1)	(3,−1)	(3,−1)
(ℓ_3,m_3)	(2,1)	(2,2)	(2,2)	(2,1)	(2,2)	(2,1)	(3,1)	(2,1)	(2,2)	(2,2)
(ℓ_4,m_4)	(1,−1)	(1,−1)	(1,−1)	(1,−1)	(1,−1)	(1,−1)	(1,−1)	(1,−1)	(1,−1)	(1,−1)
A^1_p	0.27	0.34	0.30	0.30	0.24	0.16	0.20	0.28	0.26	0.18
A^2_p	1.04	0.36	0.44	0.25	0.23	1.04	0.23	0.23	0.23	0.22
A^3_p	0.11	0.17	0.21	0.09	0.48	0.11	0.11	0.10	0.48	0.34
A^4_p	0.62	0.37	0.41	0.41	0.62	0.62	0.46	0.53	0.62	0.52
i	25	45	40	40	25	25	35	30	25	30
v_Ω	17	23	23	20	15	15	17	15	12	14
σ	5	3	1	6	8	6	8	9	9	9
Σ	5.50	5.50	5.51	5.52	5.52	5.53	5.54	5.54	5.54	5.55

by Aerts (1996) attributed the first three frequencies to $\ell = 2$ modes and f_4 to an $\ell = 1$ mode. The identification from photometry, however, was found to be incompatible with this result by De Cat (2001) since it points towards $\ell = 1$ modes for f_1, f_2 and f_3 and an $\ell = 6$ mode for f_4.

In an attempt to resolve the issue, we performed a new identification with our version of the moment method. We point out that the values of the observed first moment amplitudes and of the observed constant term of the second moment clearly impose $\ell \leq 3$ for the four frequencies, directly excluding a high degree mode for f_4. By eliminating degrees greater than 3 in the photometric outcome, the new candidate degree from Geneva data is also $\ell = 1$ for the fourth frequency.

The result with the new moment method by taking $K_1 = 41$, $K_2 = 42$, $K_3 = 43$ and $K_4 = 32$ is given in Table 5.11. This identification is not too different from the spectroscopic one found by De Cat (2001). Our calculations clearly point towards an $\ell = 1$ sectoral mode for f_4. However, the identification for the other frequencies still needs to be confirmed.

One can doubt the reliability of a mode identification by fixing K-values of SPBs. Indeed, because there are large uncertainties on the mass and radius of most of these stars, K-values can have uncertainties up to 30%, which is very large. In order to test our mode identification as done above, we performed a new one by varying the parameter from 0.7 K to 1.3 K with a step of 0.1 K and we obtained the outcome given in the upper part of Table 5.12.

Table 5.12: The ten best solutions of the mode identification through the discriminant Σ for the slowly pulsating B star HD 74195, using the Si II 4128 Å line for which the amplitudes of the first moment are $A_{\text{obs}}^1 = 2.36$ km s^{-1}, $A_{\text{obs}}^2 = 2.36$ km s^{-1}, $A_{\text{obs}}^3 = 1.18$ km s^{-1} and $A_{\text{obs}}^4 = 1.43$ km s^{-1}. The meanings of the symbols are the same as in Table 5.9. The upper part of the table is the result by varying the K-values from 0.7 K to 1.3 K with a step of 0.1 K. The lower one is the outcome for an identification using Lee & Saio's formalism for the pulsational velocity of a rotating star.

(ℓ_1,m_1)	(1,0)	(1,0)	(2,0)	(2,0)	(2,0)	(2,−1)	(2,−1)	(1,0)	(1,0)	(1,0)
(ℓ_2,m_2)	(2,−2)	(2,−2)	(2,−2)	(3,−1)	(2,−2)	(3,−1)	(3,−1)	(2,−2)	(3,−1)	(3,−1)
(ℓ_3,m_3)	(2,1)	(2,2)	(2,2)	(2,1)	(2,1)	(2,2)	(3,1)	(1,0)	(2,1)	(2,−2)
(ℓ_4,m_4)	(1,−1)	(1,−1)	(1,−1)	(1,−1)	(1,−1)	(1,−1)	(1,−1)	(1,−1)	(1,−1)	(1,−1)
A_p^1	0.38	0.26	0.23	0.23	0.22	0.18	0.15	0.37	0.22	0.22
A_p^2	1.49	0.28	0.34	0.19	1.49	0.18	0.18	1.46	0.17	0.20
A_p^3	0.16	0.13	0.16	0.07	0.16	0.38	0.08	0.18	0.08	0.42
A_p^4	0.88	0.28	0.31	0.32	0.88	0.47	0.35	0.86	0.41	0.51
K_1	28	52	52	52	28	52	52	28	52	49
K_2	29	53	53	53	29	53	53	29	53	50
K_3	29	55	55	55	29	55	55	29	55	51
K_4	22	41	41	41	22	41	41	22	41	39
i	25	45	40	40	25	25	35	25	30	25
v_Ω	27	23	23	20	17	15	17	17	15	12
σ	5	3	1	6	5	8	8	5	9	9
Σ	5.49	5.50	5.50	5.51	5.51	5.52	5.54	5.54	5.54	5.55

(ℓ_1,m_1)	(2,0)	(1,0)	(1,0)	(2,0)	(2,0)	(2,0)	(1,0)	(1,0)	(2,0)	(2,0)
(ℓ_2,m_2)	(3,−1)	(3,−1)	(2,−1)	(3,−1)	(2,−1)	(3,−1)	(2,−1)	(3,−1)	(3,−1)	(3,−1)
(ℓ_3,m_3)	(3,1)	(3,1)	(3,1)	(2,2)	(2,2)	(2,1)	(2,2)	(2,2)	(1,0)	(2,0)
(ℓ_4,m_4)	(1,−1)	(1,−1)	(1,−1)	(1,−1)	(1,−1)	(1,−1)	(1,−1)	(1,−1)	(1,−1)	(1,−1)
A_p^1	0.23	0.30	0.27	0.23	0.18	0.23	0.28	0.30	0.23	0.23
A_p^2	0.03	0.03	0.02	0.03	0.03	0.03	0.03	0.03	0.03	0.03
A_p^3	0.16	0.16	0.17	0.82	1.21	0.15	1.21	0.82	0.14	0.11
A_p^4	0.25	0.25	0.24	0.25	0.25	0.25	0.25	0.25	0.25	0.25
K_1	40	40	40	40	40	40	40	40	40	40
K_2	139	139	281	139	180	139	180	139	139	139
K_3	19	19	15	11	9	19	9	11	42	42
K_4	88	88	152	88	108	88	108	88	88	88
i	35	35	25	35	30	35	30	35	35	35
v_Ω	20	20	20	20	20	20	20	20	20	20
σ	6	6	6	6	6	6	6	6	6	6
Σ	5.51	5.52	5.52	5.53	5.55	5.55	5.55	5.56	5.56	5.56

The identification of the modes leads to exactly the same outcome as before, except that the values of A_p differ. One can conclude that the uncertainty on the K-value does not affect the identification of (ℓ, m). This result is not too surprising since line-profile variations of an SPB are mainly due to the horizontal velocity field variations and slightly to the vertical ones. The relevant amplitude is then the horizontal one $A_h = A_p \, K$, which is indeed found to be about the same for each of the modes in the two different identifications.

One can also doubt the reliability of a mode identification for SPB stars by using the non-rotating theory since their observed ratios of the rotational frequency to the pulsational frequency are in general larger than 0.1. Again to test our mode identification, we performed a new one using the formalism of Lee & Saio (1987, 1990). The K-values are then computed using the co-rotating angular frequency related to the observed one by $\sigma_c = \sigma_{\mathrm{obs}} + m\Omega$. The identification is given in the lower part of Table 5.12. This again leads to a very similar outcome for the wavenumbers (ℓ, m). Basically, the same combinations for (ℓ, m) occur each time. The K-values change considerably, but this is compensated by the values for A_p and does not affect the mode identification appreciably. We do point out that the formalism of Lee & Saio (1987, 1990) does not apply to modes with $m = 0$ so that axisymmetric modes mentioned in the lower part of Table 5.12 were computed using the non-rotating formalism.

It is clear that, particularly in the case of multiple g-modes, we need additional observational information to pinpoint definitely the wavenumbers (ℓ, m) of all the different modes. Our method, however, implies a serious improvement for the spectroscopic mode identification in such cases. In the particular case of HD 74195, De Cat et al. (2003) are currently using Dupret et al.'s (2003) method in order to improve the photometric mode identification. Line-profile fitting and an attempt at seismic modelling will be performed after further elimination of combinations from Table 5.11 according to the multicolour mode identification in progress and is beyond the scope of this thesis.

5.6   Conclusions

The study of the oscillations of a pulsating star allows us to probe its internal structure. A successful application of asteroseismic techniques requires the identification of many pulsation modes. Therefore, high quality data as well as powerful mode identification methods are needed. Among the techniques of mode identification from line-profile variations, only the line-profile fitting method and the moment method derive the full pulsational information. However, even with current computers, a simultaneous identification of multiple modes is not possible by direct line-profile fitting. Moreover, mode identification with the moment method was still difficult for multiperiodic stars. Indeed, because of large computation time, the previous version of the moment method did not take into account coupling terms appearing in the second and third moments of a mul-

tiperiodic star so that multiple modes were determined independently, often leading to inconsistent values of the continuous velocity parameters.

We implemented a new numerical version of the moment method, which is efficient in computation time and which identifies all the modes by requiring that the rotational velocity, the inclination angle and the intrinsic line width have one unique value. Consequently, all observed terms of the first three moments can be used, in particular the constant term of the second moment which is an important constraint. By means of a new discriminant which compares theoretical to observed first three moments, the new version identifies the wavenumbers of the multiple modes simultaneously, leading to only one derived value for v_Ω, i, and σ.

We performed a large number of tests on artificial data representing the presence of respectively one, two and three modes. It appears that the method performs very well on synthetic datasets. An application to two β Cephei stars and one SPB star was done. We subsequently plan to use the new version of the moment method in the near future to several datasets of pulsating B stars of different kinds. Our new method is also relevant to obtain reliable mode identification in multiperiodic bright δ Scuti and γ Doradus stars.

Part II

Analyses of pulsating B stars

Chapter 6

Eight new northern SPBs

(this chapter was originally published as **Mathias P.**, **Aerts C.**, **Briquet M.**, **De Cat P.**, **Cuypers J.**, **Van Winckel H.**, **Le Contel J.M.**, 2001, A&A 379, 905, *Spectroscopic monitoring of 10 new northern slowly pulsating B star candidates discovered from the HIPPARCOS mission*)

6.1 Observations and programme stars

In 1998, a spectroscopic monitoring of ten selected candidate SPBs started in the northern hemisphere (Mathias et al. 2001). The target SPBs were chosen from the brightest ones among the many candidate new SPBs discovered from the HIPPARCOS mission (Waelkens et al. 1998) and the observations were gathered with the AURELIE spectrograph at the Coudé focus at the 1.52 m telescope situated at the Observatoire de Haute-Provence in France. A logbook of the eight dedicated observation campaigns is given in Table 6.1. The target list, together with the observation parameters, are given in Table 6.2. The spectral domain was chosen in order to get the Si II-doublet with lines at $\lambda\lambda$ 4128, 4130 Å. It was [4085-4155] Å, containing also the Hδ line and the He I lines 4026 Å, 4120 Å and 4143 Å. The resolving power was around 15 000. The obtained raw spectra were reduced by Dr. P. Mathias. Each spectrum has been corrected for the pixel-to-pixel response by flat-field and offset spectra. The wavelength calibration was based upon about 30 lines of a thorium lamp. Finally, the spectra were normalized to the continuum by a cubic spline function.

Some physical parameters of the programme stars are given in Table 6.3. The effective temperature and the gravity were obtained by using the available Geneva photometric indexes and by means of the calibration by North & Nicolet (1990). Masses were estimated by interpolation between the evolutionary tracks published by Schaller et al. (1992).

In the following section, we present the frequency analysis performed on HIPPARCOS photometry and on spectroscopic measurements (Sect. 6.2). In Sect. 6.3, we summarize the outcome of this campaign for northern SPBs.

Table 6.1: Overview of the spectroscopic campaigns. Columns are self-explanatory.

Period	Nights	Observer(s)
February 98	7	Mathias
June 98	5	Mathias
July 98	8	De Cat
August 98	6	Van Winckel
October 98	6	Mathias
December 98	8	Mathias
April 99	7	Aerts/Mathias
May 99	6	Briquet/Le Contel

Table 6.2: Observation summary for the different targets. The columns are: the HD number of the SPB, its HR number (and name), the number of recorded spectra, the covered time base (range, in days), the averaged exposure time (in minutes), and the 1-σ averaged signal-to-noise ratio.

HD	HR (name)	Spectra	Range	Exposure	S/N
1976	91	26	197	58	140
21071	1029	35	436	64	80
25558	1253 (40 Tau)	25	313	59	140
28114	1397	17	305	64	90
138764	5780	16	185	58	130
140873	5863	14	186	60	110
147394	6092 (τ Her)	280	460	15	190
182255	7358 (3 Vul)	53	348	48	150
206540	8292	25	159	77	100
208057	8356 (16 Peg)	36	201	52	140

Table 6.3: Summary of the physical characteristics of the programme stars. For each star, we give the HD number, the spectral type, the V-magnitude, $\log T_{\mathrm{eff}}$, $\log L/L_\odot$ and $\log g$ provided by HIPPARCOS and Geneva photometry, stellar masses and radii interpolated from Schaller et al. (1992), and the projected rotation velocity we measured from the Si II-doublet. Note that, because we were unable to remove the lines of the companion for HD 140873, the corresponding v_Ω value is omitted.

HD	ST	V	$\log T_{\mathrm{eff}}$	$\log L/L_\odot$	$\log g$	$M/M_\odot$	$R/R_\odot$	v_Ω
1976	B 5 IV	5.6	4.20	2.92	4.07	5.0	3.41	< 140
21071	B 7 V	6.1	4.15	2.53	4.36	4.1	2.21	< 62
25558	B 3 V	5.3	4.23	2.81	4.21	5.1	2.93	< 22
28114	B 6 IV	6.1	4.16	3.02	4.03	5.0	3.57	< 11
138764	B 6 IV	5.2	4.15	2.69	4.24	4.3	2.60	< 13
140873	B 8 III	5.4	4.15	2.44	4.37	3.9	2.13	-
147394	B 5 IV	3.9	4.17	2.80	4.00	5.0	3.70	< 36
182255	B 6 III	5.2	4.15	2.60	4.28	4.2	2.46	< 14
206540	B 5 IV	6.1	4.14	2.81	4.14	4.5	2.99	< 10
208057	B 3 Ve	5.1	4.23	2.87	4.12	5.2	3.28	< 110
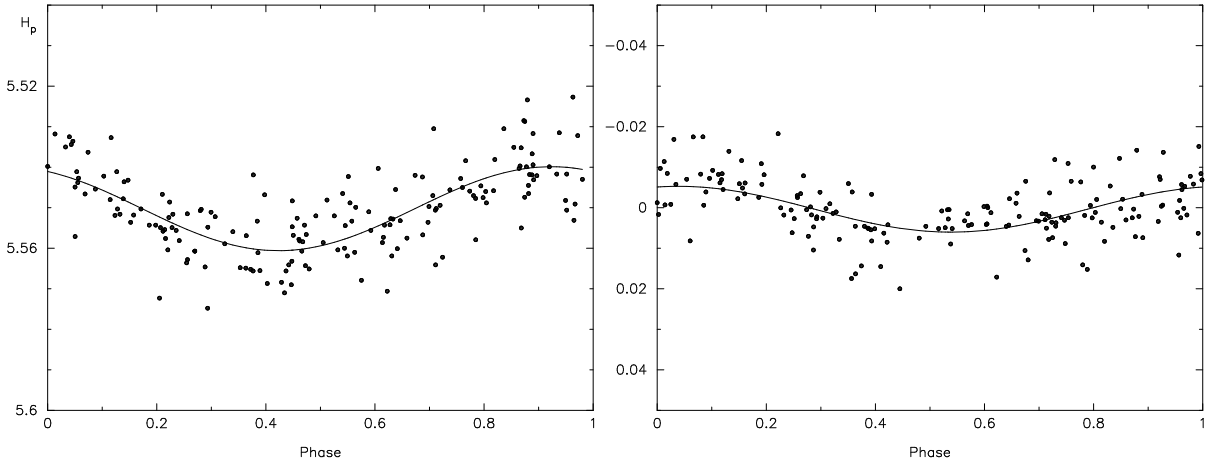
Figure 6.1: Phase diagrams of the $H_{\rm p}$-data of HD 1976. Left: fit for $f_1 = 0.93914$ c d^{-1}. Right: fit on the residuals for $f_2 = 0.39934$ c d^{-1}.

6.2   Frequency analysis

For the ten stars, a search for multiperiodicity was performed in the HIPPARCOS photometry and in the radial velocity computed from both lines of the Si II-doublet and the Hδ line. The radial velocity was computed as the mean of a gaussian fit to the whole profile (only the line core for Hδ). However, because of the non-radial pulsations, the Si II lines are very asymmetric. For this reason, the first moment as defined by Aerts et al. (1992) was also used to calculate the radial velocity. The mean value of the radial velocity determined from both methods and from the three lines was then considered.

The period analysis was performed by means of four methods: Fourier analysis, CLEAN (Roberts et al. 1987), Vanicek (1971), and PDM (Stellingwerf 1978). For the CLEAN method, 100 iterations were performed, with a gain of 0.5. For the PDM method, the bin structure was (5,2). Frequencies were tested in the [0;3] c d^{-1} interval and a frequency was accepted when it was found by each of the methods. Multiperiodicity was searched by prewhitening. We note that the HIPPARCOS photometry allows the detection of multiperiodicity for SPBs (De Cat 2001) thanks to the appropriate time sampling for finding periods of the order of one day and thanks to the long time base of 3.3 years. The outcome of the period analysis for each star is described in the following.

HD 1976

In the HIPPARCOS photometry, two frequencies appear: $f_1 = 0.93914$ c d^{-1} and $f_2 = 0.39934$ c d^{-1}. They have respectively an amplitude of 0.0097 mag and 0.0106 mag. The standard deviation of the data is reduced from 0.0106 mag to 0.0062 mag after prewhitening with both frequencies. No third frequency could be found. Phase plots for both accepted frequencies are shown in Fig. 6.1.
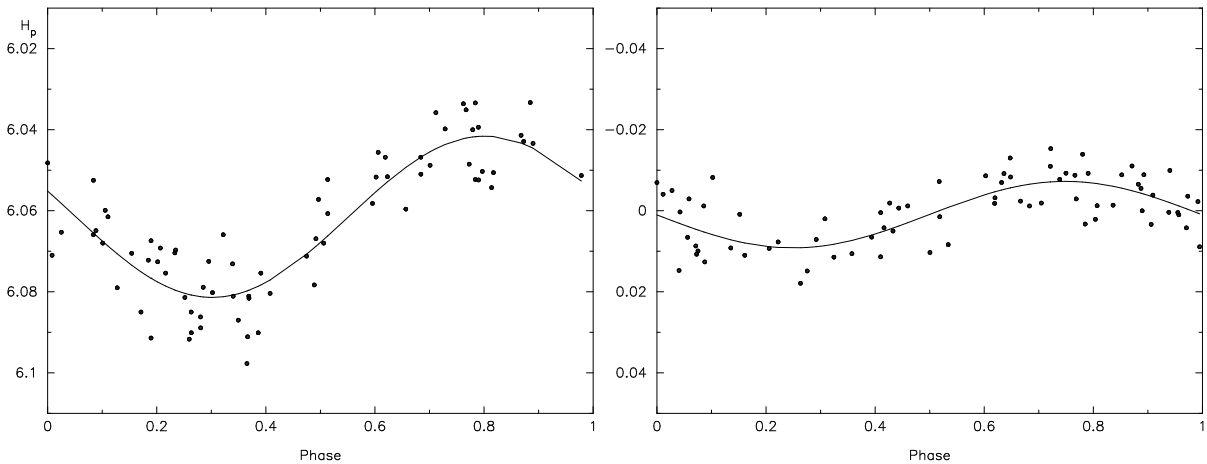
Figure 6.2: Phase diagrams of the $H_{\rm p}$-data of HD 21071. Left: fit for $f_1 = 1.18843$ c d^{-1}. Right: fit on the residuals for $f_2 = 1.14942$ c d^{-1}.

The radial velocity has a large peak-to-peak amplitude of some 30 km s^{-1}, which is connected to the orbital motion of this spectroscopic binary. Tokovinin (1997) derived an amplitude around 23.4 km s^{-1} and an orbital period of 25.44 d. After removing the orbital motion from the radial-velocity variations, no well-defined frequency could be found. However, there is some indication for the second frequency f_2 found in the HIPPARCOS data to be present in the line-profile variations.

HD 21071

Two frequencies were derived from the space data: $f_1 = 1.18843$ c d^{-1} with an amplitude of 0.0190 mag and $f_2 = 1.14942$ c d^{-1} with an amplitude of 0.0058 mag. They reduce the standard deviation from 0.0175 mag to 0.0058 mag (Fig. 6.2).

The frequency analysis applied to the radial-velocity data leads to a common peak around 1.14 c d^{-1}, close to the f_2 value derived from photometry. However, a harmonic fit to the radial velocity with both frequencies f_1 and f_2 leads respectively to amplitudes of 3.3 and 0.9 km s^{-1}. A phase diagram for f_1 is shown in the left panel of Fig. 6.3. Note that the radial-velocity variations reach a peak-to-peak amplitude around 13 km s^{-1}, which is large for an SPB (De Cat 2001) and might indicate that HD 21071 is multiperiodic.

HD 25558

For HD 25558, only one clear frequency is found in the HIPPARCOS data: $f_1 = 0.65284$ c d^{-1}, which has an amplitude of 0.0181 mag and reduces the standard deviation from 0.0142 mag to 0.0067 mag (left panel of Fig. 6.4). Two candidate frequencies appear after prewhitening: $f_2 = 0.7318$ c d^{-1} and $f_2' = 1.9298$ c d^{-1}. They both additionally reduce the standard deviation by a millimag but cannot be accepted without futher observational evidence.
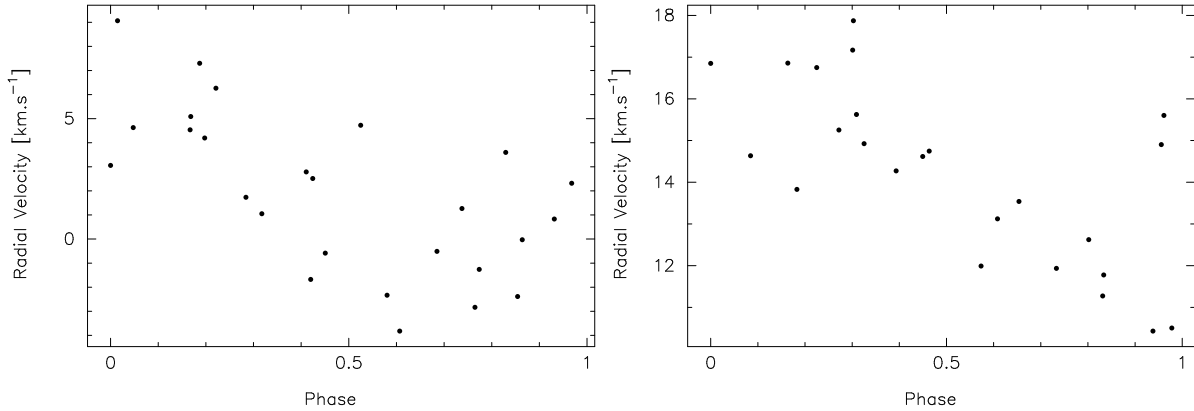
Figure 6.3: Phase diagram of the mean heliocentric velocities of HD 21071 for $f_1 = 1.18843$ c d^{-1} (left) and of HD 25558 for $f_1 = 0.65284$ c d^{-1} (right).

The different periodograms for the radial velocity show peaks in the neighbourhood of the frequency f_1, which accounts for 52% of the variance. Harmonic fits with f_1 and f_2 on the one hand, and with f_1 and f_2' on the other hand, do not allow to choose the second frequency. Amplitudes for f_1 and f_2 or f_2' are respectively 2.1 and 0.9 km s^{-1}. The phase diagrams for f_1 is represented in the right panel of Fig. 6.3. The peak-to-peak amplitude is 7 km s^{-1}.

HD 28114

The frequency $f_1 = 0.79104$ c d^{-1}, with an amplitude of 0.0159 mag, is found in the photometric data and reduces the standard deviation from 0.0132 mag to 0.0060 mag (right panel of Fig. 6.4). The HIPPARCOS team gave a different frequency of 0.93 c d^{-1} but it reduces the standard deviation to only 0.0078 mag.

The low projected rotation velocity of the star allows to see the line-profile variations immediately (Fig. 6.5). An amplitude of 1.7 km s^{-1} is found for f_1. Wolff (1978) claims, from 9 low-resolution spectrograms, that the star is a spectroscopic binary, with a 0.2-0.4 c d^{-1} orbital frequency and a peak-to-peak variation of 13 km s^{-1}. It is very likely that she misinterpreted the radial-velocity variations. The 17 spectra of HD 28114 are by far too few to disentangle the pulsational behaviour, but the clear profile variability allows to conclude that the star pulsates with a velocity amplitude compatible with the one reported by Wolff (1978).

HD 138764

HD 138764 was already extensively studied by De Cat (2001) by means of spectra and photometry taken from La Silla in Chile. This star is a slow rotator, with $v_\Omega = 18$ km s^{-1}, and presents well-marked line-profile variations in the OHP spectra (Fig. 6.6).
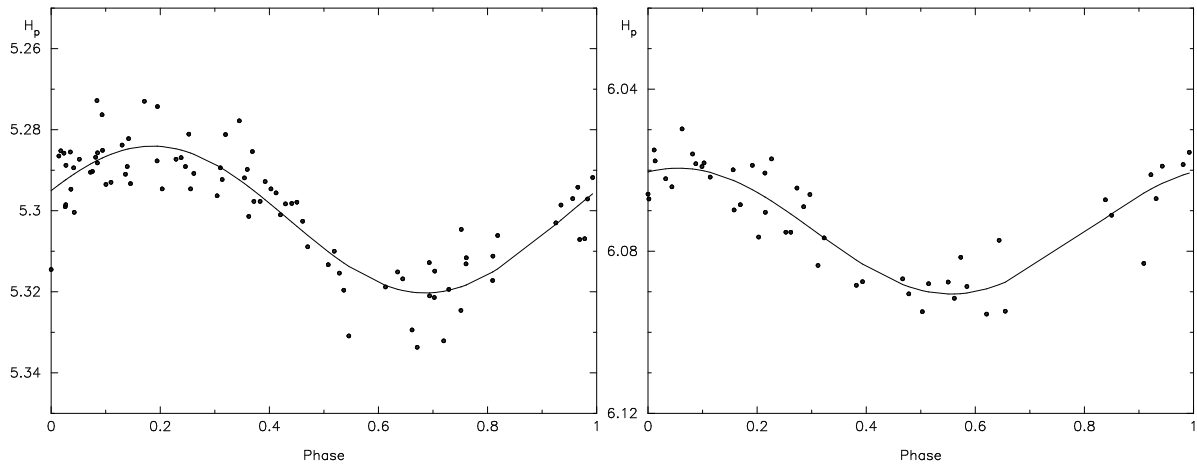
Figure 6.4: Left: phase diagram of the H_p-data of HD 25558 for $f_1 = 0.65284$ c d^{-1}. Right: phase diagram of the H_p-data of HD 28114 for $f_1 = 0.79104$ c d^{-1}.

A frequency search in the radial velocity led to the value provided in De Cat (2001), $f_1 = 0.7944$ c d^{-1}, with an amplitude of 4.7 km s^{-1} (Fig. 6.7). In De Cat (2001), the second frequency $f_2 = 0.6372$ c d^{-1} is reported. This frequency is also present in the OHP spectra and corresponds to an amplitude of about 2 km s^{-1}. We refer to De Cat (2001) for a more detailed analysis.

HD 140873

HD 140873 was also already studied by De Cat (2001) by means of spectra and photometry taken from La Silla in Chile. He showed that the star is a spectroscopic binary with a 39 d orbital period and an eccentric orbit. The large line-profile variations of the star are due to both the pulsation of the primary, which has a quite high projected rotation velocity and the presence of weak, sharp lines of the secondary. The northern data are not numerous enough, and have a too low signal-to-noise ratio, to remove the lines of the companion. Therefore no frequency search has been attempted. Note that De Cat (2001) found the frequency $f_1 = 1.1515$ c d^{-1}.

HD 147394

The first frequency found in the HIPPARCOS data of HD 147394 is $f_1 = 0.80027$ c d^{-1} with an amplitude of 0.0099 mag. It reduces the standard deviation to 0.0070 mag (Fig. 6.8). Several frequencies are candidate after prewhitening with f_1. They all reduce the standard deviation to about 0.006 mag but it is not clear which one is the most likely. After prewhitening with any of them, we find candidates for a third frequency which all differ from each other.

Adelman et al. (2001) reported that on some of their high-resolution, high signal-to-noise spectra, the metal lines are asymmetric. Line-profile variations have also been
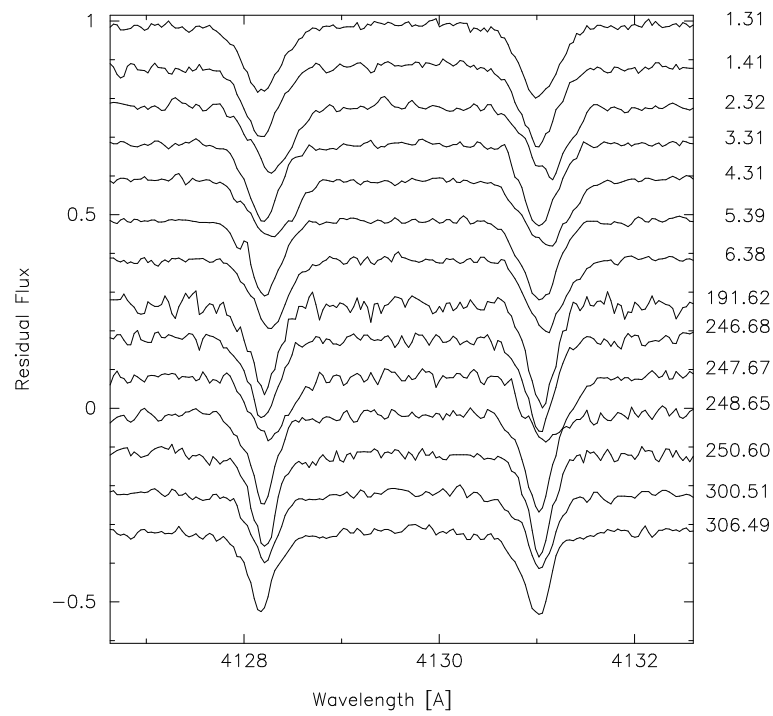
Figure 6.5: Line-profile variations of the Si II-doublet 4128-4130 Å for HD 28114. Observation dates are indicated on the right of the panel (+2450850 JD).
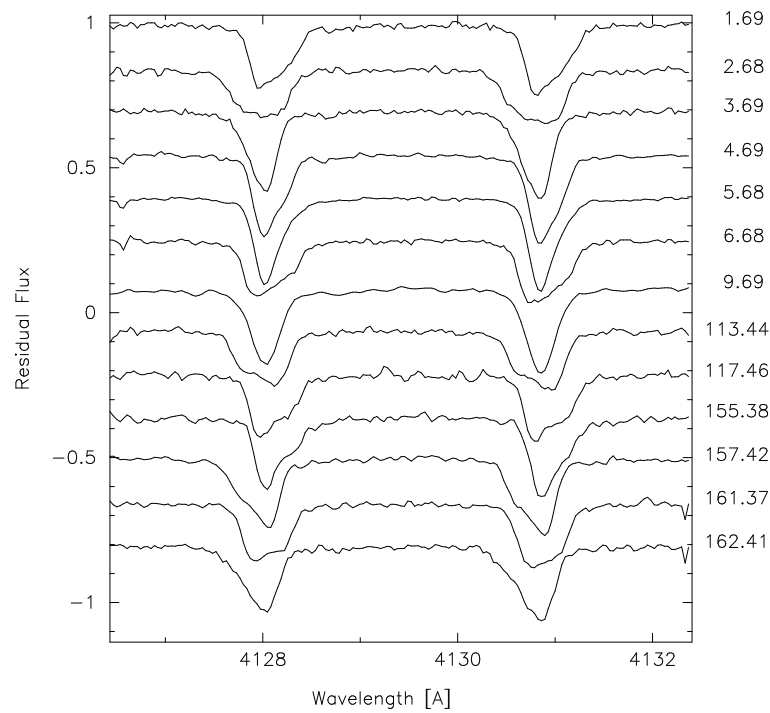
Figure 6.6: Same as Fig. 6.5 but for the star HD 138764.
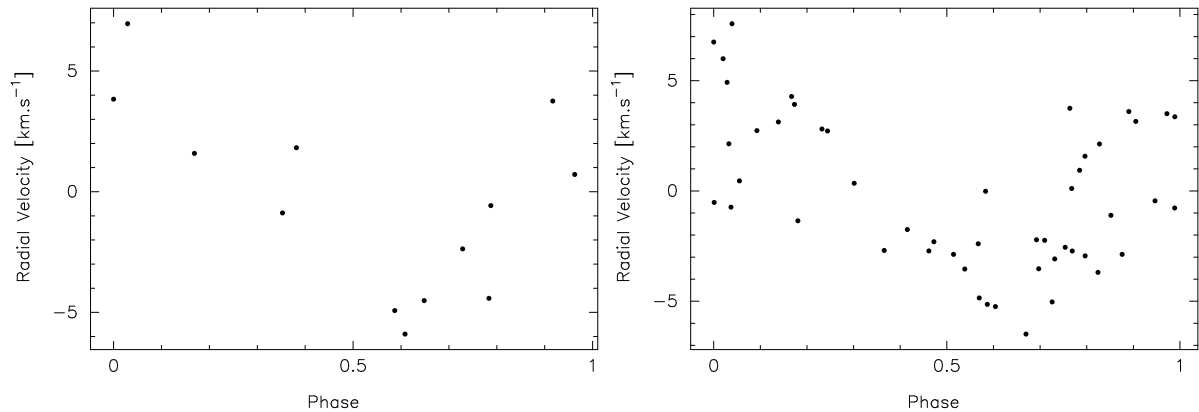
Figure 6.7: Same as Fig. 6.3, but for HD 138764 for $f_1 = 0.7944$ c d^{-1} (left) and for the star HD 182255 for $f_1 = 0.79220$ c d^{-1} (right). Note that the orbital motion has been removed first for HD 182255.

reported by Masuda & Hirata (2000), who obtained 30 spectra in 5 nights for He I 4471 Å and Mg II 4481 Å. From these data, these authors proposed one frequency: 0.855 c d^{-1} or its alias 1.866 c d^{-1}. These two frequencies do not correspond to the main frequency found in the HIPPARCOS data and account for less than 2% of the radial velocity variations. Our much more extensive dataset of 280 spectra provides a better view of the line-profile variations and allows to find multiperiodicity. We refer to Chapter 7 for a detailed spectroscopic analysis of the star.

HD 182255

The H_{p}-measurements of HD 182255 have a large standard deviation of 0.0192 mag. Three frequencies are clearly present in these data: $f_1 = 0.79220$ c d^{-1}, $f_2 = 0.97191$ c d^{-1} and $f_3 = 0.47233$ c d^{-1}, with an amplitude of 0.0173 mag, 0.0155 mag and 0.0065 mag respectively. The three frequencies together reduce the standard deviation to 0.0086 mag. Two additional candidate frequencies appeared after subsequent prewhitening. They occur in a less convincing way than the first three ones: $f_4 = 1.14708$ c d^{-1} with an amplitude of 0.0058 mag and $f_5 = 0.65933$ c d^{-1} with an amplitude of 0.0046 mag. The phase plots for the first three frequencies are shown in Fig. 6.9. After prewhitening with the five frequencies, we obtain a standard deviation of 0.007 mag.

Line-profile variations of this star were first reported by Hube & Aikman (1991), who observed "traveling bumps" in the Si II-doublet profiles and classify the star as a member of the 53 Persei class. Therefore, HD 182255 must be regarded as an already known, confirmed SPB before the present study. Its clear line-profile variations (Fig. 6.11) are easily seen thanks to the low projected rotation velocity. These variations are superposed on line shifts due to orbital motion. Indeed, HD 182255 is a member of a single-lined spectroscopic binary which has an orbital period of 367 d (Hube & Aikman 1991).
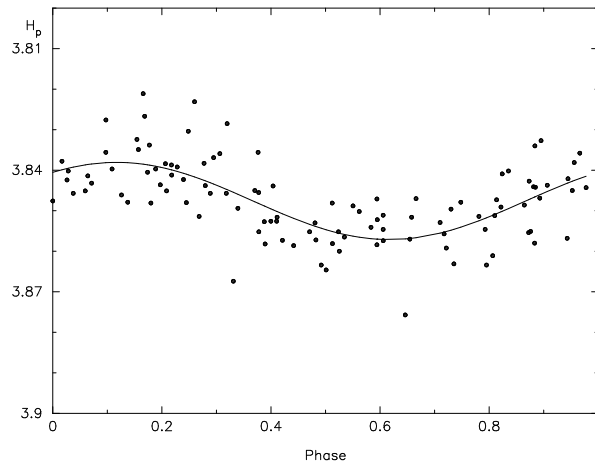
Figure 6.8: Phase diagram of the $H_{\rm p}$-data of HD 147394 for $f_1 = 0.80027$ c d^{-1}.

The frequency analysis after removal of the orbital motion, according to the orbital elements given in Hube & Aikman (1991), leads to the two frequencies f_1 and f_2. The amplitude of f_1 amounts to 3.5 km s^{-1} and the one of f_2 is around 2.1 km s^{-1}. The other frequencies are not significantly present in the spectroscopic data. The resulting phase diagram for f_1, free of the binary motion, is represented in the right panel of Fig. 6.7.

Hence, HD 182255 has a complex pulsational pattern with at least three, and possibly five, non-radial g-modes. Since there are many modes excited in this SPB, our current spectroscopic data are unfortunately not numerous enough to perform detailed modelling of the modes.

HD 206540

The standard deviation of the HIPPARCOS dataset of HD 206540 is 0.0132 mag. The search for a main frequency results in two competing candidate aliases: $f_1 = 0.65359$ c d^{-1} and $f_1' = 0.76237$ c d^{-1}. One cannot prefer one above the other on the basis of the reduction in standard deviation, amplitude or phase diagram (Top panels of Fig. 6.10). The HIPPARCOS team reports a frequency of 0.69 c d^{-1}, which is close to the average of the two candidates. This star has a complex variability pattern in the space photometry, with at least three frequencies, but it is not possible to derive one unique most likely solution because several combinations of three periods lead to fits of the same quality.

Line-profile variations are well seen for this star (Fig. 6.12) with its low projected rotation velocity. The HIPPARCOS catalogue frequency 0.694 c d^{-1} is not present in our periodograms of the radial velocity dataset either. Our spectroscopic data are too limited to perform an independent frequency search. A comparison between sine-fits for f_1 and f_1' leads to the conclusion that f_1' is the dominant frequency in the radial-velocity variations.
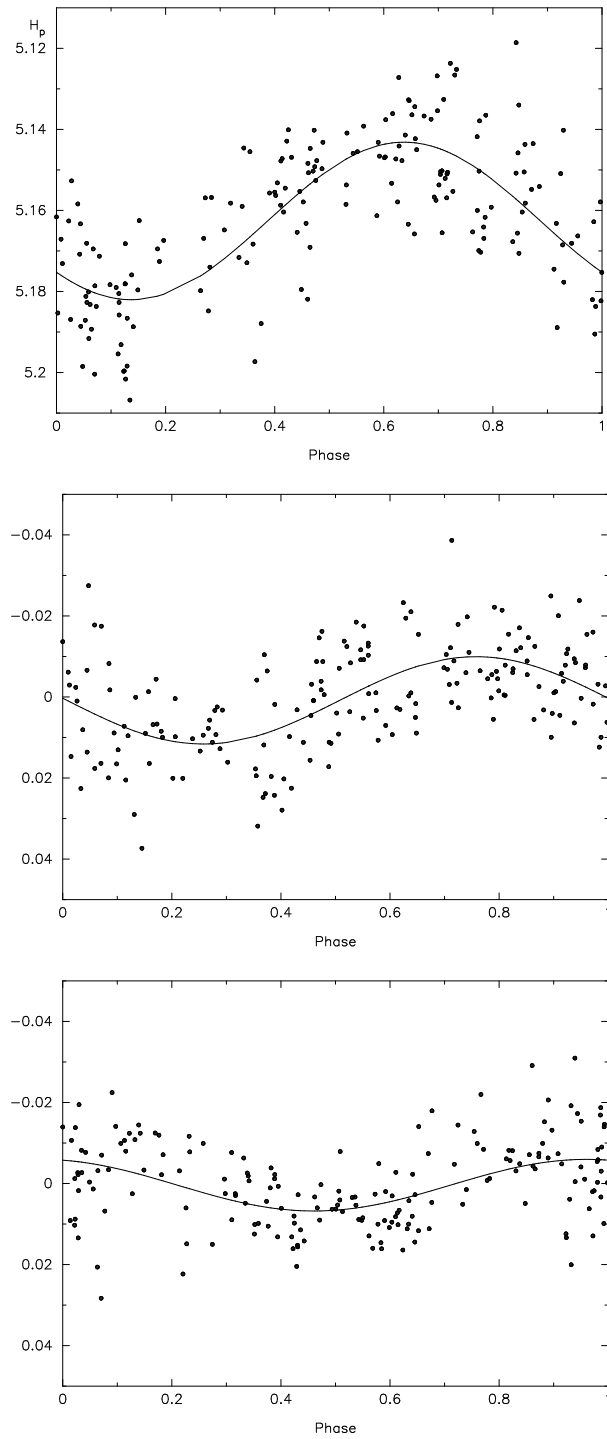
Figure 6.9: Phase diagrams of the H_{p}-data of HD 182255. The different panels display the data after subsequent prewhitening stages. From top to bottom: $f_1 = 0.79220$ c d^{-1}, $f_2 = 0.97191$ c d^{-1}, $f_3 = 0.47233$ c d^{-1}.
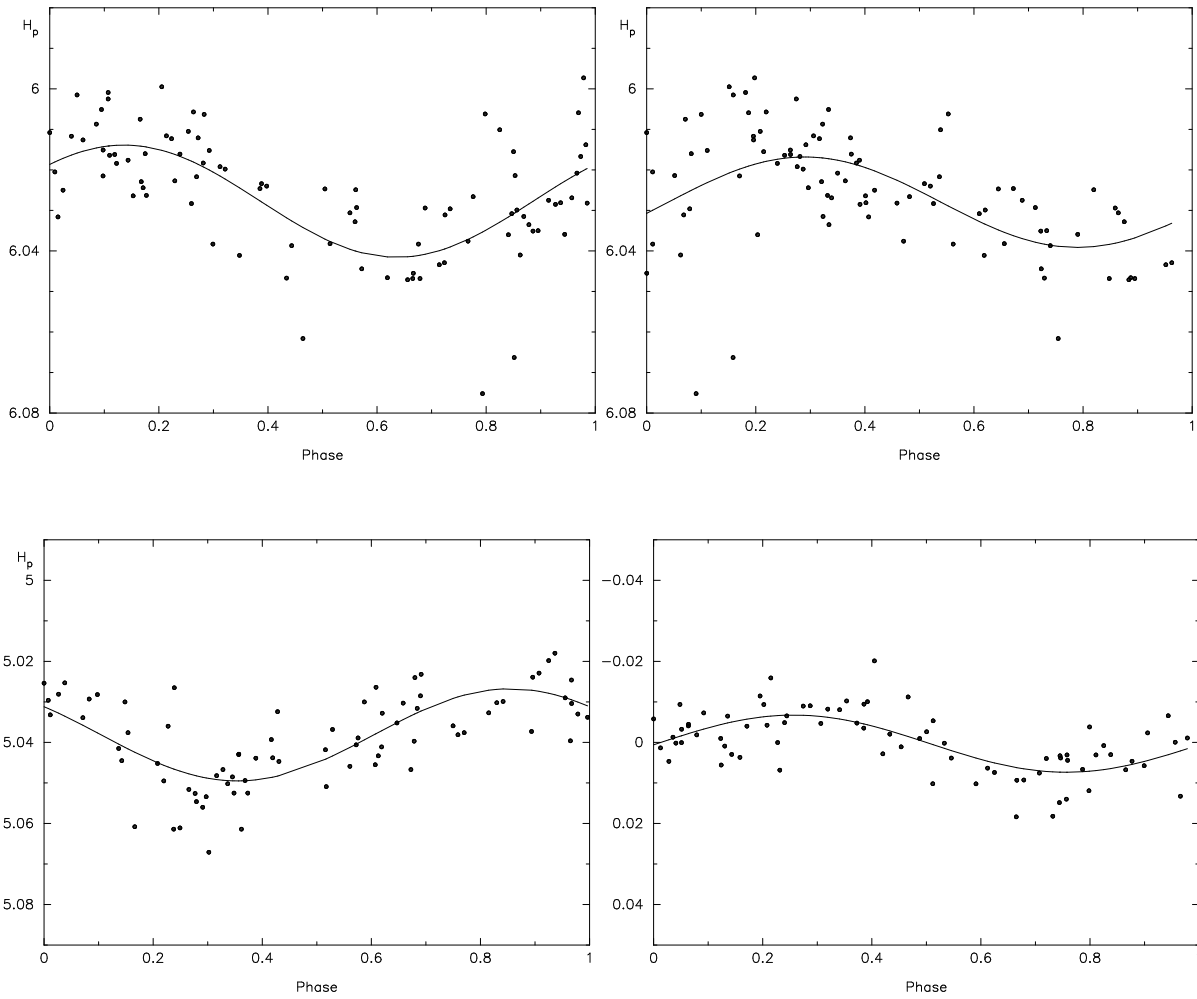
Figure 6.10: Top: phase diagrams of the $H_{\rm p}$-data of HD 206540 for $f_1 = 0.6536$ c d^{-1} (left) and for $f_1' = 0.7624$ c d^{-1} (right). Bottom: phase diagrams of the $H_{\rm p}$-data of HD 208057 for $f_1 = 0.80172$ c d^{-1} (left) and of the residuals for $f_2 = 0.89045$ c d^{-1} (right).
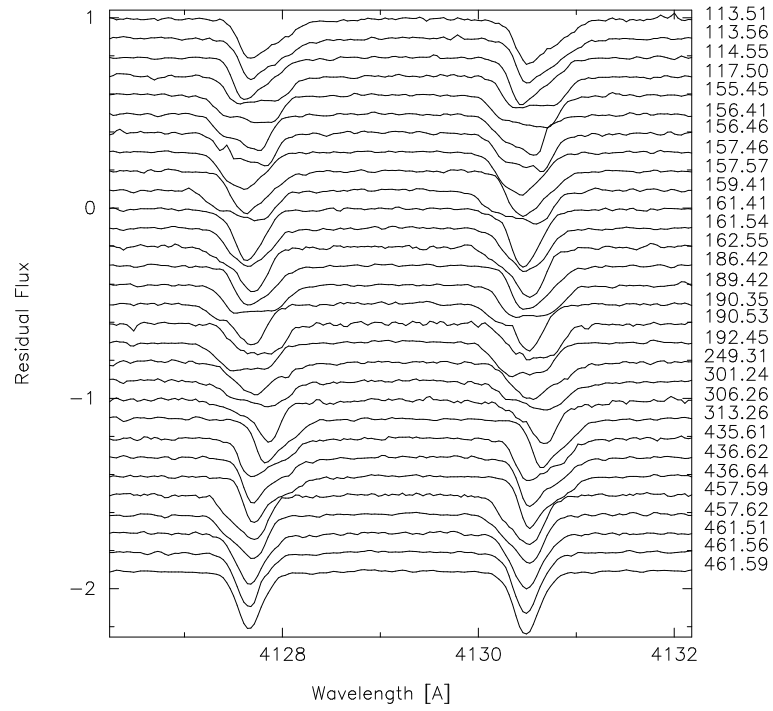
Figure 6.11: Same as Fig. 6.5, but for the star HD 182255.
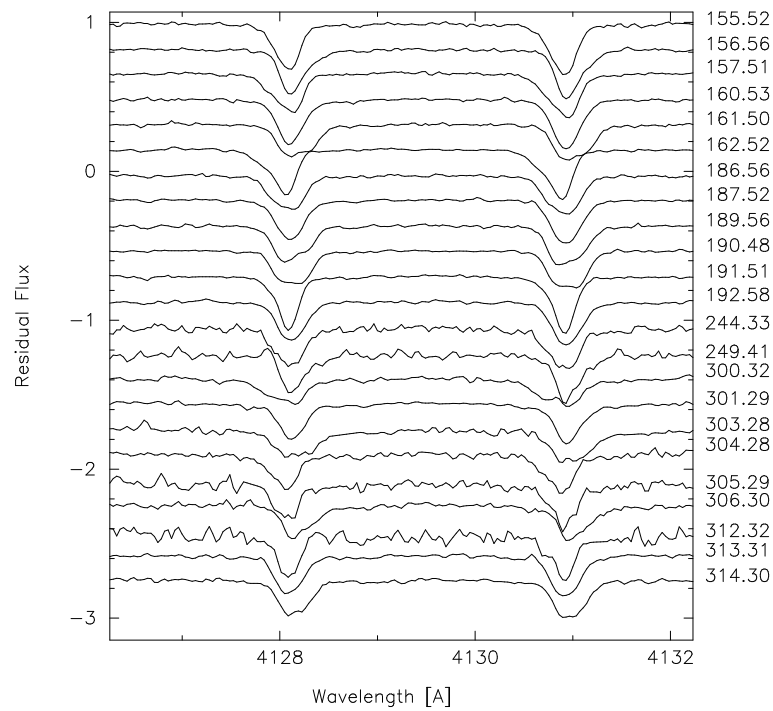
Figure 6.12: Same as Fig. 6.5, but for the star HD 206540.

HD 208057

Two frequencies emerge clearly from the period search in the H_{p}-data: $f_1 = 0.80172$ c d^{-1} with an amplitude of 0.0097 mag and $f_2 = 0.89045$ c d^{-1} with an amplitude of 0.0079 mag. They reduce the standard deviation from 0.0114 mag to 0.0058 mag (Bottom panels of Fig. 6.10). After subsequent prewhitening we find additional evidence of another frequency, but we cannot choose between the three candidates around 0.5844, 0.9406 and 1.4403 c d^{-1}.

This SPB has very broad lines due to the high projected rotation velocity. Therefore, line-profile variations, although present, are not easily seen. A frequency search on the radial-velocity datasets reveals a long period around 25 d, which might point towards binarity. In the range of SPB-like periods, no clear peak is present. Therefore we imposed the two frequencies found in the space photometry. Both are present in the variations, the "dominant" one being f_2. The peak-to-peak amplitude is around 13 km s^{-1}. This, together with the observation that the average velocity changes from one observing season to another, allows to suspect that the variability in the radial velocity is not caused by pulsations alone. We therefore tentatively propose that HD 208057 is a long-period spectroscopic binary, although this star has no known companion (Abt & Cardona 1984).

6.3   Summary

From this study, we conclude the following. All stars, except HD 28114, show evidence of multiperiodicity, confirming their pulsational nature. HD 28114 should be still considered as an SPB candidate since Adelman & Philip (1996) found abundances for this star to be compatible with values for normal main-sequence stars of similar temperatures. Note that all other targets have never been mentioned as CP stars. Each star shows line-profile variations with periods of the order of days. Except for HD 1976 and HD 208057, the main photometric frequency is also the main spectroscopic frequency, which means that these stars have a dominant low-degree mode. We note that additional spectroscopic observations are needed before concluding that, for both exceptions, the observed photometric variability is mainly due to a low-degree mode while the observed spectroscopic variability is dominated by a high-degree mode. Indeed, both stars are rapid rotators, for which the determination of the velocity curve is difficult and they are members or suspected members of binary systems. In Table 6.4, a summary of the outcome of the frequency analysis is given together with the values of the pulsation constant Q_{p} computed from the frequencies found in the photometry. Finally, we point out that we have sufficient spectra for only one star, HD 147394, to find multiperiodic signals in the line profiles and use these to undertake a mode identification, which is done in Chapter 7.

Table 6.4: Summary of the HIPPARCOS data used and of the results of the frequency analyses for 8 northern SPBs (for the results on HD 138764 and HD 140873 we refer to De Cat 2001). T stands for the total time span in days and N for the number of data points. σ denotes the original standard deviation of the data, σ_N the standard deviation due to the errors of the measurements, and σ_{res} the standard deviation of the residuals after prewhitening with all the listed frequencies f_{p}. All standard deviations are expressed in magnitudes. Successively are then given the accepted frequencies in the photometric (f_{p}) and spectroscopic (f_{s}) data [c d^{-1}], and the pulsation constant Q_{p} [d] computed from the photometric frequencies.

HD	T	N	σ	σ_N	σ_{res}	f_{p}	f_{s}	Q_{p}
1976	1173	188	0.0106	0.0055	0.0062	0.93914	0.39934	0.38
						0.39934		0.89
21071	905	85	0.0175	0.0060	0.0059	1.18843	1.18843	0.52
						1.14942		0.54
25558	766	90	0.0142	0.0045	0.0057	0.65284	0.65284	0.69
						0.7318?		0.61
						1.9298?		0.23
28114	919	56	0.0132	0.0065	0.0076	0.79104	0.79104	0.42
147394	1192	116	0.0095	0.0036	0.0059	0.80027	0.80027	0.44
							0.7813	
182255	1040	204	0.0192	0.0054	0.0086	0.79220	0.79220	0.67
						0.97191	0.97191	0.55
						0.47233		1.13
						1.14708?		0.46
						0.65933?		0.81
206540	1084	98	0.0132	0.0063	0.0076	0.65359	0.76237	0.63
						0.76237		0.54
208057	1113	88	0.0114	0.0047	0.0058	0.80172	0.89045	0.48
						0.89045		0.43

All eight target stars are currently being monitored in Geneva photometry with the Mercator telescope at La Palma, Spain. This photometric monitoring will continue during several years and will allow us to derive much more complete frequency spectra of the lowest degree modes in the forthcoming years.

Chapter 7

The SPB star HD 147394

7.1   Introduction

This chapter is devoted to the analysis of HD 147394. It is the SPB for which most high-resolution spectra are available thus far. We performed a frequency analysis on these data, followed by a mode identification from the line-profile variations. The plan of the chapter is the following. In Sect. 7.2 we give a description of our data and we derive some physical parameters of HD 147394. The results of the frequency analysis from derived quantities based upon the spectroscopic observations are described in Sect. 7.3. In Sect. 7.4 we identify the modes of HD 147394 by means of our new version of the moment method (Chapter 5). As this is one of the first spectroscopic mode identifications ever done for an SPB, we compare our identification results with theoretical pulsation models as a compatibility check in Sect. 7.5. Finally, we give a summary in Sect. 7.6.

7.2   Data and physical parameters

We selected HD 147394 among the many SPBs discovered from the HIPPARCOS mission (Waelkens et al. 1998) so that we have at our disposal HIPPARCOS photometry, which clearly reveals the frequency 0.80027 c d^{-1} (Mathias et al. 2001, Sect. 6.2). We note that this dataset shows evidence of multiperiodicity but a value for a second frequency is not clear.

Line-profile variations have already been reported by Masuda & Hirata (2000), who gathered 30 spectra in 5 nights. We have a much more extensive dataset which consists in 250 useful spectra obtained with the spectrograph Aurélie at OHP during 6 separate weeks of monitoring spread over 460 days. The number of observations and the ranges of

Table 7.1: Observing logbook of our spectroscopy of HD 147394.

Number of observations	JD 2450850 +	
	Start	End
47	1	6
14	113	117
14	155	162
13	186	192
117	431	437
45	457	461

their Julian Dates are given in Table 7.1. The spectral domain is limited and was chosen in order to get the Si II-doublet with lines at $\lambda\lambda\,4128, 4130$ Å. The signal-to-noise ratio is about 200. For a complete description of the observations and data reductions we refer to Mathias et al. (2001). Fig. 7.1 represents several of the observed line-profile variations.

We also have a few Geneva data points at our disposal of the star from which we derive the stellar parameters, as the spectra have only very small spectral coverage. The effective temperature and the gravity of HD 147394 are obtained by means of the photometric calibration by Künzli et al. (1997) to the mean magnitudes in the Geneva filters. The distance, derived from the parallax measured by HIPPARCOS, and the average visual magnitude, give the absolute visual magnitude. Taking into account the bolometric correction (BC), which is calculated by means of Flower's relation (1996) between T_{eff} and BC, one obtains the bolometric magnitude and the luminosity. With the values for the effective temperature and the luminosity one estimates the mass, e.g. by using the evolutionary tracks published by Schaller et al. (1992). We also calculated the radius. The results are the following:

$$\begin{cases} \log T_{\text{eff}} = 4.17 \pm 0.01, \\ \log g = 4.00 \pm 0.15, \\ \log L/L_\odot = 2.80 \pm 0.15, \\ M = 5.0 \pm 0.5 \ M_\odot, \\ R = 3.7 \pm 0.8 \ R_\odot. \end{cases}$$

Because we have only a few Geneva data, we checked our result with those available in the literature and derived from spectroscopic data. In Smith (1997), we found $\log T_{\text{eff}} = 4.18$ and $\log g = 3.93$, which is in agreement with our estimates based on the Geneva photometry. Smith & Dworetsky (1993) have found the star to have solar iron abundance ($\log \text{N(Fe)} = 7.65 \pm 0.15$).
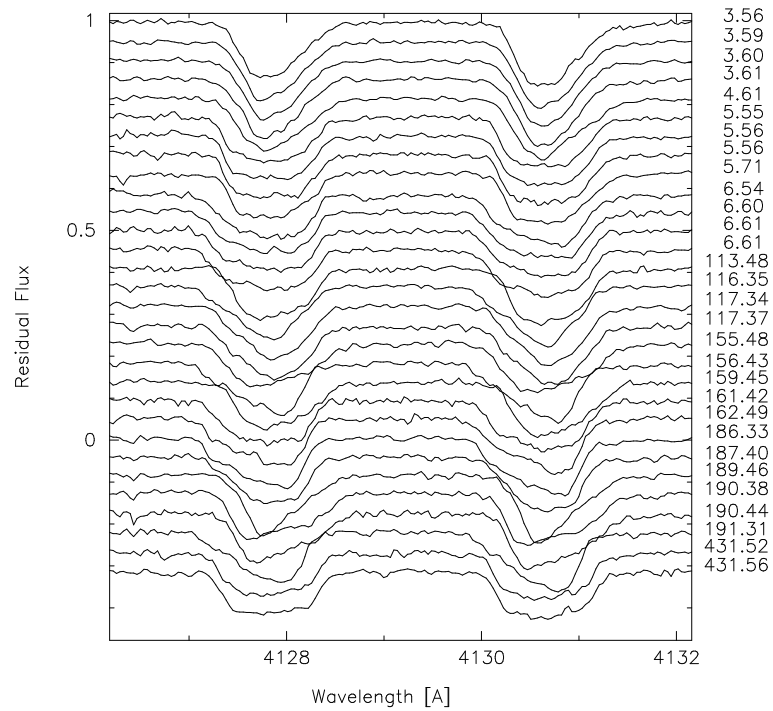
Figure 7.1: Line-profile variations of the Si II 4128-4130 Å doublet. Observation dates are indicated on the right of the panel (+2450850 JD).
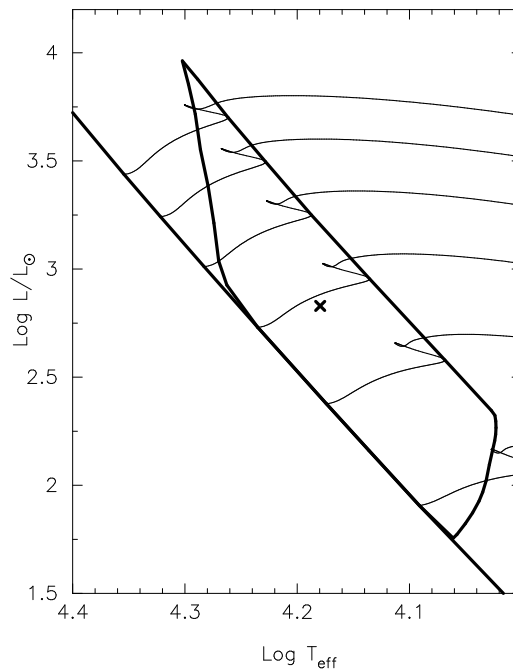
Figure 7.2: Position of HD 147394 in the HR diagram. The theoretical SPB instability strip is calculated by Pamyatnykh (1999). The star is situated on the evolutionary track published by Schaller et al. (1992) corresponding to some 5 $M_\odot$.

The position of this B 5 IV star in the theoretical HR diagram falls in the centre of the SPB instability strip (see Fig. 7.2).

7.3   Frequency analysis

We extracted the measurements of the doublet Si II centered at $\lambda\lambda\, 4128, 4130$ Å. From these spectral lines we computed the first three velocity moments $<v>$, $<v^2>$ and $<v^3>$ with the aim of performing a frequency analysis. We used the PDM method (Stellingwerf 1978), Scargle method (Scargle 1981) and the CLEAN method (Roberts et al. 1987). We tested frequencies from 0 to 3 cycles per day (c d^{-1}) with a frequency step of 0.0001 c d^{-1}. The error estimate of our determined frequencies is between 0.0001 c d^{-1} and 0.001 c d^{-1}. We obtained the same results with the three methods and for both Si lines.

In $<v>$, $<v^2>$ and $<v^3>$, we found the frequency $f_1 = 0.8008$ c d^{-1}, which corresponds to the frequency found in the HIPPARCOS data. After prewhitening of the data with this dominant frequency, we obtained a second frequency clearly present in $<v>$ and $<v^3>$, which is $f_2 = 0.7813$ c d^{-1}. These two frequencies reduce the standard deviation of the first moment by 50%. Note that a fit for $1 + f_2$ is slightly less good. f_1 and $1 + f_2$ reduce the standard deviation by 48%. A fit with f_1 and $1 + f_2$ leads to a smaller amplitude for the second mode compared to a fit with f_1 and f_2: 1.70 km s^{-1} for $1 + f_2$ instead of 2.05 km s^{-1} for f_2. We then kept f_2 for the second frequency. Scargle periodograms are shown in Fig. 7.3 and phase diagrams of the first moment for the Si II 4130 Å line are shown in Fig. 7.4.

After prewhitening of the data with f_1 and f_2, the residuals show evidence of a third frequency. Two frequencies are apparent: $f_3 = 0.7175$ c d^{-1} or $f_3' = 0.6710$ c d^{-1}. The first one (f_3) occurs after prewhitening with f_1 and f_2 (see third panel of Fig. 7.3) while the second one (f_3') is the highest peak if we prewhiten with slightly different values for f_1 and f_2 (e.g. 0.8006 c d^{-1} and 0.7814 c d^{-1}) within the error estimate. Together with f_1 and f_2, they reduce respectively 61% and 59% of the standard deviation in the first moment. Phase diagrams of the radial velocity, prewhitened with f_1 and f_2, for $f_3 = 0.7175$ c d^{-1} and for $f_3' = 0.6710$ c d^{-1} are shown in Fig. 7.4. We note that f_3 reduces the standard deviation slightly better than f_3'. The difference between both candidate frequencies is 0.0465 c d^{-1}, which corresponds to about three weeks. We also notice that the time span between two missions of observations is about three weeks or about a multiple of three weeks except between the second and third missions. This indicates that the frequencies may be aliases. We computed the window function for frequencies between 0.0001 c d^{-1} and 10 c d^{-1} with a step of 0.0001 c d^{-1}. The 15 highest peaks of this function are listed in Table 7.2. The 14-th peak is exactly 0.0465 c d^{-1}. One also remarks that only four frequencies of the list are independent. We conclude that f_3 and f_3' are aliases due to the time sampling. We also note that additional aliases of f_3 and f_3' cannot be excluded (see
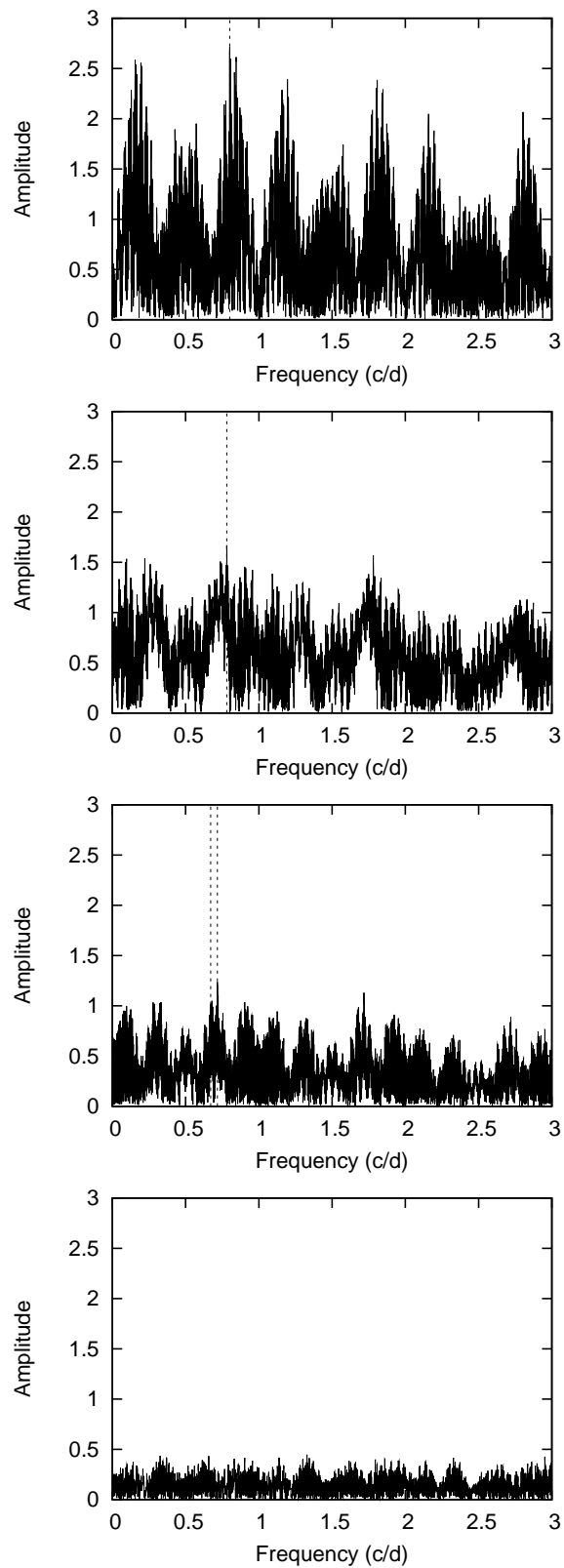
Figure 7.3: From top to bottom: Scargle periodograms of the radial velocity derived from the Si II 4130 Å line, of this data prewhitened with f_1, of this data prewhitened with f_1 and f_2, of this data prewhitened with f_1, f_2 and f_3. The $4\,S/N$ level is situated at 0.74 km s^{-1} in the third panel.
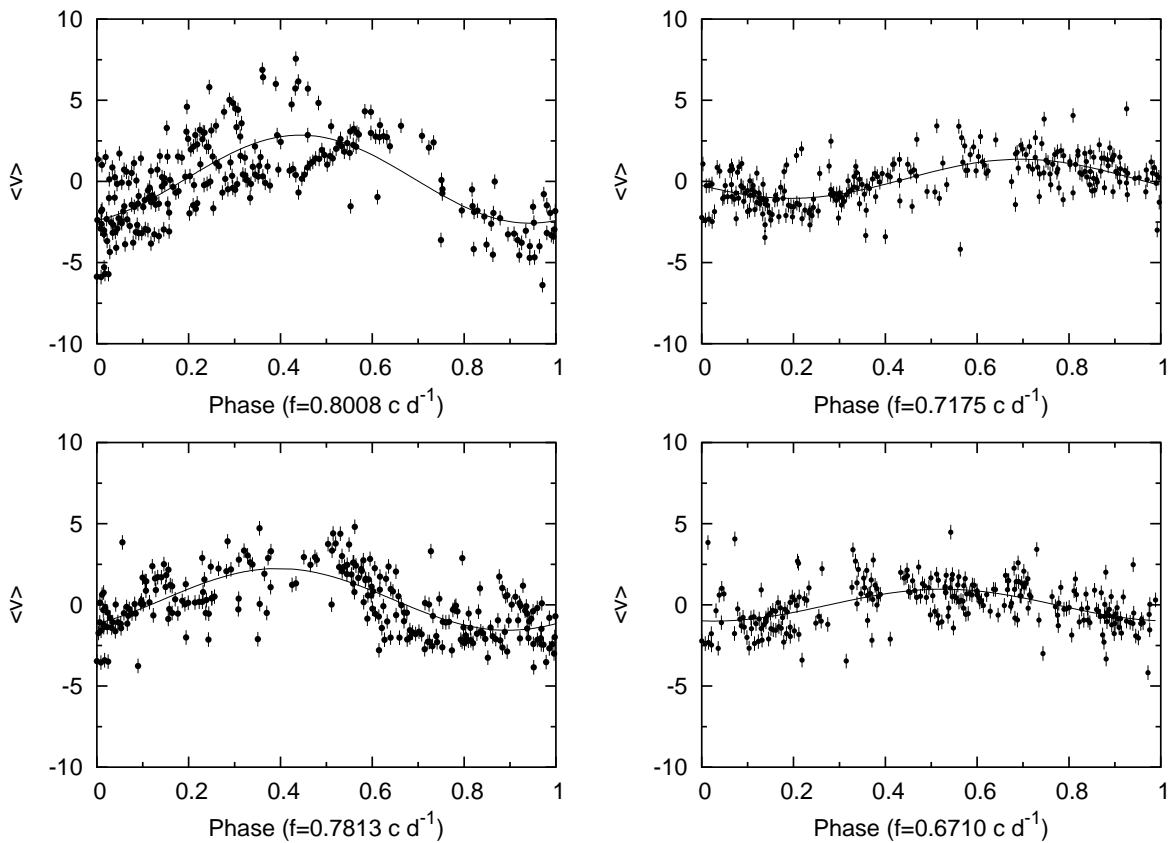
Figure 7.4: Left: upper panel: phase diagram of the radial velocity computed from the Si II 4130 Å line for $f_1 = 0.8008$ c d^{-1}. Lower panel: phase diagram of the data prewhitened with f_1 for $f_2 = 0.7813$ c d^{-1}. Right: upper panel: phase diagram of the radial velocity computed from the Si II 4130 Å line, prewhitened with f_1 and f_2, for $f_3 = 0.7175$ c d^{-1}. Lower panel: phase diagram of the data prewhitened with f_1 and f_2, for $f_3' = 0.6710$ c d^{-1}.

Table 7.2: Highest peaks in the window function (expressed in c d^{-1}).

p1	1.0001	p9	0.0024
p2	1.0026	p10	1.0070
p3	0.0068	p11	0.0397
p4	0.9957	p12	0.9629
p5	0.0440	p13	0.9561
p6	0.0372	p14	0.0465
p7	1.0398	p15	2.0027
p8	0.0044		

third panel of Fig. 7.3). In the following, we continue to work with f_3 and f_3', just to see if our results for the two main modes f_1 and f_2 are influenced by using different values for the frequency of the third mode.

In order to determine the significance of both aliases, we considered the 4 S/N criterion introduced by Breger et al. (1993). We refer to Sect. 4.1.3 for a definition of the noise level. In Fig. 7.3 we show the Scargle periodogram. As the 4 S/N level is 0.74 km s^{-1}, both aliases must be retained based on this criterion.

The amplitudes and phases of the least-squares sine fits to the observed first moment for the combinations f_1, f_2, f_3 and f_1, f_2, f_3' are listed in Table 7.3.

7.4   Mode identification with the moment method

A mode identification was performed by means of our new version of the moment method (Chapter 5). Because of the alias problem for the third mode, we identified modes simultaneously for both the combination f_1, f_2 and f_3 and the combination f_1, f_2 and f_3' in order to check the consistency of the results. Moreover, for both cases, we performed one identification by using the non-rotating formalism and one identification by using Lee & Saio's formalism (1987, 1990).

To compute the theoretical moments, we took a linear limb-darkening coefficient u of 0.36 (see e.g. Wade & Rucinski 1985). To identify the modes, we covered the parameter space by varying the free parameters in the following way: the projected rotational velocity v_Ω from 1 to 35 km s^{-1} with a step 1 km s^{-1}, the inclination of the star i from 5° to 90° with a step 5°, the line-profile width from 1 to 20 km s^{-1} with a step 1 km s^{-1}. We used the K-value given by $K = GM/\sigma^2 R^3$, where M is the mass, R the radius and σ the angular pulsation frequency. For each tested (ℓ, m, i), the velocity amplitude A_p was chosen so that the theoretical amplitudes of the first moment are equal to the observed ones (see Table 7.3).

Table 7.3: Amplitudes and phases of the least-squares sine fits to the observed first moment computed from the Si II 4130 Å line, together with their standard errors for f_1, f_2 and f_3, for f_1, f_2 and f_3'.

	Amplitude (km s^{-1})	Phase (degrees)
f_1	3.28 ± 0.11	109 ± 2
f_2	2.05 ± 0.11	136 ± 2
f_3	1.37 ± 0.11	60 ± 5
f_1	3.07 ± 0.12	108 ± 2
f_2	1.84 ± 0.12	135 ± 3
f_3'	1.07 ± 0.11	152 ± 6

The results of the mode identification by means of the non-rotating formalism using f_1, f_2 and f_3 and using f_1, f_2 and f_3' are given in respectively the upper and lower part of Table 7.4. We used $K_1 = 11$, $K_2 = 12$, $K_3 = 14$ and $K_3' = 16$. We first of all find that the discriminating function Σ has lower values for the combination f_1, f_2, f_3, giving slight preference for that combination. A clear conclusion is that none of the three modes is axisymmetric. One can conclude that the choice of the frequency for the third mode does not influence the idenfication of the second mode, for which we systematically find $(\ell_2, m_2) = (3, -1)$ or $(2, -1)$. The most likely identification for f_1 is $(\ell_1, m_1) = (1, 1)$, although $(3, -2)$ and $(2, -2)$ also occur among the best possibilities. The second solution may then point towards components of a multiplet, as f_1, f_2 are close frequencies. One also remarks that, even if it is difficult to determine the third mode, both identifications do not differ very much.

We then performed a mode identification by means of Lee & Saio's formalism. The K-values were computed using the co-rotating angular frequency related to the observed one by $\sigma_c = \sigma_{\mathrm{obs}} + m\Omega$, where Ω is the angular frequency of rotation. We checked each time if the K-values remain sufficiently low in order to obtain physically relevant velocity values, i.e. we eliminate too large K-values. For computation time reasons, we tested v_Ω from 5 to 35 km s^{-1} with a step 5 km s^{-1}. The results using f_1, f_2 and f_3 and using f_1, f_2 and f_3' are given in respectively the upper and lower part of Table 7.5. The identifications for the first and second modes are confirmed and do not change compared to those derived with the neglect of the effect of rotation.

We find systematically a projected rotational velocity above 9 km s^{-1}. Assuming that the rotation frequency equals $f_1 - f_2 = 0.0195$ c d^{-1} leads to an equatorial rotation velocity of only 3.7 km s^{-1}. This excludes the possibility that f_1 and f_2 correspond to subsequent components of one multiplet.

Table 7.4: The ten best solutions of the mode identification by means of the non-rotating formalism through the discriminant Σ, using the Si II 4130 Å line. A_p is the amplitude of the radial part of the pulsation velocity, expressed in $\mathrm{km\,s^{-1}}$; $v_{\mathrm{r,max}}$ and $v_{\mathrm{t,max}}$ are respectively the maximum radial and tangential surface velocity due to the three modes, expressed in $\mathrm{km\,s^{-1}}$; i is the inclination angle; v_Ω is the projected rotational velocity, expressed in $\mathrm{km\,s^{-1}}$ and σ is the intrinsic line-profile width, also expressed in $\mathrm{km\,s^{-1}}$. The second-but-last column contains the solution that occurs at position 20. The upper and lower part of the table correspond respectively to an identification for f_1, f_2, f_3 and for f_1, f_2, f_3'.

(ℓ_1,m_1)	(1,1)	(3,−2)	(1,1)	(3,−2)	(1,1)	(3,−2)	(1,1)	(1,1)	(2,−2)	(2,−2)	…	(3,−2)	…
(ℓ_2,m_2)	(3,−1)	(3,−1)	(3,−1)	(3,−1)	(3,−1)	(3,−1)	(2,−1)	(2,−1)	(2,−1)	(2,−1)	…	(3,−1)	…
(ℓ_3,m_3)	(1,1)	(3,−2)	(2,−2)	(1,1)	(2,−1)	(2,−2)	(3,−1)	(1,1)	(1,1)	(3,−1)	…	(5,4)	…
A_p^1	1.94	1.29	1.94	1.29	1.94	1.29	1.60	1.60	0.91	0.91	…	1.29	…
A_p^2	1.78	1.78	1.78	1.78	1.78	1.78	3.12	3.12	3.12	3.12	…	1.78	…
A_p^3	0.66	0.43	0.46	0.66	0.32	0.46	0.55	0.54	0.54	0.55	…	2.22	…
$v_{\mathrm{r,max}}$	1.29	0.61	1.17	0.67	1.21	0.63	0.73	0.72	0.28	0.26	…	0.61	…
$v_{\mathrm{t,max}}$	7.28	17.37	8.84	13.83	4.75	14.6	28.7	29.1	29.5	29.1	…	51.40	…
i	55	55	55	55	55	55	85	85	85	85	…	55	…
v_Ω	23	12	25	11	19	11	35	35	35	35	…	12	…
σ	17	19	16	19	18	19	11	11	11	11	…	7	…
Σ	5.95	5.97	5.97	5.99	6.03	6.04	6.04	6.04	6.07	6.07	…	6.14	…

(ℓ_1,m_1)	(1,1)	(1,1)	(1,1)	(2,−2)	(2,−2)	(2,−2)	(3,−3)	(1,1)	(1,1)	(2,−2)	…	(2,−2)	…
(ℓ_2,m_2)	(3,−1)	(3,−1)	(3,−1)	(3,−1)	(3,−1)	(3,−1)	(3,−1)	(3,−1)	(2,−1)	(3,−1)	…	(3,−1)	…
(ℓ_3',m_3')	(2,−2)	(2,−1)	(1,1)	(2,−2)	(1,1)	(2,−1)	(5,−3)	(1,0)	(5,3)	(5,−3)	…	(2,0)	…
A_p^1	1.82	1.59	1.59	0.96	0.96	0.96	1.20	1.82	1.50	0.86	…	0.96	…
A_p^2	1.59	2.16	2.16	2.16	2.16	2.16	1.00	1.59	2.80	0.88	…	2.16	…
$A_p'^3$	0.31	0.32	0.40	0.23	0.40	0.32	2.39	0.46	1.80	1.80	…	0.39	…
$v_{\mathrm{r,max}}$	0.99	1.22	1.35	0.29	0.52	0.39	0.78	1.12	0.27	0.65	…	0.50	…
$v_{\mathrm{t,max}}$	5.44	4.23	4.55	4.53	4.48	3.58	29.0	3.62	33.1	26.4	…	4.50	…
i	55	70	70	70	70	70	80	55	85	85	…	70	…
v_Ω	20	27	27	27	31	27	9	20	29	20	…	27	…
σ	18	15	15	15	13	15	3	18	3	12	…	15	…
Σ	6.08	6.09	6.10	6.10	6.12	6.12	6.13	6.13	6.14	6.14	…	6.17	…

Table 7.5: The ten best solutions of the mode identification by means of Lee & Saio's formalism through the discriminant Σ, using the Si II 4130 Å line. The meanings of the symbols are the same as in Table 7.4. The second-but-last column contains the solution that occurs at position 20. The upper and lower part correspond respectively to an identification for f_1, f_2, f_3 and for f_1, f_2, f_3'.

(ℓ_1,m_1)	(1,1)	(3−2)	(1,1)	(1,1)	(3,−2)	(2,−2)	(2,−2)	(2,−2)	(3,−2)	(3,−2)	…	(2,−1)	…
(ℓ_2,m_2)	(3,−1)	(3,−1)	(3,−1)	(3,−1)	(3,−1)	(3,−1)	(3,−1)	(3,−1)	(3,−1)	(3,−1)	…	(3,−1)	…
(ℓ_3,m_3)	(2,−2)	(1,1)	(1,1)	(2,−1)	(2,−2)	(1,1)	(2,−2)	(2,−1)	(3,−3)	(2,−1)	…	(2,−2)	…
A_p^1	2.20	0.93	2.20	2.20	0.93	0.44	0.44	0.44	0.76	0.93	…	0.42	…
A_p^2	1.11	1.47	1.11	1.11	1.47	0.74	0.74	0.74	1.29	1.47	…	0.36	…
A_p^3	0.21	0.72	0.76	0.22	0.33	0.80	0.12	0.17	0.28	0.27	…	0.07	…
$v_{\mathrm{r,max}}$	1.09	0.58	1.22	1.10	0.51	0.23	0.14	0.11	0.45	0.50	…	0.14	…
$v_{\mathrm{t,max}}$	9.22	14.86	6.42	4.93	15.91	12.68	16.88	11.53	21.48	16.43	…	12.36	…
K_1	8.47	16.33	8.47	8.47	16.33	43.54	43.54	43.54	20.04	16.33	…	23.60	…
K_2	17.32	14.32	17.32	17.32	14.32	21.37	21.37	21.37	15.71	14.32	…	25.34	…
K_3	35.16	11.99	10.22	21.29	21.30	8.81	68.44	26.90	40.78	17.26	…	137.01	…
i	55	55	55	55	55	55	55	55	55	55	…	50	…
v_Ω	20	10	20	20	10	30	30	30	15	10	…	35	…
σ	18	19	18	18	19	14	14	14	18	19	…	12	…
Σ	6.08	6.09	6.10	6.13	6.14	6.14	6.14	6.15	6.16	6.17	…	6.21	…
(ℓ_1,m_1)	(1,1)	(1,1)	(1,1)	(2,−2)	(2,−2)	(2,−2)	(1,1)	(3,−3)	(3,−1)	(3,−3)	…	(3−3)	…
(ℓ_2,m_2)	(3,−1)	(3,−1)	(3,−1)	(3,−1)	(3,−1)	(3,−1)	(3,−1)	(3,−2)	(2,−2)	(3,−2)	…	(3,−2)	…
(ℓ_3',m_3')	(2,−1)	(2,−2)	(2,1)	(1,0)	(2,−1)	(2,−2)	(1,0)	(2,−2)	(2,−2)	(3,−3)	…	(3,−1)	…
A_p^1	2.06	2.06	2.06	0.66	0.66	0.66	2.06	0.77	0.79	0.77	…	0.77	…
A_p^2	0.99	0.99	0.99	0.99	0.99	0.99	0.99	2.35	1.15	2.35	…	2.35	…
$A_p'^3$	0.14	0.13	0.28	0.46	0.14	0.13	0.46	0.16	0.45	0.17	…	0.32	…
$v_{\mathrm{r,max}}$	1.02	0.96	1.01	0.13	0.14	0.10	1.01	0.30	0.42	0.31	…	0.17	…
$v_{\mathrm{t,max}}$	3.07	5.70	5.66	8.18	8.09	12.35	3.34	40.11	29.30	40.31	…	39.32	…
K_1	8.47	8.47	8.47	25.15	25.15	25.15	8.47	17.93	15.24	17.93	…	17.93	…
K_2	17.32	17.32	17.32	17.32	17.32	17.32	17.32	16.16	22.77	16.16	…	16.16	…
K_3'	25.11	43.57	11.44	16.31	25.11	43.57	16.31	23.10	35.08	28.21	…	19.26	…
i	55	55	55	55	55	55	55	85	30	85	…	85	…
v_Ω	20	20	20	20	20	20	20	10	10	10	…	10	…
σ	18	18	18	18	18	18	18	17	20	17	…	17	…
Σ	6.25	6.26	6.27	6.27	6.27	6.27	6.28	6.29	6.29	6.29	…	6.32	…
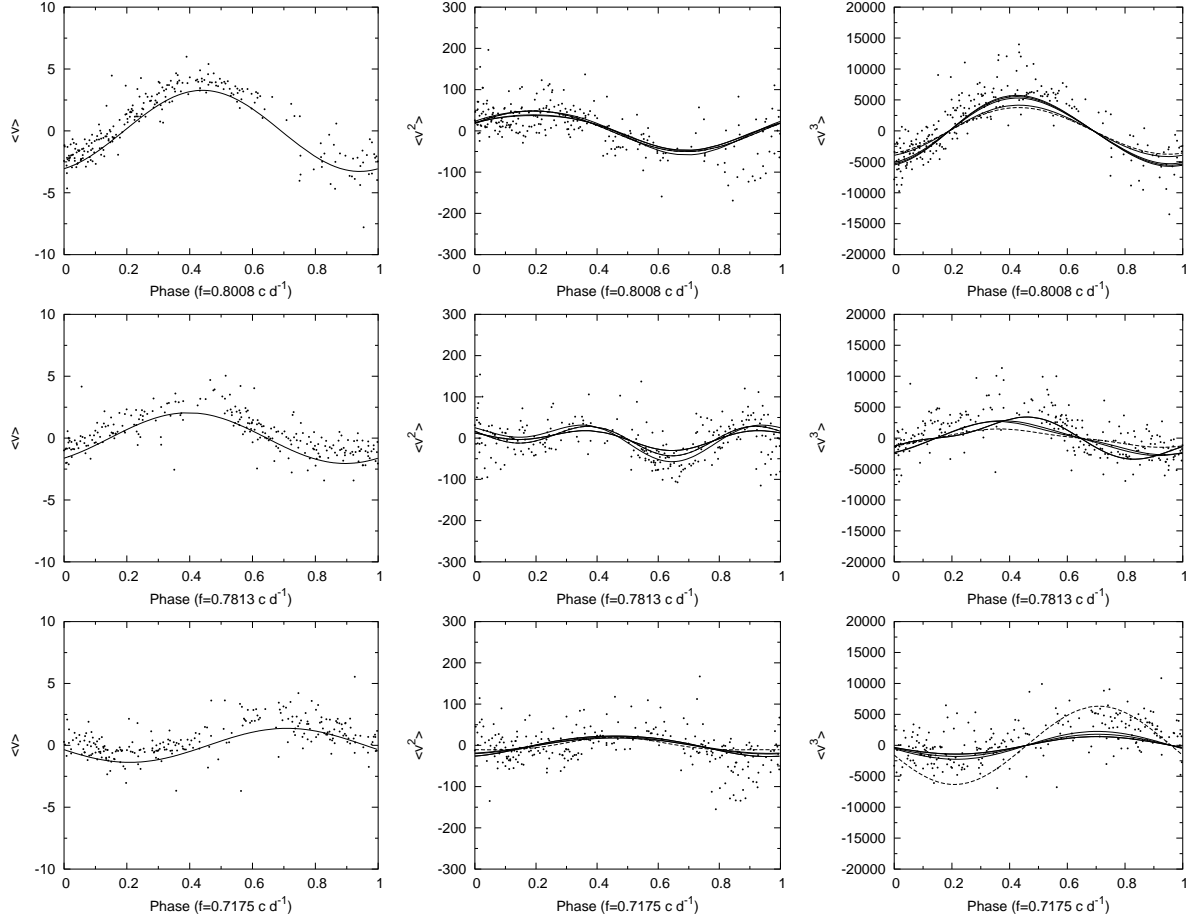
Figure 7.5: Comparisons between the observed first three moments (dots) to four of the best solutions (full lines) given in italic in Table 7.4. The dashed line represents the solution that occurs at position 20 in Table 7.4. Left: from top to bottom: phase diagram for f_1 of $< v >$ prewhitened with f_2 and f_3, phase diagram for f_2 of $< v >$ prewhitened with f_1 and f_3, phase diagram for f_3 of $< v >$ prewhitened with f_1 and f_2. Middle: from top to bottom: phase diagram for f_1 of $< v^2 >$ prewhitened with all frequencies except f_1 and $2f_1$, phase diagram for f_2 of $< v^2 >$ prewhitened with all frequencies except f_2 and $2f_2$, phase diagram for f_3 of $< v^2 >$ prewhitened with all frequencies except f_3 and $2f_3$. Right: from top to bottom: phase diagram for f_1 of $< v^3 >$ prewhitened with all frequencies except f_1, $2f_1$ and $3f_1$, phase diagram for f_2 of $< v^3 >$ prewhitened with all frequencies except f_2, $2f_2$ and $3f_2$, phase diagram for f_3 of $< v^3 >$ prewhitened with all frequencies except f_3, $2f_3$ and $3f_3$. Note that the errors on $< v >$, $< v^2 >$ and $< v^3 >$ are respectively given by 0.45 km s^{-1}, 20 (km s^{-1})^2 and 1000 (km s^{-1})^3.

Given that we cannot discriminate well between f_3, f_3' and other aliases due to bad time sampling, and that a biperiodic solution explains only about 50% of the standard deviation present in the first moment, we do not attempt line-profile fitting with the best candidate modes found in Table 7.4 for f_1 and f_2. Indeed, we cannot hope to discriminate between such fits in a meaningful way, as there is clearly still variability due to at least one, and probably even more, low-amplitude modes. Such modes are sort of filtered out in the moment variations but not in the line profiles themselves. For this reason, we have determined theoretical values for $< v >$, $< v^2 >$ and $< v^3 >$ for the best solutions listed in the upper panel of Table 7.4. For four of these solutions, we compare the moment values with the observed ones in Fig. 7.5. The four solutions are indicated in italic in Table 7.4. We point out that all first 15 best solutions result in very similar moment values and that we are unable to discriminate between the different possibilities for the mode identification. The only result that we can conclude upon with certainty is that we are dealing with non-axisymmetric $\ell \leq 3$ modes. Additional data with full coverage of the overall beat-period is needed to obtain unique mode identifications. A visual check shows that the (ℓ, m) combinations from position 16 onwards explain less well the observed moment variations. For comparison, we also list in Table 7.4, and show in Fig. 7.5, the solution that occurs on position 20. One can see from the dashed line in the lowest and rightmost panel of Fig. 7.5 that this solution leads to a too large amplitude for f_3 in the third moment. Moreover, its maximal tangential velocity is quite high. We conclude that we cannot discriminate between some 15-20 solutions from the discriminant. It will become possible to obtain unambiguous mode identifications for this star if we are able to detect a limited number of additional modes, by combining the results of the discriminant and of seismic models (see further below).

For all solutions $i \in [50°;85°]$, $v_\Omega \in [10;35]\,\mathrm{km\ s^{-1}}$. For the radius 3.7 $R_\odot$, this leads to a rotation period between 4.3 and 18.7 days.

7.5   Comparison with theoretical pulsation models

The mode identification for f_1 and f_2 is the first one derived from a spectroscopic time series for this SPB. Moreover, we find evidence for an $\ell = 3$ mode, which is seldom observed in pulsating stars. In order to check if such a solution is compatible with theoretical model predictions, we have determined evolutionary model sequences from the main sequence that pass the position of HD 147394 in the HR diagram (see Fig. 7.6) with the Code Liégeois d'Évolution Stellaire written by Dr. R. Scuflaire, assuming no convective overshooting. For each model with $4.15 \leq \log T_{\mathrm{eff}} \leq 4.19$ we have subsequently calculated the oscillation frequencies using a standard adiabatic code (Boury et al. 1975). For each evolutionary sequence, we have selected the models which give an *exact* fit for f_1 and f_2 according to the identification $(\ell_1, m_1) = (1, 1)$ and $(\ell_2, m_2) = (3, -1)$, taking into account the Ledoux rotational splitting constant and by varying the equatorial rotation velocity

M=5 M$_\odot$ X=0.7
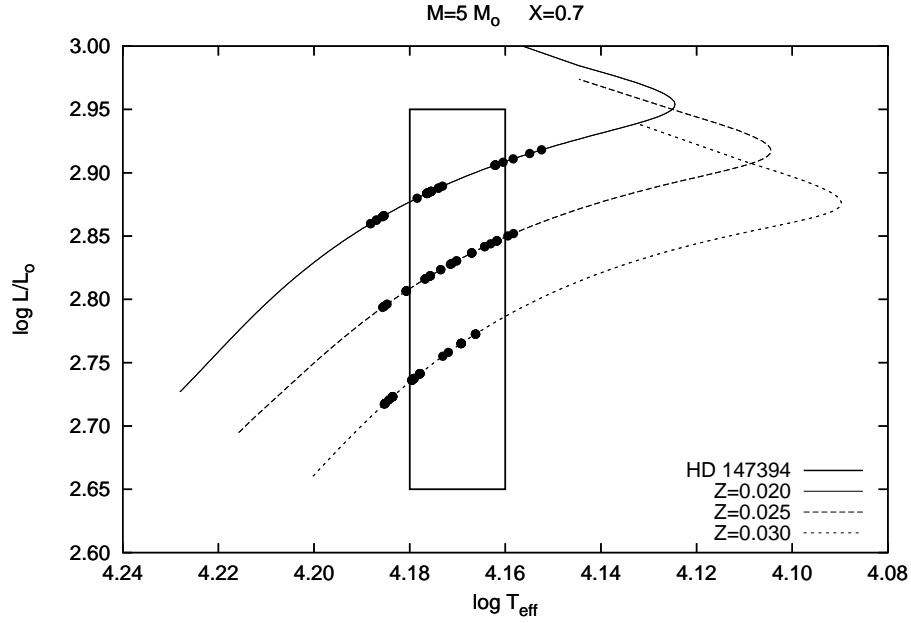
Figure 7.6: Evolutionary tracks of a 5 $M_\odot$ star without overshooting, with $X = 0.70$ and for different values of the metallicity Z, computed with CLES. The box delimits the position of HD 147394 in the HR diagram derived from photometry. Dots represent models that fit f_1 and f_2 according to the mode identification $(\ell_1, m_1) = (1, 1)$ and $(\ell_2, m_2) = (3, -1)$.
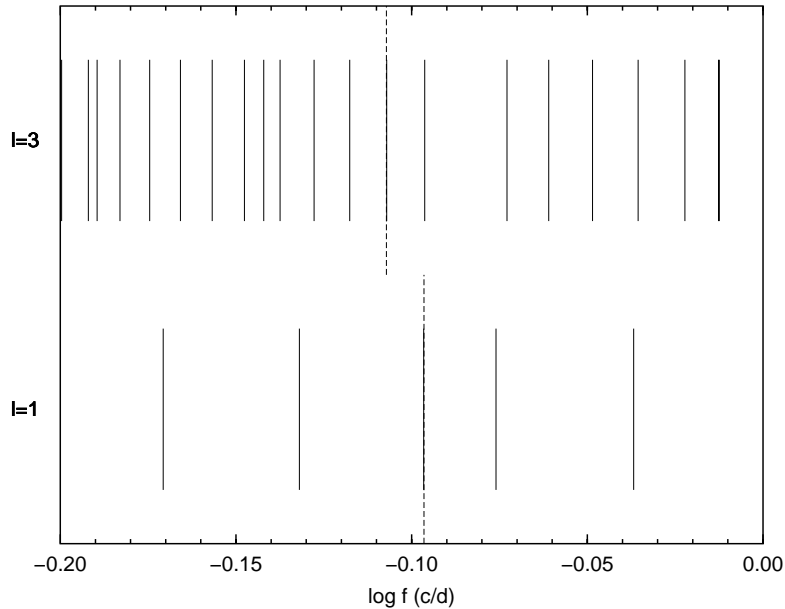
Figure 7.7: Theoretical frequencies for one of the models that fit observed frequencies (dashed lines). The $\ell = 2$ modes are not shown, but have a density in between the $\ell = 1$ and $\ell = 3$ modes.

in the range [10;50] km s^{-1} with a step of 0.1 km s^{-1}. Fig. 7.7 represents theoretical frequencies compared to observed ones for one of the *many* models that we found compatible with the observations. For this example, f_1 corresponds to the g_{12} mode and f_2 to the g_{40} mode. We note that, even with a constraint coming from mode identification, the sets of theoretical frequencies are quite dense, which makes it difficult to find one unique solution, especially as the rotation frequency is also a free parameter to a certain extent.

We have limited to the combination $(\ell_1, m_1) = (1, 1)$ and $(\ell_2, m_2) = (3, -1)$ for our compatibility check with the models. We stress, however, that other mode identifications would also lead to agreement with models of slightly different stellar parameters.

7.6   Summary

Our study of the slowly pulsating B star HD 147394 was based on 250 high-resolution high signal-to-noise spectra spread over 460 days. The moment variations of the Si II 4128-4130 Å doublet clearly reveal multiperiodicity with frequencies $f_1 = 0.8008$ c d^{-1}, $f_2 = 0.7813$ c d^{-1} and $f_3 = 0.7175$ c d^{-1} or its aliases due to the time sampling. We performed a mode identification by means of our new version of the moment method which identifies multiple modes simultaneously, leading to only one derived estimate for v_Ω, i and σ for each of the (ℓ, m) combinations. We did it by using the non-rotating formalism as well as the one derived by Lee & Saio (1987, 1990) for low-frequency g-mode pulsators. Both identifications lead to almost the same list of best candidate solutions whatever is the chosen value for the third frequency. The identification for the modes is not unique but we conclude that they are non-axisymmetric with $\ell \leq 3$. The rotation period of the star must be between 4 and 19 days.

It turns out that less than 20 combinations of (ℓ, m) are found to be equivalent by the discriminant for this SPB. It therefore should be possible to derive correct mode identifications from the discriminant and seismic modelling should we detect a small additional number of modes in the star.

Part III

Analyses of chemically peculiar B stars

The stars HD 131120 and HD 55522 were originally in the list of candidate SPBs discovered from the HIPPARCOS mission (Waelkens et al. 1998). Together with the supposedly Be star HD 105382 and the Bp star HD 138769, they showed line-profile variations similar to those of SPBs at first sight and hence were kept in photometric and spectroscopic observing runs led for the study of slowly pulsating B stars. In this part we show that these four stars are distinguishable from confirmed SPBs (De Cat 2001, Mathias et al. 2001) and we present the results of our line-profile modelling in terms of rotational modulation instead of stellar pulsation.

Chapter 8

The B 2.5 III star HD 131120

(part of this chapter was originally published as **Briquet M.**, **De Cat P.**, **Aerts C.**, **Scuflaire R.**, 2001, A&A 380, 177, *The B-type variable HD 131120 modelled by rotational modulation*)

8.1   Introduction

The star HD 131120 was classified as an SPB from the HIPPARCOS mission (Waelkens et al. 1998). However, this star shows peculiarities compared to confirmed SPBs (De Cat 2001). In Aerts et al. (1999) it is pointed out that only one frequency is found in the data of this star, while other SPBs are multiperiodic. Moreover, the first moment of the Si II 4128-4130 Å lines is non-sinusoidal: the first harmonic of the frequency found is necessary to obtain a good fit.

In this thesis we compare the observed photometric data and line-profile variations of HD 131120 with a non-radial pulsation (NRP) model and with a spot model in order to conclude on the best explanation for the origin of the periodic variability in the star. The chapter is organized as follows. In Sect. 8.2 the description of the data and some physical parameters are given. In Sect. 8.3 the result of the frequency analysis on the data is described. In Sect. 8.4 we attempt to perform a mode identification. We do this for the photometric data using the method of photometric amplitudes. For the spectroscopic data we use both the moment method and line-profile fitting. Then we try to model the variations with a rotational modulation model (Sect. 8.5). The outcome of the modelling of the variations of the star is discussed in Sect. 8.6.

8.2   Data and physical parameters

We have three datasets at our disposal: HIPPARCOS photometry, multicolour Geneva photometry and high-resolution spectroscopic data. The Geneva photometric observations were obtained with the Swiss telescope situated at La Silla in Chile, during several 3-weeks

Table 8.1: Observing log for Geneva photometry (upper) and spectroscopy (lower).

Number of observations	JD 2450000 +	
	Start	End
32	485	503
69	541	583
7	588	601
27	163	170
15	188	194
13	272	277
4	490	498
4	513	528
6	571	576
8	633	638

runs in the course of 1997. The spectroscopic data were obtained with the CAT/CES telescope of ESO in Chile, during 7 separate weeks of monitoring spread over 1996-1998. The spectral domain was [4115,4135] Å in order to get the Si II-doublet with lines at $\lambda\lambda\, 4128, 4130$ Å. The signal-to-noise ratio is about 400. The number of observations and the ranges of their Julian Dates are given in Table 8.1 for the Geneva photometry and the spectroscopy. For a complete description of the observations and data reductions we refer to Aerts et al. (1999) and De Cat (2001).

In Aerts et al. (1999) some physical parameters of the star are given. They are:

$$\begin{cases} \log T_{\mathrm{eff}} = 4.26 \pm 0.01, \\ \log g = 4.1 \pm 0.15, \\ \log L/L_\odot = 3.13 \pm 0.15, \\ M = 6.1 \pm 0.6 \; M_\odot, \\ R = 3.6 \pm 0.8 \; R_\odot. \end{cases}$$

de Geus et al. (1989) found similar values for the parameters of the star: $\log T_{\mathrm{eff}} = 4.27$, $\log g = 4.22$ and $\log L/L_\odot = 3$. In Borra et al. (1983) a photometric spectral type with observed UBV colors is given for the star, which is B 2.5. With these parameters, HD 131120 is situated in the upper part of the SPB instability domain, close to the β Cep instability domain (see e.g. Pamyatnykh 1999).

Table 8.2: Standard deviation of the Geneva data in the different filters and of the residuals after fitting with a sine for the frequency $f = 0.6374$ c d^{-1}.

Filter	Standard deviation	
	Data	Residuals
U	0.0151	0.0091
B$_1$	0.0120	0.0072
B	0.0106	0.0065
B$_2$	0.0111	0.0073
V$_1$	0.0090	0.0058
V	0.0091	0.0055
G	0.0096	0.0059

8.3　Frequency analysis

The frequency analysis on the three datasets was performed using the PDM method (Stellingwerf 1978) and the CLEAN method (Roberts et al. 1987). We refer to Chapter 4 for a description of these methods. We tested frequencies from 0 to 3 cycles per day (c d^{-1}) with a frequency step of 0.0001 c d^{-1} and we searched for multiple periods by prewhitening.

The frequency of 0.6374 c d^{-1} is found in the HIPPARCOS photometry. The same frequency is obtained from the Geneva data in the 7 filters. In Table 8.2 the standard deviation of the data in the different filters is given as well as the one of the residuals after fitting with a sine. A phase diagram for the U-filter is shown in Fig. 8.1. This frequency reduces the standard deviation in the U filter by 40%. An additional frequency cannot be found either in the HIPPARCOS data or in the Geneva data.

From the doublet Si II centered at $\lambda\lambda\, 4128, 4130$ Å we computed the first moment and performed a frequency analysis. We again obtained the frequency 0.6374 c d^{-1}. A sine fit to the first moment for this frequency explains 67% of the standard deviation and a slightly better fit leading to a reduction in standard deviation of 69% is obtained with its first harmonic included (see upper panel of Fig. 8.2). No other frequency can be found in the data and it is clear that this star is monoperiodic.

8.4　Non-radial pulsation model

In order to confront the observations with a NRP model we have to make a mode identification. To this end we used the method of photometric amplitudes, the moment method
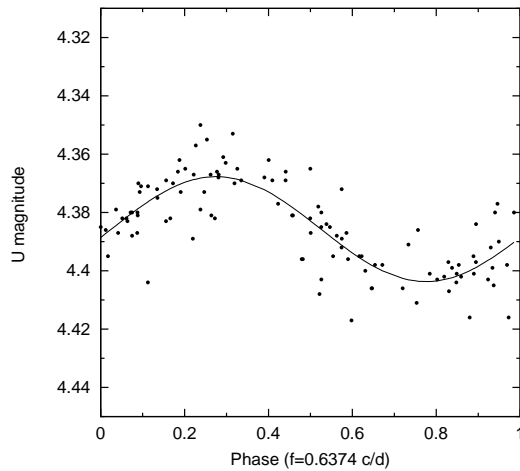
Figure 8.1: Phase diagram of the U-magnitude data (dots) and the best sinusoidal fit (full line) for the indicated frequency.

and the line-profile fitting technique. In this section, the photometric method is briefly described. For a full description, we refer to Heynderickx et al. (1994). For spectroscopic methods, we refer to Part I of this thesis.

8.4.1   The Geneva photometric data

The method of photometric amplitudes as described by Watson (1988) allows us to derive the degree ℓ of the pulsation mode from multicolour photometry by comparing the observed amplitudes at some wavelengths (i.e. those of the central wavelengths of the passbands of the used photometric system) with the theoretical amplitudes calculated for several values of ℓ and a free parameter S taking into account non-adiabatics effects ($S \in$ [0;1], 0: fully non-adiabatic, 1: adiabatic). As the theoretical amplitudes are proportional to an unknown wavelength-independent function, ratios of the amplitudes are considered in order to eliminate this function. In Table 8.3 we give the amplitudes obtained with a sine fit for the separate Geneva filters, together with the amplitude ratios with respect to the U-filter. We refer to Heynderickx et al. (1994) for a full description of the method we used in this work. In general the mode identification by this method is successful for β Cep stars (see e.g. Heynderickx et al. 1994) and SPBs (De Cat 2001). We adopt here the formalism and notation introduced by De Cat (2001). For HD 131120 we tested ℓ from 0 to 7 and we choose the degree ℓ using a discriminant $\eta_\ell(S)$. This discriminant is the square root of the sum of squares of the differences between the observed and theoretical amplitude ratios divided by 7. For each ℓ we determine the value of S for which the discriminant $\eta_\ell(S)$ is minimal. Then we choose the mode for which the discriminant attains the lowest value. The minima of the discriminant η_ℓ are given in the left columns of Table 8.4. The best solutions are $\ell = 1$, 2, 4 and 6. They all have very similar values for the discriminant and so are equivalent in quality. Moreover the derived amplitude

Table 8.3: Amplitudes of the least-squares sine fits to the Geneva data in the different filters, computed together with their standard errors using the SAS-software package. Ratios of the amplitudes with respect to the U-filter are also listed.

Filter	Amplitude	Ratio
U	0.0183 ± 0.0013	1
B_1	0.0145 ± 0.0010	0.792 ± 0.077
B	0.0125 ± 0.0009	0.685 ± 0.069
B_2	0.0123 ± 0.0010	0.672 ± 0.072
V_1	0.0103 ± 0.0008	0.566 ± 0.060
V	0.0109 ± 0.0008	0.599 ± 0.058
G	0.0111 ± 0.0008	0.608 ± 0.061

ratios have a large uncertainty (see Table 8.3). This observational uncertainty is larger than the difference between the competing pulsational models. We then conclude that the photometric data do not allow us to determine the degree ℓ, should the star be oscillating.

8.4.2   The spectroscopic data

8.4.2.1   Mode identification by the moment method

We calculated the first three observed moments of a line profile $< v >$, $< v^2 >$ and $< v^3 >$ (Chapter 5). For the first moment we only found the frequency $f = 0.6374$ c d^{-1}. The linear pulsation theory predicts that $< v^2 >$ varies with both f and $2f$ while $< v^3 >$ varies with f, $2f$ and $3f$. In order to compare the frequencies found in the observed moments to the theoretical predictions we performed a frequency analysis on the observed moments. In the second moment, it was not possible to determine a frequency and in the third moment we found only the frequency $f = 0.6374$ c d^{-1}. A phase diagram for the frequency $f = 0.6374$ c d^{-1} for $< v >$, $< v^2 >$ and $< v^3 >$ is shown in Fig. 8.2. It is clear that the second moment does not vary with f nor with $2f$. Such a situation does not correspond to linear pulsation theory as described above. We also computed the moment of order zero, which is the equivalent width of the line. The same frequency of 0.6374 c d^{-1} is present in it and a phase diagram is shown in Fig. 8.3. We point out that the relative EW variation is about 10%. Such a large value is not encountered for confirmed SPBs (see De Cat 2001).

To perform a mode identification, we used the 1996 version of the moment method for which the discriminant is a function of the differences between the observed and theoretically calculated amplitudes of the first three moments (Aerts 1996). For each set
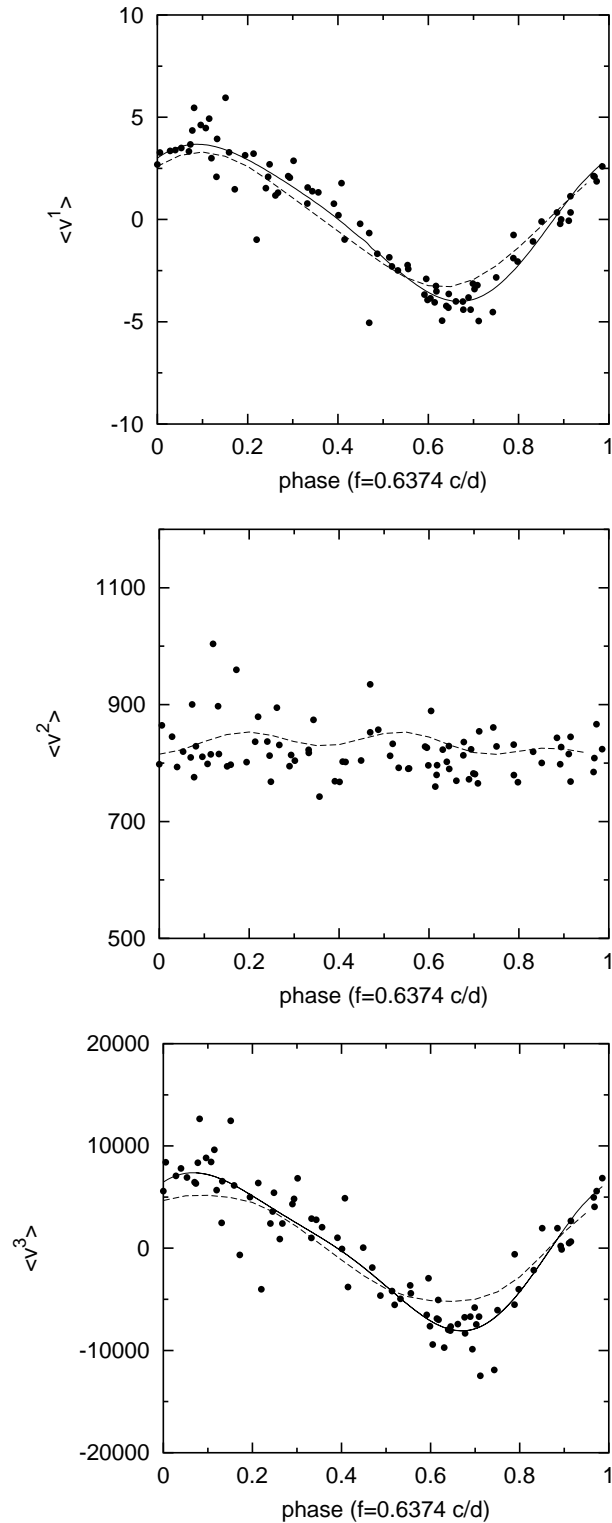
Figure 8.2: Phase diagrams of the first three moments of the Si II 4128 Å line. We show the observed values (dots), the fit using 0.6374 c d^{-1} and its first harmonic (solid line), and the moments of the best spot model (dashed line).

Figure 8.3: Phase diagram of the observed equivalent width of the Si II 4128 Å line (dots), which is expressed in Å. The equivalent width of the best spot model is represented by the dashed line.

Table 8.4: Left: the different minima of the discriminant η_ℓ of the method of photometric amplitudes together with the most likely value of the free parameter S taking into account non-adiabatic effects. Right: the different minima of the discriminant Γ_ℓ^m of the moment method for the Si II 4128 Å line for the best solutions. v_p is the amplitude of the radial part of the pulsation velocity, expressed in km s^{-1}; i is the inclination angle; v_Ω is the projected rotational velocity, expressed in km s^{-1} and σ is the intrinsic line-profile width, also expressed in km s^{-1}.

ℓ	η_ℓ	S	ℓ	m	Γ_ℓ^m	v_p	i	v_Ω	σ
1	0.025	0.09	3	0	0.30	0.2	63°	57	5
4	0.034	0.14	3	± 1	0.31	0.2	33°	57	3
2	0.038	1.00	1	0	0.34	0.5	76°	41	20
6	0.068	0.07	1	± 1	0.38	0.8	11°	57	2
5	0.133	1.00	3	± 2	0.39	0.3	73°	44	17
7	0.135	1.00	2	0	0.43	0.4	68°	48	15
3	0.172	1.00	2	± 2	0.46	0.2	31°	53	12
			⋮	⋮	⋮	⋮	⋮	⋮	⋮

of wavenumbers (ℓ, m) we determine the values of v_p, i, v_Ω and σ for which the discriminant $\Gamma_\ell^m(v_p, i, v_\Omega, \sigma)$ is minimal. Then we chose the mode for which the discriminant attains the lowest value.

The outcome of the mode identification with the discriminant is listed in the right columns of Table 8.4 for the best solutions in parameter space. We tested ℓ from 0 to 6. The other velocity parameters were varied in the interval $[0.1; 2]$ km s^{-1} with a step 0.1 km s^{-1} for the amplitude of the radial part of the pulsation velocity v_p, $[1°; 90°]$ with a step $1°$ for the inclination angle i, $[40; 70]$ km s^{-1} with a step 1 km s^{-1} for the projected rotational velocity v_Ω and $[1; 20]$ km s^{-1} with a step 1 km s^{-1} for the intrinsic line-profile width σ. The more probable mode is $(\ell, m) = (3, 0)$. However, there are other candidates of almost equal probability, as can be seen in Table 8.4.

Unfortunately no confidence intervals for the minima of the discriminant and the corresponding velocity parameters v_p, i, v_Ω and σ can be determined. Consequently we generated theoretical line-profile variations for the modes for which the discriminant attains the lowest value (see Table 8.4) in order to choose the mode which gives the best fit compared to the observed line-profile variations. We found that the smallest standard deviation in the intensity averaged over all profiles Σ has about the same value for the most likely modes listed in Table 8.4, which is 0.004 and we are then again not able to determine the most likely mode from the discriminant.

8.4.2.2   Mode identification by line-profile fitting

For a comparison between observed line-profile variations with theoretically calculated ones, we used Townsend's (1997) code, BRUCE. We refer to Chapter 3 for a description of the modelling of the line-profile variations.

We search for the parameters for which the calculated profiles best fit the observed profiles by considering a large grid of possible wavenumbers and parameters. In order to keep the computation time feasible we averaged out all the observed profiles in phase bins of 0.05 of the variability cycle and worked with these 20 averaged observed profiles. They are shown as dotted lines in Fig. 8.4. The observed profiles are compared to the theoretical profiles and to their orthogonal symmetric profiles in order not to favour a sense of rotation. As a measure of the goodness of fit we use the standard deviation Σ in the intensity averaged over all profiles. The most likely mode and parameters are those that minimize Σ.

First we consider only the velocity perturbation and we cover the parameter space by varying the free parameters in the following way: ℓ from 0 to 6, the projected rotational velocity v_Ω from 30 to 60 km s^{-1} with a step 5 km s^{-1}, the angle of inclination between the rotation axis and the line of sight i from $10°$ to $90°$ with a step $10°$, the amplitude of the radial part of the pulsation velocity A_p from 2 to 20 km s^{-1} with a step 2 km s^{-1} (A_p from 0.5 to 1.5 km s^{-1} with a step 0.5 km s^{-1} for modes with $m = 0$), the intrinsic

NRP
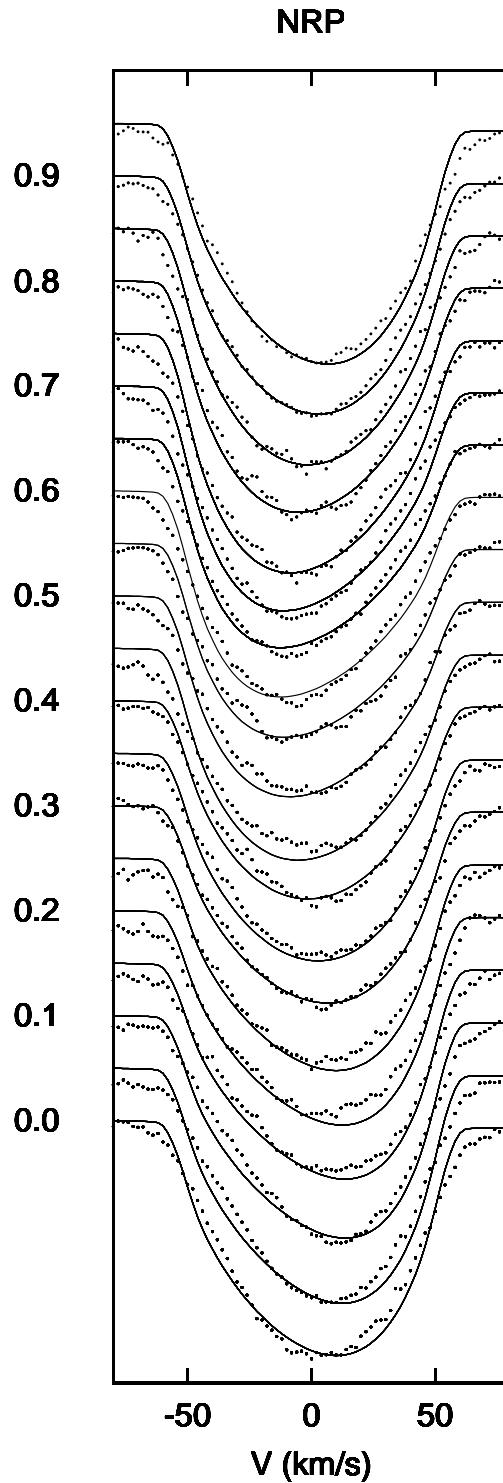
Figure 8.4: Observed line profiles of the Si II 4128 Å line (dots) averaged over phase bins of 0.05 and theoretical line profiles (full lines) for the NRP model with $(\ell, m) = (2, 0)$. The theoretical profiles were adjusted to have the same equivalent width as the observed profiles.

line-profile width σ from 2.5 to 20 km s^{-1} with a step 2.5 km s^{-1}, the initial phase of the mode from 0 to 0.95 period with a step 0.05 period. Then we consider adiabatic temperature variations and used theoretical intrinsic profiles kindly provided by Dr. T. Rivinius. These are constructed using the atmospheric codes ATLAS 9 and BHT (Baschek-Holweger-Traving, see Gummersbach et al. 1998) and fixing the microturbulence at 2 km s^{-1}. Finally we consider non-adiabatic temperature effects by introducing two extra parameters which are the non-adiabatic temperature perturbation scaling factor ΔT and the non-adiabatic temperature perturbation phase shift ψ_T. We take ΔT from 0.2 to 1 with a step 0.2 and ψ_T from 0° to 360° with a step 45°.

The parameters that give the smallest Σ are:

$$\begin{cases} \ell = 2, \\ m = 0, \\ v_\Omega = 55 \text{ km s}^{-1}, \\ i = 90°, \\ A_p = 0.5 \text{ km s}^{-1}, \\ \Delta T = 0.2, \\ \psi_T = 180°, \\ K = 24, \\ \Sigma = 0.0040 \text{ continuum units.} \end{cases}$$

We note that the amplitude of light variability corresponding to this solution is about 0.02 mag, which is compatible with the observed one. The fit for these parameters is shown in Fig. 8.4. This solution leads to the same line-profile variations as the solution without the inclusion of temperature effects and is not able to reproduce the large observed equivalent width variation. The theoretical profiles were adjusted to have the same equivalent width as the observed profiles. We note that these profiles for $(\ell, m) = (2, 0)$ are not very different from those corresponding with the other (ℓ, m) combinations listed in Table 8.4. All NRP solutions lead more or less to the same value of Σ. Thus we have shown that the pulsation hypothesis does not agree well with the data.

8.5 Rotational modulation model

8.5.1 A Bp star

We searched the literature for chemical inhomogeneities in this star. Hiltner et al. (1969) indeed classified HD 131120 as a Bp star and reported spectral peculiarities similar to those found in 3 Sco and HD 144334. These latter stars appear to be He-weak Si stars (see Garrison 1967 and Norris 1971). The average equivalent width of the He I 4121 Å line measured in our data is about 68.9 mÅ. By comparing this value with the ones for normal B 2.5 stars in Didelon (1982), we can confirm that HD 131120 is a He-weak star. We note that, in SIMBAD, we find a MK spectral type of B 7, which is misleading as it

relies on He line strengths. The average equivalent width of the Si II 4128 Å line is about 95.7 mÅ which is quite normal for a B 2.5 star.

The chemically peculiar Bp stars show monoperiodic variations. Whenever light and line-profile variations are present, the same frequency is found in both datasets. The observed periods range from 1 to 20 days in the majority of cases. The periods show an inverse correlation with the projected rotational velocity. All these characteristics indicate that the variations of Bp stars are due to rotational modulation. Moreover, up to now, the variability of He-weak stars is explained by the rotation of the star in the presence of a non-homogeneous distribution of helium on the stellar surface.

8.5.2 Model with two spots

We compared the line-profile observations of HD 131120 with a rotational modulation model by using a code kindly put at our disposal by Dr. L. Balona (Chapter 3). We took the equatorial and polar radii $R_e = R_p = 3.6\ R_\odot$, the equatorial and polar fluxes $F_e = F_p = 1$ and the linear limb-darkening coefficient $u = 0.36$.

As HD 131120 appears to be a He-weak star, it was important to test the rotational modulation model also on the He I 4121 Å line. First we computed the first three moments of this line. The frequency search again leads to $f_1 = 0.6375$ c d^{-1} and $f_2 = 2f_1 = 1.275$ c d^{-1} for $< v >$ and $< v^3 >$. No frequency can be found for $< v^2 >$. The frequency f_1 and its first harmonic f_2 reduce the standard deviation by 53% for $< v >$ and by about 37% for $< v^3 >$. A phase diagram for the frequency $f_1 = 0.6375$ c d^{-1} for $< v >$, $< v^2 >$ and $< v^3 >$ is shown in Fig. 8.5. Fig. 8.6 shows that the EW also varies with the same frequency. The relative EW variation of the He I line is about 16%.

We point out that the first moment of the Si II 4128 Å line and of the He I 4121 Å line do not have the same form. This observation is an additional strong argument against a NRP model. Morever, they are not in phase. This is not compatible with a NRP model.

Such variations can be reproduced by a spot model if the difference of longitude between a spot of Si and a spot of He is 180°. They can also appear if for one spot silicon is overabundant and helium is underabundant or silicon is underabundant and helium is overabundant.

A non-sinusoidal first moment with f and $2f$ can be obtained if we consider two spots of the same element, which have a longitude difference of 180°. Two spots give 13 free parameters to fit the line profiles, which leads to an enormous computational time. In order to reproduce the form of the first moment, we decided to test the following cases:

$$\begin{cases} \lambda_1 = \lambda_2 + 180°, \\ \beta_1 = \beta_2\ , \\ \gamma_1 = \gamma_2, \\ F_1 \neq F_2, \\ \sigma_{s1} = \sigma_{s2}, \end{cases}$$

and

$$\begin{cases} \lambda_1 = \lambda_2 + 180°, \\ \beta_1 = \beta_2 \ , \\ \gamma_1 \neq \gamma_2, \\ F_1 = F_2, \\ \sigma_{s1} = \sigma_{s2}, \end{cases}$$

where the indices 1 and 2 are respectively for the first spot and the second spot. We refer to Chapter 3 for the meanings of the symbols. We compared such a spot model to both the He line and the Si line. We again determine the parameters for which the theoretical profiles best fit the observations by minimizing the standard deviation Σ in the intensity over all profiles as done for the fitting with BRUCE. Then the parameters were varied around the best set of parameters in order to refine the solution.

For the He line, the following parameters lead to a good fit, as we can see in Fig. 8.7:

$$\begin{cases} \lambda_1 = 90°, \ \ \lambda_2 = 280°, \\ \beta_1 = 50°, \ \ \beta_2 = 80°, \\ \gamma_1 = 60°, \ \ \gamma_2 = 60°, \\ F_1 = 0.35, \ \ F_2 = 0.4, \\ v_\Omega = 54 \text{ km s}^{-1}, \\ i = 30°, \\ \sigma_i = 12 \text{ km s}^{-1}, \\ \sigma_s = 12 \text{ km s}^{-1}, \\ \Sigma = 0.0022 \text{ continuum units.} \end{cases}$$

In Fig. 8.5 the first three moments of the theoretical profiles shown in Fig. 8.7 are compared to the ones of the observed profiles of He. In Fig. 8.6 the variation of the theoretical EW is compared to the observed EW variation. It results that the behaviour of the observed moments is well reproduced by the theoretical moments.

For the Si line, we also obtain a good fitting with these parameters (see Fig. 8.7):

$$\begin{cases} \lambda_1 = 310°, \ \ \lambda_2 = 130°, \\ \beta_1 = 70°, \ \ \beta_2 = 70°, \\ \gamma_1 = 80°, \ \ \gamma_2 = 80°, \\ F_1 = 1.4, \ \ F_2 = 1.9, \\ v_\Omega = 54 \text{ km s}^{-1}, \\ i = 30°, \\ \sigma_i = 12 \text{ km s}^{-1}, \\ \sigma_s = 12 \text{ km s}^{-1}, \\ \Sigma = 0.0026 \text{ continuum units.} \end{cases}$$
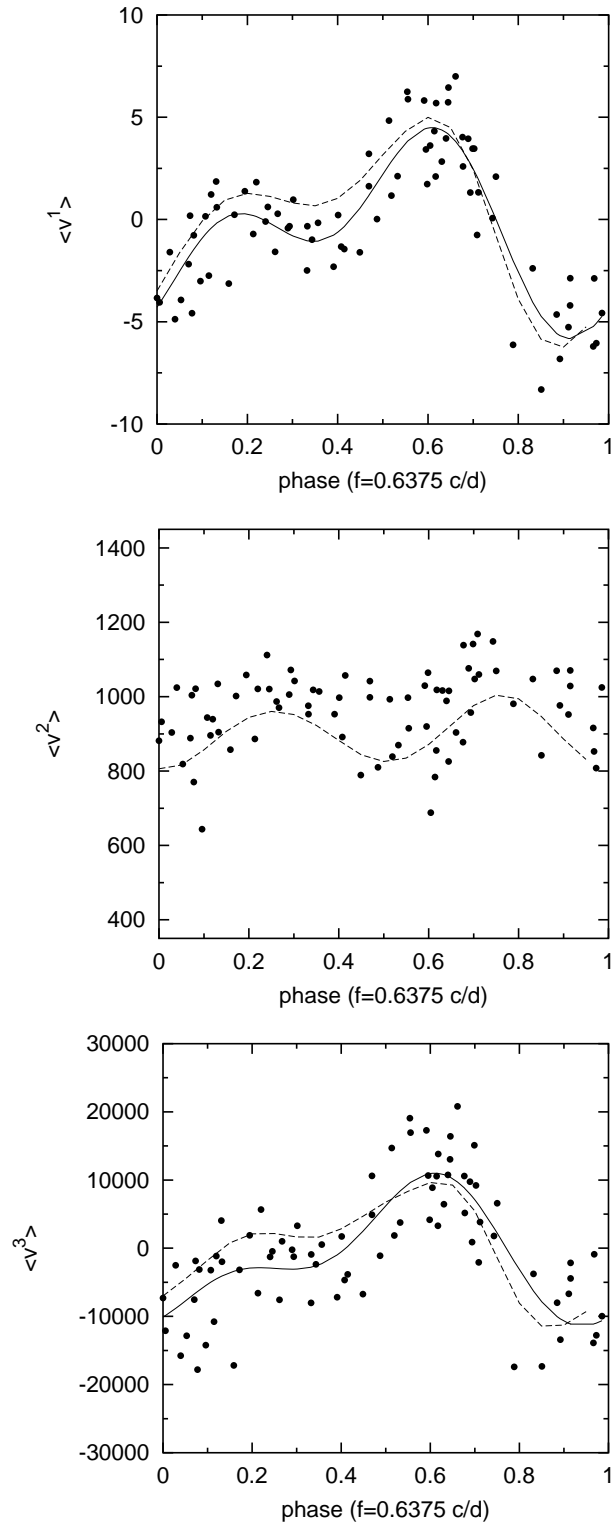
Figure 8.5: Phase diagrams of the first three moments of the He I 4121 Å line. We show the observed values (dots), the fit using 0.6375 c d^{-1} and its first harmonic (solid line), and the moments of the best spot model (dashed line).
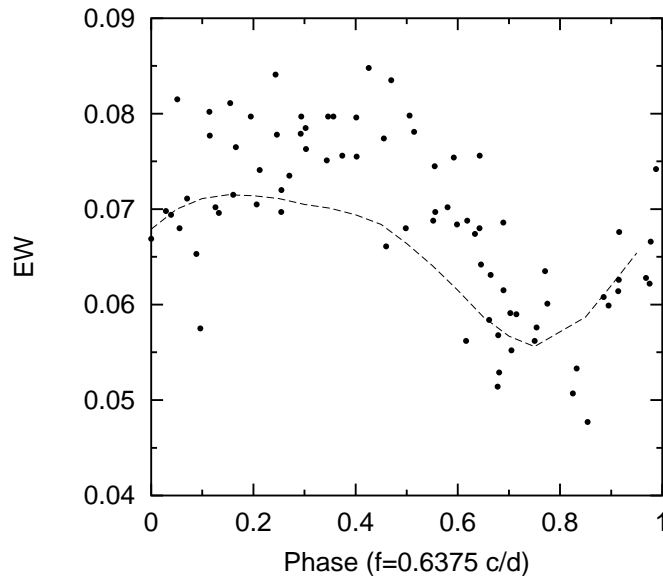
Figure 8.6: Phase diagram of the equivalent width of the He I 4121 Å line, which is expressed in Å. The comparison with the equivalent width for the best spot model is represented as a dashed line.

In Fig. 8.2 the first three moments of the theoretical profiles are compared to those of the observed profiles of Si and in Fig. 8.3 we show the comparison between the observed and theoretical EW variations of the Si line. Again we find a good agreement between observed moments and theoretical moments. We note that the amplitude of the theoretical second moment is very small, which is compatible with the fact that the observed second moment is very noisy.

We point out that the models for the He line and for the Si line are compatible since they have the same value for the parameters v_Ω and i. We also point out that we end up with a model for which helium is underabundant in huge spots while silicon is overabundant there. This naturally explains the very weak He line and the strong Si line.

It would be interesting to compute the variation of the luminosity of HD 131120 in order to compare it to the observed photometric amplitudes. As we do not know if the star presents additional non-homogeneous distributions of other elements on the stellar surface, we cannot compute this variation as long as we do not have a complete view of the chemical abundances.

8.5.3   Abundance surface mapping

Our analysis described in the previous sections clearly shows that the observed monoperiodic variability of HD 131120 is due to its rotation and inhomogeneities of elements on its stellar surface. The best method available to map surface abundances of CP stars is
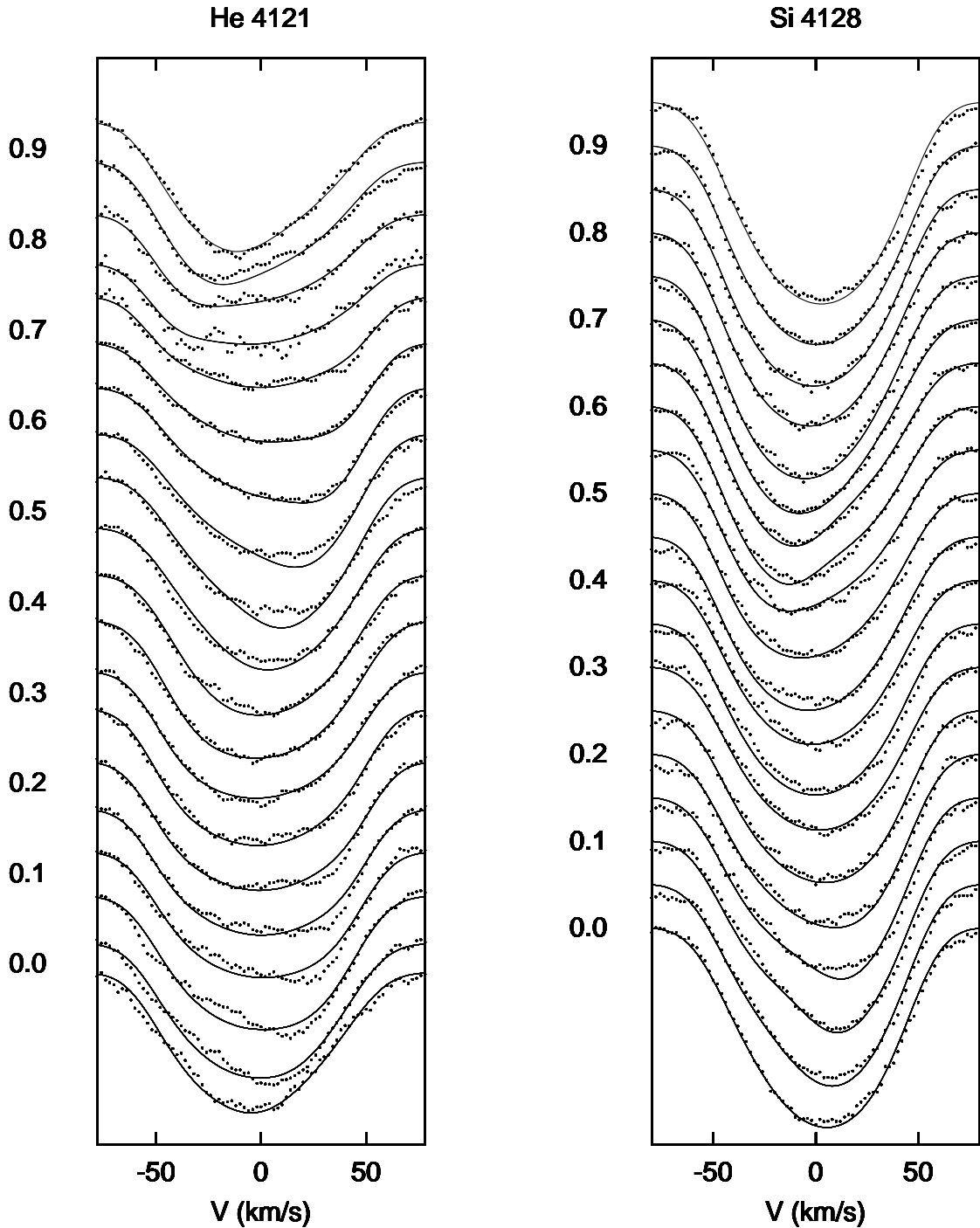
Figure 8.7: Observed line profiles (dots) of the He I 4121 Å line (left) and of the Si II 4128 Å line (right) averaged over phase bins of 0.05 and theoretical line profiles (full lines) for the spot model with two spots.

the Doppler Imaging technique (Chapter 4). With the help of Theresa Lüftinger (Vienna University) and thanks to the code INVERS11 kindly put at our disposal by Prof. N. Piskunov, we mapped the surface silicon and helium abundance by using the Si II-doublet with lines at $\lambda\lambda$ 4128, 4130 Å, the He I 4121 Å line and the He I 4143 Å line.

We varied the parameters T_{eff} and $\log g$ around their values derived from Geneva photometry. All derived maps showed very similar distributions of elements. We then decided to choose the maps for the T_{eff} and $\log g$ values found from Geneva data. To illustrate it, Fig. 8.8 and Fig. 8.9 correspond respectively to $T_{\mathrm{eff}} = 18\ 600$ K, $\log g = 4.2$ (values found by de Geus 1989) and $T_{\mathrm{eff}} = 18\ 250$ K, $\log g = 4.1$. The figures are divided as follows:
'a' is the mercator projection of the abundance distribution and comprises contour lines around regions of equal abundance.
'b' shows the mapped stellar surface in four rotational phases (0.0, 0.25, 0.5, 0.75). Below each phase, values for the mean abundance averaged over the visible part can be found. Dark colour means high, bright colour means low abundance.

The projected rotational velocity v_Ω was derived so that theoretical profiles reproduce the observed width of the line. The angle of inclination i was determined from $P_{\mathrm{obs}} = 2\pi R \sin i / v_\Omega$ by taking into account an uncertainty on the stellar radius R. Consequently we varied v_Ω from 55 km s^{-1} to 65 km s^{-1} with a step of 5 km s^{-1} and i from 20° to 60° with a step of 10°. We then chose the combination of parameters which minimizes the residuals between observations and the computed line profiles. Note that a difference of 10° for the inclination does not change very much the outcome, as illustrated by comparing Fig. 8.9 and Fig. 8.10.

The final maps were computed for $T_{\mathrm{eff}} = 18\ 250$ K, $\log g = 4.1$, $v_\Omega = 60$ km s^{-1} and $i = 30°$. Fig. 8.9 was derived from the He I 4121 Å line, Fig. 8.10 from the same line but for $i = 40°$, Fig. 8.11 from the He I 4143 Å line, Fig. 8.12 from the He I 4121 Å line taking into account the blends of Fe and O and Fig. 8.13 from the Si II-doublet with lines at $\lambda\lambda$ 4128, 4130 Å. Taking into account blends of other elements evidently gives a better fit but does not change the structure of the maps. Fig. 8.14 compares the observed and the calculated He and Si profiles at different phases of observation from phase zero (top) to the end of the rotation period (bottom).

Fig. 8.11 and Fig. 8.12 show that helium is globally significantly depleted at the stellar surface relative to solar abundance (-1.05 dex). Both figures show the same distribution of helium while they were derived from different lines, which gives confidence in our result. We note that the He I 4143 Å line is significantly blended by lines of other elements, and shows relatively large deviations for the fits for this line. A comparison between, on the one hand Fig. 8.11 and Fig. 8.12, and on the other hand Fig. 8.13, shows that helium is enhanced in regions of the stellar surface where silicon is depleted and inversely. We note that this result is entirely compatible with the one that we obtained in the previous section using a simple model with two spots for direct line-profile fitting.
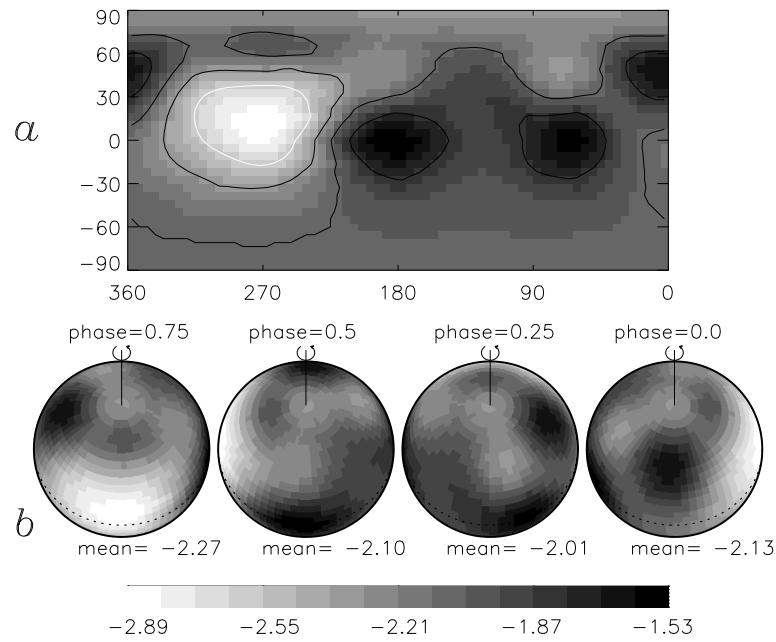
Figure 8.8: The helium distribution on the surface of HD 131120 obtained with INVERS11 from the He I 4121 Å line for $T_{\text{eff}} = 18\,600$ K, $\log g = 4.2$, $v_\Omega = 60$ km s^{-1} and $i = 30°$. For further explanation we refer to the text.
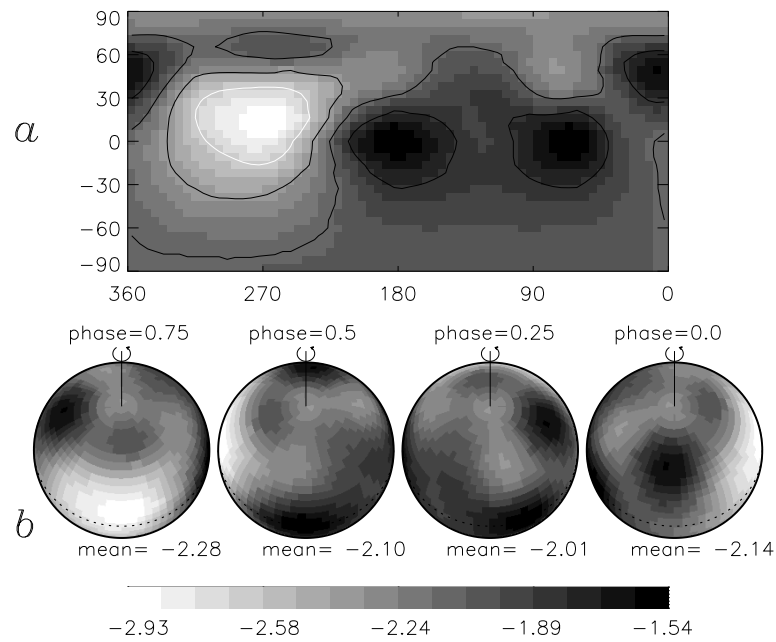
Figure 8.9: The helium distribution on the surface of HD 131120 obtained with INVERS11 from the He I 4121 Å line for $T_{\text{eff}} = 18\,250$ K, $\log g = 4.1$, $v_\Omega = 60$ km s^{-1} and $i = 30°$.
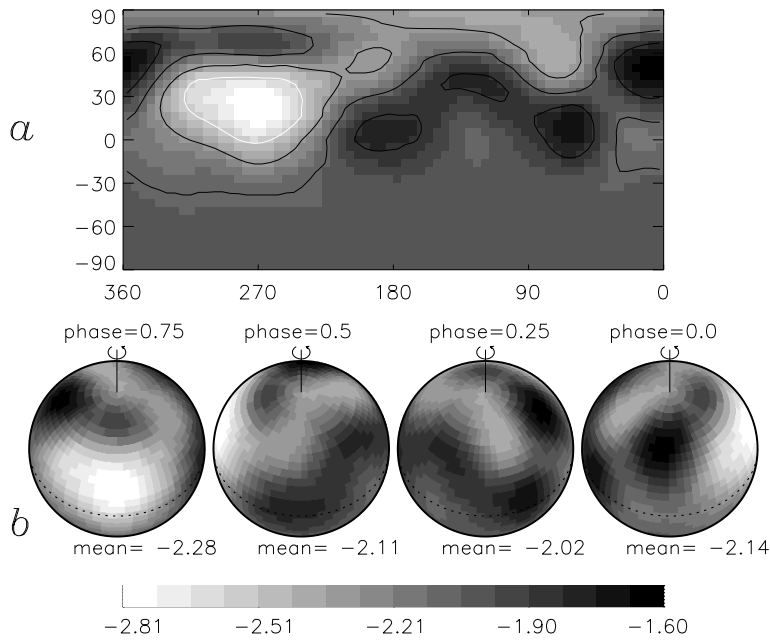
Figure 8.10: The helium distribution on the surface of HD 131120 obtained with IN-VERS11 from the He I 4121 Å line for $T_{\text{eff}} = 18\,250$ K, $\log g = 4.1$, $v_\Omega = 60$ km s^{-1} and $i = 40°$.
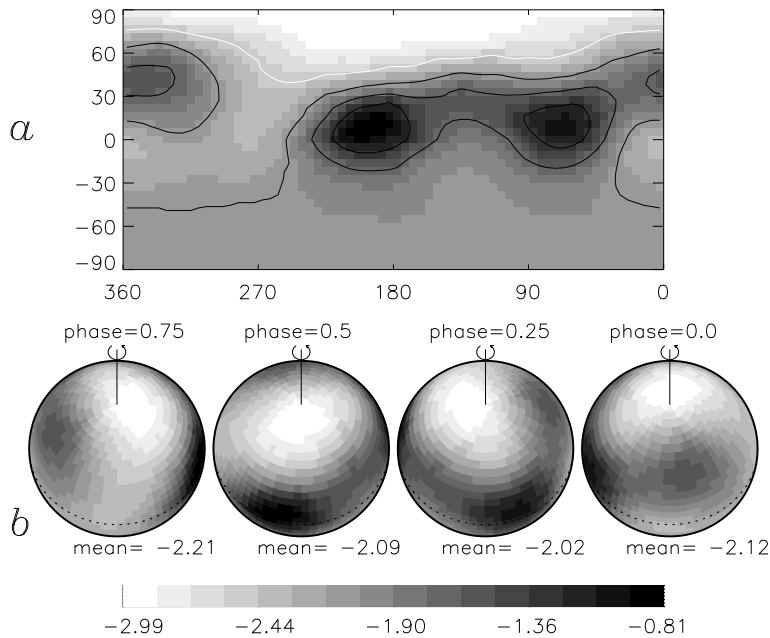
Figure 8.11: The helium distribution on the surface of HD 131120 obtained with IN-VERS11 from the He I 4143 Å line for $T_{\text{eff}} = 18\,250$ K, $\log g = 4.1$, $v_\Omega = 60$ km s^{-1} and $i = 30°$.
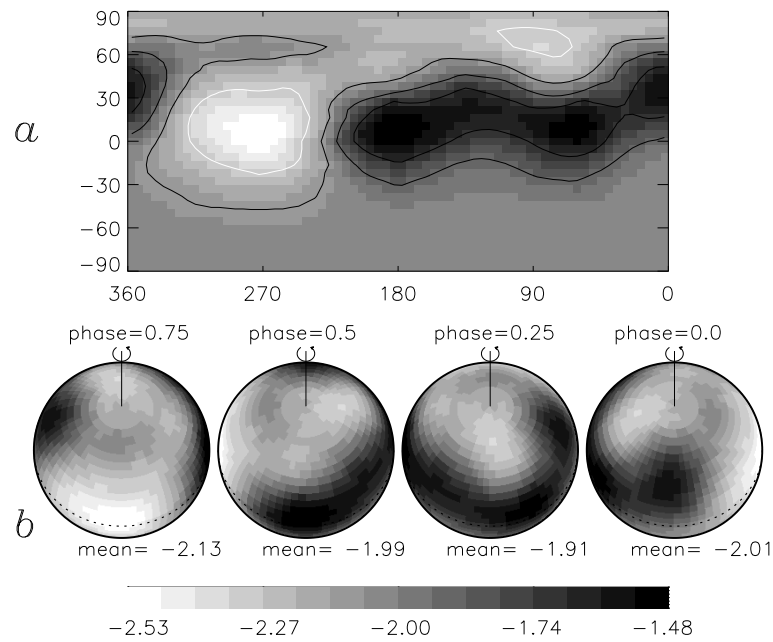
Figure 8.12: The helium distribution on the surface of HD 131120 obtained with IN-VERS11 from the He I 4121 Å line for $T_{\text{eff}} = 18\ 250$ K, $\log g = 4.1$, $v_{\Omega} = 60$ km s^{-1} and $i = 30°$, taking into account the blends of Fe and O.
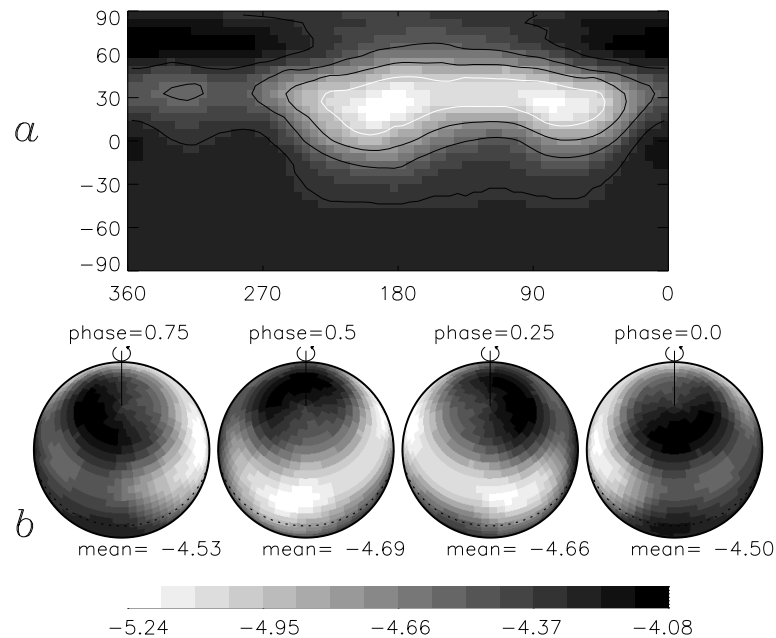
Figure 8.13: The silicon distribution on the surface of HD 131120 obtained with IN-VERS11 from the Si II 4128-4130 Å doublet for $T_{\text{eff}} = 18\ 250$ K, $\log g = 4.1$, $v_{\Omega} = 60$ km s^{-1} and $i = 30°$.
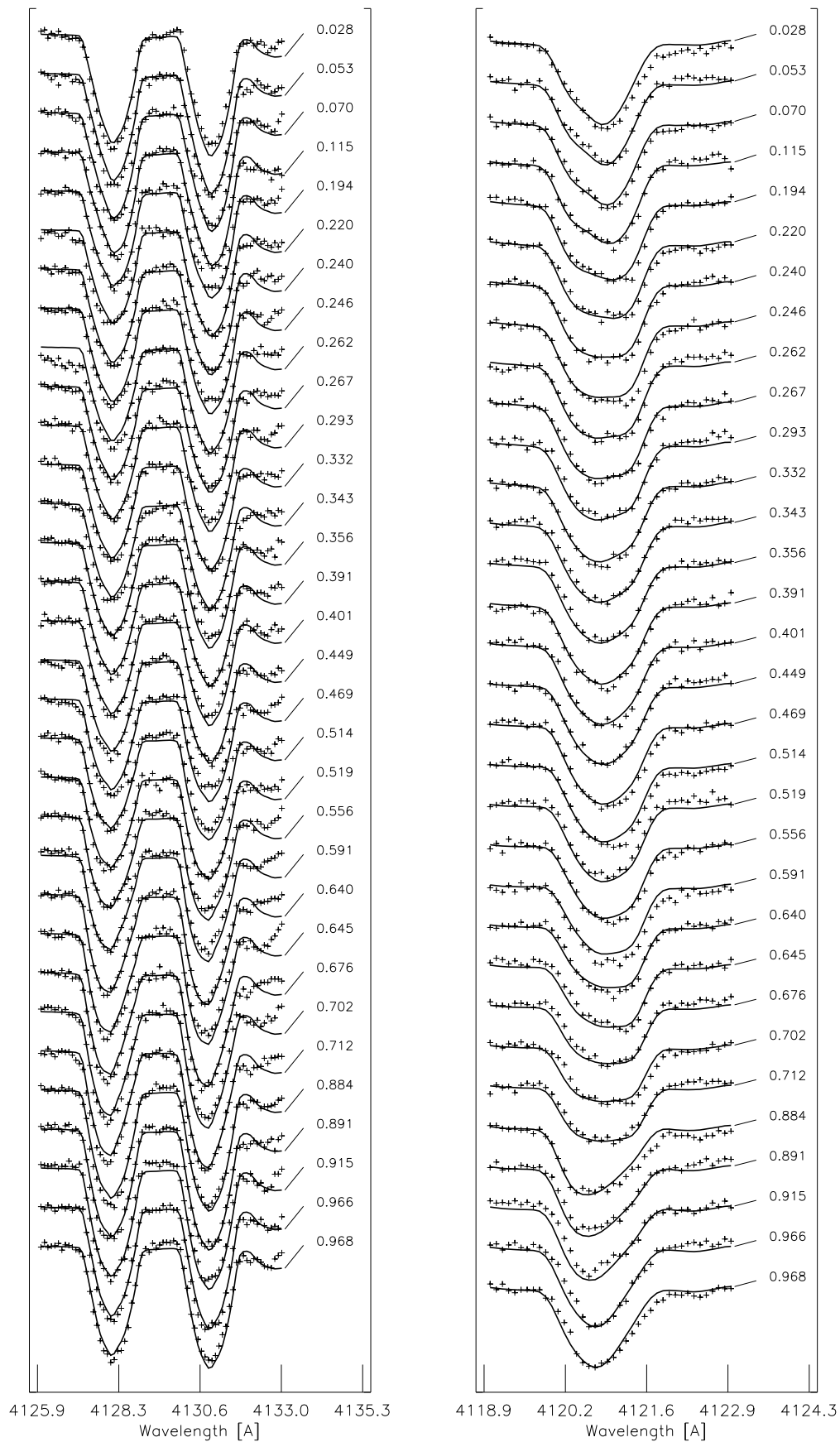
Figure 8.14: Observed line profiles (crosses) of the Si II 4128-4130 Å lines (left) and of the He I 4121 Å line (right) at different phases of observation and computed line profiles (full lines) obtained with INVERS11.

8.6 Conclusions

Our study of the star HD 131120 was based on multicolour photometry and high-resolution spectroscopy spread over respectively one and two years. From the period analysis on all the data it is clear that this star is monoperiodic with a period of 1.569 days. We compared the variations in the data with a non-radial pulsation model. The mode identification by three methods does not allow to choose one particular pulsation mode. Moreover, the line-profile behaviour of the Si and He lines is very different as far as the temporal behaviour and phasing is concerned. Such a difference cannot be explained by a pulsational model.

Next we tried to interpret the monoperiodic variations by rotational modulation. We compared the line-profile variations with a model with two spots in order to reproduce the first moment of the observed spectral lines. This leads to very good results for both He and Si lines. The best spot model is able to reproduce the behaviour of the first three moments of the lines, as well as the large equivalent width variations. Moreover, we showed that a spot model can well explain the different temporal behaviour of the moments of the two different lines. We conclude that rotational modulation is the best explanation of the variability of HD 131120 and remove the star from the list of SPBs.

Finally, we mapped surface abundance distributions for helium and silicon by means of the Doppler Imaging technique. We confirm that the star is a He-weak star for which helium is globally significantly depleted on the stellar surface. Regions more enhanced in helium are depleted in silicon. The presence of such surface inhomogeneities for Ap stars are generally correlated to an observed magnetic field. The search for a magnetic field for HD 131120 was done by Borra et al. (1983) who concluded that the observed magnetic field strength of 106 ± 168 Gauss is not significant. New detections with higher precision would be needed in order to definitely conclude on the presence or not of a weak magnetic field for the star.

Chapter 9

The B 2 IIIe star HD 105382

(part of this chapter was originally published as **Briquet M.**, **Aerts C.**, **De Cat P.**, 2001, A&A 366, 121, *Optical variability of the B-type star HD 105382: pulsation or rotation?*)

9.1 Introduction

In Briquet et al. (2001) we have made an extensive study of the B 2 IIIe star HD 105382 by means of multicolour photometry and high-resolution spectroscopy spread over respectively one and two years. We confronted the line-profile variations with both a non-radial pulsation model and with a spot model. The latter model gives a slightly better explanation for the line-profile variations, but the difference between the rivalling hypotheses was only marginal. In fact, none of the two models was able to explain the variability in a satisfactory way. The true nature of HD 105382 remained a puzzle. This analysis illustrates the fact that to derive a correct interpretation of the variability of one single line can be difficult. Another example is the one of the analyses of high-quality line-profile variations of the Be star 28 CMa. Balona et al. (1999) have interpreted the observed variations in terms of a spot model, while Maintz et al. (2000) were able to produce a successful pulsation model to explain the data.

Together with HD 105382 two other stars in the sample of selected SPBs (Aerts et al. 1999) have line profiles that vary in a similar way to those of HD 131120: the star HD 138769 which is reported as a Bp star and HD 55522 for which chemical peculiarities were never reported before. As for HD 131120, a comparison of the moment variations of the silicon lines to the ones of a helium line allowed us to exclude the pulsation model for the three stars. We hence interpret their observed variations in terms of a rotational modulation model and we derive abundance maps for both elements on the stellar surface by means of the Doppler Imaging technique.

This chapter is devoted to HD 105382 and is organized as follows. In Sect. 9.2 we disprove the Be nature of the star. In Sect. 9.3 we describe the observations that we have at our disposal and we derive some physical parameters of the star. The frequency analysis

is given in Sect. 9.4. The variations of the moments of a Si line and a He line are described in Sect. 9.5. Abundance distributions on the stellar surface of both elements are derived in Sect. 9.6. A summary is finally given in Sect. 9.7.

9.2   Disproving the Be nature of the star

Different opinions about the Be character of HD 105382 are present in the literature. The star was classified as a Be star by Hiltner et al. (1969), who found clear emission in the Balmer lines. On the other hand, Dachs et al. (1981) took spectrograms in 1978 and concluded that the star should be deleted from all Be catalogues. Next, Aerts (2000) reports a clear broad Hα emission profile, which shows double-peaked emission with a maximum of 7.5 continuum units observed in May 1996. Rivinius (private communication) pointed out to us that the Hα spectrum shown in Aerts (2000) is very alike the one he took in May 1996 of the B 2 IV e star δ Cen, who is situated only a few arcminutes away from HD 105382. Moreover, he found HD 105382 to exhibit absorption in Hα in January 2000. Because of these contradictions, we have subsequently taken several high-resolution Hα spectra during two weeks in February 2000, all of which are narrow and show absorption. We note that all our data taken for HD 105382 were obtained by remote control from Garching, so that the observer has only a very limited view of the sky.

Other authors also disprove the Be nature of the star. Slettebak et al. (1975) found that no emission is visible in April 1974 and that the spectral type (B 2 III ne) by Hiltner et al. (1969) appears to be too early. We note that this spectral type is also the one of δ Cen. Claria et al. (1981) obtained Hα and Hβ observations of a group of normal B and Be stars, among which HD 105382 that they classified as normal. We therefore conclude that HD 105382 was confused several times with δ Cen and that it is not a Be star.

9.3   Data and physical parameters

The satellite HIPPARCOS made 172 useful measurements of HD 105382 spread over a little more than 3 years. Measurements in the Geneva seven colour photometric system were obtained in 1997. We have 105 spectra gathered with the CAT/CES during 10 separate weeks of monitoring spread over 1996-1998. The number of observations and the ranges of their Julian Dates are given in Table 9.1.

The effective temperature and the gravity of HD 105382 are obtained by means of the photometric calibration by Künzli et al. (1997) to the mean magnitudes in the Geneva filters. The parallax measured by HIPPARCOS provides the distance. This, together with the average visual magnitude, gives the absolute visual magnitude. One obtains the bolometric magnitude and consequently the luminosity taking into account the bolometric correction (BC), which is calculated by means of Flower's relation (1996) between T_{eff} and BC. With the values for the effective temperature and the luminosity one estimates

Table 9.1: Observing log for Geneva photometry (upper) and spectroscopy (lower).

Number of observations	JD 2450000 +	
	Start	End
64	465	503
67	541	578
1	588	588
44	163	170
12	188	194
11	272	277
10	490	498
4	513	528
3	571	576
1	608	608
7	633	638
3	779	786
8	825	831
2	882	882

the mass by using the evolutionary tracks published by Schaller et al. (1992). We also calculated the radius. The results are:

$$\begin{cases} \log T_{\mathrm{eff}} = 4.24 \pm 0.01, \\ \log g = 4.18 \pm 0.15, \\ \log L/L_{\odot} = 2.89 \pm 0.15, \\ M = 5.7 \pm 0.4 \ M_{\odot}, \\ R = 3.0 \pm 0.6 \ R_{\odot}. \end{cases}$$

With these parameters HD 105382 is situated in the upper and blue part of the SPB instability domain (see e.g. Pamyatnykh 1999).

9.4 Frequency analysis

We performed a frequency analysis on the photometric and spectroscopic data by means of the PDM method (Stellingwerf 1978) and the CLEAN method (Roberts et al. 1987). We tested frequencies from 0 to 3 cycles per day (c d^{-1}) with a frequency step of 0.00001 c d^{-1}.
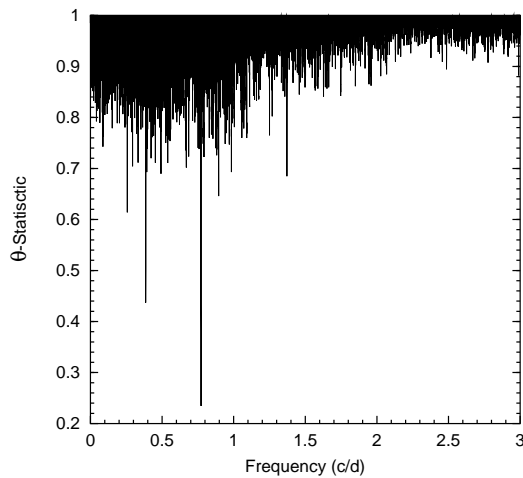
Figure 9.1: Θ-statistic of the HIPPARCOS photometric data.

The HIPPARCOS and Geneva photometric data

The Θ-statistic for the HIPPARCOS photometric data is represented in Fig. 9.1. The frequency which corresponds to the minimum of Θ is 0.77213 c d^{-1}. A phase diagram with this frequency in terms of a least-squares sine fit, is shown in the left panel of Fig. 9.2. This frequency reduces the standard deviation by 63%. Once we had found a significant frequency we searched for an additional frequency. To do so, we subtracted the sine fit from the measurements (i.e we prewhitened the data with the significant frequency) in order to apply the PDM method on the residuals. We obtained a variance of the residuals comparable with the mean error of the measurements and we could not find another frequency.

Geneva data also reveal the frequency 0.77214 c d^{-1}. A phase diagram with this frequency for the filter U is shown in the right panel of Fig. 9.2. Again we do not find an additional frequency.

The spectroscopic data

We extracted the measurements of the doublet Si II centered at $\lambda\lambda$ 4128, 4130 Å. From these spectral lines we computed the first moment with the aim of performing a frequency analysis. For each of the lines we found subsequently $f = 0.7721$ c d^{-1}, $2f$ and $3f$. The outcome of the CLEAN method for the different steps of the frequency search on the first moment of the Si II 4128 Å line is represented in Fig. 9.3. After prewhitening with f, $2f$, $3f$, no periodicity is present any more in the data. A phase diagram of $< v >$ for f, $2f$ and $3f$ is shown in the upper left panel of Fig. 9.4.
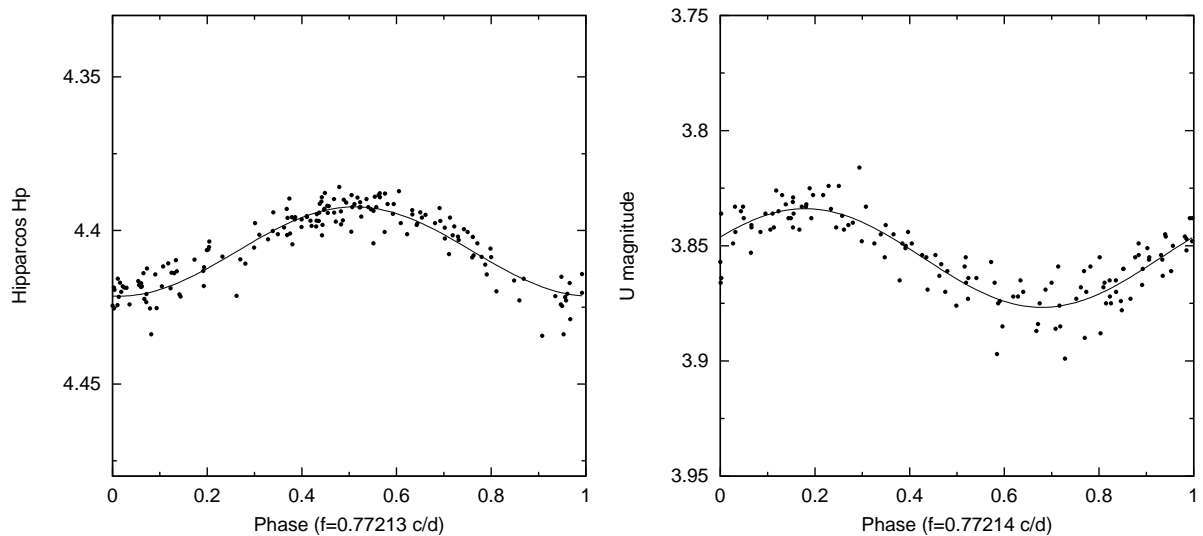
Figure 9.2: Phase diagrams of the HIPPARCOS photometric data and of the U-magnitude data. The dots are the observations and the full line is the best sinusoidal fit with the indicated frequency.

9.5   Moment variations

In order to compare the observations to theoretical predictions of a non-radial pulsation model, we also computed the second and third moments of the Si II 4128 Å line and we performed a frequency analysis on them. In the second moment we found the frequency 2.3163 c d^{-1} = $3f$ only, while f = 0.7721 c d^{-1} was found as single frequency in the third moment. We do not obtain the frequencies expected from the theory of non-radial oscillations, so we conclude that the silicon moment variations of HD 105382 (see left part of Fig. 9.4) are not typical for a standard linear pulsational model.

We then computed the first three moments of the He I 4121 Å line in order to compare their temporal variations to those of the Si lines. In $< v >$ we found subsequently $2f$ and f, which reduce together the standard deviation by 65%. In $< v^2 >$ we found subsequently $2f$, f and $3f$. In $< v^3 >$ we found $2f$. Phase diagrams for $< v >$, $< v^2 >$ and $< v^3 >$ computed from the He line are shown in the right part of Fig. 9.4.

A comparison of the behaviour of both lines allows to conclude that the cause of the observed variability of the star cannot be stellar pulsation. Indeed, for a pulsating star, we recall that the temporal behaviour and phasing of the moments are the same whatever is the line. Moreover the amplitude of the first moment, which is the radial velocity in the case of pulsation, does not depend too much on the lines for SPBs. Clearly, for HD 105382, the frequency $2f$ dominates the moments of the He line while it is the frequency f for the Si line. The minimum value for $< v >$ and $< v^3 >$ of the Si line corresponds to a maximum value for the He line. The peak-to-peak amplitude in $< v >$ obtained from the He line is about 20 km s^{-1} while the one obtained from the Si line is about 10 km s^{-1}.
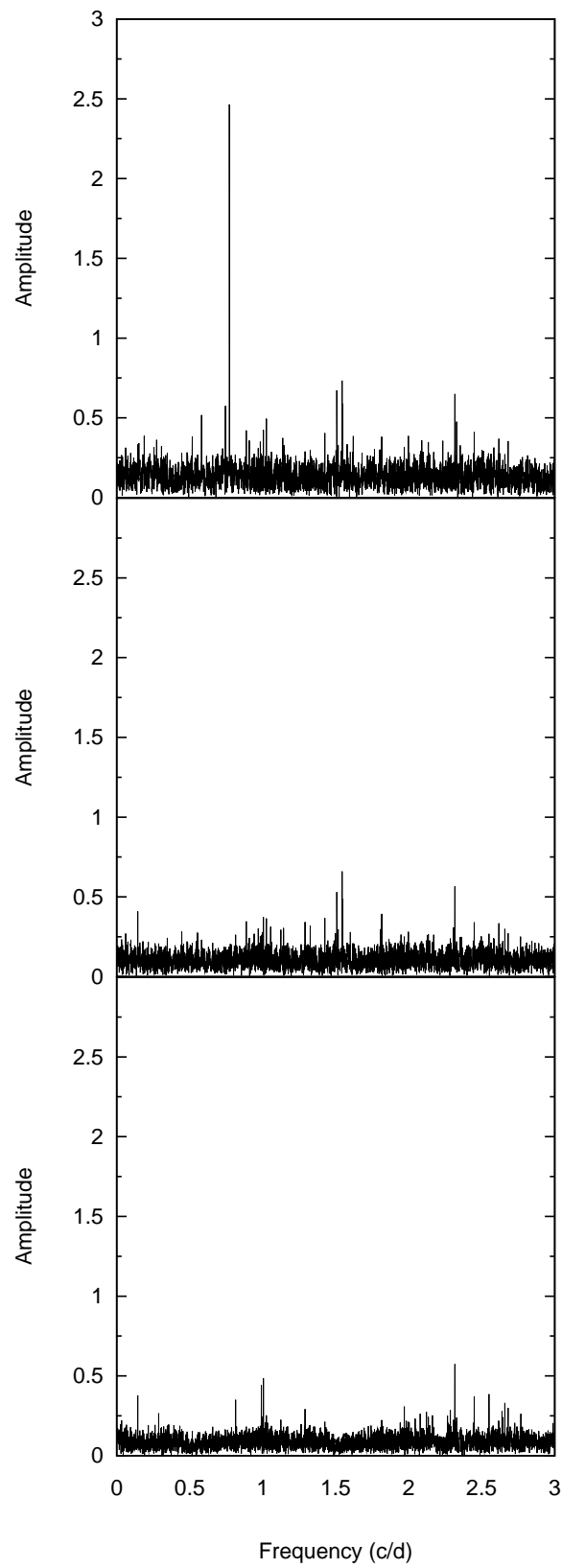
Figure 9.3: Outcome of the CLEAN method applied to the first moment derived from the Si II 4128 Å line (upper panel), to the data prewhitened with $f = 0.7721$ c d^{-1} (middle panel), to the data prewhitened with $2f$ (lower panel).
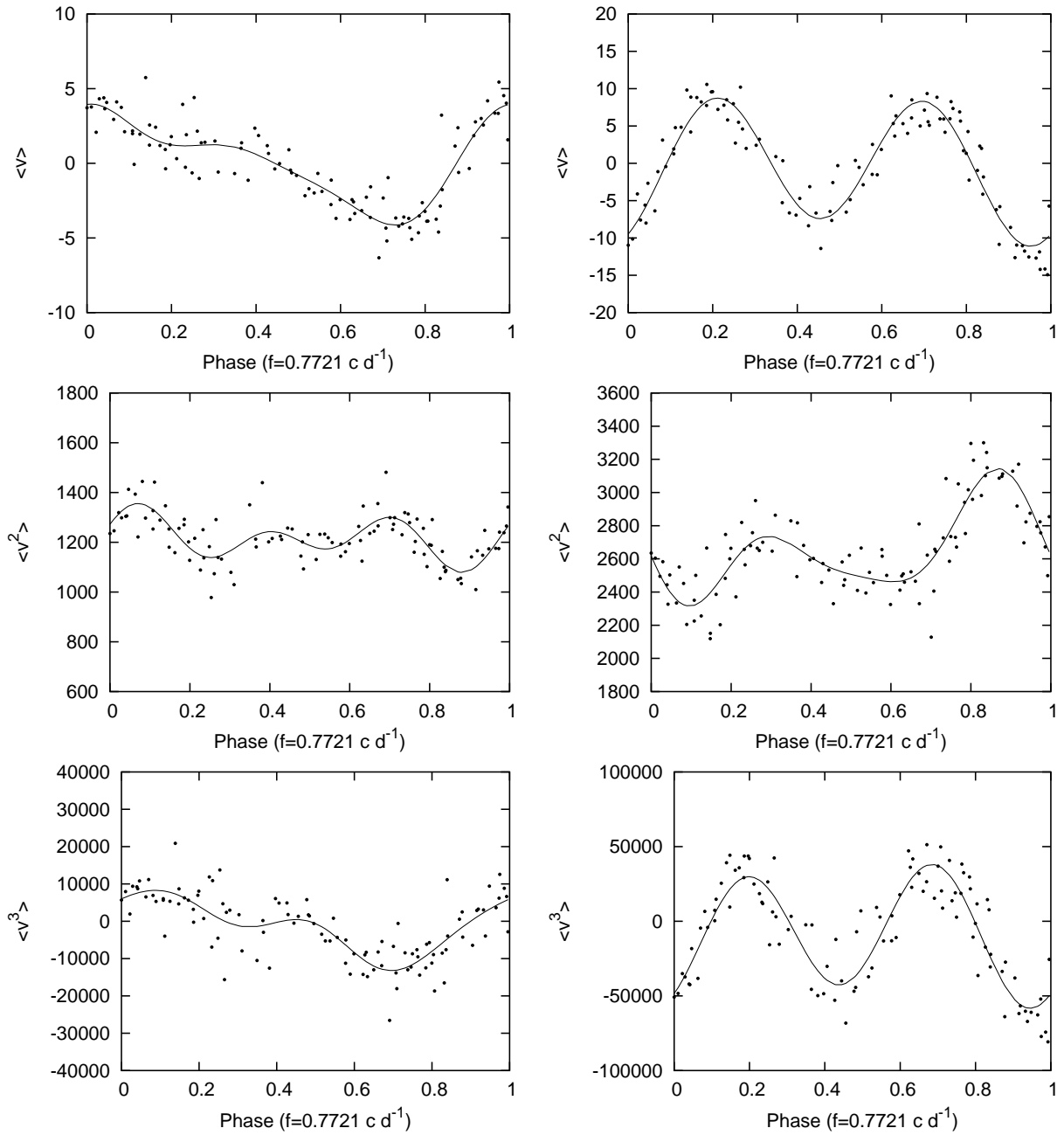
Figure 9.4: First three observed moments of the Si II 4128 Å line (dots, left) and of the He I 4121 Å line (dots, right). $< v >$, $< v^2 >$ and $< v^3 >$ are expressed respectively in km s^{-1}, (km s^{-1})^2 and (km s^{-1})^3. The full lines represent the best harmonic fits for the indicated frequency.
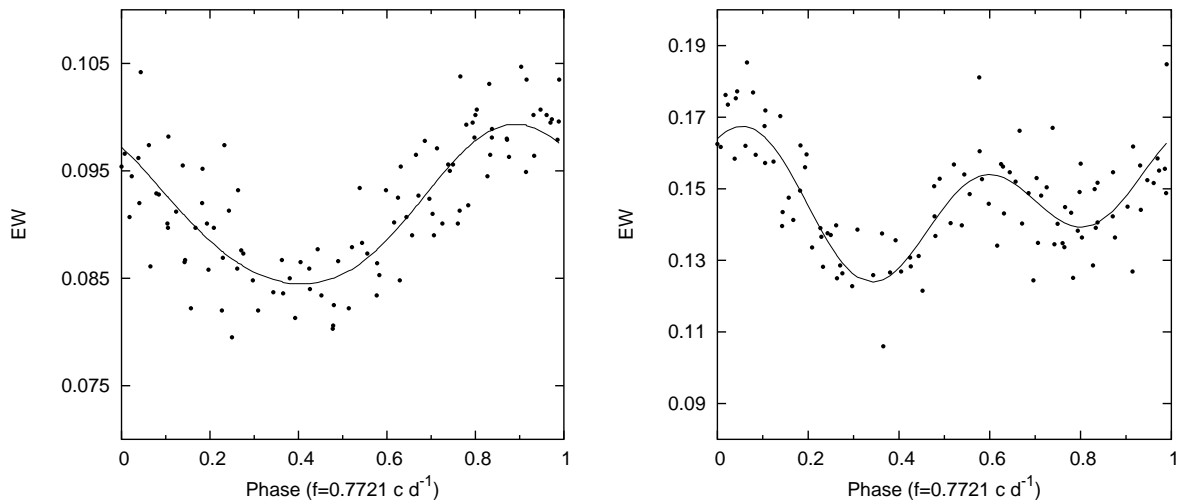
Figure 9.5: Observed equivalent width variations of the Si II 4128 Å line (dots, left) and of the He I 4121 Å line (dots, right), expressed in Å. The full line is the best harmonic fit for the indicated frequency.

We also show the equivalent width variations of the Si II 4128 Å line and of the He I 4121 Å line respectively in the left and right panel of Fig. 9.5. The equivalent widths vary with the same frequency as the higher order moments. The relative EW variations of the Si line and of the He line are about 9% and 7% respectively, which is large compared to the ones of confirmed SPBs (De Cat 2001). Moreover De Ridder et al. (2002a) have shown that relative EW variations of Si lines never exceed a few percent for slowly-rotating non-radially pulsating B stars.

All these peculiarities of the variations of the line profiles led us to exclude the pulsational model as an explanation for the variability of HD 105382. As the moment variations of the Si and He lines resemble those of HD 131120, we also attributed the variability of HD 105382 to rotational modulation. For HD 131120, the simple model implemented by Dr. L. Balona, that considers circular spots, was very useful to show that the characteristics of the observed moment variations can be easily reproduced and the results were fully compatible with those derived from the Doppler mapping. For HD 105382 and the two additional stars discussed in the following two chapters we only used the Doppler Imaging technique to map the quite complex abundance patterns on the stellar surface.

9.6   Abundance surface mapping

In this section we derive abundance surface maps for silicon and helium. For HD 131120 we have shown that an uncertainty of a few hundred Kelvin on T_{eff} and of 0.1 on $\log g$ does not influence significantly the outcome of the Doppler mapping. We therefore fixed the values of these parameters to those found from Geneva photometry. The angle of inclination of the star i is determined from the projected rotational velocity v_{Ω} that is
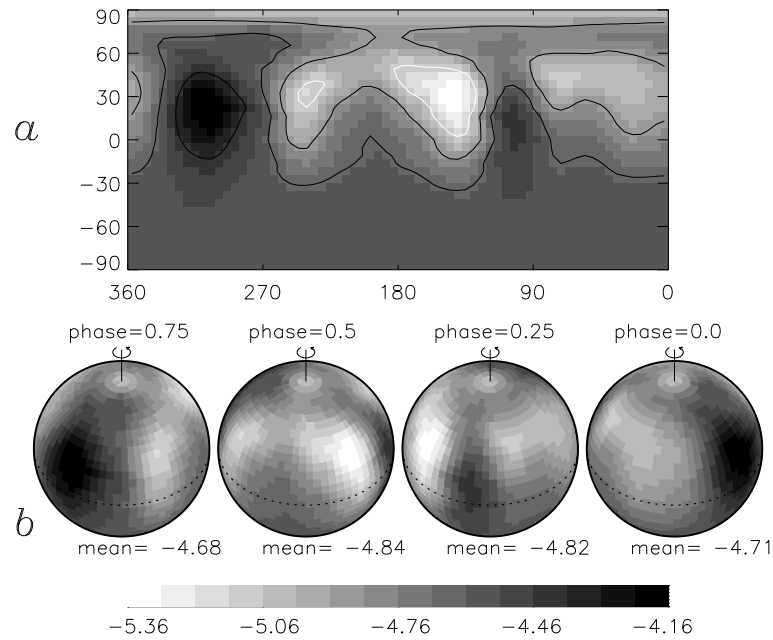
Figure 9.6: The silicon distribution on the surface of HD 105382 obtained with INVERS11 from the Si II 4128-4130 Å doublet for $T_{\text{eff}} = 17\ 400$ K, $\log g = 4.2$, $v_\Omega = 70$ km s^{-1} and $i = 50°$.
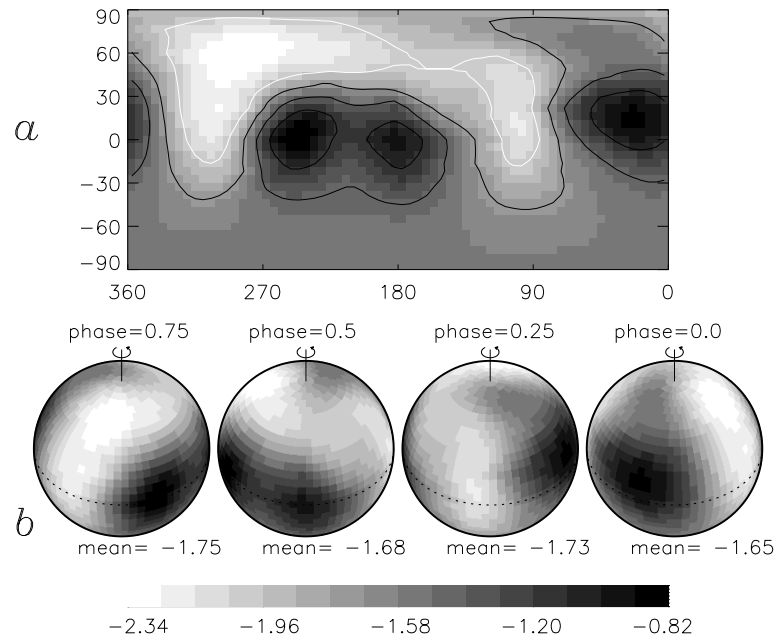
Figure 9.7: The helium distribution on the surface of HD 105382 obtained with INVERS11 from the He I 4121 Å line for $T_{\text{eff}} = 17\ 400$ K, $\log g = 4.2$, $v_\Omega = 70$ km s^{-1} and $i = 50°$.

estimated from the width of the line profile, from the rotation period that is derived from the periodicity of the variations, and from the stellar radius. However, the value of the stellar radius has a large uncertainty. For this reason, we varied v_Ω from 60 km s^{-1} to 75 km s^{-1} with a step of 5 km s^{-1} and i from 20° to 60° with a step of 10° in order to choose the parameters that minimize the deviation between observations and computed line profiles. As for the previous star, an angle of inclination of the star i that is 10° lower or higher led to very similar maps. It was then not useful to refine the grid of parameters. The derived maps are shown in Fig. 9.6 and Fig. 9.7 respectively for silicon and helium. For a description of the figures we refer to the analysis of HD 131120 (Sect. 8.5.3). Fig. 9.8 compares the observed profiles to computed ones at different phases of observation.

We conclude the following. Silicon is depleted on average over the stellar surface compared to the Sun (-4.49 dex). Helium is significantly depleted on the majority of the stellar surface. On average the stellar surface is very depleted in helium compared to the solar abundance (-1.05 dex). Two strong spots have a longitude difference of 180°. This corresponds to the two bumps observed in the first moment of the line (see right part of Fig. 9.4). A less strong third spot is also visible. As for HD 131120 the comparison of maps of both elements shows that roughly where helium is depleted, silicon is enhanced and inversely. This corresponds to the dephasing observed in the first moment of the lines (see Fig. 9.4).

9.7   Summary

We provide evidence that HD 105382 is misclassified as a Be star. All photometric and spectroscopic data point out that there is only one period of 1.295 days present in the data of the star. Moment variations of the Si II 4128 Å line and the He I 4121 Å line cannot be due to pulsation for the three following main reasons. First the temporal behaviour and phasing of both lines are different. Secondly the amplitude of the first moment computed from the two lines are different. Finally the equivalent width variations are large. We attribute the variability of the star to non-homogeneous distributions of elements on the stellar surface and we derive Doppler maps for silicon and helium. Regions in which helium is enhanced seem to correspond to regions in which silicon is depleted. The abundance of He is on average lower than the solar value. We then classify HD 105382 as a He-weak star. We note that the star was never reported as a Bp star before. We also note that a search for the presence of a magnetic field for the star was never reported upon.
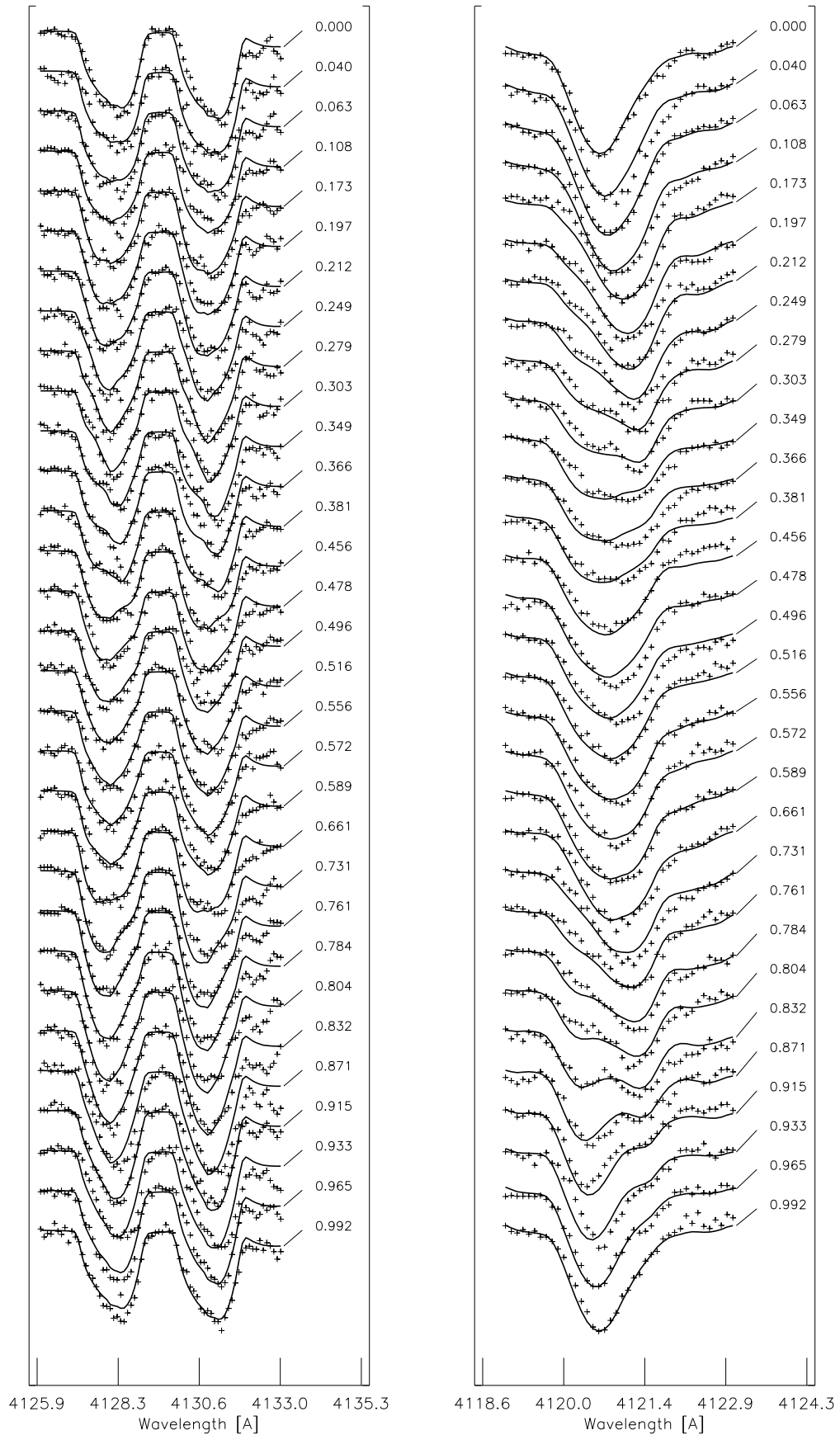
Figure 9.8: Observed line profiles (crosses) of the Si II 4128-4130 Å lines (left) and of the He I 4121 Å line (right) at different phases of observation and computed line profiles (full lines) obtained with INVERS11.

Chapter 10

The B 3 IVp star HD 138769

10.1   Introduction

The B 3 IVp star HD 138769 is a member of the Scorpio-Centaurus OB-association (Sco OB2). It is classified as a shell star first by de Geus et al. (1989) and then by Jaschek & Jaschek (1992). These latter authors observed a double emission centered on a broad absorption Hβ line. Light variations were first reported by Jakate (1979), who concluded that the star could be a slow variable with an amplitude not greater than 0.015 mag.

This chapter, reporting on our analysis of the star, is organized as follows. In Sect. 10.2 we describe observations at our disposal and we give the physical parameters of the star. In Sect. 10.3 we perform the frequency analysis on photometric and spectroscopic data. In Sect. 10.4 we show the variations of the moments of a Si line and a He line. Abundance distributions on the stellar surface of both elements are obtained in Sect. 10.5. A summary is finally given in Sect. 10.6.

10.2   Data and physical parameters

The number of observations for HD 138769 and the ranges of their Julian Dates are given in Table 10.1 for the multicolour Geneva photometry and the high-resolution spectroscopy, which were gathered with the Swiss Telescope of the Geneva Observatory and with the CAT/CES combination of ESO. We refer to De Cat (2001) for a description of the data reductions. Besides these data we also have 83 photometric observations obtained by the HIPPARCOS mission.

We determined the physical parameters of HD 138769 in the same way as for HD 105382 (Sect. 9.3). We obtained the following results:

$$\begin{cases} \log T_{\text{eff}} = 4.24 \pm 0.01, \\ \log g = 4.22 \pm 0.15, \\ \log L/L_{\odot} = 2.98 \pm 0.15, \\ M = 5.4 \pm 0.4 \ M_{\odot}, \\ R = 3.4 \pm 0.6 \ R_{\odot}. \end{cases}$$

Table 10.1: Observing log for Geneva photometry (upper) and spectroscopy (lower).

Number of observations	JD 2450000 +	
	Start	End
20	485	502
72	541	601
9	188	194
12	272	277
1	513	513
1	526	526
3	571	576
2	608	608
6	633	638
1	878	878

10.3   Frequency analysis

The HIPPARCOS and Geneva photometric data

In the HIPPARCOS measurements all three methods (see Sect. 4.1) led to a clear frequency, which is $f = 0.4786$ c d^{-1}. The Θ-statistic is shown in the left panel of Fig. 10.1. This frequency reduces the data standard deviation by 30%. A phase diagram for this frequency is represented in the left panel of Fig. 10.2. Note that the peak-to-peak amplitude of H_{p}-data is only 0.015 mag and the standard deviation of the residuals is some 0.00464 mag, which is only slightly larger than the average error on the data of 0.0043 mag. We searched for another frequency in the data but we were not able to determine one. The PDM and Scargle methods led to different candidates.

We found the same main frequency f in the seven filters of Geneva photometry, which reduces the standard deviation by 25%. The Scargle periodogram computed for the U-magnitude and a phase diagram for this frequency are respectively shown in the right panel of Fig. 10.1 and Fig. 10.2. As for HIPPARCOS photometry we were not able to derive a second frequency.

The spectroscopic data

Through the PDM method we found the frequency f in the first moment computed from the Si II 4128 Å line. After prewhitening with f we found a frequency very close to $2f$.
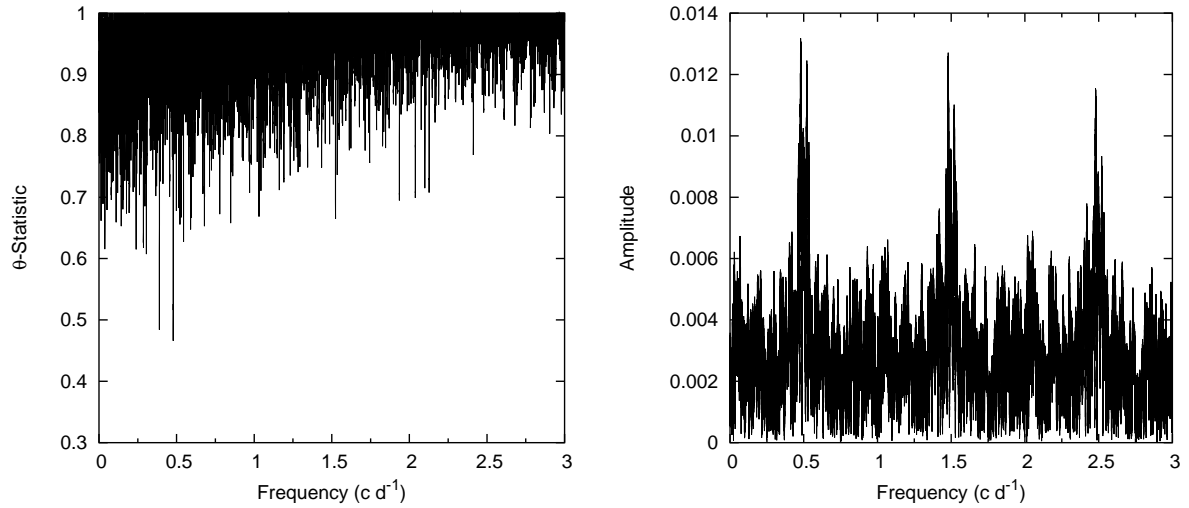
Figure 10.1: Left: Θ-statistic of the HIPPARCOS data. Right: Scargle periodogram of the Geneva U-magnitude data.
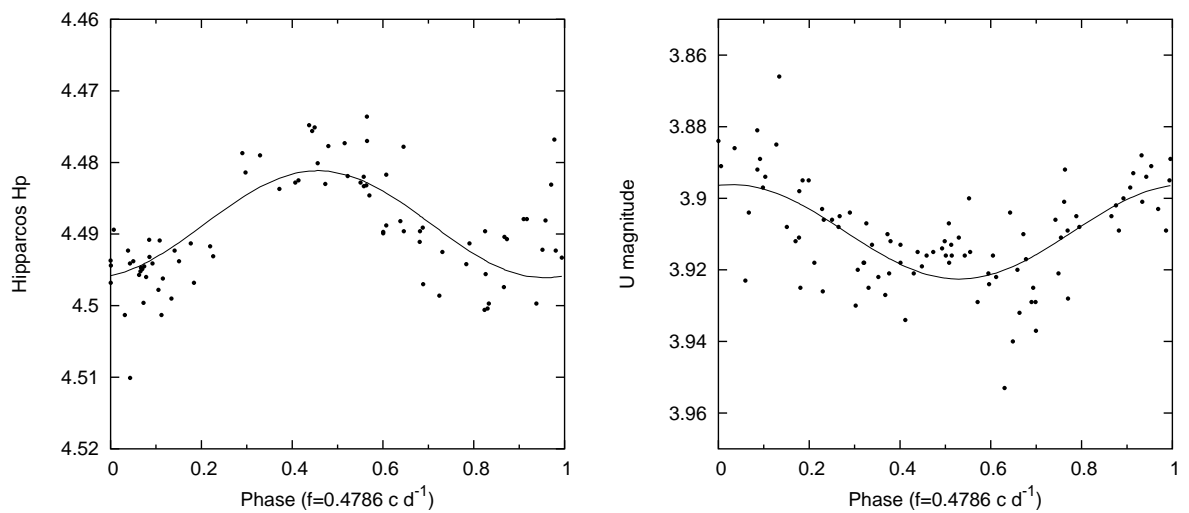
Figure 10.2: Phase diagrams of the HIPPARCOS data and of the U-magnitude data (dots) are compared with their best sinusoidal fits for the indicated frequency (full lines).
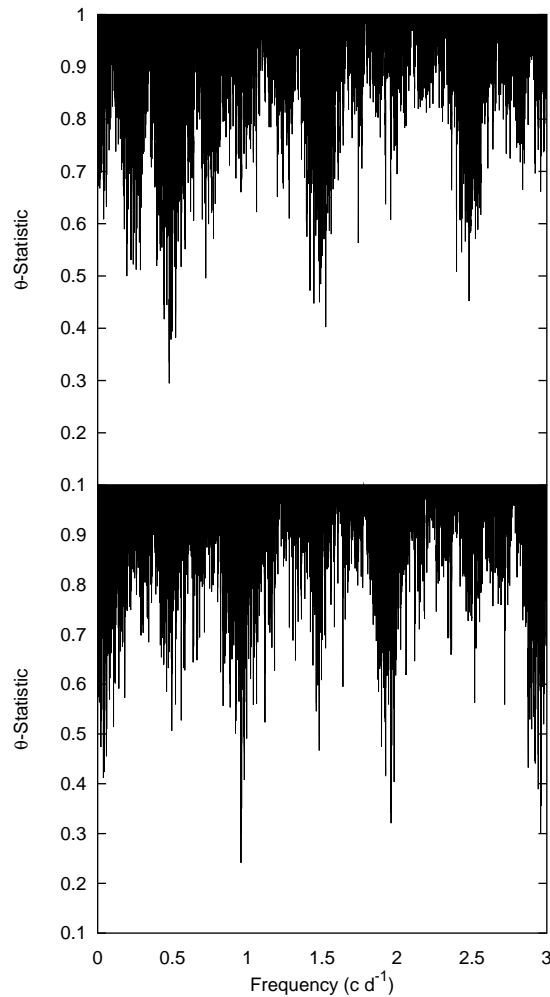
Figure 10.3: Θ-statistic of the first moment computed from the He I 4121 Å line (upper panel) and of the data prewhitened with $f = 0.4786$ c d^{-1} (lower panel).

In $< v >$ computed from the He I 4121 Å line, the PDM method leads subsequently to the frequencies f and $2f$ (Fig. 10.3). Using the Scargle method we obtained $1 - f$ as first frequency and $2f$ after prewhitening with f. Phase diagrams for $< v >$ are shown in the upper part of Fig. 10.4. The frequency f and its first harmonic reduce the standard deviation of $< v >$ computed from the He line by 74%.

10.4   Moment variations

In the second and third moment of the Si II 4128 Å line we were not able to determine a frequency. Concerning the He I 4121 Å line, its second moment does not show a clear frequency while the third moment clearly presents the frequency f and its first harmonic
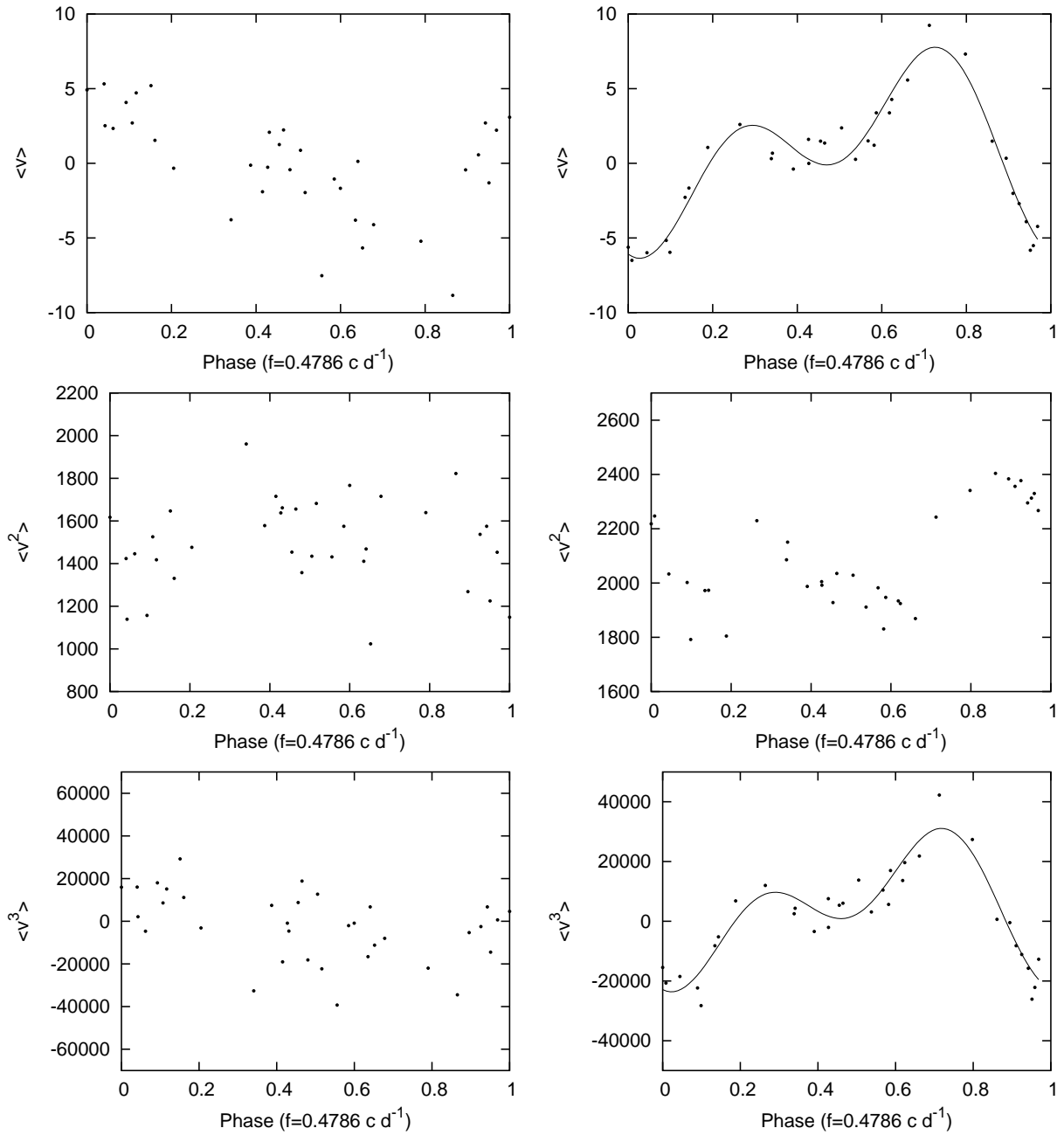
Figure 10.4: First three observed moments of the Si II 4128 Å line (dots, left) and of the He I 4121 Å line (dots, right). $< v >$, $< v^2 >$ and $< v^3 >$ are expressed respectively in km s^{-1}, (km s^{-1})^2 and (km s^{-1})^3. The full lines represent the best harmonic fits for the indicated frequency whenever it was found from a time series analysis.
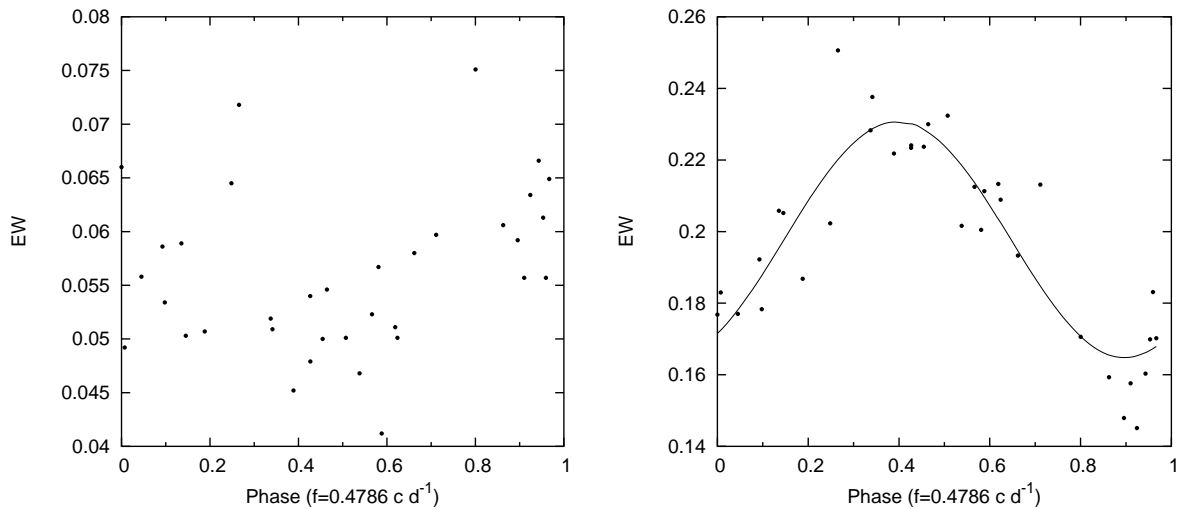
Figure 10.5: Observed equivalent width variations of the Si II 4128 Å line (dots, left) and of the He I 4121 Å line (dots, right), expressed in Å. The full line is the best fit for the EW of the He I line.

$2f$. Phase diagrams of these moments of both lines are represented in Fig. 10.4. The behaviour of $<v>$, $<v^2>$ and $<v^3>$ resemble the one of HD 131120 (see Fig. 8.2 and Fig. 8.5). Consequently we conclude that the variability of the star is due to rotational modulation. The equivalent width of both lines varies with f as shown in Fig. 10.5. The relative equivalent width variation is about 9% and 17% for respectively the Si line and the He line.

10.5   Abundance surface mapping

We derived abundance maps for silicon and helium for HD 138769 by taking $T_{\mathrm{eff}} = 17\,500$ K and $\log g = 4.2$ and by varying v_{Ω} from 60 km s^{-1} to 70 km s^{-1} with a step of 5 km s^{-1} and i from 30° to 70° with a step of 10°. The best silicon map was obtained for $v_{\Omega} = 70$ km s^{-1} and $i = 40$° and is shown in Fig. 10.6. Silicon is clearly underabundant compared to the Sun (-4.49 dex). Its observed mean abundance is constant during the rotation of the star. A depleted region is found at the pole while an enhanced spot is situated at the equator. For helium the deviation between observed and calculated profiles is very large so that we have less confidence concerning the reliability of the derived map. However it is clear that the star is also a He-weak star since the helium mean abundance is lower than the solar abundance. Fig. 10.7 compares the observed profiles to calculated ones at different phases of observation for the Si line.
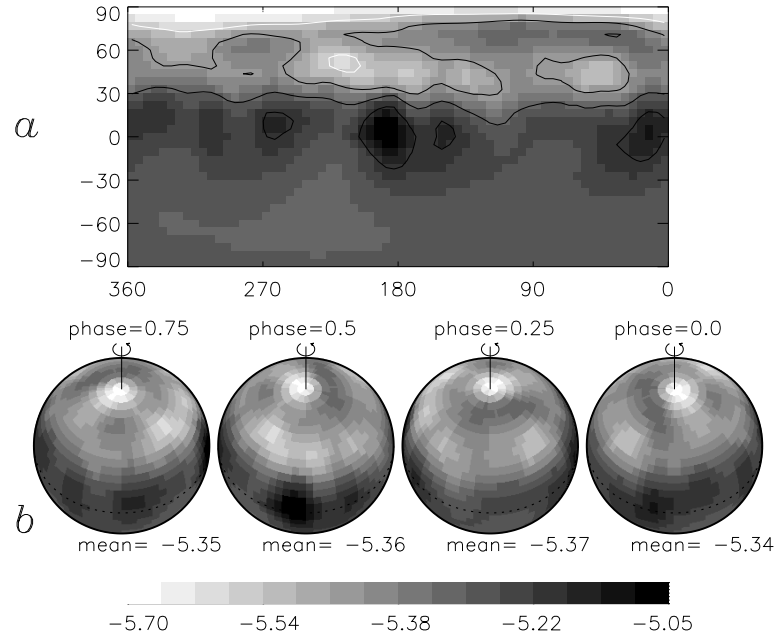
Figure 10.6: The silicon distribution on the surface of HD 138769 obtained with IN-VERS11 from the Si II 4128-4130 Å doublet for $T_{\text{eff}} = 17\,500$ K, $\log g = 4.2$, $v_\Omega = 70$ km s^{-1} and $i = 40°$.

10.6 Summary

All photometric and spectroscopic datasets of HD 138769 point towards the frequency $f = 0.4786$ c d^{-1}. The first and third moments of the He I 4121 Å line vary with f but also with its first harmonic $2f$. The variability of the moments of the Si II 4128 Å line is less clear but the frequency f is also present. As we attribute the variability of the star to chemical inhomogeneities on the stellar surface, we derive abundance maps for both elements but we are only confident for the silicon result. The star is clearly underabundant in silicon and in helium compared to the Sun. We confirm the star to be a Bp star as already reported in literature and we classify it as a He-weak star.
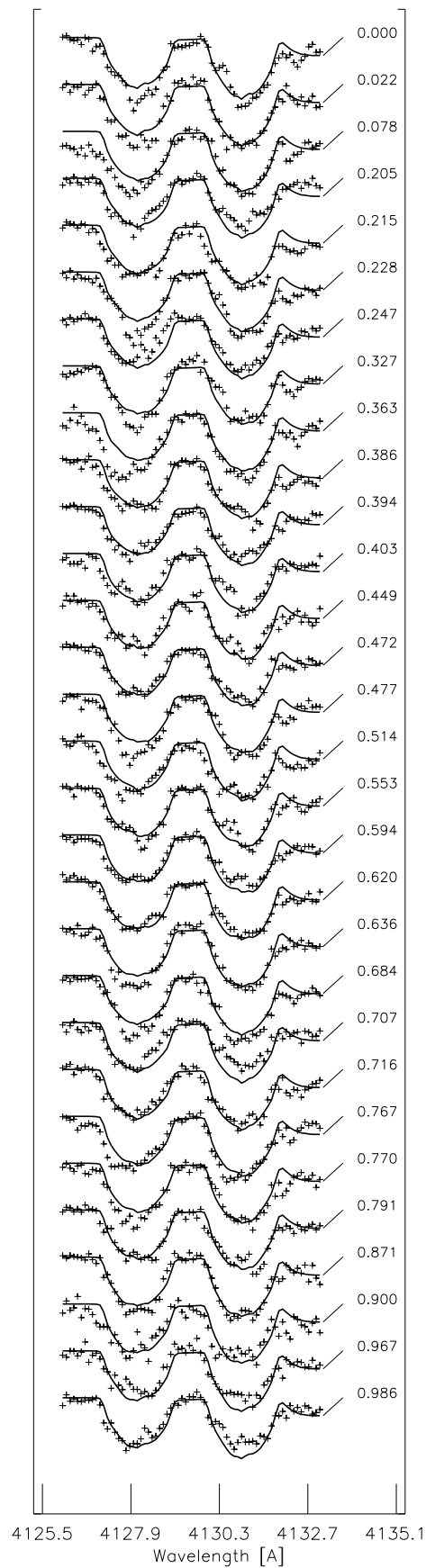
Figure 10.7: Observed line profiles (crosses) of the Si II 4128-4130 Å lines at different phases of observation and computed line profiles (full lines) obtained with INVERS11.

Chapter 11

The B 2 IV/V star HD 55522

11.1   Introduction

The B 2 IV/V star HD 55522 was already reported as a B-type variable star by van Hoof (1975) who observed light variations of the order of days. He attributed these light variations with a period of 2.68 days and an amplitude of 37 mmag to ellipsoidal variability. This light variability was confirmed by Jerzykiewicz & Sterken (1977) but it was never proven that this object is a binary.

De Cat (2001) performed an extensive study of the star by means of Geneva photometric data and spectroscopic data. From radial velocities that he had at his disposal, he was not able to confirm or rule out a binary scenario for HD 55522. The spectroscopic data show that the star might be a spectroscopic binary but with a long period of the order of years which is irrelevant for the interpretation of the short-period variability reported by van Hoof (1975). In the intrinsic photometric and spectroscopic variations he found one single frequency of 0.3664 c d^{-1} together with some of its harmonics. This frequency corresponds to the one already reported for this star by van Hoof (1975).

HD 55522 is situated in the instability strip of SPBs and reveals a frequency expected for SPBs. Moreover the star was never reported as a chemically peculiar star. Consequently De Cat (2001) compared the variability of the star to non-radial pulsation. From an application of the method of photometric amplitudes to Geneva data and from a comparison of line-profile variations to a NRP model, he concluded that the observed monoperiodic variability of HD 55522 is not well explained with stellar pulsation.

In this thesis we focus on the interpretation of the variability of HD 55522 in terms of rotational modulation. The chapter is organized as follows. In Sect. 11.2 we describe the data used for the analysis and we give the physical parameters of the star. In Sect. 11.3 we show the outcome of the frequency analysis on photometric and spectroscopic data. In Sect. 11.4 we describe the variations of the moments of a Si line and a He line. An abundance distribution on the stellar surface of both elements is obtained in Sect. 11.5. A summary is finally given in Sect. 11.6.

Table 11.1: Observing log for Geneva photometry (upper) and spectroscopy (lower).

Number of observations	JD 2450000 +	
	Start	End
12	389	407
52	465	503
25	542	582
23	745	805
6	166	170
9	188	194
14	490	498
8	736	742
7	779	786
12	825	831

11.2 Data and physical parameters

HD 55522 is a bright southern B star for which multicolour Geneva photometry and high-resolution spectroscopic data (Si II 4128-4130 Å doublet and He I 4121 Å line) were gathered respectively with the Swiss Telescope of the Geneva Observatory at La Silla and with the CAT/CES combination of ESO, also situated at La Silla. The number of observations and the ranges of their Julian Dates are given in Table 11.1. For a complete description of the observations and data reductions we refer to De Cat (2001). We also have HIPPARCOS photometry at our disposal, which consists in 187 useful measurements.

In De Cat (2001) some physical parameters of the star are given. They are:

$$
\begin{cases}
\log T_{\mathrm{eff}} = 4.24 \pm 0.01, \\
\log g = 4.15 \pm 0.15, \\
\log L/L_\odot = 2.95 \pm 0.15, \\
M = 5.5 \pm 0.3 \ M_\odot, \\
R = 3.3 \pm 0.6 \ R_\odot.
\end{cases}
$$

We point out that HD 55522, HD 105382 and HD 138769 are situated very close to each other in the upper and blue part of the SPB instability domain very near the main sequence (see e.g. Pamyatnykh 1999). Note that HD 131120 is not far away in the blue part too.
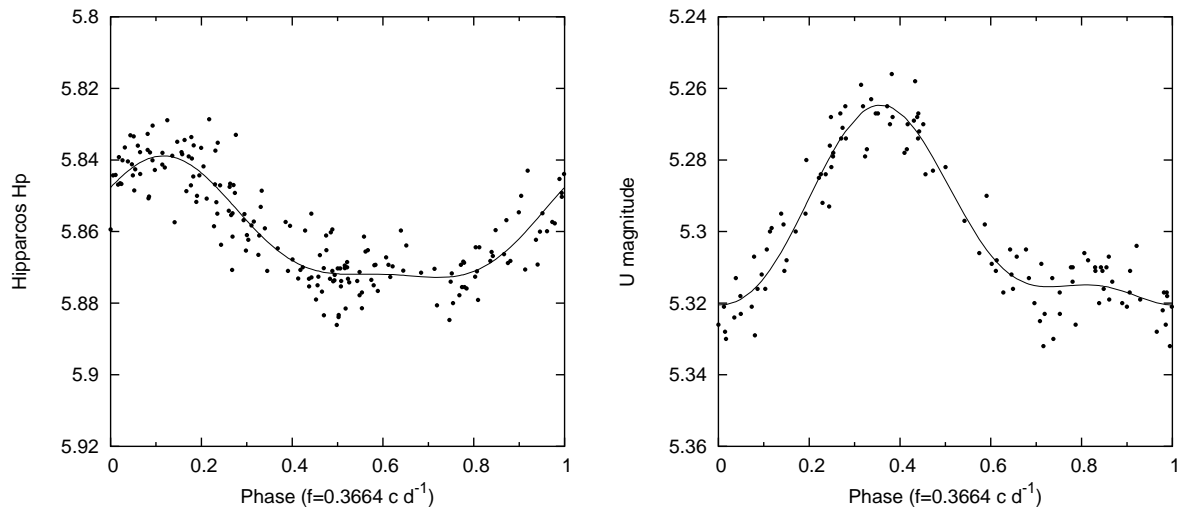
Figure 11.1: Phase diagrams of the HIPPARCOS data and of the U-magnitude data. The dots are the observations and the full line is the best harmonic fit with the indicated frequency.

11.3 Frequency analysis

The HIPPARCOS and Geneva photometric data

We performed a frequency analysis by means of the Scargle method (Scargle 1981). De Cat (2001) already made a period search by also using other methods, which led to the same result. In this thesis we show again the variations of photometry to underline the different behaviour of the star compared to confirmed SPBs. For both HIPPARCOS and Geneva photometric data we found subsequently the frequency $f = 0.3664$ c d^{-1} and $2f$. f with $2f$ reduce the standard deviation by 53% and 69% for HIPPARCOS and Geneva data respectively. Phase diagrams for both types of photometric data are shown in Fig. 11.1. Clearly the variability of the star is dominated by only one frequency and its first harmonic. The Scargle periodograms for the different steps of the frequency search on the U-magnitude data is represented in the left part of Fig. 11.2. No other frequencies can be found in the photometric datasets.

The spectroscopic data

The frequency analysis on the Si II 4128-4130 Å doublet does not lead to a clear frequency although the frequency f seems to be present in the first moment of the Si II 4128 Å line. However in the first moment of the He I 4121 Å line, the frequency f is clearly found and even its harmonics up to $4f$. The frequency search led to f, $2f$ and $3f$ subsequently. The Scargle periodograms for the different steps of the frequency search on $< v >$ are shown in the right panel of Fig. 11.2. Note that $4f$ is also present in the periodogram after prewhitening with f, $2f$ and $3f$. The frequencies f and its first three harmonics reduce the standard deviation of $< v >$ by 76% for the helium line.
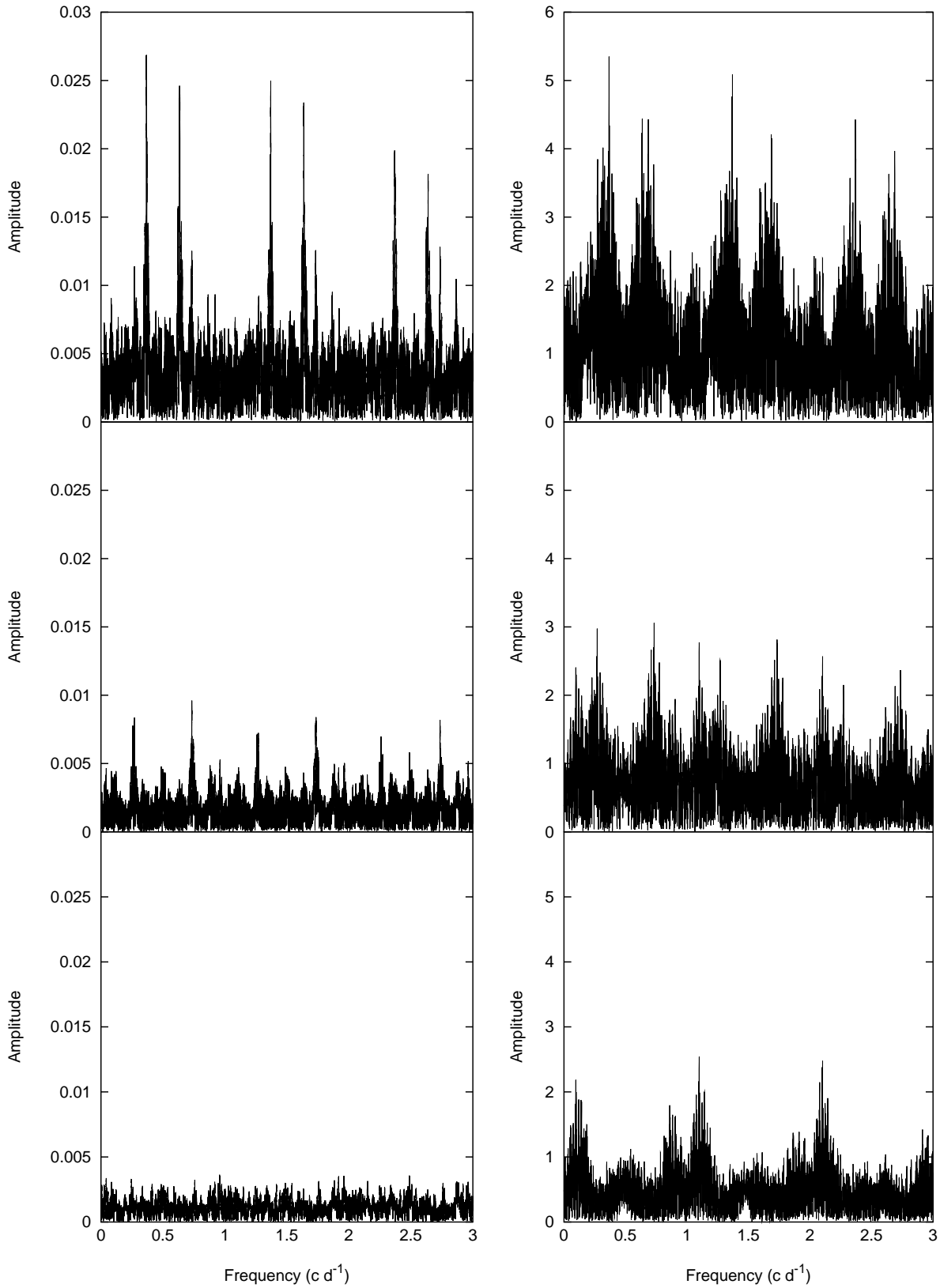
Figure 11.2: Left: Scargle periodograms of the U-magnitude data, of the data prewhitened with $f = 0.3664$ c d^{-1}, of the data prewhitened with $2f$. Right: Scargle periodograms of the first moment computed from the He I 4121 Å line, of the data prewhitened with f, of the data prewhitened with $2f$.
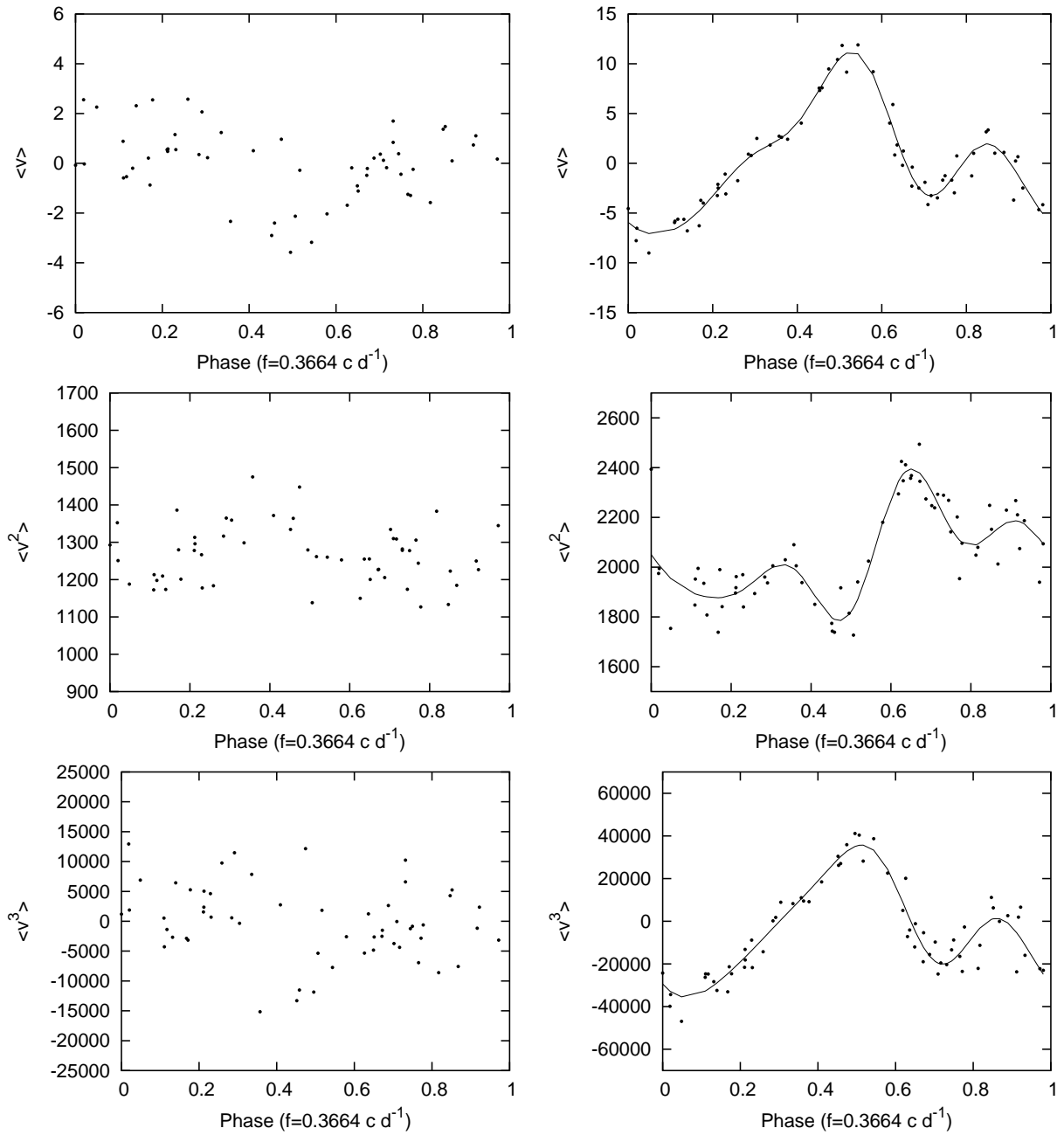
Figure 11.3: First three observed moments of the Si II 4128 Å line (dots, left) and of the He I 4121 Å line (dots, right). $< v >$, $< v^2 >$ and $< v^3 >$ are expressed respectively in km s^{-1}, (km s^{-1})^2 and (km s^{-1})^3. The full lines represent the best harmonic fits for the indicated frequency.
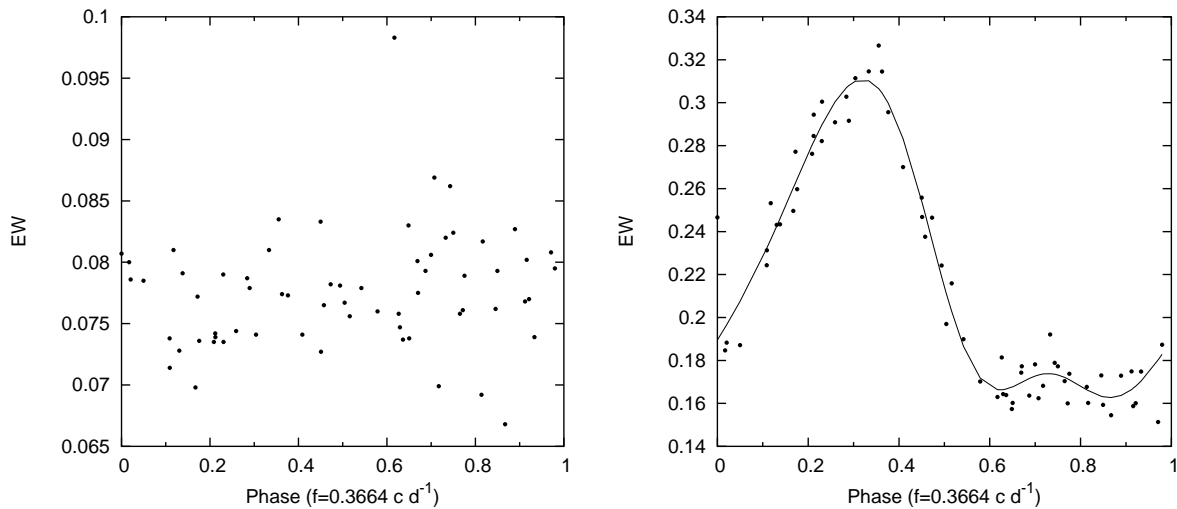
Figure 11.4: Observed equivalent width variations of the Si II 4128 Å line (dots, left) and of the He I 4121 Å line (dots, right), expressed in Å. The full line is the best harmonic fit for the indicated frequency.

11.4   Moment variations

In $<v^2>$ and $<v^3>$ of the Si II 4128-4130 Å lines it was not possible to find a frequency. Phase diagrams for f are shown in the left part of Fig. 11.3. The moments are very noisy and no clear periodicity is observed. For the He I 4121 Å line, however, we found in $<v^2>$ the frequency f followed by $3f$ and in $<v^3>$ we found f followed by $2f$. Phase diagrams of the first three moments of the helium line are shown in the right part of Fig. 11.3. No other frequency could be found in $<v>$ nor $<v^2>$ or $<v^3>$. The star is clearly monoperiodic.

As for HD 131120, HD 105382 and HD 138769 we conclude that such typical variations of the moments are not due to pulsation but can be caused by rotational modulation. We recall again their characteristics. Harmonics of the frequency are present in the datasets. The moment variations of the He line are completely different from those of the Si lines. The peak-to-peak amplitude of the first moment computed from the He line is four times larger than the one computed from the Si line. In Fig. 11.4 the equivalent width variations of both considered lines are represented. The ones of the Si line do not show any periodicity and are very noisy while the EW variations of the He line present a clear periodicity with f and harmonics as for the higher order moments. We note that the relative EW variation of the He line is about 35%, which is very large.

11.5   Abundance surface mapping

We derived abundance maps for silicon and helium for HD 55522 in the same way as for the previous stars (Sect. 8.5.3). We took $T_{eff} = 17\,400$ K and $\log g = 4.1$.
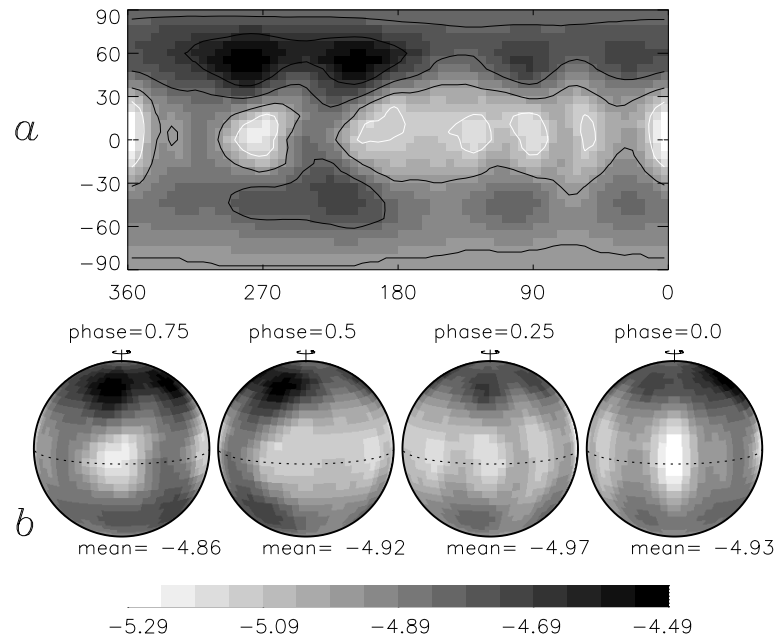
Figure 11.5: The silicon distribution on the surface of HD 55522 obtained with INVERS11 from the Si II 4128-4130 Å doublet for $T_{\mathrm{eff}} = 17\ 400$ K, $\log g = 4.1$, $v_{\Omega} = 75$ km s^{-1} and $i = 80°$.
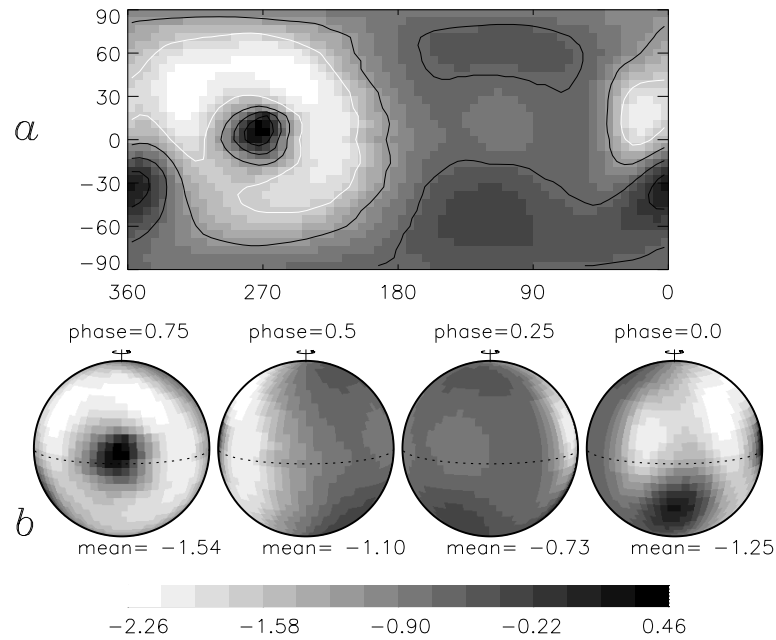
Figure 11.6: The helium distribution on the surface of HD 55522 obtained with INVERS11 from the He I 4121 Å line for $T_{\mathrm{eff}} = 17\ 400$ K, $\log g = 4.1$, $v_{\Omega} = 75$ km s^{-1} and $i = 80°$.

We varied v_Ω from 70 km s^{-1} to 80 km s^{-1} with a step of 5 km s^{-1} and i from 60°
to 90° with a step of 10°. The optimum maps were obtained for $v_\Omega = 75$ km s^{-1} and
$i = 80°$. They are shown in Fig. 11.5 and Fig. 11.6 for Si and He respectively. For silicon,
depleted regions compared to the rest of the stellar surface are situated along the equator
while enhanced regions are close to the poles. The average abundance of silicon over the
stellar surface is almost constant and lower than solar abundance (-4.49 dex). The mean
abundance of helium varies by 0.8 dex on half a period of rotation, which reflects the very
large variations of the equivalent width of this line. A strong helium spot is present on the
equator surrounded with a very depleted region. For this star, the maps of both elements
are very different as already suggested by the very different variations of the moments
of the different lines. Fig. 11.7 compares the observed profiles to the calculated ones at
different phases of observation.

11.6   Summary

HIPPARCOS and Geneva photometric data vary clearly with only one frequency $f =$
0.3664 c d^{-1} and its harmonic $2f$. Such a non-sinusoidal temporal behaviour is also ob-
served in the moments of the He I 4121 Å line in which harmonics up to $4f$ are present.
However the moments of the Si II 4128-4130 Å doublet do not show a clear variability
although the frequency f seems to be present in the Si II 4128 Å line. From the very
different temporal behaviour of both Si and He lines it is clear that pulsation is not the
cause of the variability of the star. We interpreted it by rotational modulation and we
modelled the abundance surface distributions of silicon and helium by means of Doppler
mapping. The main result is that the distribution of helium on the stellar surface has a lot
of contrasts which makes the mean helium abundance vary by 0.8 dex over the rotation
period. No magnetic field has already been searched for this star.
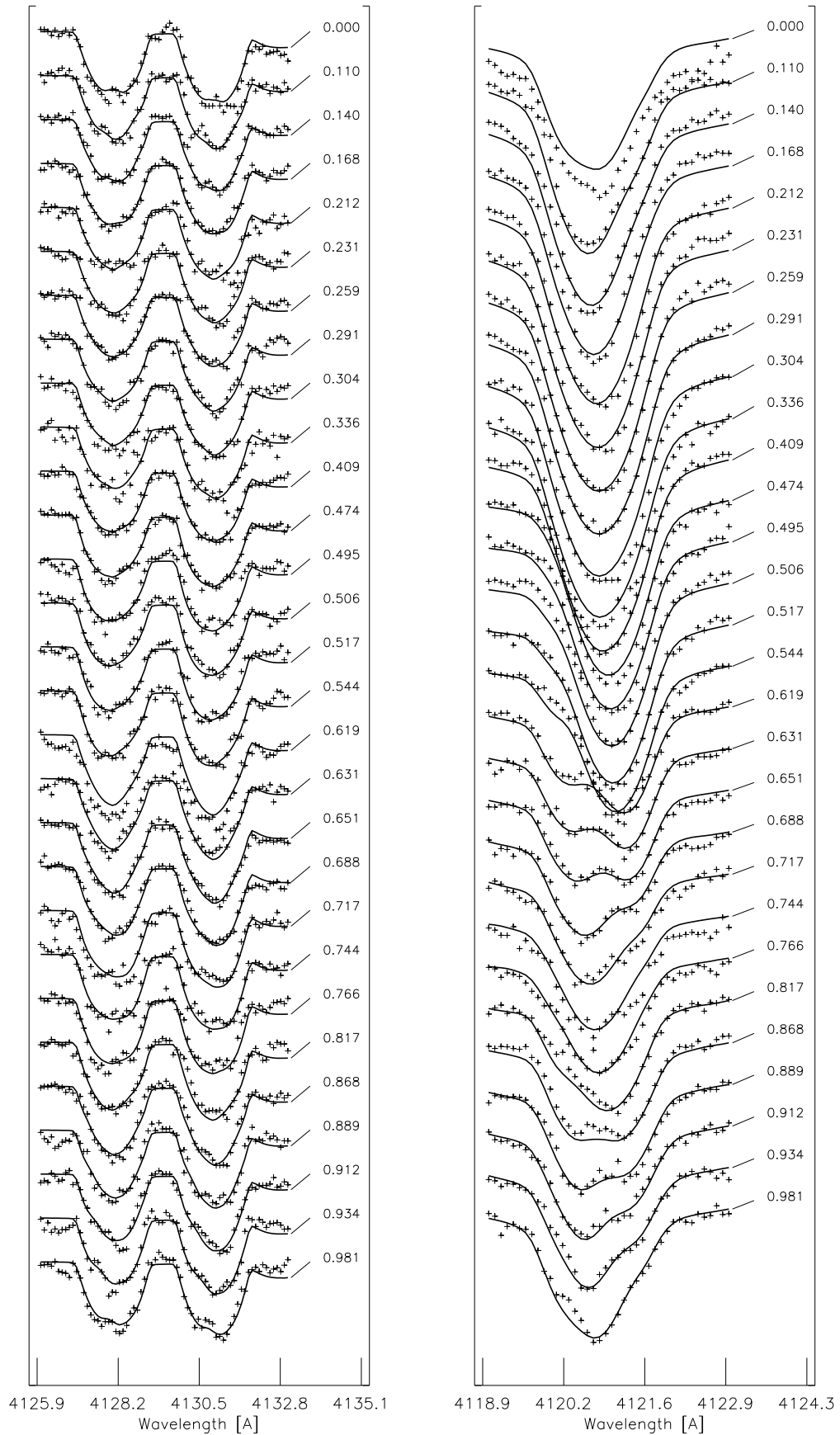
Figure 11.7: Observed line profiles (crosses) of the Si II 4128-4130 Å lines (left) and of the He I 4121 Å line (right) at different phases of observation and computed line profiles (full lines) obtained with INVERS11.

Summary

In the following table we summarize the physical parameters that we found for the four chemically peculiar B stars that we studied in Part III. Rotation periods are well determined, which is the case of very few B stars. Equatorial velocities are around 100 km s^{-1}. Silicon is found slightly underabundant for the four stars. However their average Si equivalent widths are not too different from the ones of confirmed SPBs (De Cat 2001). Three stars have on average an abundance of helium smaller than the solar one which is -1.05 dex. For HD 131120, helium is underabundant by a factor of 12 and for HD 105382, helium is underabundant by a factor of 4.5. HD 138769 is also He-weak while HD 55522 has on average the helium solar abundance. Future magnetic field measurements on the one hand would be very helpfull to understand the surface abundance patterns of our four studied stars. On the other hand, it would be interesting to try and explain our findings for the surface helium and silicon structures from diffusion processes as they are currently understood.

	HD 131120	HD 105382	HD 138769	HD 55522
T_{eff} (K)	18250 ± 420	17400 ± 400	17500 ± 400	17400 ± 400
$\log g$	4.10 ± 0.15	4.18 ± 0.15	4.22 ± 0.15	4.15 ± 0.15
$\log L/L_\odot$	3.13 ± 0.15	2.89 ± 0.15	2.98 ± 0.15	2.95 ± 0.15
P_{rot} (days)	1.569 ± 0.001	1.295 ± 0.001	2.089 ± 0.001	2.729 ± 0.001
i	$30° \pm 10°$	$50° \pm 10°$	$40° \pm 10°$	$80° \pm 10°$
v_{eq} (km s^{-1})	[86;190]	[75;116]	[85;150]	[70;85]
R ($R_\odot$)	[2.7;5.9]	[1.9;3.0]	[3.5;6.2]	[3.8;4.6]
Average Si abundance (dex)	-4.59	-4.76	-5.35	-4.92
Si abundance range (dex)	$[-4.53;-4.02]$	$[-5.36;-4.16]$	$[-5.70;-5.05]$	$[-5.29;-4.49]$
Average He abundance (dex)	-2.12	-1.70	He-weak	-1.06
He abundance range (dex)	$[-2.53;-1.48]$	$[-2.34;-0.82]$	?	$[-2.26;0.46]$
Magnetic field detection (Gauss)	106 ± 168	?	?	?

Conclusions and outlook

In this thesis, we analysed the variability of several main-sequence B-type stars through their line-profile variations. This study was performed in the framework of a collaboration with members of the University of Leuven who led a long-term project for monitoring candidate slowly pulsating B stars (Aerts et al. 1999 and Mathias et al. 2001) selected among many candidate SPBs discovered from the HIPPARCOS mission (Waelkens et al. 1998).

The main goal of such a study of pulsating B stars is to perform asteroseismology, i.e. to probe their internal structure by using their observed pulsation characteristics. To achieve this, many pulsation modes must be detected and identified. Consequently, high quality data as well as powerful mode identification techniques are needed. Our work contributed to the improvement of the moment method for mode identification from high-resolution spectroscopy. We proposed a numerical version of the technique. This new version requires less computation time than the previous one, allowing users to consider all the information contained in the first three moments of a multiperiodic star and to identify multiple modes simultaneously, leading to only one consistent value for the projected rotational velocity v_Ω, the angle of inclination of the star i, and the intrinsic line-profile width σ, which was not the case for previous versions. This, together with the use of a new discriminant that considers the moments calculated at each time of observation, increases considerably the feasibility and the accuracy of the mode identification for multiperiodic stars. Moreover, the technique is extended to rotating pulsating stars by using Lee & Saio's (1987, 1990) formalism for low-frequency non-radial g-modes. These improvements were necessary for a more confident application of the technique to SPBs which are multiperiodic and for which the rotation period may be of the same order of magnitude as the pulsation periods. Unfortunately, one single unambiguous mode identification will seldom be obtained in current practical applications and a statistically justified test that gives how many candidate combinations of modes must be kept is still lacking. However, the number of possibilities is significantly decreased with our new method and the use of additional observational information (i.e. multicolour photometric data) can allow to pinpoint definitely the wavenumbers of all modes, as was achieved for the β Cephei star 16 Lacertae (Aerts et al. 2003a).

We confirm the pulsational nature of eight northern candidate slowly pulsating B stars and give a list of observed frequencies in HIPPARCOS photometric data and in spectro-

scopic data that were gathered with the AURELIE spectrograph at the Observatoire de Haute-Provence (Mathias et al. 2001). We performed a more detailed analysis of the SPB HD 147394 for which most high-resolution spectra are available thus far. This B 5 IV star is a typical SPB of about 5 $M_\odot$ which is situated in the HR diagram in the centre of the instability strip of such a kind of stars. Our gathered 250 line profiles of the Si II 4128-4130 Å doublet reveal at least three modes. Two frequencies are well determined: $f_1 = 0.8008$ c d^{-1} and $f_2 = 0.7813$ c d^{-1} but due to bad time sampling, the value of the third one $f_3 = 0.7175$ c d^{-1} is less certain and may be one of its aliases. We used our new version of the moment method to identify the corresponding pulsation modes. The use of Lee & Saio's description of the pulsational velocity led to the same set of best solutions as the use of the usual non-rotating model. Several combinations of modes lead to very close values for the discriminant and we are unable to discriminate between some 15-20 solutions. A clear conclusion is that all three modes are non-axisymmetric $\ell \leq 3$ modes. The rotation period of the star must be between 5 and 19 days. By means of the Code Liégeois d'Évolution Stellaire that computes evolutionary model sequences and of a standard adiabatic code that computes the oscillation frequencies, we also showed that the different possibilities for the mode identifications are compatible with current stellar structure models for SPBs. However, as the frequency spectrum revealed only three modes so far and in view of the dense frequency spectra of potential modes, HD 147394 is at present not the best target for a detailed seismic analysis. Indeed, De Cat & Aerts (2002) found several SPBs with a larger number of detected modes, mainly in those objects for which very long-term multicolour photometry is available. It is our intention to apply our improved moment method and the recently improved photometric amplitudes method by Dupret et al. (2003) to all the targets in the list of De Cat & Aerts (2002). With state-of-the-art mode identifications at hand, we subsequently plan to compute numerous theoretical models to derive the stellar parameters of the SPBs with unprecedented precision and, if possible, to derive information on the (internal) rotational behaviour of these massive gravity-mode oscillators, according to the strategy outlined in Aerts et al. (2003b).

When the observed variability is monoperiodic, it can be unclear from the analysis of the variations of one single line profile to which cause they must be attributed. The example of our extensive study of the star HD 105382 (Briquet et al. 2001) speaks for itself: our first attempt to interpret its variability was not successful since we could not choose between rivalling hypotheses which are non-radial pulsation or rotational modulation. Afterwards, we were able to discriminate between stellar pulsation and stellar spots. The analysis of the moment variations of different spectral lines allowed us to exclude the non-radial pulsation model for HD 105382 as well as for three other stars, which were first classified as candidate SPBs: HD 131120, HD 138769 and HD 55522. The peculiarities of these stars compared to confirmed SPBs are the following. The stars appear to be monoperiodic while SPBs of our sample are multiperiodic (De Cat 2001 and Mathias et

al. 2001). The photometry and spectroscopy led to the same period, which is 1.569 days for HD 131120, 1.295 days for HD 105382, 2.089 days for HD 138769 and 2.769 days for HD 55522. The moments of the studied spectral lines are not sinusoidal but harmonics of the frequency are also present in data. For HD 55522, such a non-sinusoidal signal is also observed in HIPPARCOS and Geneva photometry. The moments computed from the Si II 4128-4130 Å doublet and from the He I 4121 Å line do not behave in the same way and are not in phase. The equivalent width variations are large compared to values for SPBs. In particular, the relative EW variation of the He I 4121 Å line for HD 55522 is about 35% which is remarkably large. All these characteristics cannot be reproduced by pulsation. Consequently, we compared the observed monoperiodic variability of the stars to rotational modulation. For HD 131120, we first modelled the line-profile variations by means of a simple model with circular spots for which the flux in the spots differs from the one of the rest of the star. Such a basic model was able to reproduce the first three moment variations of the lines, the large equivalent width variations as well as a different behaviour of moments of silicon and helium lines. We then concluded that a good explanation for the variability of the star is its rotation in the presence of non-homogeneous distributions of elements on the stellar surface. As the moments of the line profiles of the three other stars vary in a very similar way as those of HD 131120, we also interpreted their variability in terms of rotational modulation. For the four stars, we derived stellar surface abundance maps for silicon and helium by means of the Doppler Imaging technique. A future goal is to derive the surface abundance mapping for more elements in these four stars. For HD 131120, we found that helium is significantly depleted over all its stellar surface, which confirms that the star is a He-weak star as already reported in the literature. For this star, regions in which helium is enhanced correspond to regions in which silicon is depleted. This result is also found for HD 105382 that we classify as a new He-weak star since we also found that helium is depleted on average over the whole stellar surface. We suggest that HD 105382 be removed from all Be catalogue since we provide evidence that the star does not belong to this class. HD 138769, which is reported as a shell star in the literature, is clearly a Bp He-weak star for which helium is underabundant compared to the Sun but also silicon. For HD 55522, we found the mean abundance value of helium to vary by 0.8 dex during the stellar rotation. We point out that it is the first time that such detailed spectroscopic analyses and abundance mapping are performed for chemically peculiar B stars with such a high T_{eff} of about 17 500 K. Theoretical diffusion models for such temperatures are needed for a comparison. Moreover, inhomogeneities on the stellar surface are probably correlated to a magnetic field. A search for a magnetic field was only performed for the star HD 131120 but was not conclusive. Such investigations would then be very useful for a better understanding of the surface patterns of these four stars.

Appendix

A.1 The displacement vector in terms of scalar potentials

According to Helmholtz's decomposition theorem, the displacement vector may be expressed as the sum of the gradient of a scalar potential Ψ and the curl of a divergence-free vector potential $\vec{A}$:

$$\vec{\xi} = \text{grad } \Psi + \text{rot } \vec{A} \tag{A.1}$$

with

$$\text{div}\vec{A} = 0 \tag{A.2}$$

(see e.g. Morse and Feshbach 1953, section 1.5).

The curl of $\vec{A}$ may be replaced by the sum of a toroidal and a poloidal component so that Helmholtz's theorem becomes

$$\vec{\xi} = \text{grad } \Psi + \text{rot } (T\vec{e_r}) + \text{rot rot}(P\vec{e_r}), \tag{A.3}$$

where T and P are scalar potentials (see e.g. Morse and Feshbach 1953, section 13.1).

By expressing (A.3) in spherical coordinates, one obtains (2.16).

A.2 The associated Legendre polynomials

The associated Legendre polynomials are given by

$$P_\ell^m(z) = \frac{(1-z^2)^{m/2}}{2^\ell \ell!} \frac{d^{\ell+m}}{dz^{\ell+m}}(z^2-1)^\ell. \tag{A.4}$$

They are the solutions of the associated Legendre equation:

$$(1-z^2)\frac{d^2 P_\ell^m(z)}{dz^2} - 2z\,\frac{dP_\ell^m(z)}{dz} + \left[\ell(\ell+1) - \frac{m^2}{1-z^2}\right] P_\ell^m(z) = 0. \tag{A.5}$$

The following recurrence relations hold:

$$(\ell-m+1)\,P_{\ell+1}^m(z) = (2\ell+1)\,z\,P_\ell^m(z) - (\ell+m)\,P_{\ell-1}^m(z), \tag{A.6}$$

$$(z^2-1)\frac{dP_\ell^m(z)}{dz} = \ell\,z\,P_\ell^m(z) - (\ell+m)\,P_{\ell-1}^m(z) \tag{A.7}$$

(see e.g. Abramowitz and Stegun 1964).

A.3   The amplitudes of the first three moments

$$A_1^j = A_p^j \Big\{ I[C_{\ell_j}^{m_j}] + K_j I[D_{\ell_j}^{m_j}] \Big\},$$

$$C_1^j = \frac{1}{2}(A_p^j)^2 \Big\{ I[(C_{\ell_j}^{m_j})^2 - (E_{\ell_j}^{m_j})^2] + 2K_j I[C_{\ell_j}^{m_j} D_{\ell_j}^{m_j} - E_{\ell_j}^{m_j} F_{\ell_j}^{m_j}] + K_j^2 I[(D_{\ell_j}^{m_j})^2 - (F_{\ell_j}^{m_j})^2] \Big\},$$

$$D_2^j = 2\, v_\Omega\, A_p^j \Big\{ I[E_{\ell_j}^{m_j} \sin\theta\, \sin\phi] + K_j I[F_{\ell_j}^{m_j} \sin\theta\, \sin\phi] \Big\},$$

$$C_{b1}^{jk} = \frac{1}{2} A_p^j A_p^k \Big\{ I[C_{\ell_j}^{m_j} C_{\ell_k}^{m_k} + E_{\ell_j}^{m_j} E_{\ell_k}^{m_k}] + K_j I[D_{\ell_j}^{m_j} C_{\ell_k}^{m_k} + F_{\ell_j}^{m_j} E_{\ell_k}^{m_k}] + K_k I[C_{\ell_j}^{m_j} D_{\ell_k}^{m_k} + E_{\ell_j}^{m_j} F_{\ell_k}^{m_k}]$$
$$+K_j K_k I[D_{\ell_j}^{m_j} D_{\ell_k}^{m_k} + F_{\ell_j}^{m_j} F_{\ell_k}^{m_k}] \Big\},$$

$$C_{s1}^{jk} = \frac{1}{2} A_p^j A_p^k \Big\{ I[C_{\ell_j}^{m_j} C_{\ell_k}^{m_k} - E_{\ell_j}^{m_j} E_{\ell_k}^{m_k}] + K_j I[D_{\ell_j}^{m_j} C_{\ell_k}^{m_k} - F_{\ell_j}^{m_j} E_{\ell_k}^{m_k}] + K_k I[C_{\ell_j}^{m_j} D_{\ell_k}^{m_k} - E_{\ell_j}^{m_j} F_{\ell_k}^{m_k}]$$
$$+K_j K_k I[D_{\ell_j}^{m_j} D_{\ell_k}^{m_k} - F_{\ell_j}^{m_j} F_{\ell_k}^{m_k}] \Big\},$$

$$E_{12}^j = \frac{1}{2}(A_p^j)^2 \Big\{ I[(C_{\ell_j}^{m_j})^2 + (E_{\ell_j}^{m_j})^2] + 2K_j I[C_{\ell_j}^{m_j} D_{\ell_j}^{m_j} + E_{\ell_j}^{m_j} F_{\ell_j}^{m_j}] + K_j^2 I[(D_{\ell_j}^{m_j})^2 + (F_{\ell_j}^{m_j})^2] \Big\},$$

$$E_{\rm rot} = v_\Omega^2 I[\sin^2\theta\, \sin^2\phi],$$

$$F_1^j = \frac{1}{4}(A_p^j)^3 \Big\{ I[(C_{\ell_j}^{m_j})^3] + 3K_j I[(C_{\ell_j}^{m_j})^2 D_{\ell_j}^{m_j}] + 3K_j^2 I[C_{\ell_j}^{m_j} (D_{\ell_j}^{m_j})^2] + K_j^3 I[(D_{\ell_j}^{m_j})^3] \Big\}$$
$$-\frac{3}{4}(A_p^j)^3 \Big\{ I[C_{\ell_j}^{m_j} (E_{\ell_j}^{m_j})^2] + K_j \Big(I[D_{\ell_j}^{m_j} (E_{\ell_j}^{m_j})^2] + 2I[C_{\ell_j}^{m_j} E_{\ell_j}^{m_j} F_{\ell_j}^{m_j}] \Big)$$
$$+K_j^2 \Big(I[C_{\ell_j}^{m_j} (F_{\ell_j}^{m_j})^2] + 2I[D_{\ell_j}^{m_j} E_{\ell_j}^{m_j} F_{\ell_j}^{m_j}] \Big) + K_j^3 I[D_{\ell_j}^{m_j} (F_{\ell_j}^{m_j})^2] \Big\},$$

$$G_2^j = 3v_\Omega(A_p^j)^2 \Big\{ I[C_{\ell_j}^{m_j} E_{\ell_j}^{m_j} \sin\theta\, \sin\phi] + K_j I[C_{\ell_j}^{m_j} F_{\ell_j}^{m_j} \sin\theta\, \sin\phi + D_{\ell_j}^{m_j} E_{\ell_j}^{m_j} \sin\theta\, \sin\phi]$$
$$+K_j^2 I[D_{\ell_j}^{m_j} F_{\ell_j}^{m_j} \sin\theta\, \sin\phi] \Big\},$$

$$RST_1^j = 3v_\Omega^2 A_p^j \Big\{ I[C_{\ell_j}^{m_j} \sin^2\theta\, \sin^2\phi] + K_j I[D_{\ell_j}^{m_j} \sin^2\theta\, \sin^2\phi] \Big\} + 3\sigma^2 \Big\{ I[C_{\ell_j}^{m_j}] + K_j I[D_{\ell_j}^{m_j}] \Big\}$$
$$+\frac{3}{4}(A_p^j)^3 \Big\{ I[(C_{\ell_j}^{m_j})^3] + 3K_j I[(C_{\ell_j}^{m_j})^2 D_{\ell_j}^{m_j}] + 3K_j^2 I[C_{\ell_j}^{m_j} (D_{\ell_j}^{m_j})^2] + K_j^3 I[(D_{\ell_j}^{m_j})^3] \Big\}$$
$$+\frac{3}{4}(A_p^j)^3 \Big\{ I[C_{\ell_j}^{m_j} (E_{\ell_j}^{m_j})^2] + K_j \Big(I[D_{\ell_j}^{m_j} (E_{\ell_j}^{m_j})^2] + 2I[C_{\ell_j}^{m_j} E_{\ell_j}^{m_j} F_{\ell_j}^{m_j}] \Big)$$
$$+K_j^2 \Big(I[C_{\ell_j}^{m_j} (F_{\ell_j}^{m_j})^2] + 2I[D_{\ell_j}^{m_j} E_{\ell_j}^{m_j} F_{\ell_j}^{m_j}] \Big) + K_j^3 I[D_{\ell_j}^{m_j} (F_{\ell_j}^{m_j})^2] \Big\},$$

$$G_{b2}^{jk} = -3v_\Omega\, A_p^j A_p^k \Big\{ I[C_{\ell_j}^{m_j} E_{\ell_k}^{m_k}\, \sin\theta\, \sin\phi]$$
$$+K_j I[D_{\ell_j}^{m_j} E_{\ell_k}^{m_k}\, \sin\theta\, \sin\phi] + K_k I[C_{\ell_j}^{m_j} F_{\ell_k}^{m_k}\, \sin\theta\, \sin\phi] + K_j K_k I[D_{\ell_j}^{m_j} F_{\ell_k}^{m_k}\, \sin\theta\, \sin\phi] \Big\},$$

$$G_{s2}^{jk} = 3v_\Omega A_p^j A_p^k \Big\{ I[C_{\ell_j}^{m_j} E_{\ell_k}^{m_k}\, \sin\theta\, \sin\phi]$$
$$+K_j I[D_{\ell_j}^{m_j} E_{\ell_k}^{m_k}\, \sin\theta\, \sin\phi] + K_k I[C_{\ell_j}^{m_j} F_{\ell_k}^{m_k}\, \sin\theta\, \sin\phi] + K_j K_k I[D_{\ell_j}^{m_j} F_{\ell_k}^{m_k}\, \sin\theta\, \sin\phi] \Big\},$$

$$F_{11}^{jkn} = -\frac{3}{4}A_p^j\,A_p^k\,A_p^n\Big\{I[E_{\ell_j}^{m_j}C_{\ell_k}^{m_k}E_{\ell_n}^{m_n}] + K_jI[F_{\ell_j}^{m_j}C_{\ell_k}^{m_k}E_{\ell_n}^{m_n}] + K_kI[E_{\ell_j}^{m_j}D_{\ell_k}^{m_k}E_{\ell_n}^{m_n}] + K_nI[C_{\ell_j}^{m_j}C_{\ell_k}^{m_k}F_{\ell_n}^{m_n}]$$

$$+K_jK_kI[F_{\ell_j}^{m_j}D_{\ell_k}^{m_k}E_{\ell_n}^{m_n}] + K_jK_nI[F_{\ell_j}^{m_j}C_{\ell_k}^{m_k}F_{\ell_n}^{m_n}] + K_kK_nI[E_{\ell_j}^{m_j}D_{\ell_k}^{m_k}F_{\ell_n}^{m_n}] + K_jK_kK_nI[F_{\ell_j}^{m_j}D_{\ell_k}^{m_k}F_{\ell_n}^{m_n}]\Big\}$$

$$+\frac{1}{4}A_p^j\,A_p^k\,A_p^n\Big\{I[C_{\ell_j}^{m_j}C_{\ell_k}^{m_k}C_{\ell_n}^{m_n}] + K_jI[D_{\ell_j}^{m_j}C_{\ell_k}^{m_k}C_{\ell_n}^{m_n}] + K_kI[C_{\ell_j}^{m_j}D_{\ell_k}^{m_k}C_{\ell_n}^{m_n}] + K_nI[C_{\ell_j}^{m_j}C_{\ell_k}^{m_k}D_{\ell_n}^{m_n}]$$

$$+K_jK_kI[D_{\ell_j}^{m_j}D_{\ell_k}^{m_k}C_{\ell_n}^{m_n}] + K_jK_nI[D_{\ell_j}^{m_j}C_{\ell_k}^{m_k}D_{\ell_n}^{m_n}] + K_kK_nI[C_{\ell_j}^{m_j}D_{\ell_k}^{m_k}D_{\ell_n}^{m_n}] + K_jK_kK_nI[D_{\ell_j}^{m_j}D_{\ell_k}^{m_k}D_{\ell_n}^{m_n}]\Big\},$$

$$F_{21}^{jkn} = \frac{3}{4}A_p^j\,A_p^k\,A_p^n\Big\{I[E_{\ell_j}^{m_j}C_{\ell_k}^{m_k}E_{\ell_n}^{m_n}] + K_jI[F_{\ell_j}^{m_j}C_{\ell_k}^{m_k}E_{\ell_n}^{m_n}] + K_kI[E_{\ell_j}^{m_j}D_{\ell_k}^{m_k}E_{\ell_n}^{m_n}] + K_nI[C_{\ell_j}^{m_j}C_{\ell_k}^{m_k}F_{\ell_n}^{m_n}]$$

$$+K_jK_kI[F_{\ell_j}^{m_j}D_{\ell_k}^{m_k}E_{\ell_n}^{m_n}] + K_jK_nI[F_{\ell_j}^{m_j}C_{\ell_k}^{m_k}F_{\ell_n}^{m_n}] + K_kK_nI[E_{\ell_j}^{m_j}D_{\ell_k}^{m_k}F_{\ell_n}^{m_n}] + K_jK_kK_nI[F_{\ell_j}^{m_j}D_{\ell_k}^{m_k}F_{\ell_n}^{m_n}]\Big\}$$

$$+\frac{1}{4}A_p^j\,A_p^k\,A_p^n\Big\{I[C_{\ell_j}^{m_j}C_{\ell_k}^{m_k}C_{\ell_n}^{m_n}] + K_jI[D_{\ell_j}^{m_j}C_{\ell_k}^{m_k}C_{\ell_n}^{m_n}] + K_kI[C_{\ell_j}^{m_j}D_{\ell_k}^{m_k}C_{\ell_n}^{m_n}] + K_nI[C_{\ell_j}^{m_j}C_{\ell_k}^{m_k}D_{\ell_n}^{m_n}]$$

$$+K_jK_kI[D_{\ell_j}^{m_j}D_{\ell_k}^{m_k}C_{\ell_n}^{m_n}] + K_jK_nI[D_{\ell_j}^{m_j}C_{\ell_k}^{m_k}D_{\ell_n}^{m_n}] + K_kK_nI[C_{\ell_j}^{m_j}D_{\ell_k}^{m_k}D_{\ell_n}^{m_n}] + K_jK_kK_nI[D_{\ell_j}^{m_j}D_{\ell_k}^{m_k}D_{\ell_n}^{m_n}]\Big\},$$

$$F_{31}^{jkn} = -\frac{3}{4}A_p^j\,A_p^k\,A_p^n\Big\{I[E_{\ell_j}^{m_j}C_{\ell_k}^{m_k}E_{\ell_n}^{m_n}] + K_jI[F_{\ell_j}^{m_j}C_{\ell_k}^{m_k}E_{\ell_n}^{m_n}] + K_kI[E_{\ell_j}^{m_j}D_{\ell_k}^{m_k}E_{\ell_n}^{m_n}] + K_nI[C_{\ell_j}^{m_j}C_{\ell_k}^{m_k}F_{\ell_n}^{m_n}]$$

$$+K_jK_kI[F_{\ell_j}^{m_j}D_{\ell_k}^{m_k}E_{\ell_n}^{m_n}] + K_jK_nI[F_{\ell_j}^{m_j}C_{\ell_k}^{m_k}F_{\ell_n}^{m_n}] + K_kK_nI[E_{\ell_j}^{m_j}D_{\ell_k}^{m_k}F_{\ell_n}^{m_n}] + K_jK_kK_nI[F_{\ell_j}^{m_j}D_{\ell_k}^{m_k}F_{\ell_n}^{m_n}]\Big\}$$

$$+\frac{1}{4}A_p^j\,A_p^k\,A_p^n\Big\{I[C_{\ell_j}^{m_j}C_{\ell_k}^{m_k}C_{\ell_n}^{m_n}] + K_jI[D_{\ell_j}^{m_j}C_{\ell_k}^{m_k}C_{\ell_n}^{m_n}] + K_kI[C_{\ell_j}^{m_j}D_{\ell_k}^{m_k}C_{\ell_n}^{m_n}] + K_nI[C_{\ell_j}^{m_j}C_{\ell_k}^{m_k}D_{\ell_n}^{m_n}]$$

$$+K_jK_kI[D_{\ell_j}^{m_j}D_{\ell_k}^{m_k}C_{\ell_n}^{m_n}] + K_jK_nI[D_{\ell_j}^{m_j}C_{\ell_k}^{m_k}D_{\ell_n}^{m_n}] + K_kK_nI[C_{\ell_j}^{m_j}D_{\ell_k}^{m_k}D_{\ell_n}^{m_n}] + K_jK_kK_nI[D_{\ell_j}^{m_j}D_{\ell_k}^{m_k}D_{\ell_n}^{m_n}]\Big\},$$

$$F_{41}^{jkn} = \frac{3}{4}A_p^j\,A_p^k\,A_p^n\Big\{I[E_{\ell_j}^{m_j}C_{\ell_k}^{m_k}E_{\ell_n}^{m_n}] + K_jI[F_{\ell_j}^{m_j}C_{\ell_k}^{m_k}E_{\ell_n}^{m_n}] + K_kI[E_{\ell_j}^{m_j}D_{\ell_k}^{m_k}E_{\ell_n}^{m_n}] + K_nI[C_{\ell_j}^{m_j}C_{\ell_k}^{m_k}F_{\ell_n}^{m_n}]$$

$$+K_jK_kI[F_{\ell_j}^{m_j}D_{\ell_k}^{m_k}E_{\ell_n}^{m_n}] + K_jK_nI[F_{\ell_j}^{m_j}C_{\ell_k}^{m_k}F_{\ell_n}^{m_n}] + K_kK_nI[E_{\ell_j}^{m_j}D_{\ell_k}^{m_k}F_{\ell_n}^{m_n}] + K_jK_kK_nI[F_{\ell_j}^{m_j}D_{\ell_k}^{m_k}F_{\ell_n}^{m_n}]\Big\}$$

$$+\frac{1}{4}A_p^j\,A_p^k\,A_p^n\Big\{I[C_{\ell_j}^{m_j}C_{\ell_k}^{m_k}C_{\ell_n}^{m_n}] + K_jI[D_{\ell_j}^{m_j}C_{\ell_k}^{m_k}C_{\ell_n}^{m_n}] + K_kI[C_{\ell_j}^{m_j}D_{\ell_k}^{m_k}C_{\ell_n}^{m_n}] + K_nI[C_{\ell_j}^{m_j}C_{\ell_k}^{m_k}D_{\ell_n}^{m_n}]$$

$$+K_jK_kI[D_{\ell_j}^{m_j}D_{\ell_k}^{m_k}C_{\ell_n}^{m_n}] + K_jK_nI[D_{\ell_j}^{m_j}C_{\ell_k}^{m_k}D_{\ell_n}^{m_n}] + K_kK_nI[C_{\ell_j}^{m_j}D_{\ell_k}^{m_k}D_{\ell_n}^{m_n}] + K_jK_kK_nI[D_{\ell_j}^{m_j}D_{\ell_k}^{m_k}D_{\ell_n}^{m_n}]\Big\}.$$

A.4   Three moments are sufficient for mode identification

In all versions of the moment method for slowly rotating stars, one limits the discriminating function for mode identification to the first three moments (Balona 1986ab, 1987; Aerts et al. 1992, Aerts 1996). We provide here a justification for this.

For one mode, we rewrite the first three moments as follows:

$$<v>(t) = A\cos(2\pi ft + \psi)$$
$$<v^2>(t) = C\cos(2(2\pi f)t + 2\psi) + D\sin(2\pi ft + \psi) + E + E_{\rm rot} + \sigma^2$$
$$<v^3>(t) = F\cos(3(2\pi f)t + 3\psi) + G\sin(2(2\pi f)t + 2\psi) + RST\cos(2\pi ft + \psi),$$

with

$$\begin{cases} A = A_p(c_1 + c_2 K) \\ C = A_p^2(c_3 + c_4 K + c_5 K^2) \\ F = A_p^3(c_6 + c_7 K + c_8 K^2 + c_9 K^3) \end{cases}$$

where c_1, c_2, ..., c_9 depend on (ℓ, m, i).

Aerts et al. (1992) have shown that the second moment discriminates easily between axisymmetric modes and non-axisymmetric modes.

We search for different (ℓ, m) and (ℓ', m') so that $< v > (t) = < v >' (t)$, $< v^2 > (t) = < v^2 >' (t)$ and $< v^3 > (t) = < v^3 >' (t)$ for all t, i.e. so that $A = A'$, $C = C'$, $F = F'$ for appropriate values of the parameters. We use the fact that the K-value is determined for a given star and for a given frequency ($K = K'$). For chosen (ℓ, m, i) and (ℓ', m', i'), we then have the following system of three equations for A_p, A'_p and K to solve:

$$\begin{cases} (1)\ A_p(c_1 + c_2 K) = A'_p(c'_1 + c'_2 K) \\ (2)\ A_p^2(c_3 + c_4 K + c_5 K^2) = A_p'^2(c'_3 + c'_4 K + c'_5 K^2) \\ (3)\ A_p^3(c_6 + c_7 K + c_8 K^2 + c_9 K^3) = A_p'^3(c'_6 + c'_7 K + c'_8 K^2 + c'_9 K^3). \end{cases}$$

One excludes (ℓ, m, i) for which the first moment has no time variation, which corresponds to $c_1 = 0$ and $c_2 = 0$. One also considers $m = 0$, ..., ℓ since the absolute value of the amplitudes of the moments are the same for positive and negative m.

From (1) and (2) ($A_p, A'_p \neq 0$), one obtains an equation in K which can be solved analytically for chosen (ℓ, m, i) and (ℓ', m', i'):

$(c_1^{2'} c_3 - c_1^2 c'_3) + (c_1^{2'} c_4 + 2c'_1 c'_2 c_3 - c_1^2 c'_4 - 2c_1 c_2 c'_3)K + (c_1^{2'} c_5 + c_2^{2'} c_3 + 2c'_1 c'_2 c_4 - c_1^2 c'_5 - c_2^2 c'_3 - 2c_1 c_2 c'_4)K^2 + (c_1^{2'} c_4 + 2c'_1 c'_2 c_5 - c_1^2 c'_4 - 2c_1 c_2 c'_5)K^3 + (c_2^{2'} c_5 - c_2^2 c'_5)K^4 = 0.$

The coefficients of this equation are not simultaneously equal to zero. Consequently, the equation has four solutions or less.

From (1) and (3) as well as from (2) and (3), one obtains two equations in K, which must also be satisfied by the solutions. We tested numerically the feasibility of more than one solution (ℓ, m, i) by varying ℓ from 0 to 4 with $m = 0$, ..., ℓ. We varied i from $0°$ to $90°$ with a step of $1°$. For each combination (ℓ, m, i) and (ℓ', m', i'), we searched for solutions which satisfy the equations in K. Note that we did not confront an axisymmetric mode with a non-axisymmetric mode since they are discriminated by the behaviour of the second moment. We did not confront the same couples of wavenumbers with different i either. The outcome is that the system of three equations (1), (2) and (3) has no solution for each tested case. So the first three moments discriminate the different modes whatever the values of the velocity parameters are.

In practice, because of too few and/or too noisy data, and because of the uncertainty of K, it obviously happens that several couples (ℓ, m) fit the moment variations with almost the same quality. However, the message we want to bring here is that it in principle suffices to consider the three moments to discriminate between the wavenumbers.

References

Abramowitz M., **Stegun I.**, 1964, Dower Publications, New York, *Handbook of mathematical functions*

Abt H., **Morrell N.**, 1995, ApJS 99, 135, *The relation between rotational velocities and spectral peculiarities among A-type stars*

Abt H.A., **Cardona O.**, 1984, ApJ 285, 190, *Be stars in binaries*

Adelman S.J., **Caliskan H.**, **Kocer D.**, **Kablan H.**, **Yüce K.**, **Engin S.**, 2001, A&A 371, 1078, *Elemental abundance analyses with DAO spectrograms. XXV. The superficially normal B and A stars α Draconis, τ Herculis, γ Lyrae, and HR 7926*

Adelman S.J., **Davis Philip A.G.**, 1996, MNRAS 282, 1181, *Elemental abundances of the B and A stars. III. Gamma Geminorum, HR 1397, HR 2154, HD 60825 and 7 Sextantis*

Aerts C., **Lehmann H.**, **Briquet M.**, **Scuflaire R.**, **Dupret M.A.**, **De Ridder J.**, **Thoul A.**, 2003a, A&A, in press, *Spectroscopic mode identification for the β Cephei star EN (16) Lacertae*

Aerts C., **Scuflaire R.**, **Thoul A.**, 2003b, In IAU Symposium 215: Stellar Rotation, eds. A. Maeder & P. Eenens, ASP Conference Series, in press

Aerts C., 2000, ASP Conference Proceedings, Vol. 214, p. 192, *Multimode detections from surveys*

Aerts C., **De Cat P.**, **Peeters E.**, **Decin L.**, **De Ridder J.**, **Kolenberg K.**, **Meeus G.**, **Van Winckel H.**, **Cuypers J.**, **Waelkens C.**, 1999, A&A 343, 872, *Selection of a sample of bright southern slowly pulsating B stars for long-term photometric and spectroscopic monitoring*

Aerts C., **De Cat P.**, **Cuypers J.**, **Becker S.R.**, **Mathias P.**, **De Mey K.**, **Gillet D.**, **Waelkens C.**, 1998, A&A 329, 137, *Evidence for binarity and multiperiodicity in the β Cephei star β Crucis*

Aerts C., 1996, A&A 314, 115, *Mode identification of pulsating stars from line-profile variations with the moment method: a more accurate discriminant*

Aerts C., **Waelkens C.**, 1993, A&A 273, 135, *Line-profile variations of rotating pulsating stars*

Aerts C., **De Pauw M.**, **Waelkens C.**, 1992, A&A 266, 294, *Mode identification of pulsating stars from line-profile variations with the moment method. An example - The β Cephei star δ Ceti*

Balona L.A., **Aerts C.**, **Stefl S.**, 1999, MNRAS 305, 519, *Simultaneous photometry and spectroscopy of the Be star 28 (ω) CMa. II. Line profile modelling*

Balona L.A., 1987, MNRAS 224, 41, *Mode identification from line-profile variations. III. Temperature variation and toroidal modes*

Balona L.A., 1986a, MNRAS 220, 647, *Mode identification from line-profile variations. II. A quantitative least-squares algorithm*

Balona L.A., 1986b, MNRAS 219, 111, *Mode identification from line-profile variations*

Borra E.F., **Landstreet J.D.**, **Thompson I.**, 1983, ApJS 53, 151, *The magnetic fields of the helium-weak B stars*

Boury A., **Gabriel M.**, **Noels A.**, **Scuflaire R.**, **Ledoux P.**, 1975, A&A 41, 279, *Vibrational instability of a 1 solar mass star towards non-radial oscillations*

Breger M., **Stich J.**, **Garrido R.**, **Martin B.**, **Jiang S.Y.**, **Li Z.P.**, **Hube D.P.**, **Ostermann W.**, **Paparo M.**, **Scheck M.**, 1993, A&A 271, 482, *Nonradial pulsation of the δ Scuti star BU Cancri in the Praesepe cluster*

Briquet M., **Aerts C.**, **De Cat P.**, 2001, A&A 366, 121, *Optical variability of the B-type star HD 105382: pulsation or rotation?*

Catalano F.A., **Renson P.**, 1997, A&AS 121, 57, *Fourth supplement to the catalogue of observed periods of Ap stars*

Chapellier E., **Sadsaoud H.**, **Valtier J.C.**, **Garrido R.**, **Sareyan J.P.**, **Le Contel J.M.**, **Alvarez M.**, 1998, A&A 331, 1046, *53 Persei: a slowly pulsating B star*

Chapellier E., **Lecontel J.M.**, **Lecontel D.**, **Sareyan J.P.**, **Valtier J.C.**, 1995, A&A 304, 406, *Pulsation and binarity in β Cephei stars. II. 16 Lacertae*

Claria J.J., **Escosteguy L.A.**, 1981, PASP 93, 636, *Narrow-band photometry of bright Be stars*

Cuypers J., **Aerts C.**, **Buzasi D.**, **Catanzarite J.**, **Conrow T.**, **Laher R.**, 2002, A&A 392, 599, *Multiperiodicity in the light variations of the β Cephei star β Crucis*

Dachs J., **Eichendorf W.**, **Schleicher H.**, **Schmidt-Kaler T.**, **Stift M.**, **Tueg H.**, 1981, A&AS 43, 427, *Photoelectric scanner measurements of Balmer emission line profiles for southern Be stars. II. A survey for variations*

De Cat P., 2002, ASP Conference Series, Vol. 259, p. 196, *An observational overview of pulsations in β Cephei stars and slowly pulsating B stars*

De Cat P., **Aerts C.**, 2002, A&A 393, 965, *A study of bright southern slowly pulsating B stars. II. The intrinsic frequencies*

De Cat P., 2001, *An observational study of bright southern slowly pulsating B stars*, PhD Thesis, Katholieke Universiteit Leuven, Belgium

De Cat P., **Aerts C.**, **De Ridder J.**, **Kolenberg K.**, **Meeus G.**, **Decin L.**, 2000, A&A 355, 1015, *A study of bright southern slowly pulsating B stars. I. Determination of the orbital parameters and of the main frequency of the spectroscopic binaries*

de Geus E.J., **de Zeeuw P.T.**, **Lub J.**, 1989, A&A 216, 44, *Physical parameters of stars in the Scorpio-Centaurus OB association*

De Ridder J., **Dupret M.A.**, **Neuforge C.**, **Aerts C.**, 2002a, A&A 385, 572, *Influence of non-adiabatic temperature variations on line-profile variations of slowly rotating β Cephei stars and SPBs. II. Simulations of line profile time series*

De Ridder J., **Molenberghs G.**, **Aerts C.**, 2002b, in "Asteroseismology across the HR diagram", Kluwer Academic Publishers, in press

De Ridder J., 2001, *Contributions to the interpretation of line-profile variations of pulsating B stars*, PhD Thesis, Katholieke Universiteit Leuven, Belgium

De Ridder J., **Gordon K.D.**, **Muliss C.L.**, **Aerts C.**, 1999, A&A 341, 574, *New observations of 53 Persei*

Didelon P., 1982, A&AS 50, 199, *Equivalent widths of spectral lines in B stars*

Dupret M.A., **De Ridder J.**, **De Cat P.**, **Aerts C.**, **Scuflaire R.**, **Noels A.**, **Thoul A.**, 2003, A&A 398, 677, *A photometric mode identification method, including an improved non-adiabatic treatment of the atmosphere*

Dupret M.A., **De Ridder J.**, **Neuforge C.**, **Aerts C.**, **Scuflaire R.**, 2002, A&A 385, 563, *Influence of non-adiabatic temperature variations on line-profile variations of slowly rotating β Cep stars and SPBs. I. Non-adiabatic eigenfunctions in the atmosphere of a pulsating star*

Dupret M.A., 2001, A&A 366, 166, *Nonradial nonadiabatic stellar pulsations: a numerical method and its application to a β Cephei model*

Dziembowski W.A., **Moskalik P.**, **Pamyatnykh A.A.**, 1993, MNRAS 265, 588, *The opacity mechanism in B-type stars. II. Excitation of high-order g-modes in main sequence stars*

Eyer L., 1998, *Les étoiles variables de la mission Hipparcos*, PhD Thesis, Geneva University, Switzerland

Flower P.J., 1996, ApJ 469, 355, *Transformations from theoretical Hertzsprung-Russell diagrams to color-magnitude diagrams: effective temperatures, B-V colors, and bolometric corrections*

Garrison R.F., 1967, ApJ 147, 1003, *Some characteristics of the B and A stars in the upper Scorpius Complex*

Gautschy A., **Saio H.**, 1993, MNRAS 262, 213, *On non-radial oscillations of B-type stars*

Golay M., 1980, Vistas in Astronomy 24, 141, *The Geneva seven-colour photometric system*

Gummersbach C.A., **Kaufer A.**, **Schäfer D.R.**, **Szeifert T.**, **Wolf B.**, 1998, A&A 338, 881, *B stars and the chemical evolution of the galactic disk*

Heynderickx D., **Waelkens C.**, **Smeyers P.**, 1994, A&AS 105, 447, *A photometric study of β Cephei stars. II. Determination of the degrees ℓ of pulsation modes*

Hiltner W.A., **Garrison R.F.**, **Schild R.E.**, 1969, ApJ 157, 313, *MK spectral types for bright southern OB stars*

Hube D.P., **Aikman G.C.L.**, 1991, PASP 103, 49, *3 Vulpeculae - A nonradial pulsator in a one-year binary system*

Jakate S.M., 1979, AJ 84, 552, *A search for β Cephei stars. III. Photometric studies of southern B-type stars*

Jaschek C., **Jaschek M.**, 1992, A&A 95, 535, *A southern Be star survey - Spectra and envelope radii*

Jerzykiewicz M., **Sterken C.**, AcA 27, 365, *Search for β Cephei stars south of declination -20 deg. I. Incidence of light variability among early B giants and subgiants: Summer objects*

Jurkevich I., 1971, Ap&SS 13, 154, *A method of computing periods of cyclic phenomena*

Künzli M., **North P.**, **Kurucz R.L.**, **Nicolet B.**, 1997, A&ASS 122, 51, *A calibration of Geneva photometry for B to G stars in terms of T_{eff}, log g and [M/H]*

Kurucz R.L., 1993, ATLAS9, Stellar atmospheres programs, CD-ROM No. 13, Smithonian Astrophysical Observatory

Kuschnig R., 1998, *Surface abundance structures of Ap stars*, PhD Thesis, University of Vienna, Austria

Lee U., **Saio H.**, 1990, ApJ 349, 570, *Line-profile variations caused by low-frequency nonradial pulsations of rapidly rotating stars*

Lee U., **Saio H.**, 1987, MNRAS 224, 513, *Low-frequency oscillations of uniformly rotating stars*

Lehmann H., **Harmanec P.**, **Aerts C.**, **Bozic H.**, **Eenens P.**, **Hildebrandt G.**, **Holmgren D.**, **Mathias P.**, **Scholz G.**, **Slechta M.**, **Yang S.**, 2001, A&A 367, 236, *A new analysis of the radial velocity variations of the eclipsing and spectroscopic binary EN Lacertae*

Lomb N.R., 1976, Ap&SS 39, 447, *Least-squares frequency analysis of unequally spaced data*

Lüftinger T., 2000, *Elemental distribution on the surface of ϵ Ursae Majoris*, Master Thesis, University of Vienna, Austria

Maintz M., **Rivinius T.**, **Tubbesing S.**, **Wolf B.**, 2000, PASP Conference Series, Vol. 214, p. 244, *Non-radial pulsation modeling of $\omega(28)$ CMa*

Masuda S., **Hirata R.**, 2000, A&A 356, 209, *Line-profile variation in τ Herculis*

Mathias P., **Aerts C.**, **Briquet M.**, **De Cat P.**, **Cuypers J.**, **Van Winckel H.**, **Le Contel J.M.**, 2001, A&A 379, 905, *Spectroscopic monitoring of 10 new northern slowly pulsating B star candidates discovered from the HIPPARCOS mission*

Mathias P., **Aerts C.**, **de Pauw M.**, **Gillet D.**, **Waelkens C.**, 1994, A&A 283, 813, *A spectroscopic analysis of the β Cephei star α Lupi*

Michaud G., 1970, ApJ 160, 641, *Diffusion processes in peculiar A stars*

Morse P., **Feshbach H.**, 1953, Mc Graw-Hill book Company, New York, *Methods of theoretical physics*

Norris J., 1971, ApJS 23, 213, *Neutral-helium line strengths. V. The weak-helium stars of population I*

North P., **Nicolet B.**, 1990, A&A 228, 78, *A new calibration of Geneva photometry in terms of T_{eff}, log g and mass for B stars*

Pamyatnykh A.A., 1999, AcA 49, 119, *Pulsational instability domains in the upper main sequence*

Piskunov N.E., **Rice J.B.**, 1993, PASP 105, 1415, *Techniques for surface imaging of stars*

Preston G.W., 1974, ARA&A 12, 257, *The chemically peculiar stars of the upper main sequence*

Rice J.B., 1996, IAUS 176, 19, *Doppler imaging of stellar surfaces (review)*

Roberts D.H., **Lehar J.**, **Dreher J.W.**, 1987, AJ 93, 968, *Time series analysis with Clean. I. Derivation of a spectrum*

SAS/User's Guide, 1990, Version 6, Volume 1-2, SAS Institute Inc., Cary, NC

Scargle J.D., 1981, ApJS 45, 1, *Studies in astronomical time series analysis. I. Modeling random processes in the time domain*

Schaller G., **Schaerer D.**, **Meynet G.**, **Maeder A.**, 1992, A&A 96, 269, *New grids of stellar models from 0.8 to 120 solar masses at Z = 0.020 and Z = 0.001*

Schrijvers C., **Telting J.H.**, **Aerts C.**, **Ruymaekers E.**, **Henrichs H.F.**, 1997, A&AS 121, 343, *Line-profile variations due to adiabatic non-radial pulsations in rotating stars. I. Observable characteristics of spheroidal modes*

Slettebak A., **Collins G.W.**, **Parkinson T.D.**, **Boyce P.B.**, **White N.M.**, 1975, ApJS 29, 137, *A system of standard stars for rotational velocity determinations*

Smith K.C., 1997, A&A 319, 928, *Elemental abundances in normal late-B and HgMn stars from co-added IUE spectra V. Mercury.*

Smith K.C., **Dworetsky M.M.**, 1993, A&A 274, 335, *Abundances in normal late-B and HgMn stars*

Smith M.A., 1977, ApJ 215, 574, *Nonradial pulsations in early to mid-B stars*

Stellingwerf R.F., 1978, ApJ 224, 953, *Period determination using phase dispersion minimization*

Tikhonov A.N., 1963, Soviet Math. Dokl. 4, 1624

Tokovinin A.A., 1997, A&AS 124, 75, *MSC - a catalogue of physical multiple stars*

Townsend R.H.D., 1997, MNRAS 284, 839, *Spectroscopic modelling of non-radial pulsation in rotating early-type stars*

van Hoof A., 1975, Informational Bulletin on Variable Stars 992, 1

Vanicek P., 1971, Ap&SS 12, 10, *Further development and properties of the spectral analysis by least-squares*

Wade R.A., **Rucinski S.M.**, 1985, A&ASS 60, 471, *Linear and quadratic limb-darkening coefficients for a large grid of LTE model atmospheres*

Waelkens C., **Aerts C.**, **Kestens E.**, **Grenon M.**, **Eyer L.**, 1998, A&A 330, 215, *Study of an unbiased sample of B stars observed with Hipparcos: the discovery of a large amount of new slowly pulsating B stars*

Waelkens C., 1991, A&A 246, 453, *Slowly pulsating B stars*

Waelkens C., **Rufener F.**, 1985, A&A 152, 6, *Photometric variability of mid-B stars*

Watson R.D., 1988, Ap&SS 140, 255, *Contributing factors to flux changes in nonradial stellar pulsations*

Wolff S.C., 1978, ApJ 222, 556, *Duplicity of late B-type stars*

Publications in proceedings of conferences

Aerts C., **Lehmann H.**, **Scuflaire R.**, **Dupret M.A.**, **Briquet M.**, **De Ridder J.**, **Thoul A.**, 2003, in "Asteroseismology across the HR diagram", Kluwer Academic Publishers, in press, *Mode identification and seismic modelling of the β Cep star EN (16) Lac*

Briquet M., **Aerts C.**, 2003, in "Asteroseismology across the HR diagram", Kluwer Academic Publishers, in press and ASP Conference Series, Vol. 292, p. 365, *A new version of the moment method, optimized for mode identification in multiperiodic stars*

Mathias P., **Le Contel J.M.**, **Aerts C.**, **De Cat P.**, **Van Winckel H.**, **Robbrecht E.**, **Briquet M.**, **Cuypers J.**, 2002, ASP Conference Series, Vol. 259, p. 232, *Spectroscopic monitoring of 10 northern SPB candidates*

Briquet M., **Aerts C.**, **Mathias P.**, **Noels A.**, 2002, ASP Conference Series, Vol. 259, p. 234, *The slowly pulsating B star HD 147394*

Briquet M., **Aerts C.**, **De Cat P.**, **Scuflaire R.**, 2002, ASP Conference Series, Vol. 259, p. 266, *Detailed line-profile modeling of B stars with chemical inhomogeneities*

Aerts C., **De Cat P.**, **De Ridder J.**, **Kolenberg K.**, **Waelkens C.**, **Mathias P.**, **Briquet M.**, 2000, ASP Conference Series, Vol. 203, p. 395, *Long-term photometric and spectroscopic monitoring of slowly pulsating B stars*

Briquet M., **Aerts C.**, **De Cat P.**, 2000, ASP Conference Series, Vol. 203, p. 437, *Optical variability of the λ Eri star HD 105382: pulsation or rotation?*

Publications in international refereed journals

Thoul A., **Scuflaire R.**, **Noels A.**, **Vatovez B.**, **Briquet M.**, **Dupret M.A.**, **Montalban J.**, 2003, A&A 402, 293, *A new seismic analysis of α Centauri*

Briquet M., **Aerts C.**, **Mathias P.**, **Scuflaire R.**, **Noels A.**, 2003, A&A 401, 281, *Spectroscopic mode identification for the slowly pulsating B star HD 147394*

Aerts C., **Lehmann H.**, **Briquet M.**, **Scuflaire R.**, **Dupret M.A.**, **De Ridder J.**, **Thoul A.**, 2003, A&A 399, 639, *Spectroscopic mode identification for the β Cephei star EN (16) Lacertae*

Briquet M., **Aerts C.**, 2003, A&A 398, 687, *A new version of the moment method, optimized for mode identification in multiperiodic stars*

Briquet M., **De Cat P.**, **Aerts C.**, **Scuflaire R.**, 2001, A&A 380, 177, *The B-type variable HD 131120 modelled by rotational modulation*

Mathias P., **Aerts C.**, **Briquet M.**, **De Cat P.**, **Cuypers J.**, **Van Winckel H.**, **Le Contel J.M.**, 2001, A&A 379, 905, *Spectroscopic monitoring of 10 new northern slowly pulsating B star candidates discovered from the HIPPARCOS mission*

Briquet M., **Aerts C.**, **De Cat P.**, 2001, A&A 366, 121, *Optical variability of the B-type star HD 105382: pulsation or rotation?*